

# CMS Draft Analysis Note

*The content of this note is intended for CMS internal use and distribution only*

2020/12/28

Archive Hash: a528e14-D

Archive Date: 2020/12/28

## Search for a light charged Higgs boson in the $H^+ \rightarrow c\bar{s}$ channel with lepton+jets final states at 13 TeV

S.R. Dugad<sup>1</sup>, G. Kole<sup>3</sup>, G.B. Mohanty<sup>1</sup>, A. Nayak<sup>2</sup>, and R.K. Verma<sup>1</sup>

<sup>1</sup> Tata Institute of Fundamental Research, Mumbai, India

<sup>2</sup> Institute of Physics, Bhubaneswar, India

<sup>3</sup> University of California San Diego, USA

### Abstract

A search is conducted for a low-mass charged Higgs boson produced in a top quark decay and subsequently decaying into a charm and an antistrange quark. The data sample was recorded in proton-proton collisions at  $\sqrt{s} = 13$  TeV by the CMS experiment at the LHC and corresponds to an integrated luminosity of  $35.9 \text{ fb}^{-1}$ . The signal search is conducted in the process of top-quark pair production, where one top quark decays to a bottom quark and a charged Higgs boson, and the other to a bottom quark and a W boson. With the W boson decaying to a charged lepton (electron or muon) and a neutrino, the final state comprises an isolated lepton, missing transverse momentum, and at least four jets, of which two are tagged as b jets. To enhance the search sensitivity, one of the jets originating from the charged Higgs boson is required to satisfy a charm tagging requirement. No significant excess beyond standard model predictions is found in the dijet invariant mass distribution. An upper limit in the range 0.26–1.68% is set on the branching fraction of the top quark decay to the charged Higgs boson and bottom quark for a Higgs mass between 80 and 160 GeV.

This box is only visible in draft mode. Please make sure the values below make sense.

PDFAuthor: S.R. Dugad, G. Kole, G.B. Mohanty, A. Nayak, R.K. Verma

PDFTitle: Search for a light charged Higgs boson in the  $H^+$  to  $c\bar{s}$ -bar channel with lepton + jets final states at 13 TeV with 2016 data

PDFSubject: CMS

PDFKeywords: CMS, physics, software, computing

Please also verify that the abstract does not use any user defined symbols



## 1 Contents

2	1	Introduction . . . . .	3
3	2	Search strategy at 13 TeV . . . . .	6
4	3	Data and Simulated Samples . . . . .	10
5	3.1	Data Samples . . . . .	10
6	3.2	Simulated Samples . . . . .	10
7	4	Physics Object Reconstruction and Selection . . . . .	15
8	4.1	Primary Vertex and Diffuse Offset Energy Density . . . . .	15
9	4.2	Muon . . . . .	16
10	4.3	Electron . . . . .	20
11	4.4	Jet . . . . .	22
12	4.5	Missing Transverse Energy . . . . .	23
13	5	b-jet Tagging . . . . .	23
14	5.1	Track Selection . . . . .	24
15	5.2	Reconstruction of Secondary Vertex . . . . .	24
16	5.3	Multi-layer Perceptron Training . . . . .	24
17	6	Kinematic fit . . . . .	25
18	6.1	Input to the TopKinFitter . . . . .	26
19	6.2	Separation of jets . . . . .	28
20	6.3	Kinematic constraints . . . . .	28
21	6.4	Chi-square of the fit . . . . .	28
22	6.5	Output of the KinFit . . . . .	29
23	6.6	Selection and Performance . . . . .	29
24	7	c-jet Tagging . . . . .	30
25	8	Corrections on MC . . . . .	31
26	8.1	Luminosity Scale Factors . . . . .	31
27	8.2	Pileup Reweighting . . . . .	31
28	8.3	Lepton Scale Factors . . . . .	33
29	8.4	Jet and MET Correction . . . . .	33
30	8.5	b-tag Scale Factor . . . . .	37
31	8.6	c-tag Scale Factor . . . . .	37
32	9	Event Filters and Triggers . . . . .	38
33	9.1	Filters . . . . .	38
34	9.2	Triggers . . . . .	39
35	10	Event Selection . . . . .	39
36	11	QCD Multijet Estimation . . . . .	44
37	11.1	Determination of transfer scale factor . . . . .	44
38	11.2	Estimation of QCD multijet in the signal region . . . . .	48
39	11.3	Comparison of data-driven QCD multijet shapes . . . . .	48
40	12	Control Plots in Signal Region . . . . .	51
41	13	Mass Reconstruction . . . . .	58
42	14	Systematic Uncertainties . . . . .	60
43	14.1	Experimental Uncertainties . . . . .	60

44	14.2	Theoretical Uncertainties . . . . .	61
45	15	Categorization of Events . . . . .	63
46	15.1	Inclusive Event Category without charm-jet Tagging . . . . .	63
47	15.2	Inclusive Event Category with Loose charm-jet Tagging . . . . .	63
48	15.3	Exclusive Event Categories Based on charm-jet Tagging . . . . .	66
49	16	Post-fit Analysis from Charm Categories . . . . .	73
50	16.1	Profile of Nuisance Parameter: shape vs lnN . . . . .	73
51	16.2	Distributions of Pulls . . . . .	75
52	16.3	Post-fit Yields and Distributions . . . . .	75
53	16.4	Corelation Among the Nuisance Parameters . . . . .	85
54	17	Goodness of Fit . . . . .	87
55	18	Exclusion Limits . . . . .	90
56	18.1	Limits from inclusive event category without c tagging . . . . .	90
57	18.2	Limits from inclusive event category with loose c tagging . . . . .	92
58	18.3	Limits from exclusive event categories based on c tagging . . . . .	92
59	19	Conclusion . . . . .	96
60	A	Background Contribution from SM Higgs Production Process . . . . .	103
61	B	MadGraph vs POWHEG Sample . . . . .	103
62	C	Event Categorization in Bins of b-jet pT . . . . .	108
63	D	Data, MC Comparison in Low MET Region . . . . .	108
64	E	Effect of Systematics on dijet Distributions . . . . .	114
65	F	Impact of Uncertainties: Multi-dimensional Fit . . . . .	114
66	G	Useful Commands . . . . .	124
67	H	2 DeltaNLL vs NPs: Multi-dimensional Fit . . . . .	126
68	I	Revision history of the Analysis Note . . . . .	127

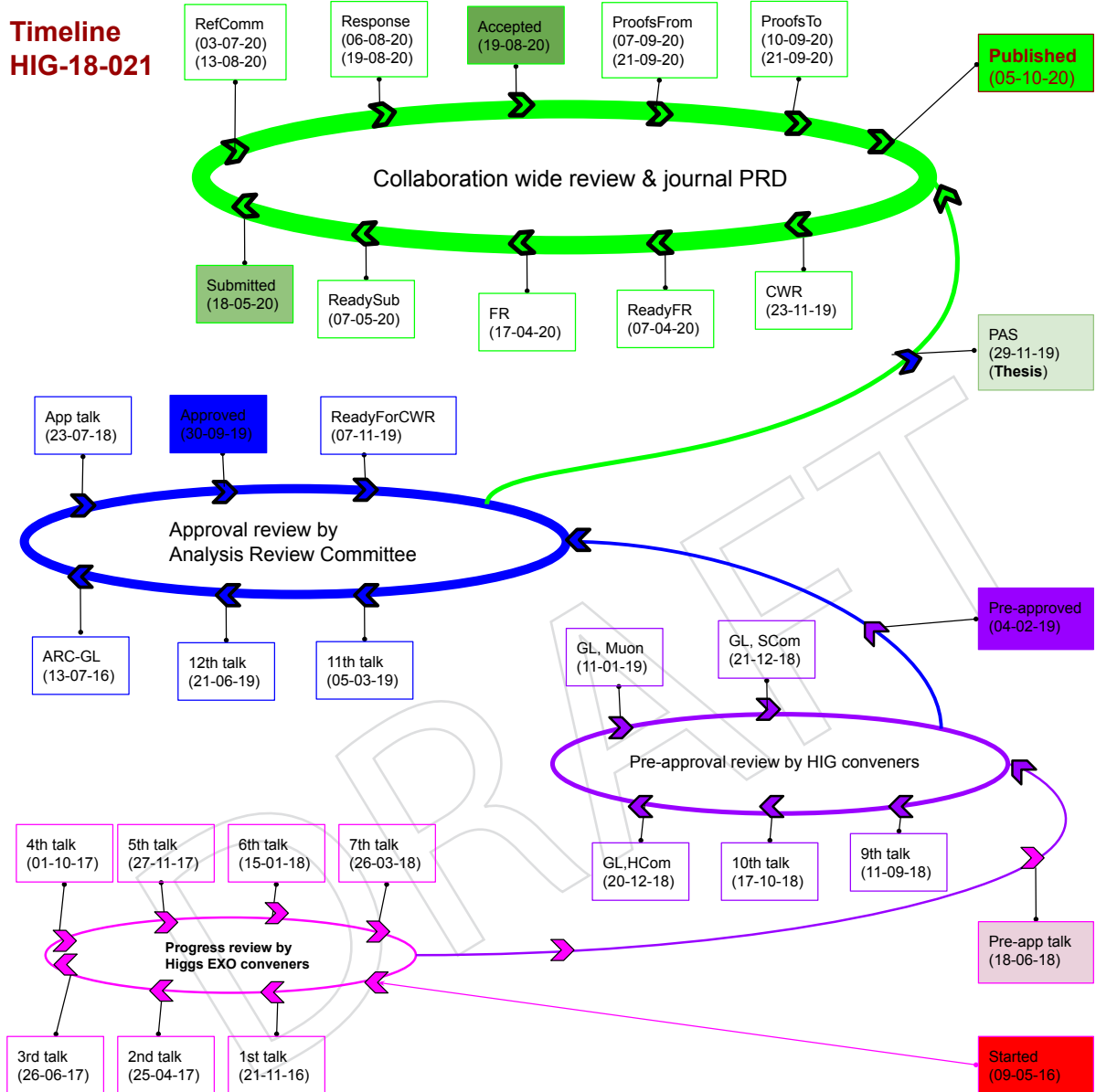
## 69 1 Introduction

70 The discovery of the Higgs Boson in 2012 by CMS [1] and ATLAS [2] experiments at the LHC  
71 open up a new era in the field of High Energy Physics. The Higgs Boson may only be one  
72 of the many fundamental scalar particles present in nature. Most extensions of the Standard  
73 Model, such as supersymmetry [3–5], predict several scalars. The two Higgs doublet model  
74 (2HDM) [6] which postulates the presence of an additional  $SU(2)_L$  scalar doublet is a well-  
75 motivated extension of the Standard Model. It may be considered as an effective low energy  
76 model of many models such as the minimal supersymmetric standard model (MSSM) [7]. The  
77 model leads to very rich phenomenology and has been studied in considerable detail both  
78 theoretically and experimentally.

79 The 2HDM postulates two scalar  $SU(2)_L$  doublets with same quantum numbers. After sponta-  
80 neous symmetry breaking it leads to five physical scalar particles out of which three are neutral  
81 ( $H, h, A$ ) and two charged  $H^\pm$ . The model can be divided into different categories depending  
82 on the interaction of the two Higgs doublets with quarks and leptons. For example, in Type  
83 I the fermions have Yukawa couplings only to the second doublet. The nature of the Yukawa  
84 couplings determines the branching fraction of the charged Higgs into different final states.  
85 Here we shall be interested in the decay channel  $H^+ \rightarrow c\bar{s}$  (and its charge conjugate). The  
86 branching fraction for this channel ranges anywhere from 0 to 100% depending on the choice  
87 of Yukawa couplings for the two Higgs doublets. It depends on the parameter  $\tan\beta = v_2/v_1$   
88 where  $v_1$  and  $v_2$  are the vacuum expectation values of the two Higgs doublets. In Minimal  
89 Supersymmetry Model (MSSM) for low values of  $\tan\beta$  this is the dominant decay channel [7].  
90 The branching ratio of charged Higgs decaying to various channel as a function of  $\tan\beta$  for  
91 different masses of charged Higgs are shown in Figure (1). In our analysis, we shall assume  
92 that  $\mathcal{BR}(H^+ \rightarrow c\bar{s}) = 100\%$ .

93 There have been many earlier searches for charged Higgs at LEP, Tevatron, and LHC. At LEP it  
94 is dominantly produced by the process  $e^+e^- \rightarrow H^+H^-$ . The search is conducted by assuming  
95 that it decays only to  $c\bar{s}$  and  $\tau\nu_\tau$ . Assuming that the sum of the branching fractions  $\mathcal{BR}(H^+ \rightarrow$   
96  $\tau^+\nu_\tau) + \mathcal{BR}(H^+ \rightarrow c\bar{s}) = 1$ , a lower limit of 79.3 GeV is obtained for the charged Higgs mass at  
97 95% confidence level [8–10]. Under a more general assumption  $\mathcal{BR}(H^+ \rightarrow \tau^+\nu_\tau) + \mathcal{BR}(H^+ \rightarrow$   
98  $q\bar{q}) = 1$ , a slightly less stringent constraint of 76.3 GeV is obtained at 95% confidence level [11].

99 The hadron colliders at Fermilab and LHC have also imposed limits on charged Higgs param-  
100 eters assuming the production mode  $t \rightarrow H^+b$ . The CDF collaboration [12] has set a 95% CL  
101 upper limit on the branching fraction  $\mathcal{BR}(t \rightarrow H^+b) < 10 - 30\%$  for the charged Higgs lying  
102 in the mass range 60 – 150 GeV assuming that  $H^+$  decays dominantly to  $c\bar{s}$ . Similar limits  
103 have been obtained by the D0 [13] experiment. Using the 7 TeV data, the ATLAS collaboration  
104 has set 95% CL upper limit on the product  $\mathcal{BR}(t \rightarrow H^\pm b) \times \mathcal{BR}(H^\pm \rightarrow \tau^\pm\nu) < 0.23 - 1.3\%$   
105 for the charged Higgs mass in the range 80-160 GeV. [14]. The search for charged Higgs Bo-  
106 son decaying into the  $c\bar{s}$  was performed at 8 TeV in the CMS which set 95% CL upper limit  
107 on  $\mathcal{BR}(t \rightarrow H^+b)$  in the range 1.2-6.5% [15]. The analysis presented in this note is carried  
108 out at 13 TeV with pp collision data in the CMS experiments recorded in 2016. The integrated  
109 luminosity of this dataset is  $35.9 \text{ fb}^{-1}$ .



Advancement of the analysis at various review stages. As a continuation of 8 TeV analysis, which was published on 29th December 2015 in the journal JHEP, this analysis at 13 TeV started in early 2016. The first progress report in the Higgs-Exotica meeting was presented on 21st November 2016. The date on which this analysis was presented during pre-approval, approval, collaboration wide review, final reading, and publication in the journal PRD is shown in this figure.

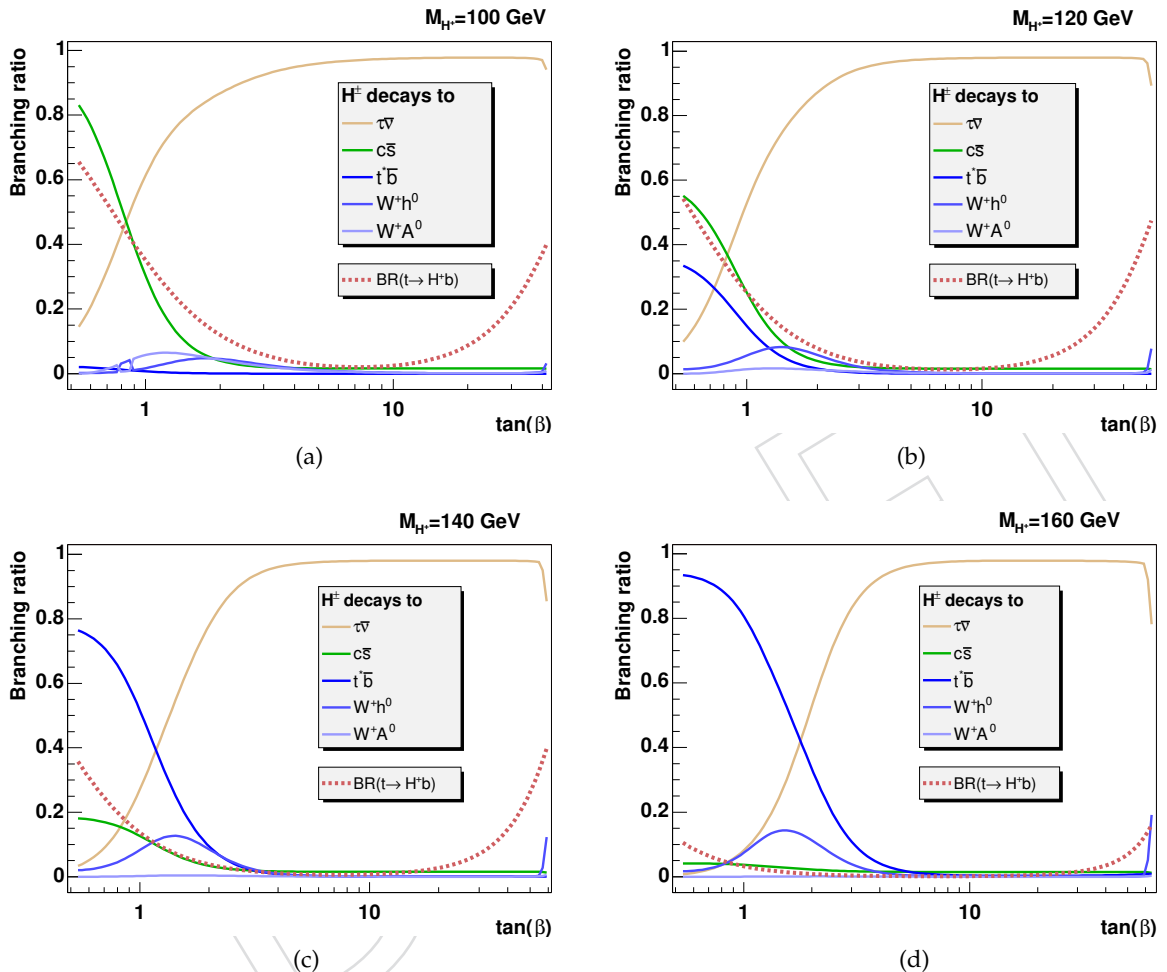


Figure 1: The branching ratio of charged Higgs decaying to various channel as a function of  $\tan\beta$  for different masses of charged Higgs. For low  $\tan\beta$  ( $< 1$ ) the  $\mathcal{BR}(H^+ \rightarrow c\bar{s})$  is the dominant at lower charged Higgs masses (100 GeV, 120 GeV). However, for higher charged Higgs masses (140 GeV, 160 GeV), the  $\mathcal{BR}(t \rightarrow H^+ b)$  becomes dominant for low  $\tan\beta$ . These figures are taken from [16].

## 110 2 Search strategy at 13 TeV

111 The search for the charged Higgs boson in the  $c\bar{s}$  channel at 13 TeV in the CMS experiment  
 112 adopted a similar strategy as that of the previous analysis at 8 TeV [15]. An additional charm  
 113 quark tagging have been further exploited to improve sensitivity. The invariant mass of the  
 114 jets originating from charm and strange antiquark is taken as the observable for the search of  
 115 charged Higgs, in the low mass region from 80 to 160 GeV. In the absence of an excess in the  
 116 observed data, a 95% CL limit is put on the  $\mathcal{B}(t \rightarrow H^+ b)$ . The charm tagging is extensively used  
 117 to improve this limit. As shown on the right side of the Figure 2, for the signal process, one  
 118 t quark decays to  $H^+ b$  and the other one to  $W^- \bar{b}$ . The  $W^+/H^+$  decays hadronically, whereas  
 119 the  $W^-$  decays leptonically. As a result, in the final states, there will be four jets (2 b jets, 1 c  
 120 jet, 1 s jet), one lepton (electron or muon,  $\tau$  is not considered) and missing transverse energy  
 121 attributed to neutrino. In this analysis, we assume that the  $\mathcal{B}(H^+ \rightarrow c\bar{s}) = 100\%$ .

122 The standard model processes that give same final states (4 jets + 1 lepton + missing energy)  
 123 are considered as backgrounds for this analysis. The standard model  $t\bar{t}$  production is the most  
 124 dominant, irreducible background process. As shown in the left side of the Figure 2, for SM  
 125  $t\bar{t}$  process, one t quark decays to the  $W^+$  and b quark ( $t \rightarrow W^+ b$ ) and the other decays to  
 126  $W^- \bar{b}$  ( $\bar{t} \rightarrow W^- \bar{b}$ ). The SM  $t\bar{t}$  contributes around 94% of the total backgrounds. Other sub-  
 127 dominant backgrounds that give rise to similar final states are single t quark production, QCD  
 128 multijet,  $W +$  jets,  $Z/\gamma +$  jets, and vector boson fusion processes. The following background  
 129 processes are considered for the search for charged Higgs. They are ordered in their significance  
 130 of contribution.

- 131 1. **SM  $t\bar{t} +$  jets:** Feynman diagrams for  $t\bar{t} +$  jets production are shown on the left hand side  
 132 of Figure 2. This is the most dominant background channel in the search for the signal  
 133 search region (SR).
- 134 2. **Single t:** The single t quark production process can also mimic the signal topology. Three  
 135 different ways, as shown in Figure 3, of production of single top quark considered in this  
 136 analysis. It is produced through s-channel, t-channel, and tW-channel. In the s-channel  
 137 and t-channel the initial quarks can be u, d, c and s (4-flavour scheme). However, in the  
 138 tW-channel, the initial quark is only b quark (5-flavor scheme).
- 139 3. **QCD multijet:** The QCD multijet events contain only jets at parton level. However, after  
 140 event reconstruction, they can still have leptons from misidentifications, and  $E_T^{\text{miss}}$  due  
 141 to poor measurement of energy in the detector. Thus these events also mimic the signal  
 142 topology.
- 143 4.  **$W +$  jets:** In this process, a W boson is produced in the proton-proton collisions which  
 144 subsequently decays leptonically ( $W^\pm \rightarrow l^\pm \nu(l^- \bar{\nu})$ ). The following  $W +$  jets background  
 145 process are considered in this analysis:
  - 146 (a)  $W +$  jets
  - 147 (b)  $W + 1$  jet
  - 148 (c)  $W + 2$  jets
  - 149 (d)  $W + 3$  jets
  - 150 (e)  $W + 4$  jets

151 The Feynman diagram for these processes are shown in Figure 4.

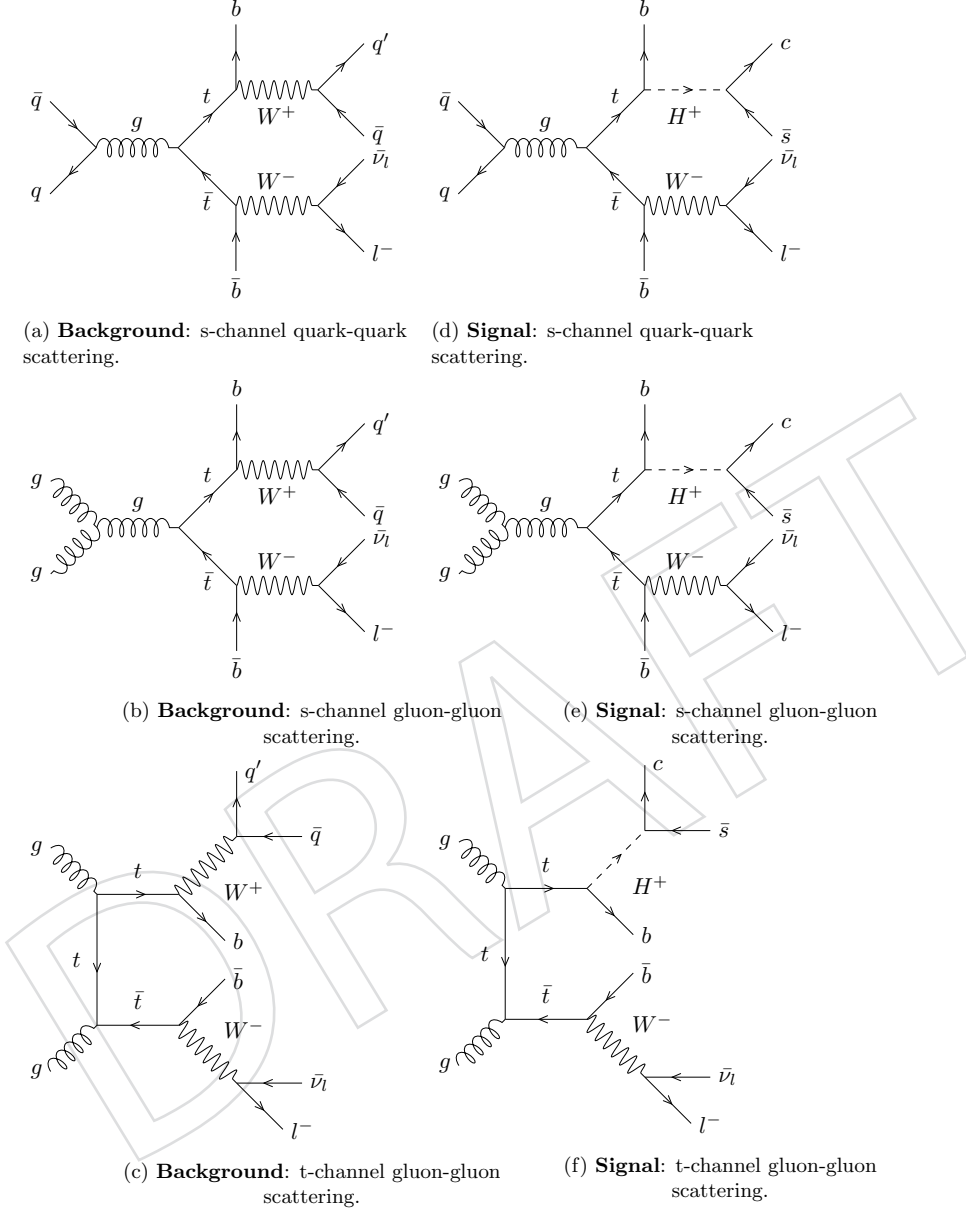


Figure 2: Production of  $t\bar{t}$  from gluon-gluon and quark-quark scattering. The quark-scattering production process has a dominant contribution at Tevatron energies whereas gluon-gluon scattering diagrams are dominant at LHC energies [17, 18]. The SM production of  $t\bar{t}$  is shown in (a), (b) and (c). The charged Higgs boson production and its decay are shown in (d), (e) and (f).

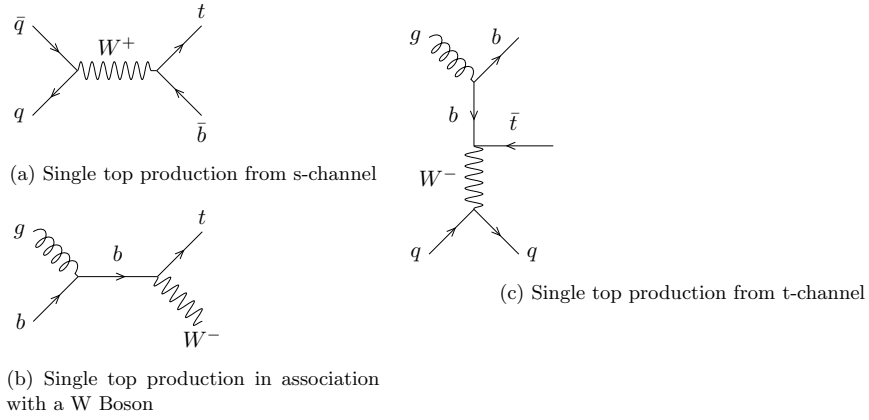


Figure 3: Representative Feynman diagrams for single t quark production processes.

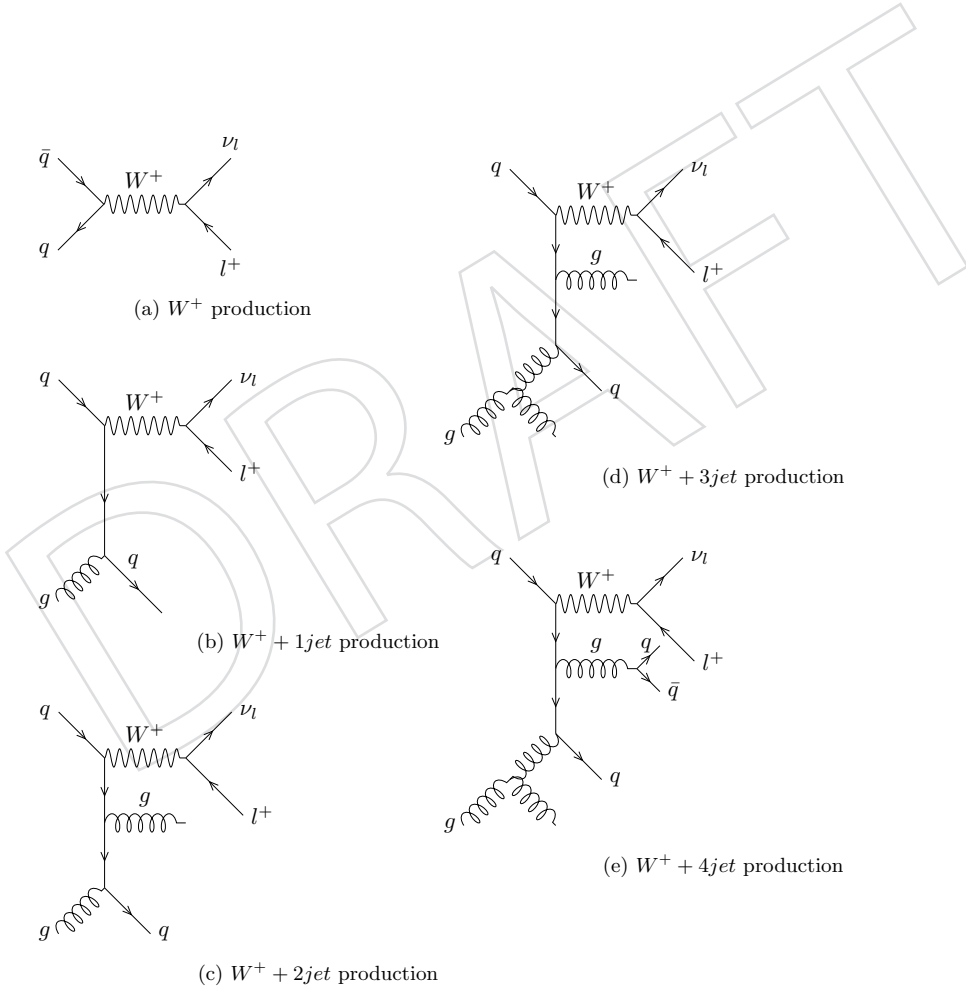


Figure 4: Representative Feynman diagrams for  $W + n$  jets channel. The  $W$  boson is produced by quark-quark and quark-gluon scattering along with  $n$  jets ( $n = 0, 1, 2, 3, 4$ ).

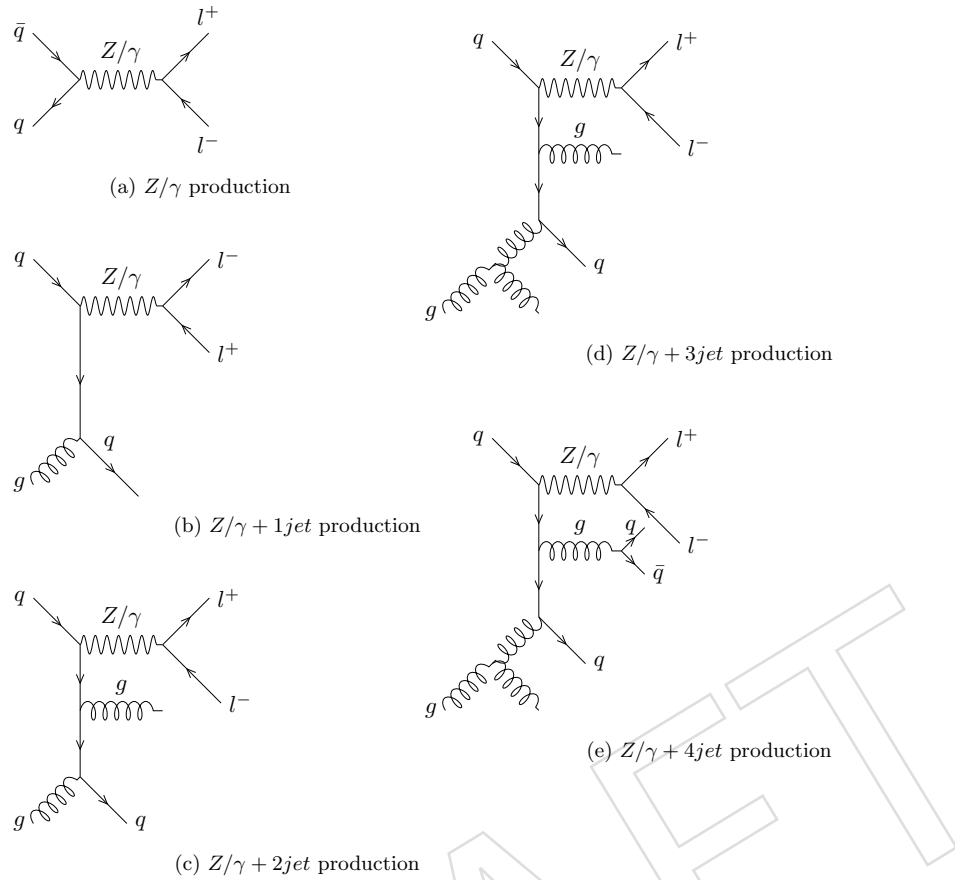


Figure 5: Representative Feynman diagrams for  $Z/\gamma + n$  jets channel. The  $Z/\gamma$  is produced by quark-quark and quark-gluon scattering along with  $n$  jets ( $n = 0, 1, 2, 3, 4$ ).

152     5.  **$Z/\gamma + \text{jets}$ :** The Drell-Yan processes in which  $Z/\gamma$  are produced along with jets, subse-  
 153       quently decaying to two leptons ( $Z/\gamma \rightarrow l^+ l^-$ ), have lepton and jets at parton level as  
 154       shown in Figure 5. However, after the reconstruction, the  $E_T^{\text{miss}}$  is also found in the events  
 155       due to the poor measurement of energy in the detector.

- 156       (a)  $Z/\gamma + \text{jets}$   
 157       (b)  $Z/\gamma + 1\text{ jet}$   
 158       (c)  $Z/\gamma + 2\text{ jets}$   
 159       (d)  $Z/\gamma + 3\text{ jets}$   
 160       (e)  $Z/\gamma + 4\text{ jets}$

161     6. **VV:** Vector boson fusion processes are the smallest background in the signal search re-  
 162       gion. The fusion happens via tri-linear coupling between the  $W^\pm$  and  $Z$ . The  $Z$  boson  
 163       further decays to  $l^+ l^-$ . The VV process has three sub-categories: WW, WZ, and ZZ. The  
 164       vector Boson fusion process is shown in Figure 6.

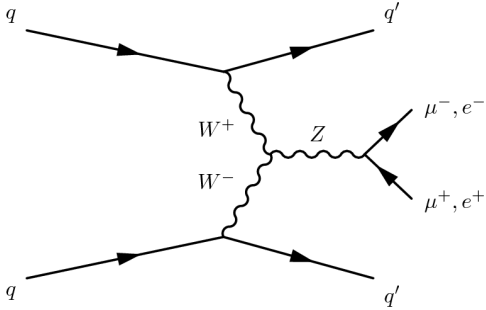


Figure 6: Representative Feynman diagram for vector Boson fusion process.

### 165 3 Data and Simulated Samples

#### 166 3.1 Data Samples

167 The reconstructed data is broadly divided into different event topologies. Only those  
 168 datasets matching with event topology under consideration are used for the analy-  
 169 sis. Such approach help in optimising the computing resources. The single muon  
 170 and single electron data sample used for this analysis are shown in Table (1). The  
 171 data was collected in 2016 corresponding to Run number 273158 to 284044. To se-  
 172 lect good quality data, where most of the sub-detectors of the CMS operates in a  
 173 normal condition; the following lumi mask, as recommended by the PdMV group is  
 174 applied: Cert\_271036-284044\_13TeV\_23Sep2016ReReco\_Collisions16\_JSON.txt.  
 175 The integrated luminosity after applying the mask reduces marginally from  $37.0\text{ fb}^{-1}$   
 176 to  $35.9\text{ fb}^{-1}$ . The luminosity is calculated using the Command (35). The global  
 177 tag 80X\_dataRun2\_2016SeptRepro\_v7 is used to process the MINIAOD data in the  
 178 CMSSW\_8\_0\_28 for the production of the *ntuples*. The same version of the CMSSW is used to  
 179 produce *ntuples* for data, background, and signal samples.

#### 180 3.2 Simulated Samples

181 The centrally produced official simulated samples are used in this analysis. Produc-  
 182 tion of most of the samples (except QCD\_Pt-15to20\_EMEnriched) started with cam-  
 183 paign RunIISummer16MiniAODv2 and final reconstruction was done with campaign  
 184 PUMoriond17 using Global Tag  
 185 80X\_mcRun2\_asymptotic\_2016\_TrancheIV\_v6. The simulated samples used in this  
 186 analysis are shown in Table (2) with corresponding cross-section and number of simulated  
 187 events. The k-factor is the ratio of cross-sections from next-to-leading-order and leading-order,  
 188  $k_f = \sigma_{\text{NLO}} / \sigma_{\text{LO}}$ .

189 The signal and background simulated samples are generated using MAD-  
 190 GRAPH5\_aMC@NLO [19, 20] as well as POWHEG [21–23] generators at parton level. These  
 191 parton level events are hadronised using PYTHIA [24, 25]. The hadronised events were tuned  
 192 using CUETP8M1 [26] which are then passed through GEANT4 [27] for detector simulation.  
 193 Finally, the events are reconstructed after complete detector simulation. In summary, the  
 194 following steps are followed to produce simulated samples for a single process:

##### 195 1. GEN-SIM:

- 196 • GEN: Physics process generation.
- 197 • SIM: Detector simulation.

Table 1: Muon and Electron data samples recorded in 2016 with an integrated luminosity  $35.9 \text{ fb}^{-1}$ . The re-reco campaign was used for Run B to Run G. For Run H, prompt reconstructions were used. The luminosity is calculated using `brilcalc` tool. Where M = MINIAOD.

<b>Dataset</b>	$L_{int} (\text{fb}^{-1})$	<b>Run</b>	<b>Events</b>
/SingleMuon/Run2016B-03Feb2017_ver2-v2/M	5.78	273158-275376	154054252
/SingleMuon/Run2016C-03Feb2017-v1/M	2.57	275657-276283	64718679
/SingleMuon/Run2016D-03Feb2017-v1/M	4.25	276315-276811	96657799
/SingleMuon/Run2016E-03Feb2017-v1/M	4.01	276831-277420	87362752
/SingleMuon/Run2016F-03Feb2017-v1/M	3.10	277981-278808	65047318
/SingleMuon/Run2016G-03Feb2017-v1/M	7.54	278820-280385	147945745
/SingleMuon/Run2016H-03Feb2017_ver2-v1/M	8.40	281613-284035	166591136
/SingleMuon/Run2016H-03Feb2017_ver3-v1/M	0.21	284036-284044	4389914
<b>Total</b>	<b>35.86</b>	<b>273158-284044</b>	<b>786767595</b>
/SingleElectron/Run2016B-03Feb2017_ver2-v2/M	5.78	273158-275376	237366108
/SingleElectron/Run2016C-03Feb2017-v1/M	2.57	275657-276283	91591087
/SingleElectron/Run2016D-03Feb2017-v1/M	4.25	276315-276811	146495223
/SingleElectron/Run2016E-03Feb2017-v1/M	4.01	276831-277420	113169852
/SingleElectron/Run2016F-03Feb2017-v1/M	3.10	277981-278808	70143321
/SingleElectron/Run2016G-03Feb2017-v1/M	7.54	278820-280385	152098617
/SingleElectron/Run2016H-03Feb2017_ver2-v1/M	8.40	281613-284035	123900510
/SingleElectron/Run2016H-03Feb2017_ver3-v1/M	0.21	284036-284044	3189661
<b>Total</b>	<b>35.86</b>	<b>273158-284044</b>	<b>937954379</b>

## 198    2. RECO:

- 199    • DIGIPREMIX\_S2:  
<https://twiki.cern.ch/twiki/bin/view/CMSPublic/SWGuideSimulation>,
- 200    • DATAMIX:  
<https://twiki.cern.ch/twiki/bin/view/CMSPublic/SWGuideSimulation>,
- 201    • L1: L1 trigger emulation,
- 202    • DIGI2RAW: Conversion of the digitised data format to raw data format,
- 203    • HLT: Applying high level trigger,
- 204    • RAW2DIGI: Conversion of the raw data format to DIGI data format,
- 205    • RECO: Reconstruction of physics object,
- 206    • EI: High-level reconstruction step used in validation.

## 209    3. MINIAOD: Re-reconstruction of physics object.

210    The  $t\bar{t} + \text{jets}$  channel is the most significant irreducible background for this analysis. It con-  
 211    tributes around 94% of the total backgrounds in the signal region. The parton level events for  
 212     $t\bar{t} + \text{jets}$  samples of Table 2 are generated using POWHEG [21–23] at next-to-leading (NLO) or-  
 213    der. The NNPDF30\_nlo\_as\_0118 [28] parton distribution function (PDF) was used for this  
 214    purpose. The partonic events were then hadronised using PYTHIA [24, 25]. To simulate this  
 215    channel at higher orders and to take care of non-perturbative effects,  $t\bar{t} + \text{jets}$  samples were  
 216    tuned with CUETP8M1 [26]. The NNLO cross section for  $t\bar{t} + \text{jets}$  process is estimated to be  
 217     $831.76 \pm^{20}_{29}$  (scale)  $\pm 35(\text{PDF} + \alpha_s)$  pb [29].

218    Initially, the  $t\bar{t} + \text{jets}$  sample was simulated using MadGraph generator ( /TTJets\_TuneCUETP8M1\_13TeV-madgraphMLM-pythia8/year+M, where year and M  
 219    are defined in Table (2). However, MadGraph-MLM sample was found to be improperly mod-  
 220    eled for high jet multiplicity due to which there was a surplus of 5% (4%) simulated events w.r.t.  
 221    observed data for muon (electron) + jets channel in the signal region as shown in Figure 57. In  
 222    view of this, the POWHEG  $t\bar{t} + \text{jets}$  sample is used in this analysis. Comparison of POWHEG  
 223    and Madgraph  $t\bar{t} + \text{jets}$  sample is described in Appendix B.

225    Single t quark samples are shown in Table 2, where a t quark is produced with jets in t-channel  
 226    ( $ST_t$ ), s-channel ( $ST_s$ ), and t W-channel ( $ST_{tW}$ ). The  $ST_{tW}$  and  $ST_t$  samples are pro-  
 227    duced using POWHEG + PYTHIA and CUETP8M1, where  $ST_{tW}$  has 5-flavor scheme whereas  
 228     $ST_t$ , has 4-flavor scheme and further, the t quark decays inclusively. The  $ST_s$  are generated  
 229    using MADGRAPH5\_aMC@NLO [20] in the 4-flavor scheme and was hadronised using PYTHIA.  
 230    The NLO cross section for single t process [30, 31] are shown in Table 2.

231    The inclusive  $W + \text{jets}$  and  $Z/\gamma + \text{jets}$  samples were generated using MADGRAPH5\_aMC@NLO  
 232    and are hadronised using PYTHIA. The MLM [32] technique was used to take care of dou-  
 233    ble counting. There are exclusive  $W + n$  jets and  $Z/\gamma + n$  jets samples available for  $n = 1,$   
 234    2, 3, 4. The inclusive ( $W + \text{jets}$  and  $Z/\gamma + \text{jets}$ ) and exclusive ( $W/Z/\gamma + n$  jets) samples  
 235    have our event topology i.e. 4 jets + 1 lepton +  $E_T^{\text{miss}}$ . Therefore, the inclusive and exclu-  
 236    sive samples are added appropriately to have more statistics. To avoid double counting, an  
 237    event weight based on luminosity and number of particles (NUP) including incoming, inter-  
 238    mediate, and outgoing at generator level is applied to each sample. After that, the final event  
 239    yields from each of them are added linearly. The event weight for  $NUP = 5, 6, 7, 8$ , and  $\geq 9$  is  
 240     $L_{\text{data}}/(L_{W+\text{jets}})$ ,  $L_{\text{data}}/(L_{W+\text{jets}} + L_{W+1\text{jet}})$ ,  $L_{\text{data}}/(L_{W+\text{jets}} + L_{W+2\text{jet}})$ ,  
 241     $L_{\text{data}}/(L_{W+\text{jets}} + L_{W+3\text{jet}})$ ,  $L_{\text{data}}/(L_{W+\text{jets}} + L_{W+4\text{jet}})$ , respectively. Where, for example,  $L_{W+\text{jets}}$  is the generated lumino-  
 242    sity (number of events divided by the cross section) of  $W + \text{jets}$  sample. A similar procedure is

followed to add  $Z/\gamma + n$  jets with  $Z/\gamma + \text{jets}$ . However, the NUP variable does not count the intermediate photon as the status of photon is not displayed in the LHE event file. Hence it is incremented by 1 when a  $Z$  boson is not the intermediate particle. The NLO cross section for these processes are shown in Table 2.

The vector boson fusion process ( $WW$ ,  $WZ$ , and  $ZZ$ ) samples are generated and hadronised using PYTHIA and are tuned using CUETP8M1. The NLO cross section for these samples are shown in Table 2.

The muon (electron) enriched QCD multijet samples are used for  $\mu + \text{jets}$  ( $e + \text{jets}$ ) channel. These samples are generated using PYTHIA and CUETP8M1. After multiplying with filter efficiency, the NLO cross sections are shown in Table 2. From this table, it can be seen that the luminosity for these samples are significantly smaller as compared to the observed luminosity and therefore, a data-driven approach is used to make more precise estimation of QCD multijet background.

The charged Higgs signal samples were generated using MADGRAPH5\_aMC@NLO, and hadronized using PYTHIA. The signal sample for several mass points in the range of 80 to 160 GeV (80, 90, 100, 120, 140, 150, 155, 160) are generated for the search for charged Higgs. The cross section for the signal is  $831.76 \times 0.2132$  pb, where 831.76 pb is the inclusive (fully-hadronic, fully-leptonic, semi-leptonic)  $t\bar{t} + \text{jets}$  production cross section and factor 0.2132 is the branching fraction of  $W^- \rightarrow l^-\bar{\nu}_l$  (where  $l = \mu, e, \tau$  is not considered in this analysis) [33]. The factor 0.2132 is multiplied because  $t\bar{t}$  decays semi-leptonically ( $(t \rightarrow H^+ b, H^+ \rightarrow c\bar{s})$ ,  $(\bar{t} \rightarrow W^- \bar{b}, W^- \rightarrow l^-\bar{\nu}_l)$ ), where  $l = \mu, e$  in the charged Higgs signal samples. Furthermore, the signal events are scaled by the maximum observed upper limit obtained at 8 TeV. The upper observed limit on  $\mathcal{B}(t \rightarrow H^+ b)$  is 6.5% for the  $m_{H^+} = 90$  GeV [15]. Therefore, the signal samples are scaled by a factor  $2 \times 0.065 \times (1 - 0.065) = 0.12155$  in every plot and table except in the data cards used for limit computation.

In the  $t\bar{t} + \text{jets}$  samples, the NLO matrix element parton shower matching is varied by the damping parameter ( $h_{\text{damp}}$ ). Additional  $t\bar{t} + \text{jets}$  samples are generated by varying  $h_{\text{damp}}$  up and down and are used to observe the effect of  $h_{\text{damp}}$ . Similarly,  $t\bar{t} + \text{jets}$  samples where the renormalization and factorisation scales have been varied up and down are used to evaluate the uncertainties due to these scales. Also, alternate  $t\bar{t} + \text{jets}$  samples with  $m_t = 171.5$  and 173.5 GeV are considered to observe the effect of mass of the t quark. All the additional  $t\bar{t} + \text{jets}$  samples used for systematics study are shown in Table 3.

Table 2: Signal and background simulated samples. Where  
 $\text{run} = \text{RunIISummer16MiniAODv2-PUMoriond17\_80X\_mcRun2\_asymptotic\_2016\_TrancheIV\_v6}$ ,  
 $\text{run2} = \text{RunIISpring16MiniAODv2-FlatPU8to37HcalNZSRAW\_withHLT\_80X\_mcRun2\_asymptotic\_v14-v1}$ ,  
 $M = /MINIAODSIM$ ,  $yext1\_v2 = \text{run\_ext1-v2}$ ,  $yext1\_v1 = \text{run\_ext1-v1}$ ,  $\text{year} = \text{run-v1}$ .

MC Dataset	$\sigma$ (pb)(Order)	$k_f$	Events
/TT_TuneCUETP8M2T4_13TeV-powheg-pythia8/+year+M	$831.76_{-29}^{+20} \pm 35(\text{NNLO})$	—	77081156
/ST_tW_antitop_5f_inclusiveDecays_13TeV-powheg-pythia8_TuneCUETP8M1/+yext1_v1+M	$71.7 \pm 1.80 \pm 3.40(\text{NLO})$	—	6933094
/ST_t-channel_antitop_4f_inclusiveDecays_13TeV-powhegV2-madspin-pythia8_TuneCUETP8M1/+year+M	$80.95_{-5.2}^{+5.8} \pm 0.16(\text{NLO})$	—	38811017
/ST_s-channel_4f_InclusiveDecays_13TeV-amcatnlo-pythia8/+year+M	$10.32_{-0.5}^{+0.6} \pm 0.01(\text{NLO})$	—	2989199
/WJetsToLNu_TuneCUETP8M1_13TeV-madgraphMLM-pythia8/+year+M	$50690 \pm 389.1(\text{LO})$	1.21	29181900
/W1JetsToLNu_TuneCUETP8M1_13TeV-madgraphMLM-pythia8/+year+M	$9493 \pm 25.52(\text{LO})$	1.21	44813600
/W2JetsToLNu_TuneCUETP8M1_13TeV-madgraphMLM-pythia8/+year+M	$3120 \pm 78.5(\text{LO})$	1.21	29878415
/W3JetsToLNu_TuneCUETP8M1_13TeV-madgraphMLM-pythia8/+year+M	$942.3 \pm 36.8(\text{LO})$	1.21	19798117
/W4JetsToLNu_TuneCUETP8M1_13TeV-madgraphMLM-pythia8/+year+M	$524.2 \pm 23.6(\text{LO})$	1.21	9170576
/DYJetsToLL_M-50_TuneCUETP8M1_13TeV-madgraphMLM-pythia8/+yext1_v2+M	$4895 \pm 41(\text{LO})$	1.17	48103700
/DY1JetsToLL_M-50_TuneCUETP8M1_13TeV-madgraphMLM-pythia8/+year+M	$1016 \pm 16.8(\text{LO})$	1.17	62079400
/DY2JetsToLL_M-50_TuneCUETP8M1_13TeV-madgraphMLM-pythia8/+year+M	$331.3 \pm 8.5(\text{LO})$	1.17	19970551
/DY3JetsToLL_M-50_TuneCUETP8M1_13TeV-madgraphMLM-pythia8/+year+M	$96.6 \pm 3.9(\text{LO})$	1.17	5856110
/DY4JetsToLL_M-50_TuneCUETP8M1_13TeV-madgraphMLM-pythia8/+year+M	$51.4 \pm 2.5(\text{LO})$	1.17	4197868
/WW_TuneCUETP8M1_13TeV-pythia8/+year+M	$118.7_{-2.2}^{+2.5}(\text{NNLO})$	—	994012
/WZ_TuneCUETP8M1_13TeV-pythia8/+year+M	$46.74_{-1.5}^{+1.9}(\text{NLO})$	—	1000000
/ZZ_TuneCUETP8M1_13TeV-pythia8/+year+M	$17.72_{-0.4}^{+0.6}(\text{NLO})$	—	990064
/QCD_Pt-15to20_MuEnrichedPt5_TuneCUETP8M1_13TeV_pythia8/+year+M	$3819570(\text{NLO})$	—	4141251
/QCD_Pt-20to30_MuEnrichedPt5_TuneCUETP8M1_13TeV_pythia8/+year+M	$2960198(\text{NLO})$	—	31475157
/QCD_Pt-30to50_MuEnrichedPt5_TuneCUETP8M1_13TeV_pythia8/+year+M	$1652471(\text{NLO})$	—	29954815
/QCD_Pt-50to80_MuEnrichedPt5_TuneCUETP8M1_13TeV_pythia8/+year+M	$437504(\text{NLO})$	—	19806915
/QCD_Pt-80to120_MuEnrichedPt5_TuneCUETP8M1_13TeV_pythia8/+year+M	$106033(\text{NLO})$	—	13786971
/QCD_Pt-120to170_MuEnrichedPt5_TuneCUETP8M1_13TeV_pythia8/+year+M	$25190(\text{NLO})$	—	8042721
/QCD_Pt-170to300_MuEnrichedPt5_TuneCUETP8M1_13TeV_pythia8/+year+M	$8654(\text{NLO})$	—	7947159
/QCD_Pt-300to470_MuEnrichedPt5_TuneCUETP8M1_13TeV_pythia8/+year+M	$797(\text{NLO})$	—	7937590
/QCD_Pt-20to30_EMEEnriched_TuneCUETP8M1_13TeV_pythia8/+year+M	$5352960(\text{NLO})$	—	9218954
/QCD_Pt-30to50_EMEEnriched_TuneCUETP8M1_13TeV_pythia8/+year+M	$9928000(\text{NLO})$	—	4730195
/QCD_Pt-50to80_EMEEnriched_TuneCUETP8M1_13TeV_pythia8/+year+M	$2890800(\text{NLO})$	—	22337070
/QCD_Pt-80to120_EMEEnriched_TuneCUETP8M1_13TeV_pythia8/+year+M	$350000(\text{NLO})$	—	35841783
/QCD_Pt-120to170_EMEEnriched_TuneCUETP8M1_13TeV_pythia8/+year+M	$62964(\text{NLO})$	—	35817281
/QCD_Pt-170to300_EMEEnriched_TuneCUETP8M1_13TeV_pythia8/+year+M	$18810(\text{NLO})$	—	11540163
/QCD_Pt-300toInf_EMEEnriched_TuneCUETP8M1_13TeV_pythia8/+year+M	$1350(\text{NLO})$	—	7373633
/ChargedHiggsToCS_M080_13TeV-madgraph/+year+M	$0.2132 \times 831.76(\text{NNLO})$	—	996170
/ChargedHiggsToCS_M090_13TeV-madgraph/+year+M	$0.2132 \times 831.76(\text{NNLO})$	—	994498
/ChargedHiggsToCS_M100_13TeV-madgraph/+year+M	$0.2132 \times 831.76(\text{NNLO})$	—	987730
/ChargedHiggsToCS_M120_13TeV-madgraph/+year+M	$0.2132 \times 831.76(\text{NNLO})$	—	990645
/ChargedHiggsToCS_M140_13TeV-madgraph/+year+M	$0.2132 \times 831.76(\text{NNLO})$	—	952984
/ChargedHiggsToCS_M150_13TeV-madgraph/+year+M	$0.2132 \times 831.76(\text{NNLO})$	—	992264
/ChargedHiggsToCS_M155_13TeV-madgraph/+year+M	$0.2132 \times 831.76(\text{NNLO})$	—	976710
/ChargedHiggsToCS_M160_13TeV-madgraph/+year+M	$0.2132 \times 831.76(\text{NNLO})$	—	988480

Table 3:  $t\bar{t}$  + jets samples used for systematics study. Where M = MINIAODSIM, year = run-v1, run = `RunIISummer16MiniAODv2-PUMoriond17_80X_mcRun2_asymptotic_2016_TrancheIV_v6`.

MC Dataset for Systematics	$\sigma$ (pb)	Events
/TT_TuneCUETP8M2T4up_13TeV-powheg-pythia8/+year+M	730	29310620
/TT_TuneCUETP8M2T4down_13TeV-powheg-pythia8/+year+M	730	28354188
/TT_TuneCUETP8M2T4_mttop1735_13TeV-powheg-pythia8/+year+M	711	19419050
/TT_TuneCUETP8M2T4_mttop1715_13TeV-powheg-pythia8/+year+M	750	19578812
/TT_hdampUP_TuneCUETP8M2T4_13TeV-powheg-pythia8/+year+M	750	29689380
/TT_hdampDOWN_TuneCUETP8M2T4_13TeV-powheg-pythia8/+year+M	750	29117820

## 275 4 Physics Object Reconstruction and Selection

276 The physics objects of our interest are primary and secondary vertex, lepton and jets, missing  
 277 transverse energy and particle/jet id. The Particle Flow (PF) algorithm [34, 35] is used to re-  
 278 construct these objects. Four-momentum of final state objects is tuned by applying top mass  
 279 constraint using kinematic fitting package. This helps in improving the dijet mass resolution.  
 280 Reconstruction of primary and secondary vertex, physics objects, b-tagging, c-tagging, and  
 281 kinematic fitting are described in the following sections.

### 282 4.1 Primary Vertex and Diffuse Offset Energy Density

#### 283 4.1.1 Primary Vertex

284 To reconstruct a primary vertex (PV) following three steps are performed [36]:

- 285 • **track selection:** Primary vertices are associated with a large number of tracks emerg-  
 286 ing from the same point. Tracks satisfying following criteria are used to reconstruct  
 287 the collision point (vertex).
  - 288 • distance of closest approach from the center of beam-spot  $< 2.4$  cm,
  - 289 • number of the associated pixel hits  $\geq 2$ , and
  - 290 • number of the associated pixel+strips hits  $\geq 5$ .
- 291 • **track clustering:** After track selection, the level of association of tracks from a vertex  
 292 is quantified. This procedure is called track clustering where tracks are clustered  
 293 according to their z-position from the center of beam-spot. The Deterministic An-  
 294nealing algorithm [37, 38] is used for such clustering. After clustering, the candidate  
 295 vertices are found along with the tracks associated with them.
- 296 • **vertex-position fitting:** The z-position of candidate vertices with at least two tracks  
 297 are fitted using the *adaptive vertex fitter* [39]. The fit returns  $x$ ,  $y$ ,  $z$ -position, and  
 298 covariance matrix of the PV along with other parameters such as the number of  
 299 degrees of freedom ( $n_{\text{dof}}$ ) and a weight associated with each track. We require  $n_{\text{dof}} >$   
 300 4.

301 The tag used to access PV information from MINIAOD samples is: `offlineSlimmedPrimaryVer-`  
 302 `tices`. The pileup distribution in data is calculated with `pileupCalc` tool using the JSON file:  
 303 `Cert_271036-284044_13TeV_23Sep2016ReReco_Collisions16_JSON.txt`, with a  
 304 minimum bias cross-section of 69.2 mb. The MC samples listed in Table 2 were generated  
 305 before the actual data taking in 2016. While simulating these samples, the pileup distribution  
 306 as initially seen in the data was used. During the actual data taking, however, the pileup dis-

tributions were changed. To have a similar pileup distribution as in data, the MC events are re-weighted. The weights applied on MC are shown in Figure 15e. After applying the pileup weights, the distribution of number of primary vertices per event (n vtx) is shown in Figures 7a and 7b for the  $\mu + \text{jets}$  and  $e + \text{jets}$  channel, respectively.

#### 4.1.2 Diffuse Offset Energy Density

From Figures 7a and 7b it can be seen that there is a poor agreement between data and simulations even after applying the pileup reweighting. A similar trend is seen in many analyses at 13 TeV [40, 41]. There is another variable similar to n vtx called diffuse offset energy density ( $\rho$ ) [42, 43]. For  $n$  number of jets in an event,  $\rho$  is given by [44]

$$\rho = \text{median} \left( \frac{p_{T,n}}{A_n} \right) \quad (1)$$

where  $p_{T,n}$  and  $A_n$  are the transverse momentum and area of  $n$ -th jet. The tag `fixedGridRhoAll` is used to get  $\rho$  from the MINIAOD files. The  $\rho$  distribution is shown in Figures 7c and 7d. It can be seen that  $\rho$  has a better agreement between data and simulations compared to the n vtx distribution. The  $\rho$  is used in the calculation of isolation variable for muon and electron as shown in Equation (4). The jet energy corrections are also derived using  $\rho$  as discussed in Section (4.4.2).

## 4.2 Muon

### 4.2.1 Reconstruction

Muons are often referred to as minimum ionising particles. Their energy loss is much smaller than electrons due to its larger mass. Muon in CMS detector with sufficiently higher  $p_T$  can traverse through most of the sub-detectors such as tracker calorimeter and the muon detector. Most of the high  $p_T$  muons go out of the CMS detector. Due to the presence of a magnetic field, trajectories of muon are bent in the CMS detector. The number of hits in the tracker, energy deposit in the calorimeter and the hits in the muon chambers (DT, CSC, and RPC) are used in the Kalman filtering technique [45] to reconstruct muon candidates. There are several categories of muons [46] described below:

- **Standalone Muons:** These are reconstructed from the muon chambers only. Here, the Kalman filtering technique uses the hits from DT, CSC, and RPC to reconstruct standalone muons.
- **Global Muons:** The trajectory of a standalone muon is extrapolated up to the tracker. The best pair consisting of the standalone muon and tracker track is selected using the Kalman filtering technique. Finally, these two tracks are combined to reconstruct the Global Muon. As the global muons are reconstructed starting from the outer part of the CMS detector (muon chambers) back to the inner part (strip tracker), this approach of reconstruction is called *outside-in*.
- **Tracker Muons:** There is an *inside-out* approach to reconstruct muons, which starts from the tracks reconstructed in the strip tracker to the energy deposits in the calorimeters up to the hits in the muon chamber. Muons reconstructed with this approach are called Tracker muons.
- **RPC Muons:** These muons are also reconstructed using the *inside-out* approach where only RPC hits of the muon chamber are used [47].
- **Calo Muons:** Some of the reconstructed muon tracks consist of energy deposits from the calorimeters. Such muons are called Calo muons.

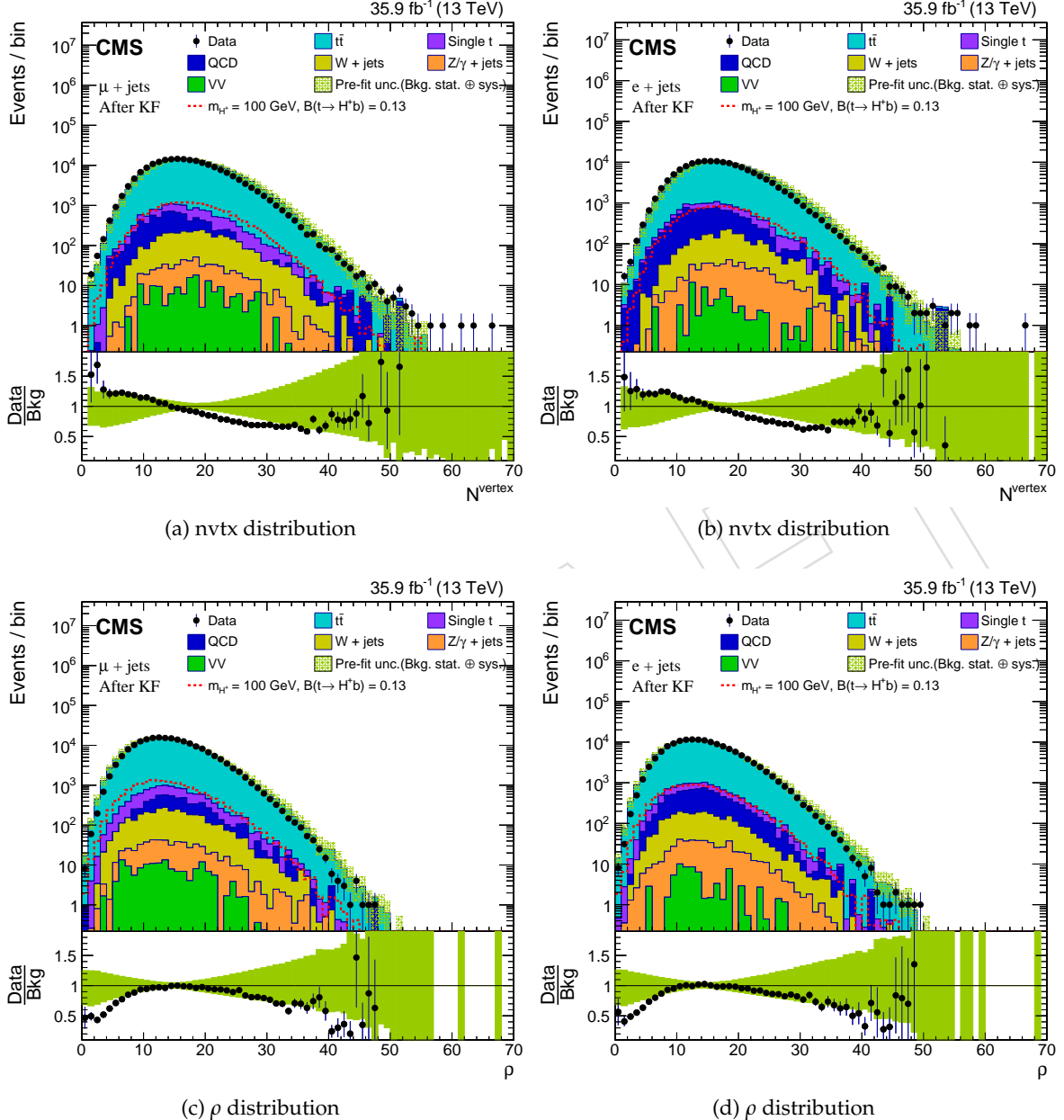


Figure 7: Number of primary vertices (n <sub>vtx</sub>) and diffuse offset energy density ( $\rho$ ) distributions for  $\mu + \text{jets}$  and  $e + \text{jets}$  channels. The data-MC agreement is better for  $\rho$  compared to the n <sub>vtx</sub> distribution. For lower values of  $\rho$ , there is a significant mismatch between data and MC. Similar trend is seen in other analysis as well [40, 41].

Table 4: Selection and veto cuts applied on muon.

Variable	Selection	Veto
$p_T$ (GeV)	$> 26$	$> 15$
$ \eta $	$< 2.4$	$< 2.4$
Global or tracker muon	Yes	Global
Normalised $\chi^2$	$< 3$	
$\chi^2$ local position	$< 12$	
Tracker kink	$< 20$	
Segment compatibility	$> 0.303$	
$ d_{xy}(\text{vertex}) $ (cm)	$< 0.05$	
$ d_z(\text{vertex}) $ (cm)	$< 0.2$	
Inner track valid fraction	$> 0.8$	
$I_{\text{rel}}^\mu$	$< 0.15$	$< 0.25$

### 345 4.2.2 Identification and Selection

346 In the event topology of our interest, there only one lepton (electron or muon) as shown in  
 347 Figure 2. These are the ‘prompt’ lepton coming directly from the electroweak decay of W  
 348 bosons. However, there could ‘extra’ leptons that come from other sources such as misidentifi-  
 349 cation of light flavored jets or charged pion decay in case of muons. Medium identification  
 350 criteria as recommended by the muon POG are applied to select prompt muons. These are  
 351 listed in Table 4. The efficiency of medium muon ID as a function of  $p_T$  and  $\eta$  is shown in Fig-  
 352 ure 8 for data and MC. From this figure, it can be seen that the efficiency at lower  $p_T$  is relatively  
 353 low compared to that from high  $p_T$ . However there is a sudden drop in the efficiency for data  
 354 from era BCDEF in the  $p_T > 120$  GeV region. These efficiency plots are provided by the muon  
 355 POG [48].

### 356 4.2.3 Rochester correction

357 Due to misalignment of the magnetic field and azimuth dependent in-efficiency of the muon  
 358 detector, the efficiency of the muon needs to be corrected. The efficiency depends on the charge,  
 359  $p_T$ ,  $\eta$  and  $\phi$  of muon. These corrections referred as Rochester correction are applied on data as  
 360 well as MC samples. The muon  $p_T$  is corrected using Rochester correction tools at 13 TeV [49].  
 361 The Rochester scale factors depend on the  $p_T$ ,  $\eta$ ,  $\phi$  and charge of the muon. Selection criteria  
 362 (Table 4) on muon are applied after Rochester correction.

### 363 4.2.4 Isolation

A muon track in the pp collision is not necessarily isolated i.e., it can be surrounded by other particles. On the other hand, muons from the W decay are expected to be isolated. To achieve this, we apply a criterion on the relative isolation, defined as the  $p_T$  sum of all particles excluding the muon within a cone of radius 0.4 around the muon direction divided by the muon  $p_T$  i.e.  $I_{\text{rel}}^\mu = \sum_{i \neq \mu} p_T^i / p_T^\mu$ . We use a more specific definition given by

$$I_{\text{rel}}^\mu = \frac{\sum p_T^{\text{ch}} + \max[(\sum E_T^\gamma + \sum E_T^{\text{neut}} - 0.5 \times \sum p_T^{\text{chPU}}), 0]}{p_T^\mu}, \quad (2)$$

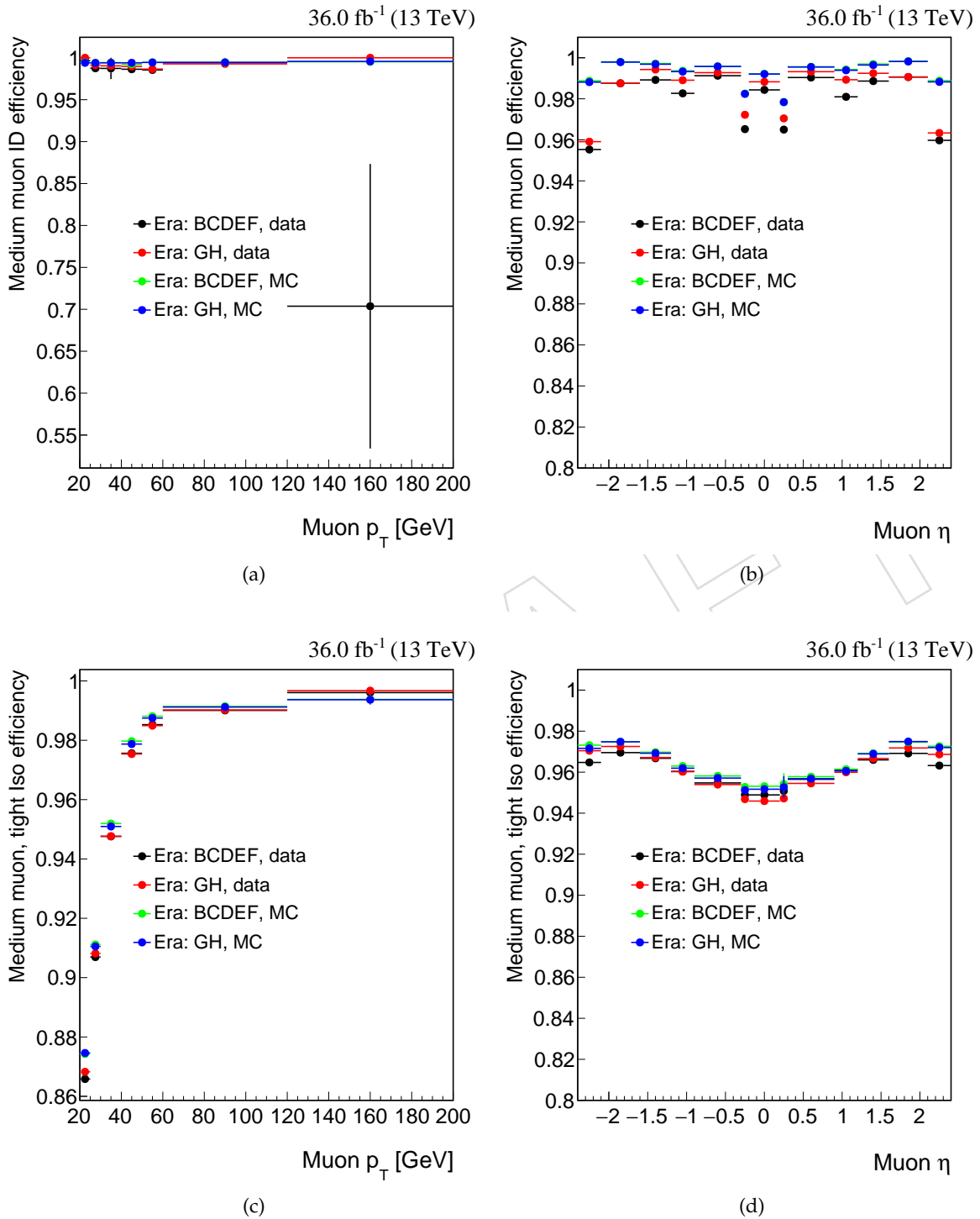


Figure 8: The distribution of efficiencies for medium muon ID and tight relative isolation (with medium ID) as a function of  $p_T$  and  $\eta$  of muon from MC and data from different eras.

Table 5: Selection and veto cuts applied on electron.

Variable	Selection		Veto	
	$ \eta_{\text{sc}}  \leq 1.479$	$ \eta_{\text{sc}}  > 1.479$	$ \eta_{\text{sc}}  \leq 1.479$	$ \eta_{\text{sc}}  > 1.479$
$p_{\text{T}}$ (GeV)	> 30	> 30	> 15	> 15
$ \eta $	< 2.5	< 2.5	—	—
$\text{full } 5 \times 5 \sigma_{\eta_{\text{inj}}}$	< 0.00998	< 0.0298	< 0.0115	< 0.037
$ \Delta\eta(\text{sc, track}) $	< 0.00311	< 0.00609	< 0.00749	< 0.00895
$ \Delta\phi(\text{sc, track}) $	< 0.103	< 0.045	< 0.228	< 0.213
$E_{\text{had}}/E_{\text{em}}$	< 0.253	< 0.0878	< 0.356	< 0.211
$I_{\text{rel}}^e$	< 0.0821	< 0.0695	< 0.175	< 0.159
$ \frac{1}{E} - \frac{1}{p}  (\text{GeV})^{-1}$	< 0.134	< 0.13	< 0.299	< 0.15
Missing inner hits	$\leq 1$	$\leq 1$	$\leq 2$	$\leq 3$
Conversion veto	Yes	Yes	Yes	Yes
$ d_{xy}(\text{vertex})  (\text{cm})$	< 0.05	< 0.10	< 0.05	< 0.05
$ d_z(\text{vertex})  (\text{cm})$	< 0.10	< 0.20	< 0.1	< 0.1

where  $p_{\text{T}}^{\text{ch}}$  is the transverse momentum of charged hadrons;  $E_T^{\gamma}$  and  $E_T^{\text{neut}}$  are the transverse energy of photons and neutral hadrons; and  $p_{\text{T}}^{\text{chPU}}$  is the transverse momentum of charged hadrons associated with the pileup vertices. The factor 0.5 takes into account the neutral tracks from the leading vertex and charged tracks from the pileup vertices [50]. A tight muon isolation cut of  $I_{\text{rel}}^{\mu} < 0.15$  is applied. The efficiency as a function of  $p_{\text{T}}$  and  $\eta$  of tight muon isolation with medium ID is shown in Figure 8 [48].

### 4.3 Electron

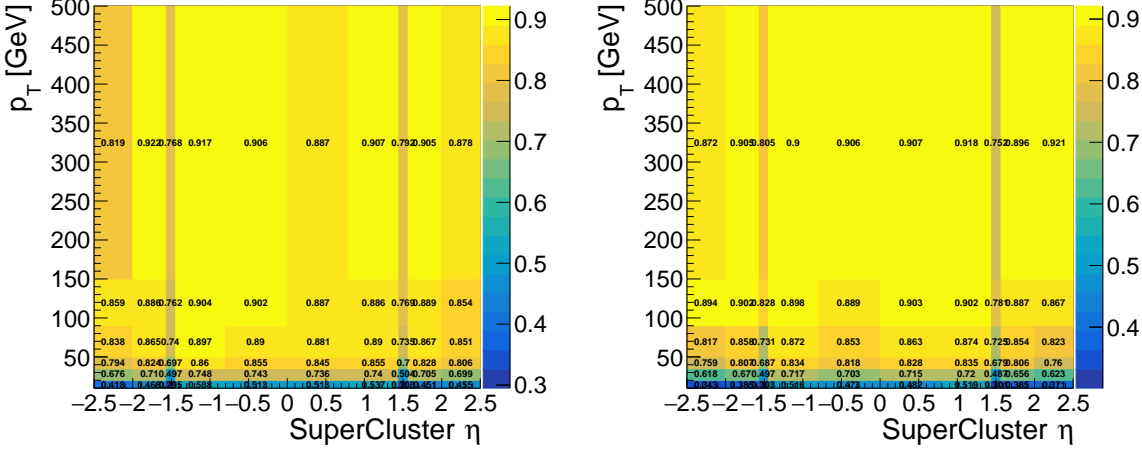
#### 4.3.1 Reconstruction

Electrons are reconstructed using the PF algorithm [34, 35] based on the tracks in the tracker and energy deposits in the electromagnetic calorimeter [51]. Being a charged particle electrons radiate as they travel inside the huge magnetic field of the CMS. Thus the energy deposited by an electron in the ECAL is spread in  $\eta$  and  $\phi$  direction across several crystals. The energy deposited in various crystals are clustered using "hybrid" algorithm in the barrel and "multi-5x5" in endcap part of the ECAL. For given hits in the innermost layer of the tracker, the Kalman Filter technique is used to find hits in the next layer of the tracker. The hits collected from all layers of the tracker is mapped to the energy deposit in the ECAL to form an electron candidate. To take care of the effect of bremsstrahlung, the "Gaussian sum filter" method is used to fit the tracks. The electron charge is estimated from the curvature of the electron track and by matching associated KF track with GSF tracks. The vector joining (SC, beam-spot) and (SC, first hit of the GSF track) in  $\phi$  is also used for electron charge estimation. The measurements from tracker and ECAL are combined to estimate the electron momentum [51].

#### 4.3.2 Identification and Selection

To select prompt electrons, medium cut-based ID as listed in Table 5 is used. Electrons with  $p_{\text{T}} > 30 \text{ GeV}$  and  $|\eta| < 2.5$  are excluded.

A brief description of the variables listed in Table 5 is given below:



(a) Efficiency for medium ID

(b) Efficiency for veto ID

Figure 9: The distribution of efficiency for medium and veto electron ID.

- full  $5 \times 5 \sigma_{i\eta i\eta}$  is defined as [51]

$$\sigma_{i\eta i\eta} = \sqrt{\sum(0.0175 \times \eta_i + \eta_{\text{cryst}}^{\text{seed}} - \bar{\eta}_{5 \times 5})^2 \times w_i} / \sum w_i, \quad w_i = 4.2 + \log(E_i/E_{5 \times 5}) \quad (3)$$

The summation is carried over the  $5 \times 5$  matrix around the highest  $E_T$  crystal of the supercluster.

- $|\Delta\eta(\text{sc, track})|$ : Difference in  $\eta$  of the supercluster and the electron track.
- $|\Delta\phi(\text{sc, track})|$ : Difference in  $\phi$  the supercluster and the electron track.
- $E_{\text{had}}/E_{\text{em}}$ : Ratio of the electron energy deposited in the HCAL and ECAL.
- $|\frac{1}{E} - \frac{1}{p}|$ :  $E$  is the energy of the supercluster and  $p$  is the track momentum at the point of closest approach from the PV.
- Missing inner hits: Number of missing hits in the strip tracker.
- $|d_{xy}(\text{vertex})|$ : Distance of closest approach of the electron track from the PV in the  $xy$  plane.
- $|d_z(\text{vertex})|$ : Difference in the  $z$ -coordinate of the PV and the electron track.

The relative isolation  $I_{\text{rel}}^e$  and conversion veto of Table 5 are discussed in Sections 4.3.3 and 4.3.4. The efficiency of medium and veto electron ID as a function of  $p_T$  and  $\eta$  is shown in Figure 9 [52].

403

### 4.3.3 Isolation

The relative isolation of an electron is given by:

$$I_{\text{rel}}^e = \frac{\sum p_T^{ch} + \max[(\sum E_T^\gamma + \sum E_T^{\text{neut}} - \rho \times A_{\text{eff}}), 0]}{p_T^e}, \quad (4)$$

405 where  $\rho$  is as defined in Eq. (1) and  $A_{\text{eff}}$  is the effective area. (To get  $\rho$  for  $I_{\text{rel}}^e$  from MINIAOD, 406 `fixedGridRhoFastjetAll` tag is used.) These two quantities are used to correct electron isolation

Table 6: Effective area for different  $\eta_{\text{sc}}$  range.

Super-cluster pseudorapidity ( $\eta_{\text{sc}}$ )	$A_{\text{eff}}$
$0.0 \leq \eta_{\text{sc}} < 1.0$	0.1703
$1.0 \leq \eta_{\text{sc}} < 1.5$	0.1715
$1.5 \leq \eta_{\text{sc}} < 2.0$	0.1213
$2.0 \leq \eta_{\text{sc}} < 2.2$	0.1230
$2.2 \leq \eta_{\text{sc}} < 2.3$	0.1635
$2.3 \leq \eta_{\text{sc}} < 2.4$	0.1703
$2.4 \leq \eta_{\text{sc}}$	0.2393

407 from pileup. The effective area for different  $\eta_{\text{sc}}$  are shown in Table 6. The tight isolation cut of  
 408  $I_{\text{rel}}^e < 0.0821(0.0695)$  is applied on electrons from the barrel (endcap) regions.

#### 409 4.3.4 Conversion rejection

410 Some of the reconstructed electrons are end products of photon conversion inside the tracker.  
 411 While selecting prompt electrons these secondary electrons need to be rejected. The tag used  
 412 for conversion rejection is *reducedEgamma:reducedConversions*. As the secondary electrons don't  
 413 have hits in the innermost layer of the tracker [51], one can use this feature to reject them. By  
 414 fitting the electron tracks, these secondary electrons are also rejected [51].

### 415 4.4 Jet

#### 416 4.4.1 Reconstruction

417 Due to color confinement [53], the quarks and gluons produced in pp collisions cannot exist  
 418 in the free states. Instead, they hadronise into a cluster of colorless particles such as hadrons,  
 419 leptons, and photons. We form a jet out of these particles, emanating in a cone around the  
 420 initial direction quarks and gluons. In CMS the PF algorithm is used to reconstructs all possible  
 421 particles that can be inside a jet. Subsequently, the clustering of, or the reconstruction of jets  
 422 from, these particles are done with the anti- $k_T$  algorithm [54].

#### 423 4.4.2 Identification and Selection

424 The recommended [55] selection criteria applied on jets are listed in Table 7. The identification  
 425 of b and c-jet are discussed in Sections 5 and 7. The charged hadron subtraction technique  
 426 [56] is used to take care of the pileup effects. It ignores the charged particles coming from  
 427 the pileup vertices. The jet energy in data and simulated samples are corrected to account for  
 428 the non-linear response of the ECal and HCal. A set of corrections are applied in a factored  
 429 manner, that is the output of previous serves as the input to the next step. The raw  $p_{\text{T}}$  of a  
 430 jet is corrected at every step and the corrected  $p_{\text{T}}$  is used in the subsequent analysis. These  
 431 set of corrections are known as L1FastJet (pileup correction through offset energy density)  
 432 L2RelativeL3Absolute (detector response corrections), and L2L3Residual (residual cor-  
 433 rections on data). The first two are applied on simulated samples whereas all the three are  
 434 applied on data. All these corrections are applied while processing the MiniAOD datasets  
 435 listed in the Table (2, 1). Furthermore, the jet  $p_{\text{T}}$  in the simulation are smeared to have same  
 436 resolution as that of data using the jet energy resolution (JER) scale factors. Before applying the  
 437 selection cuts listed in Table 7, the jet  $p_{\text{T}}$  is corrected as discussed in Section 8.4.

Table 7: Selection criteria applied on jets.

Variable	selection
$p_T$ (GeV)	> 25
$ \eta $	< 2.4
Neutral hadron energy fraction	< 0.99
Neutral electromagnetic energy fraction	< 0.99
Number of constituent	> 1
Charged hadron energy fraction	> 0
Charged hadron multiplicity	> 0
Charged hadron electromagnetic energy fraction	< 0.99

#### 438 4.4.3 Cleaning

439 The prompt leptons (electrons and muons) are required to be outside the jet cone. This proce-  
 440 dure is called jet cleaning, where we require the angular separation between the jet and lepton,  
 441  $\Delta R > 0.5$ .

### 442 4.5 Missing Transverse Energy

443 The missing transverse energy ( $E_T^{\text{miss}}$ ) is the negative vector sum of momenta of all objects  
 444 reconstructed with the PF algorithm. Being a weakly interacting particle, neutrinos are not di-  
 445 rectly detected through the CMS detector and thus contribute to  $E_T^{\text{miss}}$ . Note that this is not true  
 446 only for the SM; there are some beyond-the-SM particles e.g., neutralinos in supersymmetry  
 447 that could also contribute to  $E_T^{\text{miss}}$ . Nevertheless, as there is a neutrino in our signal events (see  
 448 Figure 2) we expect large  $E_T^{\text{miss}}$  due to its escape from the detector. The  $E_T^{\text{miss}}$  in MC and data  
 449 can have different resolutions. Therefore,  $E_T^{\text{miss}}$  from MC events are smeared using the *Type-1*  
 450 correction in which jet energy correction is propagated to the  $E_T^{\text{miss}}$ . The events having  $E_T^{\text{miss}} >$   
 451 20 GeV are selected.

## 452 5 b-jet Tagging

453 There are two b-jets in the final state as shown in Figure 2 for charged Higgs signal as well as  
 454 SM  $t\bar{t}$  + jets background. Accurate identification of these b-jets will substantially reduce the SM  
 455 backgrounds where there are no b-quarks at parton level such as  $Z/\gamma + \text{jets}$ ,  $VV$ ,  $W + \text{jets}$  etc.  
 456 The *combined secondary vertex* (CSVv2) method [57] is used to tag a b-jet. The main idea behind  
 457 the method is that b-hadrons produced from the b-quark (originating from the PV) have a  
 458 relatively larger lifetime due to which they can travel measurable distance w.r.t. primary vertex  
 459 in the transverse plane before decaying further (Figure 10). The position resolution of vertex in  
 460 the transverse plane is about few  $\mu\text{m}$ . Therefore, a secondary vertex displaced by few hundred  
 461 microns w.r.t. primary vertex can be identified and reconstructed. The transverse distance of  
 462 tracks from the PV is called impact parameter (IP). To calculate the b-discriminator, first tracks  
 463 of reasonable quality are selected, following which secondary vertex is reconstructed. Finally,  
 464 multi-layer perceptrons [58] is used to accept or reject the secondary vertex, discriminator value  
 465 of the jet.

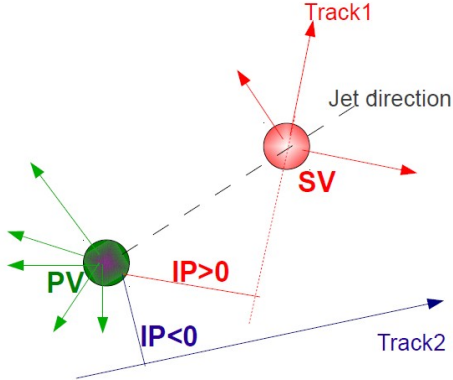


Figure 10: Primary and secondary vertex with tracks and impact parameter. IP  $> 0$  or  $< 0$  if tracks are upstream or downstream along the jet direction. This figure is taken from Ref. [59].

Table 8: Track selection criteria. PCA stands for the point of closest approach.

Variable	Selection
$p_T$ associated with tracks	$> 0.8 \text{ GeV}$
number of hits associated with tracks in the tracker	$> 8$
longitudinal component of IP	$< 0.3 \text{ cm}$
distance between PCA of tracks from the PV and jet-axis	$< 0.07 \text{ cm}$
distance between PCA of tracks from the jet-axis and PV	$< 5 \text{ cm}$
the displaced track should have	$\text{IP} > 50 \mu\text{m}$ and $\frac{\text{IP}}{\sigma_{\text{IP}}} > 1.2$

## 466 5.1 Track Selection

467 The tracks are selected with the criteria listed in Table 8. These requirements ensure the tracks  
 468 are closer to the PV and not coming from pileup vertices. After track selection, the SV is recon-  
 469 structed.

## 470 5.2 Reconstruction of Secondary Vertex

471 For Run-I, the *combined secondary vertex* (CSV) method used the adaptive vertex reconstruction  
 472 algorithm [60], which is based on adaptive vertex fitter [39] to reconstruct the SV. On the other  
 473 hand, in case of Run-II, the CSVv2 uses the inclusive vertex finder (IVF) algorithm [61] for  
 474 the same purpose. The collection of selected tracks are used as inputs to the IVF. The displaced  
 475 tracks are used as seed. The cluster of tracks is formed from seed track depending on the angles  
 476 and distance between them. The adaptive vertex fitter is used to fit the clusters. The selection  
 477 listed in Table 9 are applied for the SV.

## 478 5.3 Multi-layer Perceptron Training

479 Three types of discriminating variable, as shown below, are used in multi-layer perceptron  
 480 training to identify the secondary vertex.

- 481 • category-I: jet with  $N_{\text{SV}} > 1$ ,

Table 9: Secondary vertex selection criteria.  $d_{\text{PV},\text{SV}}^{\text{trans}}$  is the 2D flight distance or the distance between a primary and secondary vertex in the transverse plane.

Variable	selection
number of tracks associated with the SV	$> 2$
$d_{\text{PV},\text{SV}}^{\text{trans}}$	$> 0.1 \text{ mm}$
$d_{\text{PV},\text{SV}}^{\text{trans}}$	$< 2.5 \text{ cm}$
mass associated with the SV	$< 6.5 \text{ GeV}$
$\Delta R$ (jet axis, secondary flight direction)	$< 0.4$

Table 10: The efficiency of loose, medium, and tight b-tag working points for different quark-flavor of jets [62]. These efficiencies are calculated from  $t\bar{t}$  events with jet  $p_T > 20 \text{ GeV}$ .

WP	$\epsilon^b$ (%)	$\epsilon^c$ (%)	$\epsilon^{uds}$ (%)	CSVv2
b-tagger L	81	37	8.9	$> 0.5426$
b-tagger M	63	12	0.9	$> 0.8484$
b-tagger T	41	2.2	0.1	$> 0.9535$

- 482 • category-II: jet with pseudo-vertex [58], and  
 483 • category-III: jet with no SV or no pseudo-vertex.

484 The discriminating variables from the vertex-categories are combined using a likelihood ratio,  
 485 which gives the b-discriminator value. The b-discriminator value for the  $\mu + \text{jets}$  and  $e + \text{jets}$   
 486 channel is shown in Figure 11. There are three official b-tag working points: *loose*, *medium*,  
 487 and *tight* with b-tag efficiency [defined in Eq. (21)] 81%, 63%, and 41%, respectively. The cor-  
 488 responding probability of a light jet being misidentified as a b-jet is 10%, 1%, and 0.1%. In this  
 489 analysis, we use the medium working point i.e., b-discriminator  $> 0.8484$  for b-tagging. The  
 490 efficiency of all b-taggers for b, c, and light-quarks are shown in Table (10).

491

## 492 6 Kinematic fit

493 In this analysis, the charged Higgs boson is decaying to the  $c$  and  $\bar{s}$  quark. The invariant mass  
 494 of the  $c\bar{s}$  system ( $m_{jj}$ ) is thus used as the final observable. The  $m_{jj}$  distribution of two highest  
 495  $p_T$ , non-b-jets is shown in Figure 12a and 12b for both channels. For the true semileptonic  $t\bar{t}$   
 496 events, the mean of the  $m_{jj}$  should be close to 80.0 GeV, which is the mass of the W Boson.  
 497 However, the mean of  $m_{jj}$ , as shown in Figure 12a and (12b), is about 138 GeV because the two  
 498 light jets in every event may not necessarily come from the decay of a W Boson. Secondly, the  
 499  $m_{jj}$  distribution has a long tail which might constrain the search for new resonances in the dijet  
 500 mode.

501 To select true semi-leptonic  $t\bar{t}$  events, a kinematic fit is performed on the reconstructed objects  
 502 using the top kinematic fitter package [63]. The TopKinFitter takes physics objects such  
 503 as lepton, jets,  $E_T^{\text{miss}}$ , and their resolutions as input, and gives improved four-vectors of lep-  
 504 ton, jets, and neutrino with associated  $\chi^2$  and probability of the fit as output. It constrains

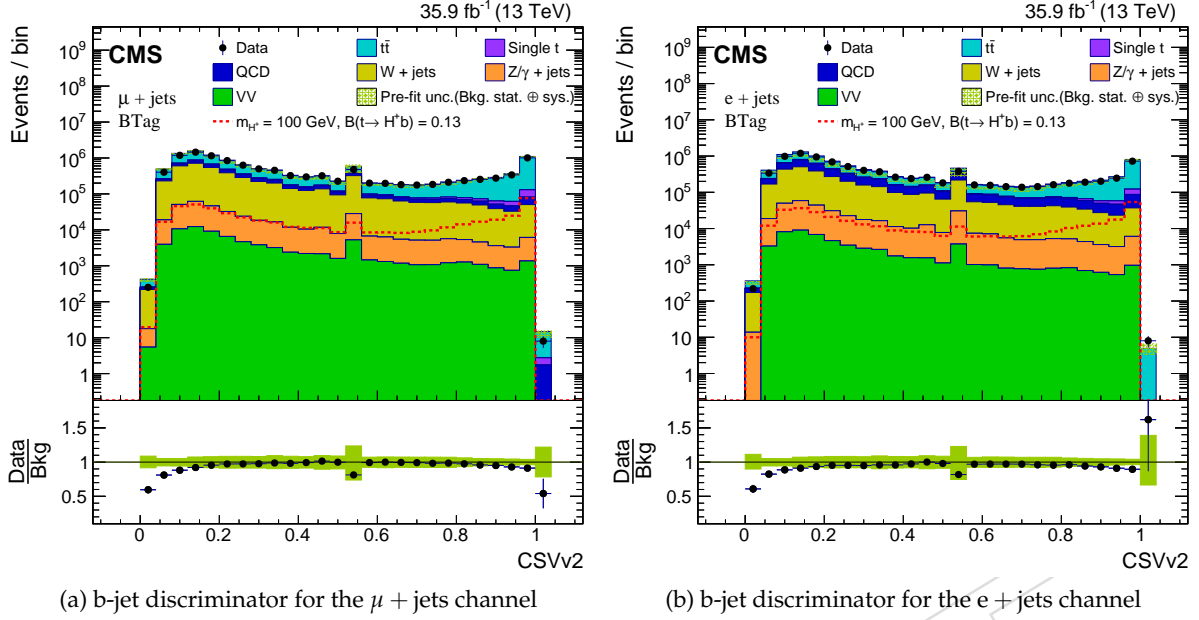


Figure 11: The b-discriminator distributions of all jets, after  $N_{\text{jets}} \geq 4$  selection as described in Sec. 10, obtained using CSVv2 method for the  $\mu + \text{jets}$  and  $e + \text{jets}$  channel.

the reconstructed top-quark mass to its nominal value ( $m_t = 172.5$  GeV). In the output, the TopKinFitter gives only 4-jets (2 b-jets from leptonic and hadronic modes, and 2 light-jets from hadronic mode), 1 lepton, and neutrino. It also separates jets coming from leptonic and hadronic decay modes of  $t\bar{t}$ . The 2 light-jets coming from hadronic decay mode are further used for charm-tagging. A more detailed description of the kinematic fitting is given below.

## 6.1 Input to the TopKinFitter

After applying identification and selection criteria on physics objects as described in Section (4), the event passed to the TopKinFitter contains only one lepton,  $E_T^{\text{miss}}$  and at least 4 jets. The b-discriminator value with the medium working point is also given as the input to the TopKinFitter to separate b-jet from light jets (more details in Section (6.2)). The constraints on the  $t\bar{t}$  system along with the theoretical mass of the top-quark are also specified (more details in Section (6.3)). All the constraints and invariant mass are parameterized in terms of  $E_T$ ,  $\eta$ , and  $\phi$  variables of the physics objects. The components of 4-momentum vector in terms of these variables are given as

$$E = E_T \sin \theta, p_x = E_T \cos \phi, p_y = E_T \sin \phi, p_z = E_T \cot \theta, \quad (5)$$

And the invariant mass of two particles, in the relativistic limit, is given by

$$M_{\text{inv}} = \sqrt{2E_{T1}E_{T2}(\cosh(\eta_1 - \eta_2) - \cos(\phi_1 - \phi_2))} \quad (6)$$

Where  $\eta = \ln \cot(\theta/2)$ . The resolution of each physics object as a function of pt and eta, and the JER scale factors from different  $\eta$  binning are also given in the input. Apart from the physics objects, various inputs related to the minimization of  $\chi^2$  such as the maximum number of iterations, criteria on the convergence of the  $\chi^2$  are also specified (more details in Section (6.4)).

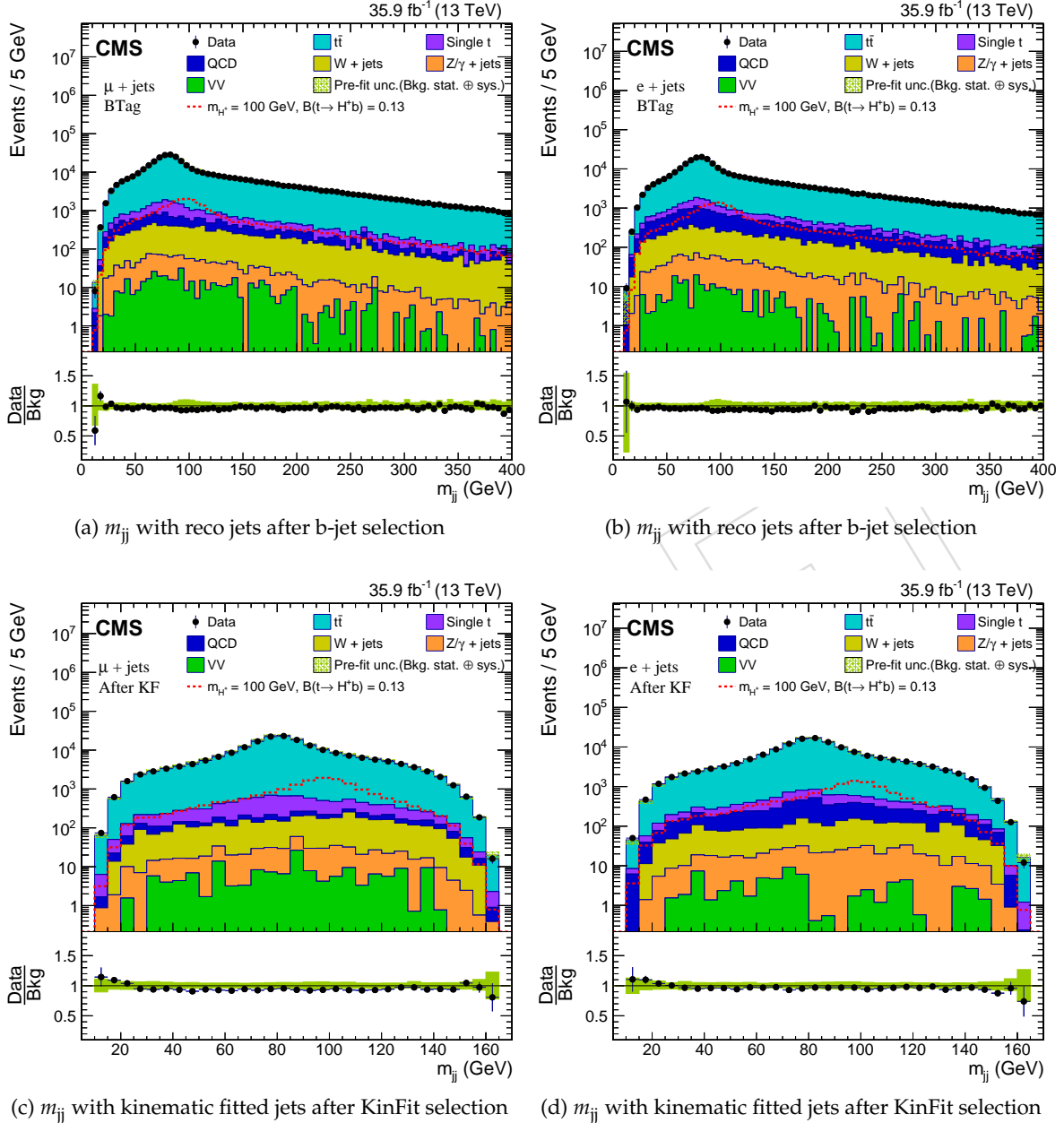


Figure 12:  $m_{jj}$  distributions of two non-b, highest  $p_T$ -jets for the  $\mu + \text{jets}$  and  $e + \text{jets}$  channel. The distributions of Figure 12a and 12b are obtained using reconstructed jets after applying b-tag scale factor as described in Sec. 10. On the other hand, the distributions of Figure 12c and 12d are calculated using kinematic fitted jets after kinematic fit selection. The mean of the invariant mass distribution from kinematic fitted jets is closer to the W mass as compared to that of reconstructed jets.

516 **6.2 Separation of jets**

For the semileptonic decay mode of the ttbar, the first step is to separate 2 b-jets from light-jets and the second step is to identify each b-jet from hadronic and leptonic modes. All the jets are sorted in their  $p_T$  order and first 4 jets are selected. To find out the two b-jets, a b-tag probability is calculated using following formula [63]

$$L_b(x) = \frac{PDF_b(x)}{\sum_{i=1}^5 PDF_i(x)} \quad (7)$$

Where  $PDF_i(x)$  is the probability distribution function of b-tag discriminator value (x) for flavour  $i$ . An event is selected if two jets have b-tag probability of more than 60%. The jet-parton matching is also performed for each jet. For n number of jets, there are exactly n number of partons. The number of permutations in the jet-parton matching is given by

$$N_{perm} = \frac{n!}{(n-4)!} \quad (8)$$

517 Therefore for 4 jets, there are 24 permutations. All the 24 permutations are shown in [64]  
 518 through diagrams. However, after identifying two b-jets, the number of permutations reduces  
 519 to 12 as the two b-jets are interchangeable. For each jet-parton permutation, a  $\chi^2$  is constructed,  
 520 as described in Section (6.4), and the permutation with the lowest value of  $\chi^2$  is treated as the  
 521 correct matching. Afterward, three jets (1 b-jet and 2 light-jets) have to be selected to form  
 522 hadronic decaying top-quark. For this, several sensitive variables are used [63] such as the an-  
 523 gle between jets and lepton, angular separation between the generated and reconstructed jets,  
 524 etc.

525 **6.3 Kinematic constraints**

526 The semileptonic decay mode of the  $t\bar{t}$  has 4 jets, 1 lepton and the neutrino in the final state. The  
 527 x and y-component of the neutrino are taken from the  $E_T^{\text{miss}}$ , as the missing transverse energy  
 528 is attributed to the neutrino. And the z-component of the neutrino,  $p_z^v$ , is determined from the  
 529 fit. The following kinematic constraints are imposed on the semileptonic  $t\bar{t}$  system

$$m_{inv}(b^{had}q\bar{q}) = m_t = 172.5 \text{ GeV} \quad (9a)$$

$$m_{inv}(b^{lep}l\nu_l) = m_{\bar{t}} = 172.5 \text{ GeV} \quad (9b)$$

530 After the fit, the  $p_z^v$  is determined from the Equation (9b). For every event, a  $\chi^2$  is constructed  
 531 as discussed in Section (6.4). The  $\chi^2$  is minimized by varying  $P_T$ ,  $\eta$ , and  $\phi$  of each object within  
 532 their resolution. Those values of  $P_T$ ,  $\eta$ , and  $\phi$  variables are finally selected which minimises the  
 533  $\chi^2$  and at the same time satisfies the Equation (9).

534 **6.4 Chi-square of the fit**

For every selected event, a  $\chi^2$  is constructed as given by [AN2012\_477]

$$\chi^2 = \left( \frac{m_t - 172.5}{\sigma_{m_t}} \right)^2 + \left( \frac{m_{\bar{t}} - 172.5}{\sigma_{m_{\bar{t}}}} \right)^2 + \sum_i \left( \frac{p_i^{fit,lep} - p_i^{lep}}{\sigma_{p_i^{lep}}} \right)^2 + \sum_j \sum_i \left( \frac{p_i^{fit,jet_j} - p_i^{jet_j}}{\sigma_{p_i^{jet_j}}} \right)^2 \quad (10)$$

535 where  $\sigma_{m_t}$  is the resolution of the mass of the top-quark and  $\sigma_{p_i}$  is the momentum resolution of  
 536 three component ( $i = 1, 2, 3$ ) of the lepton and jets. The  $p_i^{fit}$  is the fitted momentum of lepton

and jets. The  $\chi^2$ , given in Equation (10) is minimized using the Lagrangian multipliers under the constraints given in Equation (9).

A detailed mathematical description for the minimization of the  $\chi^2$  is given in [63]. The  $\chi^2$  is minimized iteratively wherein each step the 4 components of the momentum vector of each object are varied within their resolution and a  $\chi^2$  and the constraint is calculated. The object resolutions used in the kinematic fitting are conservative, derived from 8 TeV analysis.

The fit is declared to be converged if the following condition is satisfied

$$\frac{\chi^2(n-1) - \chi^2(n)}{ndf} < \epsilon_\chi \quad (11a)$$

$$m_{inv}(b^{had}q\bar{q}) - 172.5 < \epsilon_c \quad (11b)$$

$$m_{inv}(b^{lep}l\nu_l) - 172.5 < \epsilon_c \quad (11c)$$

where  $\epsilon_\chi = 5 \times 10^{-5}$ ,  $\epsilon_c = 0.0001$ , and  $ndf$  is the number of degrees of freedom which is equal to 1 as we have two constraints and one free parameter ( $p_z^v$ ). The total number of iterations ( $n$ ) is 500.

## 6.5 Output of the KinFit

For every event, the TopKinFitter gives the status of fit which is 0 if the fit converged and 1 if it did not,  $\chi^2$  of the fit, probability ( $P_\chi$ ) of the goodness-of-fit of  $\chi^2$ , and the 4 momentum vector of physics objects such as jets, lepton and a neutrino. The  $\chi^2$  and  $P_\chi$  are related by the following equation

$$P_\chi = \exp\left(\frac{-\chi^2}{2}\right) \quad (12)$$

The fit also separates jets from hadronic and leptonic decay mode of  $t\bar{t}$ , that is, it gives hadronic 1 b-jet, 1-leptonic b-jet, and 2 light jets from hadronic decay separately. The c-tagging criteria are applied further on the 2 light jets as discussed in Section 7. The  $m_{jj}$  distribution of the light jets is used in further analysis.

## 6.6 Selection and Performance

Due to wrong jet combinatorics, the fit does not converge for every event. Only those events are selected for which the fit converges. The efficiency of fit convergence is 73% for MC  $t\bar{t}$  sample and 71% for data for both channels. Further, the angular separation between reconstructed and kinematic fitted lepton and jets are required to be less than 0.2 to make sure that they are in the same direction. The same  $\Delta R$  cut is applied on reconstructed jets and kinematic fitted jets. Also, the  $p_T$  cut on kinematic fitted lepton and jets are required to be the same as that on the reconstructed jets and lepton. After applying these additional cut on  $\Delta R$  and  $p_T$ , the kinematic fit efficiency reduces to 47% for  $t\bar{t}$  and 44% for data for both channels. The  $m_{jj}$  distribution from the two light jets after KinFit selection is shown in (12c) and (12d) for both channels. The mean value of the  $m_{jj}$  distribution is 84 GeV for both channels.

The KinFit is performed after applying jet energy corrections such as JES and JER. For up and down systematics of JES and JER, the KinFit is performed separately on every event after correcting jet  $p_T$  using the corresponding scale factors. The output of the KinFit for each systematic is stored in a different collection using the EDProducer. The kinematic fitting is a time-consuming process which takes, on average 0.002 seconds per event for  $t\bar{t}$  process. Therefore, performing all (nominal, JESup, JESdown, JERup, and JERdown) the kinematic fitting takes a reasonable amount of time.

Table 11: The efficiency of loose, medium, and tight c-tag working points for different quark-flavor of jets [62]. These efficiencies are calculated from  $t\bar{t}$  events with jet  $p_T > 20$  GeV.

WP	$\epsilon^c$ (%)	$\epsilon^b$ (%)	$\epsilon^{uds}$ (%)	pfCCvsL	pfCBvsB
c-tagger L	88	36	91	> -0.48	> -0.17
c-tagger M	40	17	19	> -0.1	> 0.08
c-tagger T	19	20	1.2	> 0.69	> -0.45

## 570 7 c-jet Tagging

571 As the charged Higgs Boson decays to a charm and an anti-strange quark, the identification  
 572 of charm jet is expected to increase the signal significance. The charm tagging or c-tagging is  
 573 recently developed in the CMS collaboration [65] based on the CSV method for the analyses  
 574 at 13 TeV data. This procedure is similar to that of b-tagging described in Section 5. At the  
 575 end, we have two charm discriminators: charm vs. b-jet (pfCCvsB) and charm vs. light jet  
 576 (pfCCvsL). Distribution of these two discriminators is shown in Figure 14 for the  $\mu +$  jets and  
 577 e + jets channel. These are collectively used to tag a jet as a c-jet. Three working points are  
 578 provided by BTV POG for the charm tagging, as shown in Table (11) and Figure 13.

579 At least one of the light jets from hadronic decay mode of  $t\bar{t}$  is required to pass one of the charm-  
 580 jet working points. First, each WP was separately used for c-tagging. However, the limits were  
 581 not getting improved for medium and tight working points. Therefore the loose WP is finally  
 582 used. Although the signal to background ratio increases as one goes from loose to tight working  
 583 point, the limits are not improved because the event yield also goes down. However, it is  
 584 found that, as described in Section (15.3), that if the events after KinFit selection are exclusively  
 585 divided into the categories based on loose, medium, and the tight charm working points and  
 586 the limit is computed by combining data cards from these three categories, as described in  
 587 Section (18.3), then the limit is improved.

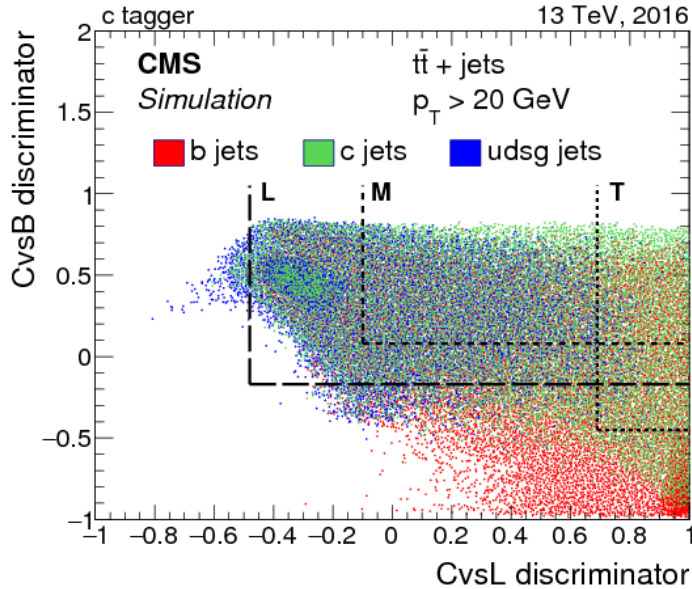


Figure 13: The 2D plot between charm-taggers. The region right to the vertical and above to the horizontal line correspond to different charm working points (WPs). Unlike the b-tag WPs, there is an overlap between the loose, medium, and tight c-tag WPs. This figure is taken from [65].

## 588 8 Corrections on MC

### 589 8.1 Luminosity Scale Factors

The MC events listed in Table 2 are arbitrarily generated. While comparing distributions obtained using MC events with that of data, the former has to be normalised with the integrated luminosity of data. To achieve this, each MC sample is multiplied by the following luminosity scale factor ( $SF_L$ ):

$$SF_L = \frac{L_{\text{data}}}{L_{\text{MC}}} = \frac{L_{\text{data}} \times \sigma_{\text{MC}}}{N_{\text{MC}}}, \quad (13)$$

590 where  $L_{\text{data}} = 35.5 \text{ fb}^{-1}$  and  $N_{\text{MC}}$  is the number of generated MC events and  $\sigma_{\text{MC}}$  is the cross 591 section of MC samples. As listed in Table 2, the  $SF_L$  value is less than 1 for most of the back- 592 ground samples except for QCD. For QCD it is very large compared to other backgrounds 593 owing to less number of generated events compared to its cross-section. Simulation of large 594 number of QCD events is not feasible because of computing limitations.

### 595 8.2 Pileup Reweighting

596 The pileup distributions in the data and MC are different. To match the MC pileup distribution 597 with that of data, MC events are reweighted. Depending on the number of primary vertices, 598 each MC event is multiplied by corresponding pileup weight. The pileup weights are the ratio 599 of pileup distributions from data and MC. The pileup distributions in data and MC samples 600 are calculated as follows:

- 601 • **pileup distribution in data:** The pileup distribution in the data is calculated using  
602 the Command (36) and shown in Figure 15d.
- 603 • **pileup distribution in MC:** The pileup distribution in MC are accessed through the  
604 *slimmedAddPileupInfo* tag from *MINIAOD* datasets for all MC samples. The "in-  
605 time" pileup distributions for  $t\bar{t} + \text{jets}$ ,  $W + \text{jets}$ , and  $Z/\gamma + \text{jets}$  are shown in Fig-

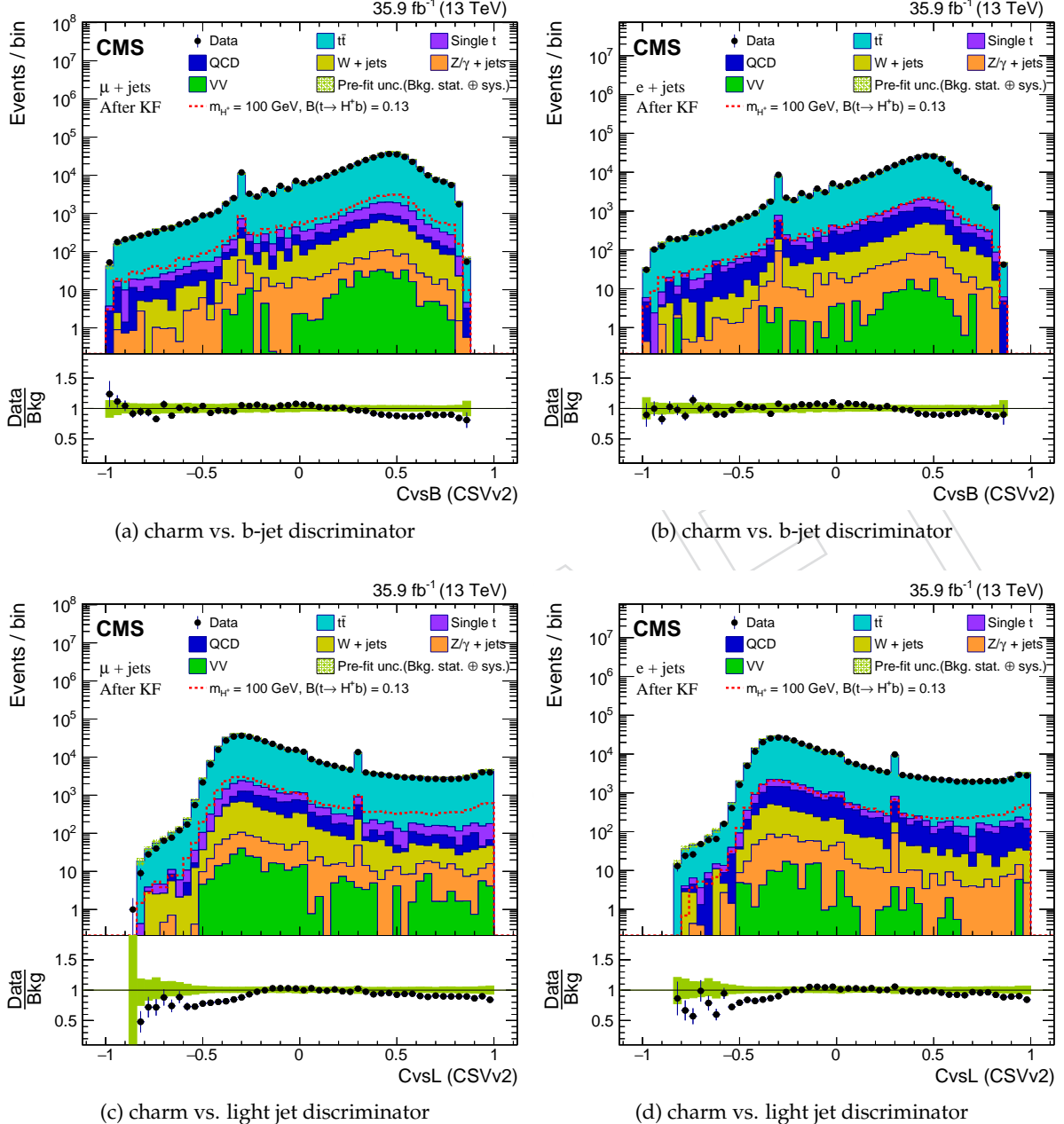


Figure 14: The charm-discriminator distributions of two non-bjets after kinematic fitting selection as described in Sec. 10, obtained using the CSV method for the  $\mu + \text{jets}$  and  $e + \text{jets}$  channel. The jets with associated tracks not satisfying a set of selection criteria, as listed in [65], are responsible for the spikes in these distributions.

ures 15a, 15b, and 15c, respectively. Since the pileup distributions are campaign dependent, not sample dependent, we see similar distribution for all the MC samples.

The pileup weights are calculated using standard LumiReweighting tool of CMSSW. The pileup weights as shown in Figure 15e are normalised ratio of the pileup distribution from data and MC.

### 8.3 Lepton Scale Factors

Trigger, tracking, isolation and identification efficiencies are different between MC and data.  $p_T$  and  $\eta$  dependent scale factors are applied to MC events to take care of this difference. The 2D histograms used to calculate muon scale factors are shown in Figure 16. The muon scale factors are era dependent. There are different muon scale factors for era BCDEF and GH. However, electron scale factors are the same for full 2016 data taking period. The maximum  $p_T$  range of 2d-histogram for muon identification and isolation scale factors is 120 GeV. If a muon has  $p_T > 120$  GeV, then the scale factor for  $p_T = 120$  GeV is used. Similarly scale factor of  $p_T = 500$  GeV is used for  $p_T > 500$  GeV for muon trigger scale factors, and electron scale factors. Separate scale factors are combined into one as

$$SF^\mu = SF_{ID}^\mu \times SF_{iso}^\mu \times SF_{track}^\mu \times SF_{trig}^\mu, \quad SF^{ele} = SF_{ID}^{ele} \times SF_{reco}^{ele} \times SF_{trig}^{ele}, \quad (14)$$

where  $SF_{ID}^\mu$ ,  $SF_{iso}^\mu$ ,  $SF_{track}^\mu$  and  $SF_{trig}^\mu$  are weighted average with luminosity ( $L$ ) for different eras (Run-BCDEF and Run-GH) e.g.

$$SF_{ID}^\mu = \frac{SF_{ID}^\mu(\text{BCDEF}) \times L(\text{BCDEF}) + SF_{ID}^\mu(\text{GH}) \times L(\text{GH})}{L(\text{BCDEF}) + L(\text{GH})}. \quad (15)$$

Where, for example,  $SF_{ID}^\mu(\text{BCDEF})$  is the scale factor for Run-B to Run-F and  $L(\text{BCDEF})$  is the luminosity during this period. A similar formula for  $SF_{iso}^\mu$ ,  $SF_{track}^\mu$  and  $SF_{trig}^\mu$  is used. The scale factors of Eq. (14) are applied on MC events.

616

617 The electron scale factors, as shown in Figure 17 are read from 2D histograms provide by [52].

618

### 8.4 Jet and MET Correction

Jets from simulations are smeared using jet energy scale (JES) and jet energy resolution (JER) to have the same resolution as that in data [66]. For smearing  $p_T$  and  $\eta$  dependent scale factors ( $SF$ ) are used as listed in Table 12. The  $p_T$  of jet in simulations is scaled by the following factor:

$$p_{T, scale} = \max[0.0, 1.0 + (SF - 1) \times (p_{T,jet}^{gen} - p_{T,jet}^{sim}) / p_{T,jet}^{sim}] \quad (16)$$

with the following constraint:

$$p_{T,jet}^{gen} > 0, \quad \Delta R < 0.2, \quad |p_{T,jet}^{gen} - p_{T,jet}^{sim}| < 3 \times \sigma_{JER} \times p_{T,jet}^{sim}, \quad (17)$$

620 where  $\Delta R$  is the angular separation between the reconstructed and generated jet and  $\sigma_{JER}$  is resolution of reconstructed jet- $p_T$ , calculated using Spring16\_25nsV10\_MC\_PtResolution\_AK4PF.txt and global tag 80X\_mcRun2\_asymptotic\_2016\_TrancheIV\_v10.

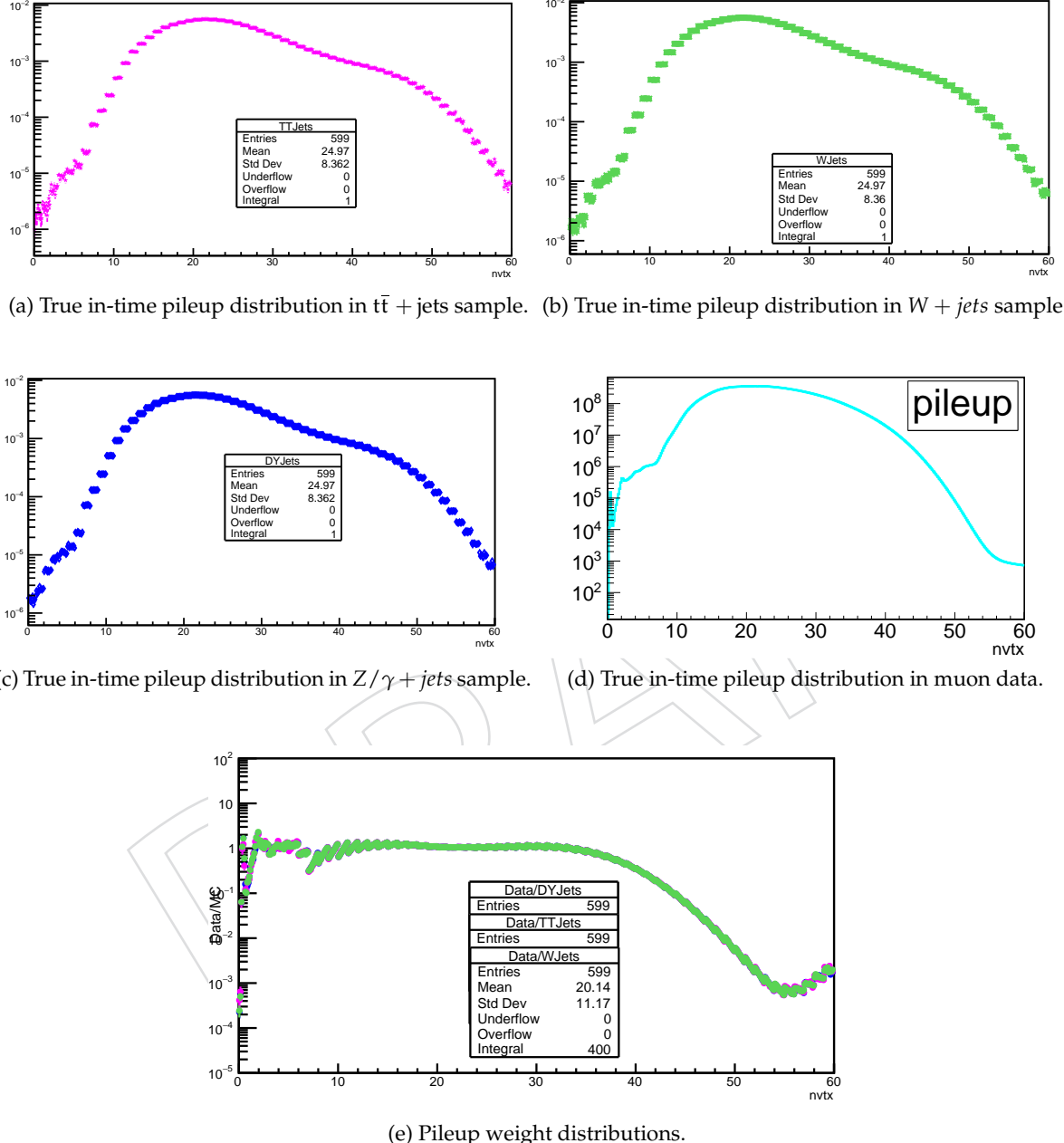


Figure 15: True in-time pileup distribution in (a)  $t\bar{t} + \text{jets}$ , (b)  $W + \text{jets}$ , (c)  $Z/\gamma + \text{jets}$  MC samples, and (d) single muon data. The pileup distribution is campaign dependent that is why all the MC samples have same pileup distribution as these MC samples were generated in the same campaign.

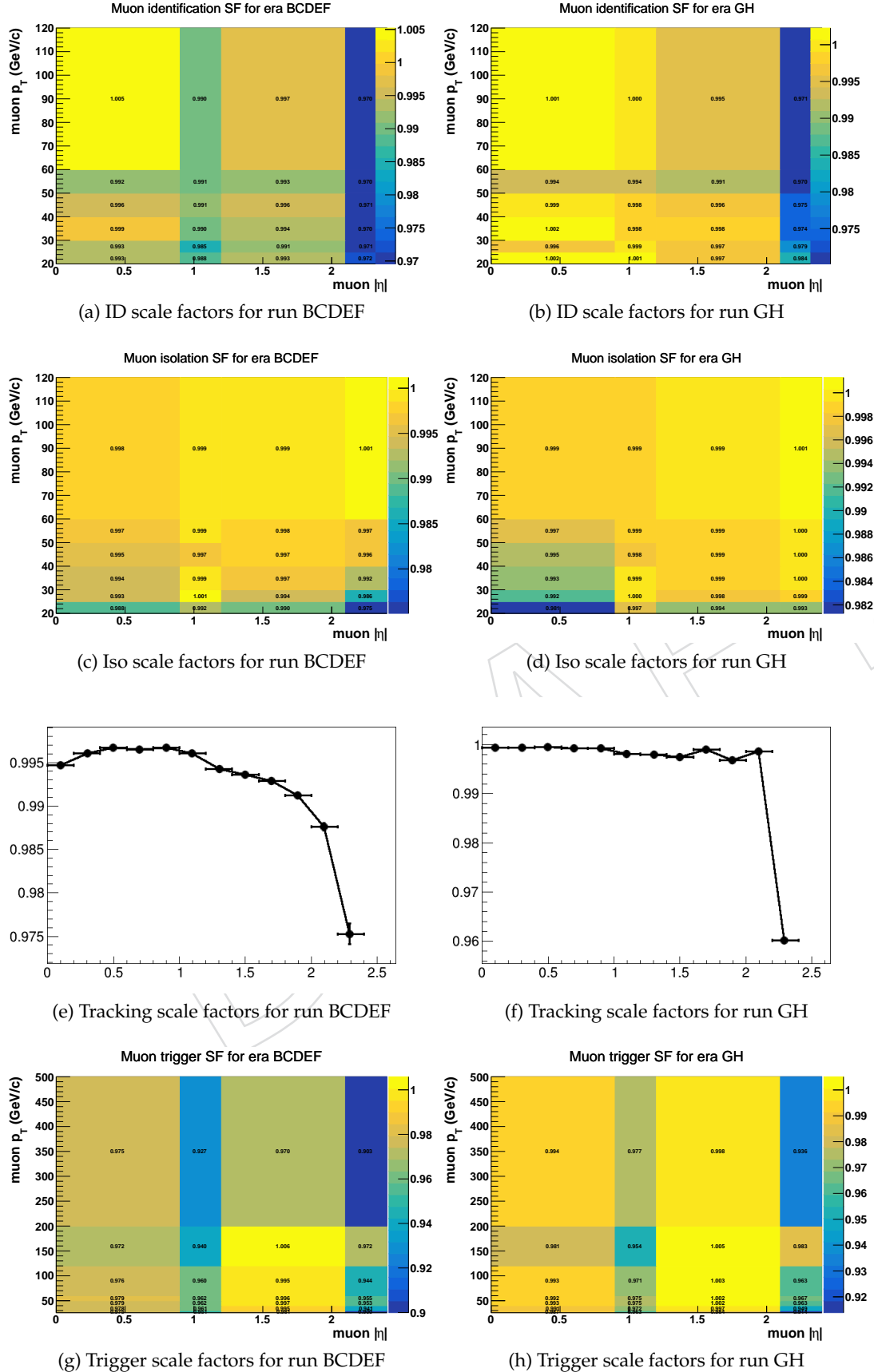


Figure 16: Identification, isolation, tracking and trigger scale factors for muon.

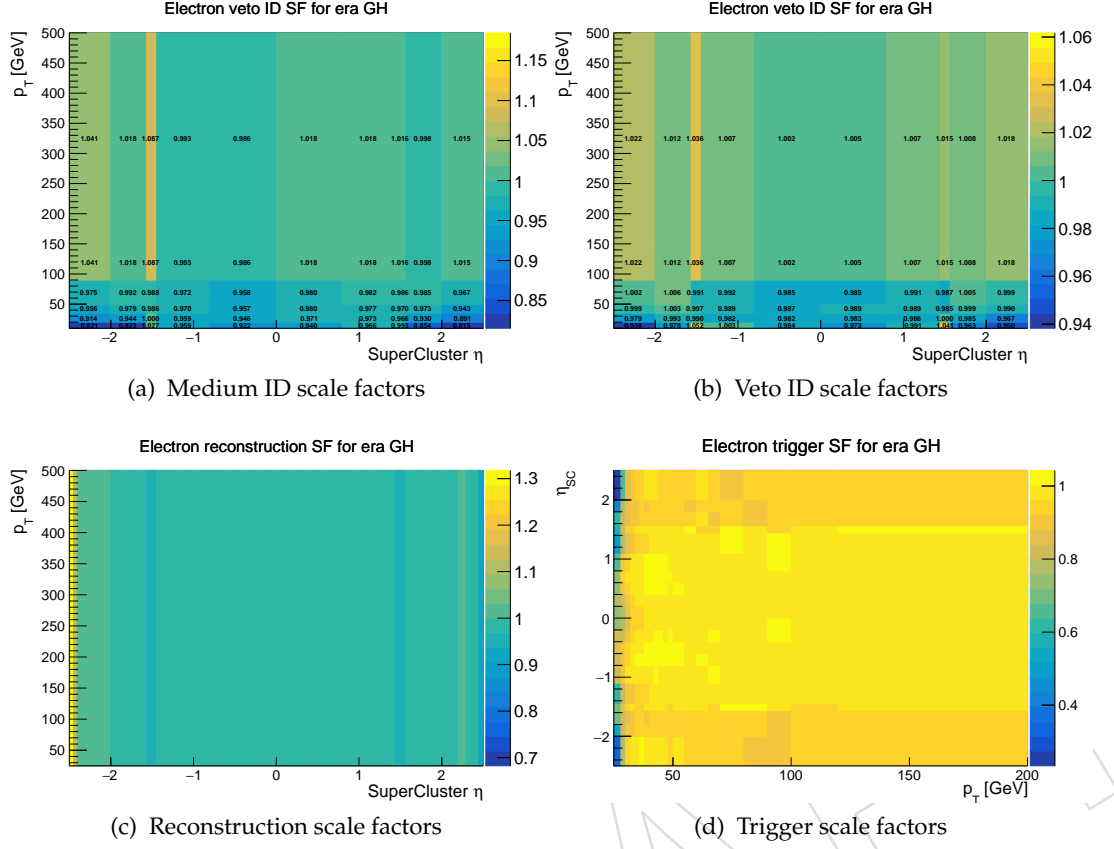


Figure 17: Identification, Reconstruction and Trigger scale factors for electron.

Table 12: Jet energy resolution scale factors for different  $\eta$  range

$\eta$ range	base	down	up
$0.0 \leq  \eta  < 0.5$	1.109	1.044	1.174
$0.5 \leq  \eta  < 0.8$	1.138	1.072	1.204
$0.8 \leq  \eta  < 1.1$	1.114	1.050	1.178
$1.1 \leq  \eta  < 1.3$	1.123	1.022	1.224
$1.3 \leq  \eta  < 1.7$	1.084	0.985	1.183
$1.7 \leq  \eta  < 1.9$	1.082	0.973	1.191
$1.9 \leq  \eta  < 2.1$	1.140	1.020	1.260
$2.1 \leq  \eta  < 2.3$	1.067	0.953	1.181
$2.3 \leq  \eta  < 2.5$	1.177	0.967	1.387
$2.5 \leq  \eta  < 2.8$	1.364	1.203	1.525
$2.8 \leq  \eta  < 3.0$	1.857	1.654	2.060
$3.0 \leq  \eta  < 3.2$	1.328	1.203	1.453
$3.2 \leq  \eta  < 5.0$	1.160	1.013	1.307

624 **8.5 b-tag Scale Factor**

The b-tagging efficiency is different between MC and data. An event weight as given by Eq.20 is applied on the simulated events to take care of this difference [67].

$$P(MC) = \prod_{i=\text{tagged}} \epsilon_i \prod_{j=\text{not tagged}} (1 - \epsilon_j) \quad (18)$$

$$P(Data) = \prod_{i=\text{tagged}} SF_i \epsilon_i \prod_{j=\text{not tagged}} (1 - SF_j \epsilon_j) \quad (19)$$

$$w = \frac{P(Data)}{P(MC)} \quad (20)$$

The b-tag efficiency  $\epsilon_f(m, n)$  in the  $(m, n)$  bin of  $p_T$  and  $\eta$  is calculated using the following formula

$$\epsilon_f(m, n) = \frac{N_f^{\text{b-tagged}}(m, n)}{N_f^{\text{total}}(m, n)}, \quad (21)$$

625 where  $N_f^{\text{b-tagged}}(m, n)$  is the number of b-tagged jets with flavor  $f$  (b-quark, c-quark, light-  
 626 quark and gluon) and  $N_f^{\text{total}}(m, n)$  is the total number of events. The scale factor ( $SF_i$ )  
 627 depends on  $p_T$ ,  $\eta$ , parton-flavor of jet and b-jet discriminator value, and are read from  
 628 CSVv2\_Moriond17\_B\_H.csv file provided by BTV POG [68], using BTagCalibration frame-  
 629 work [69].

630 **8.6 c-tag Scale Factor**

631 Similar to the event weights from b-tagging, the event weight for c-jet tagging is also applied  
 632 due to the mismatch in the efficiencies between MC and data. The mistagging of c-tagged jet or  
 633 tagging a non-c-tagged jet as c-jet is done using the same procedure as that of Section 8.5. For  
 634 the c-tag scale factor, ctagger\_Moriond17\_B\_H.csv file is used as given by BTV POG [68].  
 635 The c-tagging decision is taken based on the c-tagging status of two taggers of Figure 14.

## 636 9 Event Filters and Triggers

### 637 9.1 Filters

638 A series of filters as recommended by the JetMET POG [70] are applied to filter "bad" events,  
 639 such as those where there is a huge difference in the  $p_T$  of muon measured from the tracker  
 640 and the muon chambers. Although the occurrence of such "bad" events is rare, these filters  
 641 are applied as sanity measures. These filters mostly affect the actual data, most of them have  
 642 no effect on the simulated events. The efficiency of all combined filters is 99.4% for data, and  
 643 99.9% for SM  $t\bar{t}$  + jets MC sample. These filters are particularly useful in those analyses where  
 644 there is a requirement of very high missing transverse energy (MET) and the final event yield  
 645 is small. A detailed description of each filter is given below:

- 646 • **HBHE noise filter:** It is known that the barrel and endcap part of the HCAL records  
 647 noise (sporadic anomalous signals) at a fixed rate even if there is no stable beam  
 648 for physics data taking [70]. An event is supposed to have such a noise if the flag  
 649 `Flag_HBHENoiseFilter` is set to 1. Such an event is filtered.
- 650 • **HBHE isolated noise filter:** This filter first finds the candidates for rechits and re-  
 651 jects the event if the sum of iso-tagged energy is  $> 50$  GeV, the sum of iso-tagged  
 652 transverse energy  $> 25$  GeV, and the number of iso-tagged rechits is  $> 9$ . The flag  
 653 `Flag_HBHENoiseIsoFilter` is used for this purpose.
- 654 • **CSC beam halo filter:** The actual physics objects of interest are those which are pro-  
 655 duced in the pp collision. However, there are machine induced particles, produced  
 656 through beam-gas or beam-pipe interactions, which fly with the beam at a large ra-  
 657 dius (up to 5m). These machine induced particles are reconstructed mainly in the  
 658 Cathode Strip Chambers (CSC) as muon candidate. A set of selection is applied  
 659 through `Flag_globalSuperTightHalo2016Filter` [70]. This flag is set to 1 if the  
 660 CCS beam halo filter is applied and 0 if not applied.
- 661 • **Good primary vertex filter:** The events are required to have at least one good pri-  
 662 mary vertex. Therefore, those events are filtered where there is no good vertex. A  
 663 good vertex is required to be real, the z-component of the position is  $< 24$  cm, the  $\rho$   
 664 component of the position  $< 2$  cm, and the minimum number of degrees of freedom  
 665 are  $> 4$ . The `Flag_goodVertices` is set to 1 if the event has passed this filter.
- 666 • **Bad EE supercrystal filter:** The events are filtered if there is an unusually large en-  
 667 ergy deposit in the four superclusters of ECAL endcaps [70]. This filter is applied  
 668 only on data through the `Flag_eeBadScFilter`.
- 669 • **ECAL dead cell trigger primitive filter:** If the energy of the ECAL crystals are es-  
 670 timated from the trigger primitive and lies near the saturation energy then that event  
 671 is filtered [70]. The `Flag_EcalDeadCellTriggerPrimitiveFilter` flag is used  
 672 to indicate if an event passes this filter or not.
- 673 • **Bad PF muon filter:** An event is filtered if the muon is although qualified as a PF  
 674 muon but the quality is very low, and the  $p_T$  is large. The events are filtered if a  
 675 muon is found which has  $p_T > 100$  GeV, segment compatibility  $< 0.3$  or relative  
 676 percentage error in the  $p_T$  of the best (inner) track is more than 200% (100%), and  $\Delta R$   
 677 ( $\text{muon}, \text{PFmuon}$ )  $< 0.001$ .
- 678 • **Bad charged hadron filter:** Those events are filtered where the quality of the muon  
 679 is low and it is not declared as PF muon. However, this non-PF muon is used in  
 680 the calculation of PF-MET as a candidate for charged hadron. To reject such events,  
 681 the muon is required to have same  $p_T$ , segment compatibility, and error in track cuts

Table 13: List of event filters applied to data and MC samples. Most of the filters are available in the MINIAOD through the trigger collection. The unavailable filters are applied on the fly using EDFilters.

Name of the filter	Available in MINIAOD	Applied on
HBHE noise filter	Yes	Data & MC
HBHE isolated noise filter	Yes	Data & MC
CSC beam halo filter	Yes	Data & MC
Good primary vertex filter	Yes	Data & MC
Bad EE supercrystal filter	Yes	Data
ECAL dead cell trigger primitive filter	Yes	Data & MC
Bad PF Muon Filter	No	Data & MC
Bad Charged Hadron Filter	No	Data & MC

as that of the above filter. An additional requirement of  $\Delta R$  (muon, charge hadron)  $< 0.00001$ , and  $\text{PtDiffRel} < 0.00001$  is applied where  $\text{PtDiffRel} = (p_T \text{ of PF candidate} - p_T \text{ of muon inner track}) / (0.5 * (p_T \text{ of PF candidate} + p_T \text{ of muon inner track}))$ .

All of the above filters are not directly stored in the trigger collection of the MINIAOD data set. The EDFilters are used on the fly to apply unavailable filters. The list of filters with their availability and applicability is shown in Table (13).

## 9.2 Triggers

The high-level triggers (HLT) are applied to select events enriched with desired physics objects. The trigger conditions are stored in the form of programming strings also called trigger paths. For every event, these paths are stored. Depending on the topology of an analysis, an event is selected if the corresponding trigger path is available in that event. For this analysis, an event is selected if it has a trigger path of `HLT_IsoMu24*` and `HLT_IsoTkMu24*` with logical OR for the muon channel, and `HLT_Ele27_WPTight_Gsf` for electron channel. The efficiency of these triggers depends on  $p_T$  and  $\eta$  of the lepton. For lower  $P_T$ , the efficiency is very poor and has a sudden increase at a particular value. That sudden increase is called trigger turn-on and the leptons are required to have  $p_T$  higher than that at the turn-on.

The muon and electron trigger efficiency as a function of  $p_T$  is shown in Figure (18). The trigger turn-on for muon trigger is at about  $p_T = 24$  GeV, hence in the subsequent selection, the muon is required to have  $p_T > 26$  GeV. For the electron trigger (`HLT_Ele27_WPTight_Gsf`), the trigger turn-on is a little higher at about  $p_T = 33$  GeV, therefore a cut of  $p_T > 35$  GeV is applied on electrons in the subsequent selection.

## 10 Event Selection

In the final state, there are four jets, one charged lepton and  $E_T^{\text{miss}}$ . Various selection cuts are applied to ensure the resulting events to have this topology. Cut-flow plots after various selection cuts are shown in Figure 19. Below we list out various selection requirements applied.

1. **Event filter and trigger:** The events are passed to the filters and triggers, as discussed in Section (9). The lepton trigger is used to enrich events with lepton and significantly reduces QCD compared to other SM background. The number of events surviving trigger

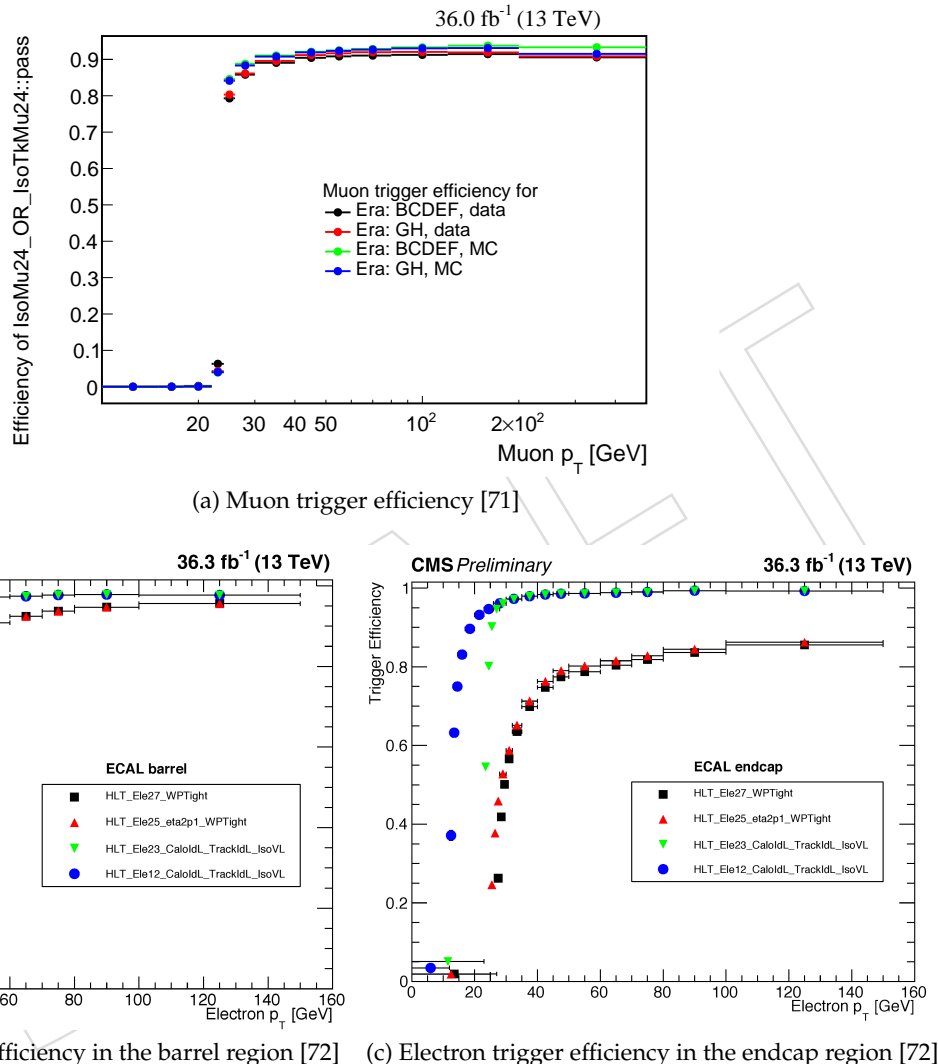


Figure 18: Muon and electron trigger efficiency as a function of transverse momentum. The trigger turn-on is at about  $p_T = 24$  GeV for muon, and 33 GeV for electron (HLT\_Ele27\_WPTight\_Gsf) triggers.

711 cuts for signal, background MC and data are shown in the 2nd column of Tables 14, 15,  
 712 16 and 17.

- 713 2. **Lepton selection:** The event topology has only one lepton thus events having a second  
 714 loose lepton are not selected. The lepton-veto selection for the  $\mu + \text{jets}$  and  $e + \text{jets}$  channel  
 715 are listed in Tables 4 and 5. For the  $\mu + \text{jets}$  ( $e + \text{jets}$ ) channel there cannot be any electron  
 716 (muon) in an event. Those events where there is any electron (muon) in the  $\mu + \text{jets}$   
 717 ( $e + \text{jets}$ ) channel are rejected. Lepton scale factors as described in Sec. 8.3 are applied  
 718 to MC events. The relative isolation cut for muon and electron is  $I_{\text{rel}}^{\mu} < 0.15$  and  $I_{\text{rel}}^{e\ell} <$   
 719 0.08, respectively. Event yields after one lepton selection are shown in the 3rd column of  
 720 Tables 14, 15, 16 and 17.
- 721 3. **Jet selection:** There should be at least four jets in an event. Jet selection cuts are listed in  
 722 Table 7. The jet energy is corrected using JES and JER scale factors. After correcting jet  
 723 energy, the selections on jet as shown in Table 7 are applied. Number of events after jet  
 724 selection are shown in the 4th column of Tables 14, 15, 16 and 17.
- 725 4.  **$E_T^{\text{miss}}$  selection:** The  $E_T^{\text{miss}}$  should be greater than 20 GeV. Event yields after  $E_T^{\text{miss}}$  selection  
 726 are shown in the 5th column of Tables 14, 15, 16 and 17. After applying  $E_T^{\text{miss}}$  selection  
 727 QCD,  $Z/\gamma + \text{jets}$  event yields reduce more compared to  $t\bar{t} + \text{jets}$ , single  $t$ ,  $W + \text{jets}$ , and  $VV$   
 728 processes because there is no genuine  $E_T^{\text{miss}}$  (neutrino) at the parton level.
- 729 5. **b-jet selection:** For b-jet selection, the medium working point is used i.e.,  $b_{\text{discr}} > 0.8484$ .  
 730 The b-tag event weights, as described in Sec. 8.5, are applied on MC events. The events  
 731 are required to have at least two b-jets. Event yields for MC signal, background and data  
 732 are shown in the 6th column of Table 14, 15, 16 and 17.
- 733 6. **Kinematic fit selection:** The kinematic fit does not converge for every event [63]. Only  
 734 those events are selected for whom the fit converges. Also, the same cuts on kinematically  
 735 fitted objects as that of reconstructed objects are used. The direction of kinematically fitted  
 736 jets should be almost same to that of the reconstructed jets. The following kinematic fit  
 737 selections are applied:

- 738 • the kinematic fit converges for selected events,
- 739 •  $\Delta R(KF_{\text{lep}}, Reco_{\text{lep}}) < 0.2$ ,
- 740 •  $\Delta R(KF_{\text{jets}}, Reco_{\text{jets}}) < 0.2$

741 Event yields after kinematic fit selections are shown in the 7th column of Tables 14, 15, 16  
 742 and 17. From these tables, we see that almost half the number of events is reduced after  
 743 these selections.

- 744 7. **c-jet selection:** The loose charm tagging working point ( $\text{pfCCvsL} > -0.48$  and  $\text{pfCCvsB} > -0.17$ )  
 745 is used to tag a jet as c-jet. The c-tag event weights are applied following the  
 746 same procedure as that for b-tag event weights. Event yield after demanding at least  
 747 1 c-jet with the loose working point for signal, background, and data are shown in 8th  
 748 column of Tables 14, 15, 16 and 17.

749 From Table 14 (15) it can be seen that the  $W + \text{jets}$  process is the dominant background upto  
 750 1-lepton selection. However, when the events are required to have  $N_{\text{jets}} \geq 4$ , the  $t\bar{t} + \text{jets}$  be-  
 751 comes the dominant background. The  $t\bar{t} + \text{jets}$  remains dominant background after subsequent  
 752 selection cuts. The QCD events are from MC QCD samples as shown in Table 2.

753 The signal event yields for a different mass of charged Higgs after various selection cuts are  
 754 shown in Table 16 (17) for the muon (electron) + jets channel. It can be seen from Table 16 (17)

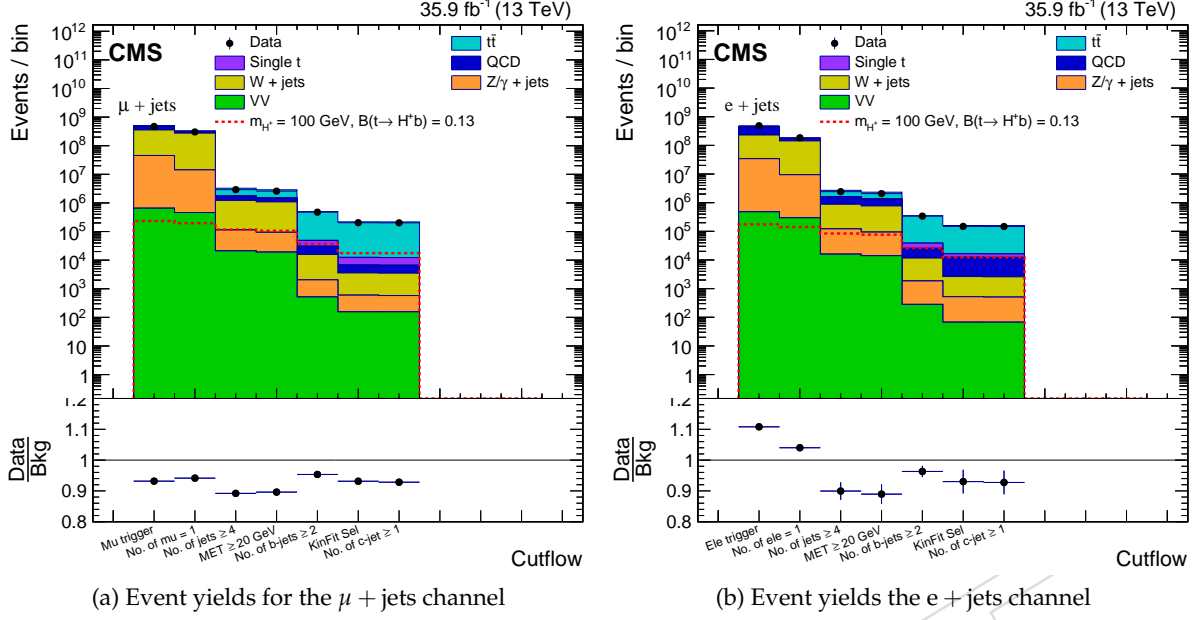


Figure 19: Event yields after various selection cuts for the  $\mu + \text{jets}$  and  $e + \text{jets}$  channel.

Table 14: Event yields after various selection cuts for the  $\mu + \text{jets}$  channel. The  $W + \text{jets}$  process is the dominant background upto 1-lepton selection. When the events are required to have  $N_{\text{jets}} \geq 4$ , the  $t\bar{t} + \text{jets}$  becomes the dominant background. The QCD events are from MC QCD samples as listed in Table 2. The MC signal process corresponds to  $m_{H^+} = 120 \text{ GeV}$ .

Process	Trigger	$N_{\text{muon}} = 1$	$N_{\text{jets}} \geq 4$	$E_T \geq 20 \text{ GeV}$	$\geq 2 \text{ b-jets}$	KinFit Sel.	$\geq 1 \text{ c-jet}$
MC signal	232076	195177	116921	106839	35050.5	16932.3	16995.4
SM $t\bar{t} + \text{jets}$	4.02823e+06	2.84791e+06	1.4925e+06	1.37212e+06	449363	205678	204577
Single t	589360	455794	92348.6	84612	18402.3	5738.97	5692.71
$W + \text{jets}$	3.0976e+08	2.60782e+08	1.11136e+06	992060	13768.1	2979.1	2931.53
$Z/\gamma + \text{jets}$	4.48471e+07	1.38263e+07	92247.8	74957.5	1527.75	440.68	423.088
MC QCD	1.44528e+08	4.33387e+07	454277	340874	14787.7	3159.25	3108.99
VV	653644	462752	21110.8	19097.7	515.918	155.957	156.093
Bkg	5.04407e+08	3.21714e+08	3.26384e+06	2.88373e+06	498365	218152	216890
Data	4.69926e+08	3.02859e+08	2.91118e+06	2.58404e+06	475120	203180	201332
Data/Bkg	0.931641	0.941392	0.891948	0.896078	0.953358	0.931368	0.92827

that the event yields are almost same upto 1-lepton selections for all masses of charged Higgs. However, after the  $N_{\text{jets}} \geq 4$  selection, when  $t\bar{t} + \text{jets}$  becomes the dominant background as shown in Table 14 (15), the event yield for higher masses of the charged Higgs are reduced more compared to the lower masses. The event yield reduces because of the less phase space available between top-quark and charged Higgs for higher masses.

Table 15: Event yields after various selection cuts for the  $e + \text{jets}$  channel. A similar trend as that of Table 14 is seen. The MC signal process corresponds to  $m_{H^+} = 120 \text{ GeV}$ .

Process	Trigger	$N_{ele} = 1$	$N_{jets} \geq 4$	$\cancel{E}_T \geq 20 \text{ GeV}$	$\geq 2 \text{ b-jets}$	KinFit Sel.	$\geq 1 \text{ c-jet}$
MC signal	176707	142579	85553.5	77733.4	24927.6	11958.6	11989.3
SM $t\bar{t} + \text{jets}$	3.00506e+06	2.02494e+06	1.06093e+06	972693	313133	143178	142432
Single t	436965	312490	66953.2	61092.8	13159.7	4030.43	3995.41
W + jets	1.95738e+08	1.33639e+08	760254	675272	9814.24	2115.41	2074.13
Z/ $\gamma$ + jets	3.38253e+07	9.14985e+06	105837	79926	1568.69	453.363	438.934
MC QCD	2.04408e+08	3.23709e+07	685990	524208	13850.2	9798.04	9734.67
VV	479876	297512	15953.1	14091.4	281.626	67.4654	67.2817
Bkg	4.37893e+08	1.77795e+08	2.69591e+06	2.32728e+06	351807	159643	158742
Data	4.85205e+08	1.84925e+08	2.42496e+06	2.07011e+06	338836	148500	147210
Data/Bkg	1.10804	1.0401	0.899494	0.889495	0.96313	0.9302	0.927354

Table 16: Signal event yields for the different mass of charged Higgs after various selection cuts for the  $\mu + \text{jets}$  channel. Event yields are almost same upto 1-lepton selection for all mass points. However, after the  $N_{jets} \geq 4$  selection (when  $t\bar{t} + \text{jets}$  becomes the dominant background as shown in Table 14) the event yield for higher masses of the charged Higgs are reduced more compared to the lower masses. The event yield reduces because of the less phase space available between top-quark and charged Higgs for higher masses.

Process	Trigger	$N_{muon} = 1$	$N_{jets} \geq 4$	$\cancel{E}_T \geq 20 \text{ GeV}$	$\geq 2 \text{ b-jets}$	KinFit Sel.	$\geq 1 \text{ c-jet}$
$m_{H^+} = 80 \text{ GeV}$	233600	195175	112992	103481	36887.4	16719.5	16742
$m_{H^+} = 90 \text{ GeV}$	232950	194926	115096	105146	36828	16891.4	16906.2
$m_{H^+} = 100 \text{ GeV}$	233988	196003	117252	106948	37135.8	17547.6	17593.1
$m_{H^+} = 120 \text{ GeV}$	232076	195177	116921	106839	35050.5	16932.3	16995.4
$m_{H^+} = 140 \text{ GeV}$	233823	197826	111266	101823	28255.5	13404.1	13466.2
$m_{H^+} = 150 \text{ GeV}$	232614	197255	104083	95152	21645.2	9579.07	9627.62
$m_{H^+} = 155 \text{ GeV}$	233259	197836	100267	91809.7	17943.8	7561.99	7608.53
$m_{H^+} = 160 \text{ GeV}$	234566	199099	96825.5	88770	14826.9	5766.86	5790.45

Table 17: Signal event yields for different mass of charged Higgs after various selection cuts for the  $e + \text{jets}$  channel. Similar trend as that of Table 16 is seen.

Process	Trigger	$N_{ele} = 1$	$N_{jets} \geq 4$	$\cancel{E}_T \geq 20 \text{ GeV}$	$\geq 2 \text{ b-jets}$	KinFit Sel.	$\geq 1 \text{ c-jet}$
$m_{H^+} = 80 \text{ GeV}$	174714	140646	81310.9	74103.5	25873.1	11842	11850.9
$m_{H^+} = 90 \text{ GeV}$	175754	141375	83669	76257.2	26346.8	12196.8	12193
$m_{H^+} = 100 \text{ GeV}$	175150	140806	83893.1	76393.1	26123.4	12339.2	12362.7
$m_{H^+} = 120 \text{ GeV}$	176707	142579	85553.5	77733.4	24927.6	11958.6	11989.3
$m_{H^+} = 140 \text{ GeV}$	175443	141772	80110.2	73069.3	20198.9	9570.42	9618
$m_{H^+} = 150 \text{ GeV}$	177091	143189	75906.1	69103.3	15625.6	6948.44	6980.46
$m_{H^+} = 155 \text{ GeV}$	176517	142551	72361.6	66027.3	12889.3	5463.95	5497.52
$m_{H^+} = 160 \text{ GeV}$	176105	142405	70079.3	64024	10594.7	4224.59	4244.77

## 760 11 QCD Multijet Estimation

761 In the signal region, events consist of 1 lepton, at least 4 jets, and  $E_T^{\text{miss}}$ . The QCD multijet events  
 762 contain only jets at parton level. However, after event reconstruction, these events can still  
 763 have leptons from the misidentifications of light jets, and  $E_T^{\text{miss}}$  due to the poor measurement of  
 764 energy in the detector. The leptons can also be produced from the decay of bottom and charm  
 765 hadrons. The  $E_T^{\text{miss}}$  can also arise due to the mismeasurement of hadronic activity inside the  
 766 CMS detector. Having the same event topology as that of signal, the QCD multijet process is  
 767 also considered as a background for this analysis. However, it contributes only around 2% of  
 768 the total backgrounds.

769 The simulation of QCD multijet events are CPU time consuming due to which we can not  
 770 generate them in large numbers due to computing limitations. Due to the lesser number of  
 771 events, compared to the cross section, the statistical uncertainty is high. Also, the simulated  
 772 events are not properly modeled for high jet multiplicities. After lepton trigger selection, the  
 773 relative isolation plots from data and simulated events are shown in Figures 20a, 20b for  $\mu +$   
 774 jets and  $e +$  jets channel, respectively. From these figures, it is obvious that the events with  
 775  $I_{\text{rel}}^\mu \geq 0.20$  and  $I_{\text{rel}}^e \geq 0.10$  are dominated by QCD multijet processes. However, there is a poor  
 776 agreement between data and simulation for  $I_{\text{rel}}^\mu > 0.20$  and  $I_{\text{rel}}^e > 0.10$  for both  $\mu +$  jets and  
 777  $e +$  jets channel. In view of the above, the QCD multijet background is estimated from data to  
 778 have a precise estimation.

779 To estimate QCD multijet events from data, a method similar to the ABCD method is followed.  
 780 The ABCD region, as shown in Figure 22, is formed from two uncorrelated variables,  $E_T^{\text{miss}}$  and  
 781  $I_{\text{rel}}$  (relative isolation as defined in Equations (2) and (4)). The correlation between  $E_T^{\text{miss}}$  and  
 782  $I_{\text{rel}}$  are shown in Figures 21a (21b), 21c (21d) from data and simulated QCD multijet process for  
 783  $\mu +$  jets ( $e +$  jets) channel. The comparison between data and simulation for  $E_T^{\text{miss}}$  and  $I_{\text{rel}}$  are  
 784 shown in Figure 20 after 1-lepton selection, of Section 10, for  $\mu +$  jets and  $e +$  jets channel. From  
 785 this figure, it can be seen that the QCD multijet process is dominated in high  $I_{\text{rel}}$  region. The  
 786 signal region lies in high  $E_T^{\text{miss}}$  and low  $I_{\text{rel}}$  (region-A of Figure 22). We estimate QCD multijet  
 787 in the region-A from other regions as described in the following sections.

### 788 11.1 Determination of transfer scale factor

The phase space of  $E_T^{\text{miss}}$  and  $I_{\text{rel}}$  are divided into 4 regions as shown in Figure 22. The transfer  
 scale factors are determined using the following formula

$$\text{SF}_{\text{qcd}} = \frac{N_{(\text{Data} - \text{other backgrounds})}^D}{N_{(\text{Data} - \text{other backgrounds})}^C} \quad (22)$$

789 The number of events in different regions after kinematic fit selection are shown in Table 18 for  
 790  $\mu +$  jets and in Table 19 for  $e +$  jets channel. The  $\text{SF}_{\text{qcd}}$  is calculated after each selection step,  
 791 of Section 10, using Equation (22). It is to be noted that in some of the bins of a distribu-  
 792 tion the number of events in other background is greater than that from data which makes the  
 793 difference negative for that bin. The bin content of these negative bins is set to zero keeping  
 794 the uncertainty as it is. Therefore, for many negative bins there is a larger uncertainty asso-  
 795 ciated with the transfer factor. For the different distributions, the number of negative bins is  
 796 also different which leads to different transfer factor for them. In this analysis, we compute  
 797 the transfer factor separately for each distribution, each channel, and each selection step. The  
 798 transfer scale factors using  $m_{jj}$  distributions after kinematic fit and charm tagging are shown in  
 799 Table 20 for both channels. It can be seen that the transfer scale factors are of different orders  
 800 for the different selection steps.

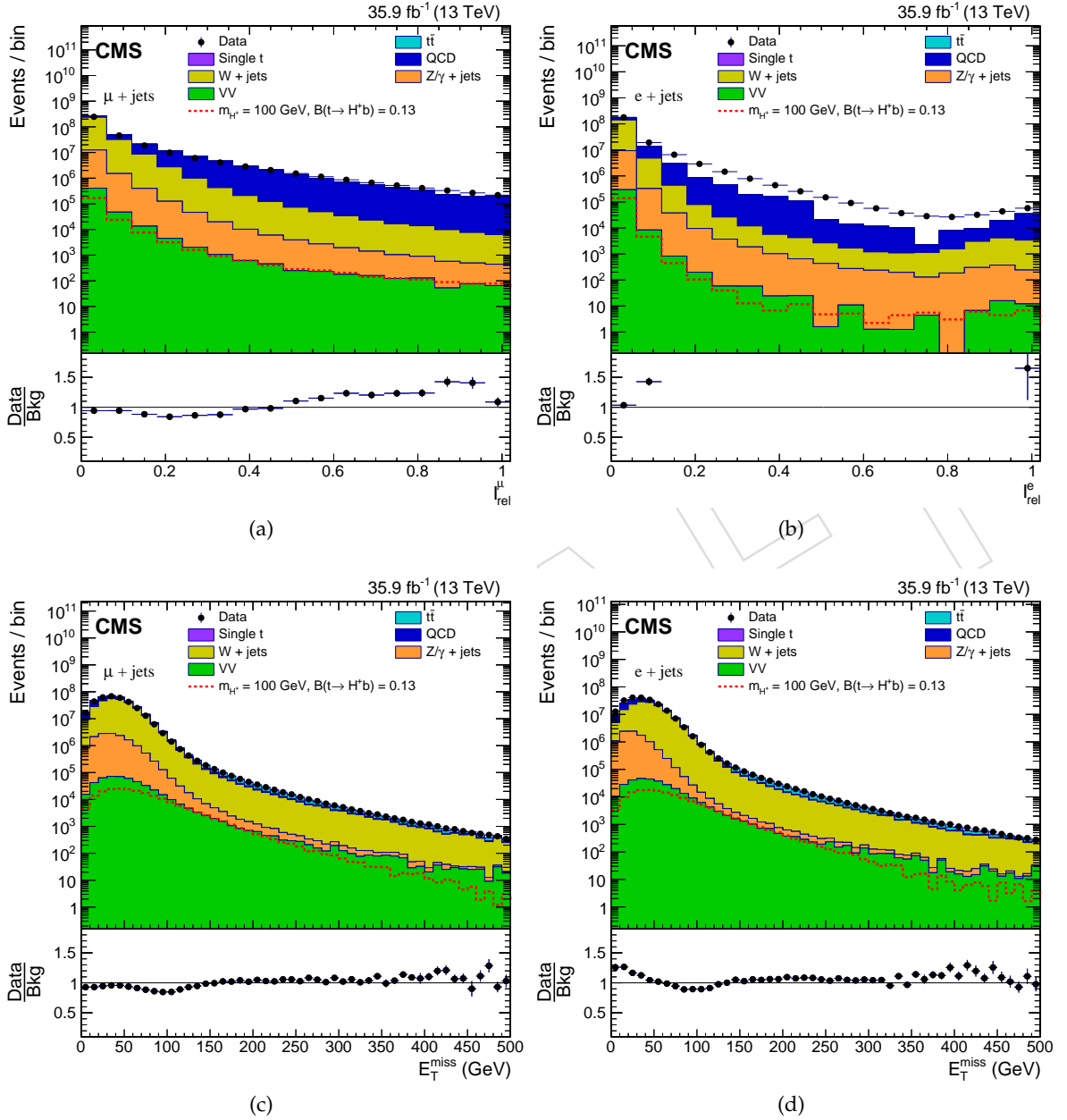


Figure 20: Distribution of relative isolation and missing transverse energy after lepton trigger selection for  $\mu + \text{jets}$  and  $e + \text{jets}$  channel. The QCD multijet process is dominated in the high  $I_{\text{rel}}$  region.

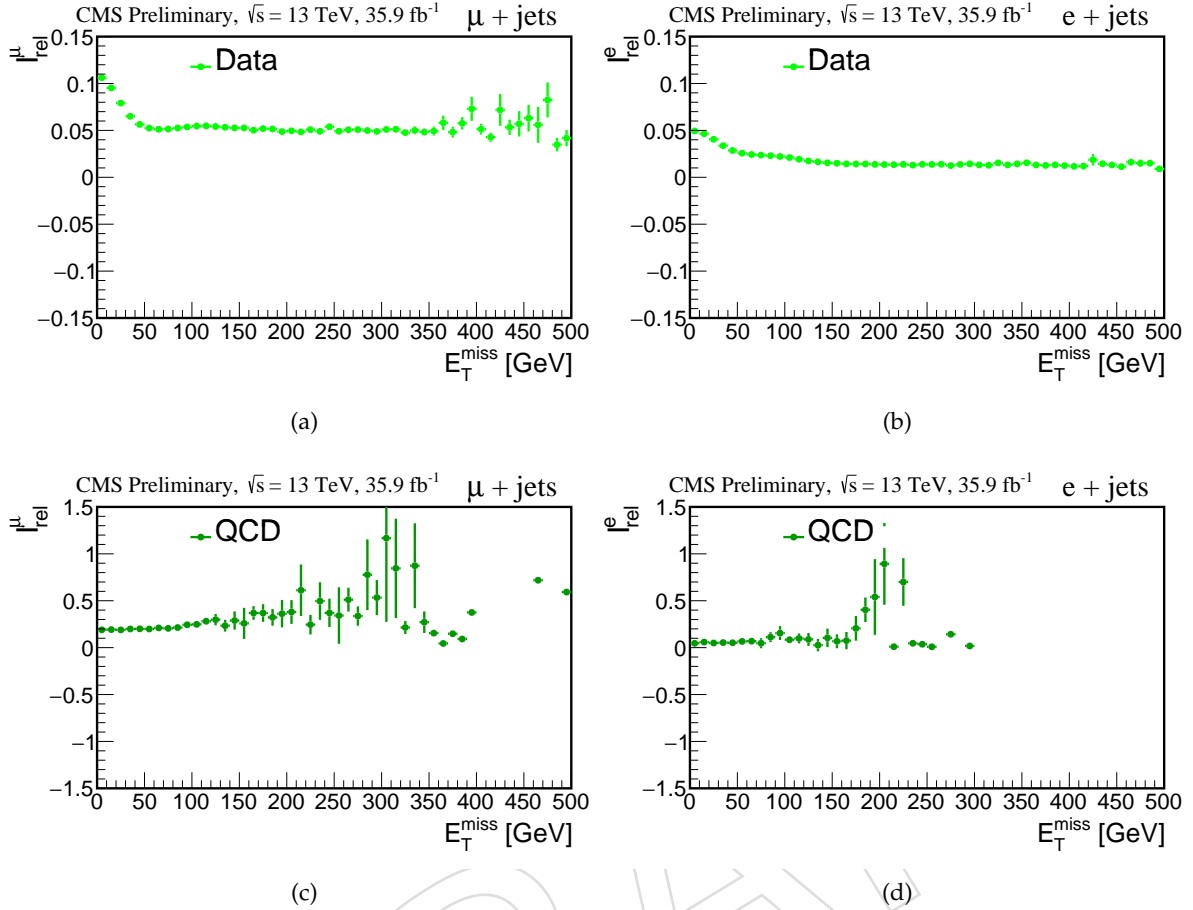


Figure 21: Distribution of mean of  $I_{\text{rel}}$  in different  $E_{\text{T}}^{\text{miss}}$  bins after lepton trigger selection for  $\mu + \text{jets}$  and  $e + \text{jets}$  channel. There seems to be some correlation between  $E_{\text{T}}^{\text{miss}}$  and  $I_{\text{rel}}$  in the low  $E_{\text{T}}^{\text{miss}} < 50$  GeV region for data as shown in Figures 21a, 21b. However, from simulated QCD multijet events, the  $E_{\text{T}}^{\text{miss}}$  and  $I_{\text{rel}}$  are uncorrelated, as shown in Figures 21c, 21d.

Table 18: Event yields from different regions, for  $\mu + \text{jets}$  channel after kinematic fit selection.

Process	Region-A (Iso, high MET)	Region-B (Non iso, high MET)	Region-C (Non iso, low MET)	Region-D (Iso, low MET)
Simulated QCD	$3159 \pm 1022$	$2225 \pm 597$	$1145 \pm 793$	$3221 \pm 2138$
$t\bar{t} + \text{jets}$	$205677 \pm 278$	$10006 \pm 61$	$1006 \pm 20$	$24890 \pm 97$
Single $t$	$5739 \pm 30$	$262 \pm 7$	$25 \pm 2$	$744 \pm 11$
$W + \text{jets}$	$2979 \pm 86$	$149 \pm 19$	$7 \pm 4$	$485 \pm 35$
$Z/\gamma + \text{jets}$	$441 \pm 17$	$16 \pm 3$	$4 \pm 1$	$120 \pm 8$
VV	$156 \pm 21$	$6 \pm 5$	$0 \pm 28$	$32 \pm 10$
nonQCDBkg	$216096 \pm 316$	$10440 \pm 65$	$1041 \pm 20$	$26270 \pm 104$
Data	$203178 \pm 451$	$12767 \pm 113$	$1948 \pm 44$	$26307 \pm 162$

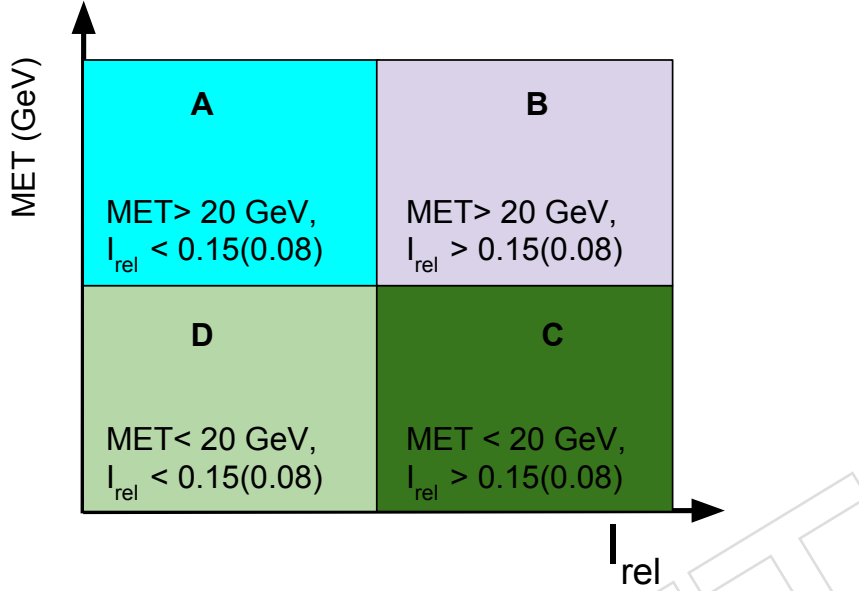


Figure 22: Different regions between  $I_{\text{rel}}$  and MET (missing transverse energy also known as  $E_{\text{T}}^{\text{miss}}$ ) to estimate QCD multijet events from data. For  $\mu + \text{jets}$  channel, the isolation region corresponds to  $I_{\text{rel}}^{\mu} < 0.15$  whereas the non-isolation corresponds to  $0.15 < I_{\text{rel}}^{\mu} < 0.40$ . For  $e + \text{jets}$  channel, the isolation region corresponds to  $I_{\text{rel}}^e < 0.0821(0.0695)$  whereas the non-isolation region corresponds to  $0.0821 < I_{\text{rel}}^e < 0.30$  ( $0.0695 < I_{\text{rel}}^e < 0.30$ ) for electron found in barrel (endcap) regions.

Table 19: Event yields from different regions, for  $e + \text{jets}$  channel after kinematic fit selection.

Process	Region-A (Iso, high MET)	Region-B (Non iso, high MET)	Region-C (Non iso, low MET)	Region-D (Iso, low MET)
Simulated QCD	$9798 \pm 6596$	$0 \pm 53$	$49 \pm 49$	$688 \pm 353$
$t\bar{t} + \text{jets}$	$143178 \pm 228$	$3931 \pm 38$	$424 \pm 12$	$18398 \pm 82$
Single $t$	$4030 \pm 25$	$97 \pm 4$	$9 \pm 1$	$544 \pm 9$
$W + \text{jets}$	$2115 \pm 72$	$47 \pm 10$	$2 \pm 2$	$344 \pm 28$
$Z/\gamma + \text{jets}$	$453 \pm 15$	$11 \pm 2$	$4 \pm 1$	$191 \pm 11$
VV	$67 \pm 13$	$0 \pm 53$	$0 \pm 18$	$31 \pm 8$
nonQCDBkg	$154153 \pm 309$	$4086 \pm 39$	$439 \pm 13$	$19508 \pm 88$
Data	$148499 \pm 385$	$6995 \pm 84$	$1271 \pm 36$	$20740 \pm 144$

Cuts	SF <sub>qcd</sub> ( $\mu$ + jets)	SF <sub>qcd</sub> (e + jets)
$N_b$ jets $\geq 2$	$1.345 \pm 0.133$	$1.851 \pm 0.117$
Kinematic fit selection	$0.474 \pm 0.214$	$1.481 \pm 0.214$
$N_c$ jets $\geq 1$	$0.396 \pm 0.217$	$1.395 \pm 0.215$
Exclusive loose	$0.325 \pm 0.281$	$1.017 \pm 0.267$
Exclusive medium	$0.629 \pm 0.425$	$1.267 \pm 0.412$
Exclusive tight	$0.717 \pm 0.782$	$1.279 \pm 0.742$

Table 20: The QCD multijet transfer scale factors ( $SF_{qcd}$ ) for  $\mu$  + jets and e + jets channel after various selection steps. The categorization of events based on exclusive loose, medium, and tight c quark tagging is described in Section 15.

## 801 11.2 Estimation of QCD multijet in the signal region

All the other backgrounds are subtracted from data in region-B and the resulting distribution is multiplied with the transfer scale factor to estimate the contribution of data-driven QCD multijet events in region-A (signal region) i.e.

$$(QCD)_A = SF_{qcd} \times (\text{Data} - \text{other backgrounds})_B \quad (23)$$

802 In the control plots of Figures 25, 26, 27 and 28, 29, 30, the data-driven QCD multijet events are  
803 shown.

## 804 11.3 Comparison of data-driven QCD multijet shapes

805 The validity of ABCD method relies on the fact that the data-driven QCD multijet shape should  
806 be similar in all the four regions. For sake of comparison, we compare shapes of few variables  
807 after b jet and kinematic fit selection steps. In the low  $E_T^{\text{miss}}$  region, the shape of  $p_T$ ,  $\eta$  of jets  
808 and lepton from the isolated and anti-isolated region are shown in Figures 23, 24. From these  
809 figures, it can be seen that the data-driven shape in isolated and anti-isolated matches quite well  
810 for these distributions. In few bins, the number of events in other background is greater than  
811 that in data. Therefore the number of data-driven QCD multijet events ( $n_{\text{Data} - \text{other background}}$ )  
812 becomes negative. We set bin content of such bin to zero keeping the statistical uncertainty as  
813 it is.

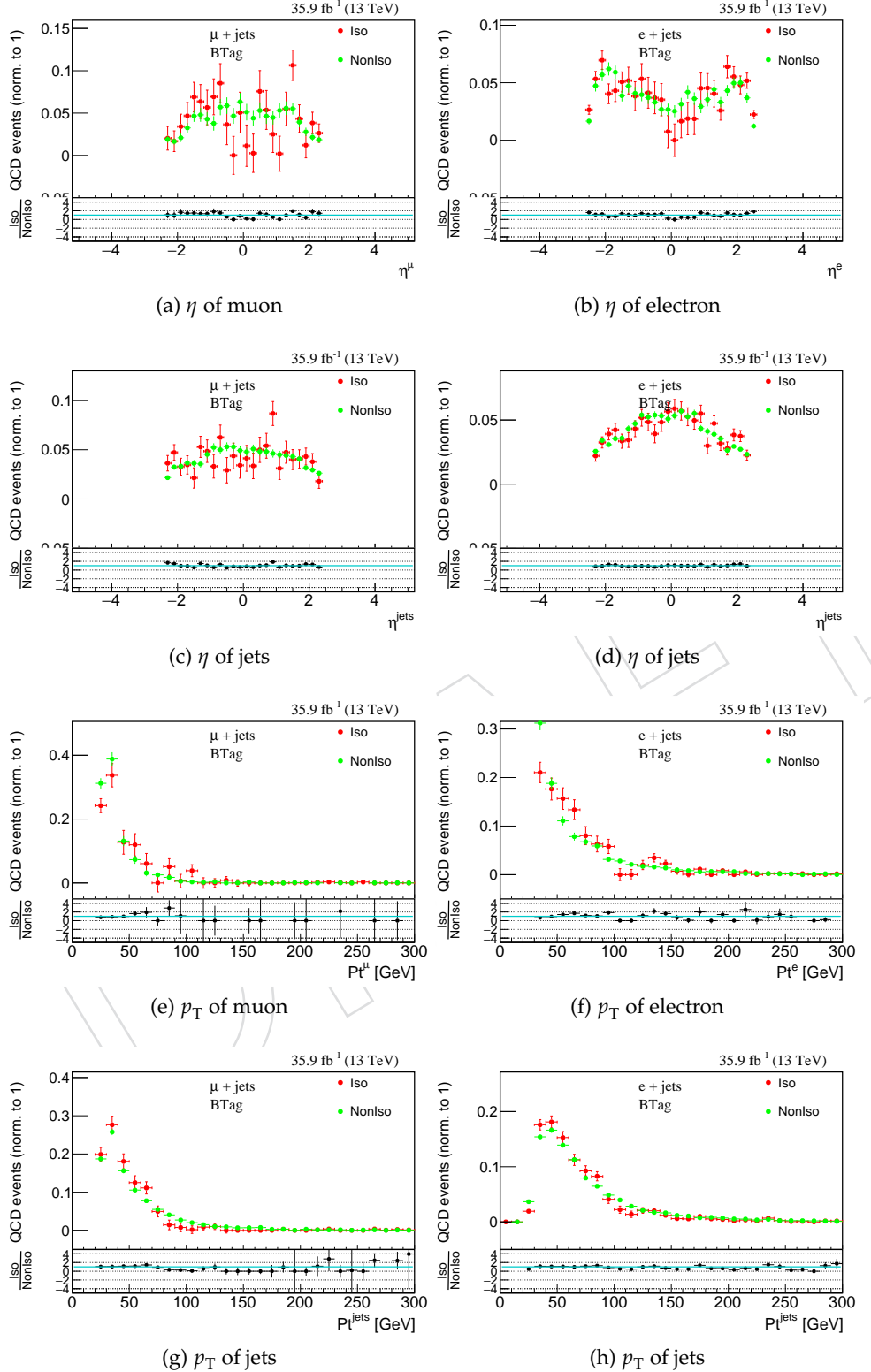


Figure 23: Comparison of data-driven QCD multijet shapes in low  $E_T^{\text{miss}}$  region ( $< 20 \text{ GeV}$ ), from the isolated and anti-isolated region with reconstructed jets after b jet selection for  $\mu + \text{jets}$  and  $e + \text{jets}$  channel.

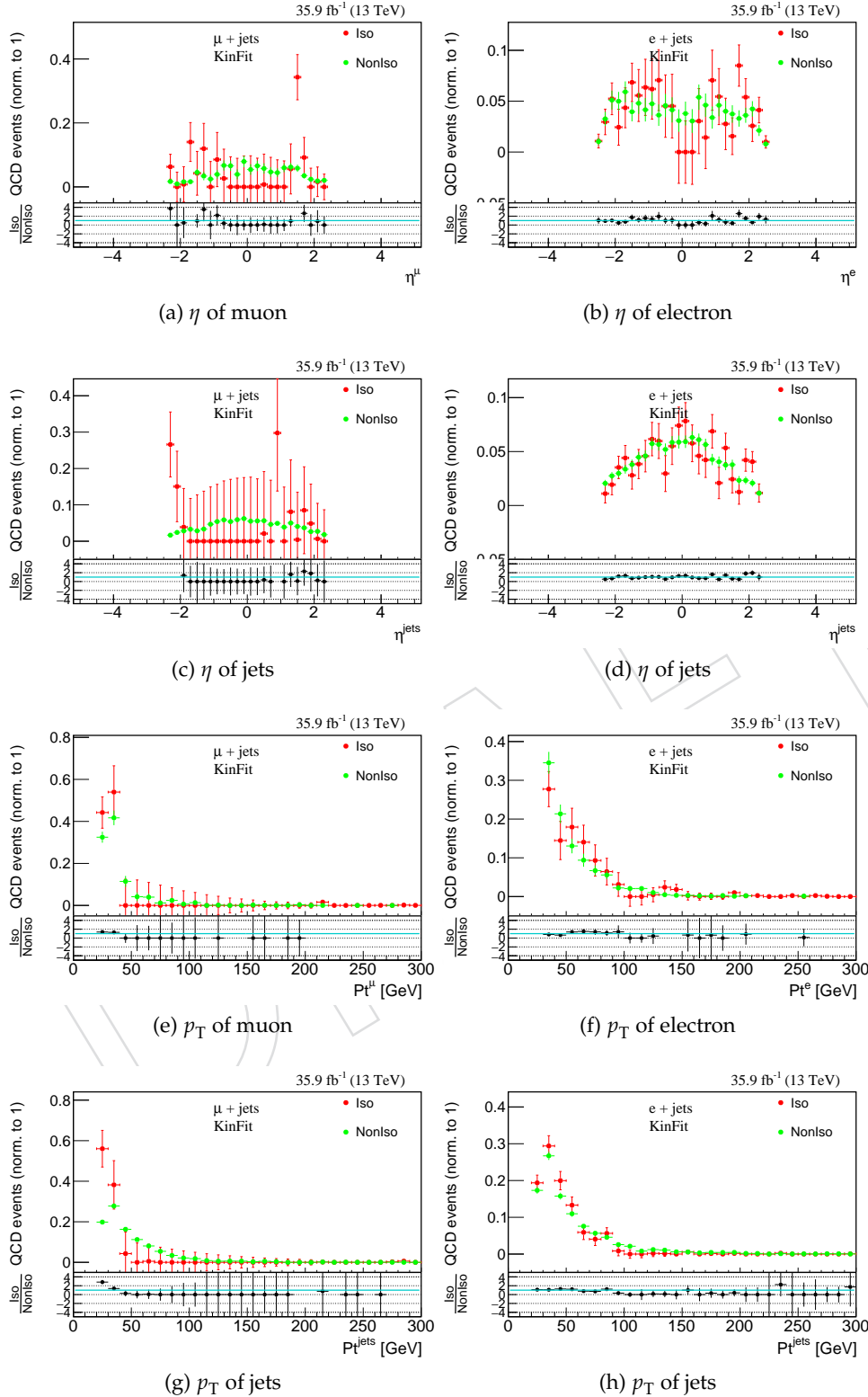


Figure 24: Comparison of data-driven QCD multijet shapes in low  $E_T^{\text{miss}}$  region ( $< 20$  GeV), from the isolated and anti-isolated region with kinematic fitted objects after kinematic fit selection for  $\mu + \text{jets}$  and  $e + \text{jets}$  channel.

## 814 12 Control Plots in Signal Region

815 In the signal region, each event must have at least 4 jets, 1 lepton, and  $E_T^{\text{miss}} > 20 \text{ GeV}$ . Var-  
816 ious selection cuts are applied, as described in Sec. 10, to improve the signal to background  
817 ratio. These cuts suppress most of the SM background such as QCD,  $W + \text{jets}$ ,  $Z/\gamma + \text{jets}$  etc.  
818 For example, the single lepton trigger reduces QCD background more because there are no  
819 "prompt" leptons in QCD events. Similarly, a requirement of  $E_T^{\text{miss}} > 20 \text{ GeV}$  reduces QCD,  
820  $Z/\gamma + \text{jets}$  background significantly. Various kinematic variables such as  $p_T$ ,  $\eta$  of lepton and  
821 jets, jet-multiplicity,  $E_T^{\text{miss}}$ ,  $M_T$  (transverse mass of leptonic decaying W Boson) for data and MC  
822 are plotted in the signal region.

823 Data to MC comparison of variables from reconstructed objects after applying b-jet selection as  
824 described in Sec. 10 are shown in Figure 25, 26, 27 for  $\mu + \text{jets}$  and electron + jets channel. There  
825 is a good agreement between data and MC within statistical and systematics uncertainties for  
826 all variables except for the  $p_T$  (of lepton and jets) and  $E_T^{\text{miss}}$ . There is a poor agreement between  
827 data and background for higher values of  $p_T$  and  $E_T^{\text{miss}}$ . The disagreement in these distributions  
828 can be fixed by applying the top  $p_T$  weights. However, the top- $p_T$  weights do not affect the  $m_{jj}$   
829 distribution and hence there is no change in the exclusion limits. In fact, in the earlier version of  
830 the note (AN\_18\_061\_v4), the top- $p_T$  weights were applied where one can see good agreement  
831 between the  $p_T$  and  $E_T^{\text{miss}}$  distributions. Data to MC comparison of variables from the kinematic  
832 fitted objects after kinematic fit selection as described in Sec. 10 are shown in Figure 28, 29 30.  
833 There is also a good agreement between data and MC within the statistical and systematic  
834 uncertainties. Here also we see similar disagreement for the higher value of  $p_T$  and  $E_T^{\text{miss}}$ .

DRAFT

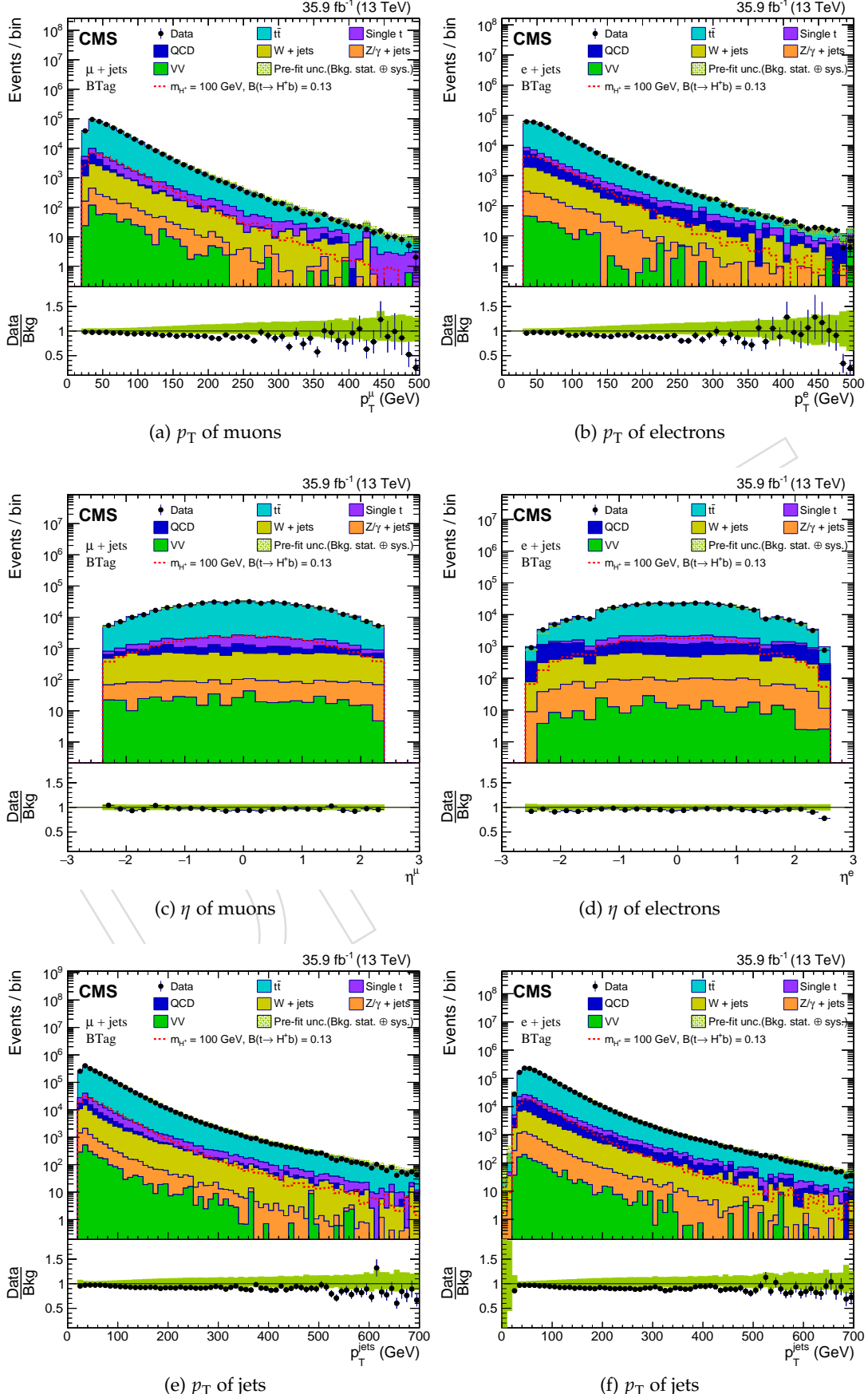


Figure 25: Distribution of  $p_T$ ,  $\eta$  of reconstructed lepton and  $p_T$  of jets after b-jet selection as described in Sec. 10, for muons + jets and e + jets channel.

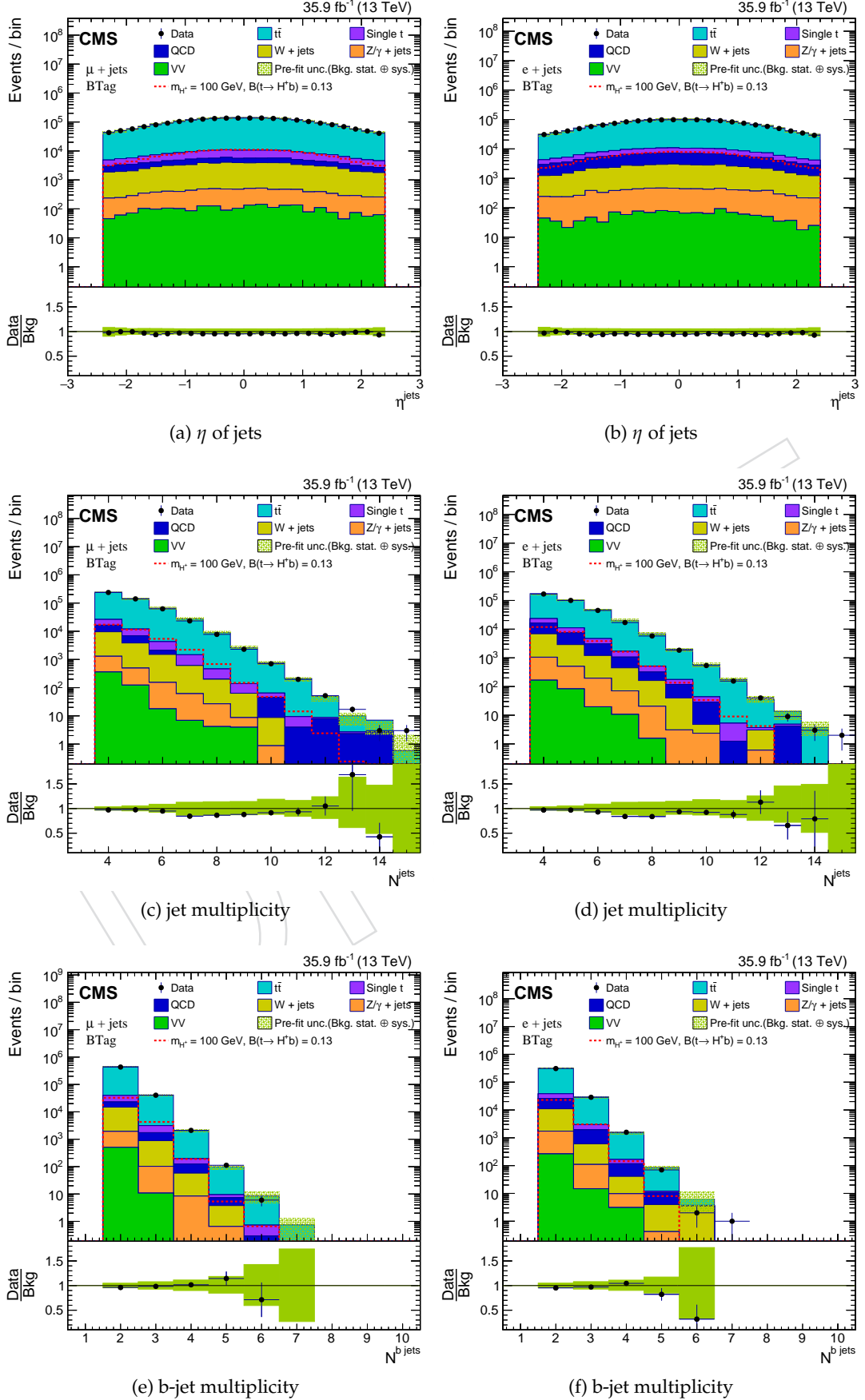


Figure 26: Distribution of reconstructed  $\eta$  of jets, jet-multiplicity, and b-jet multiplicity after b-jet selection as described in Sec. 10, for muons + jets and e + jets channel.

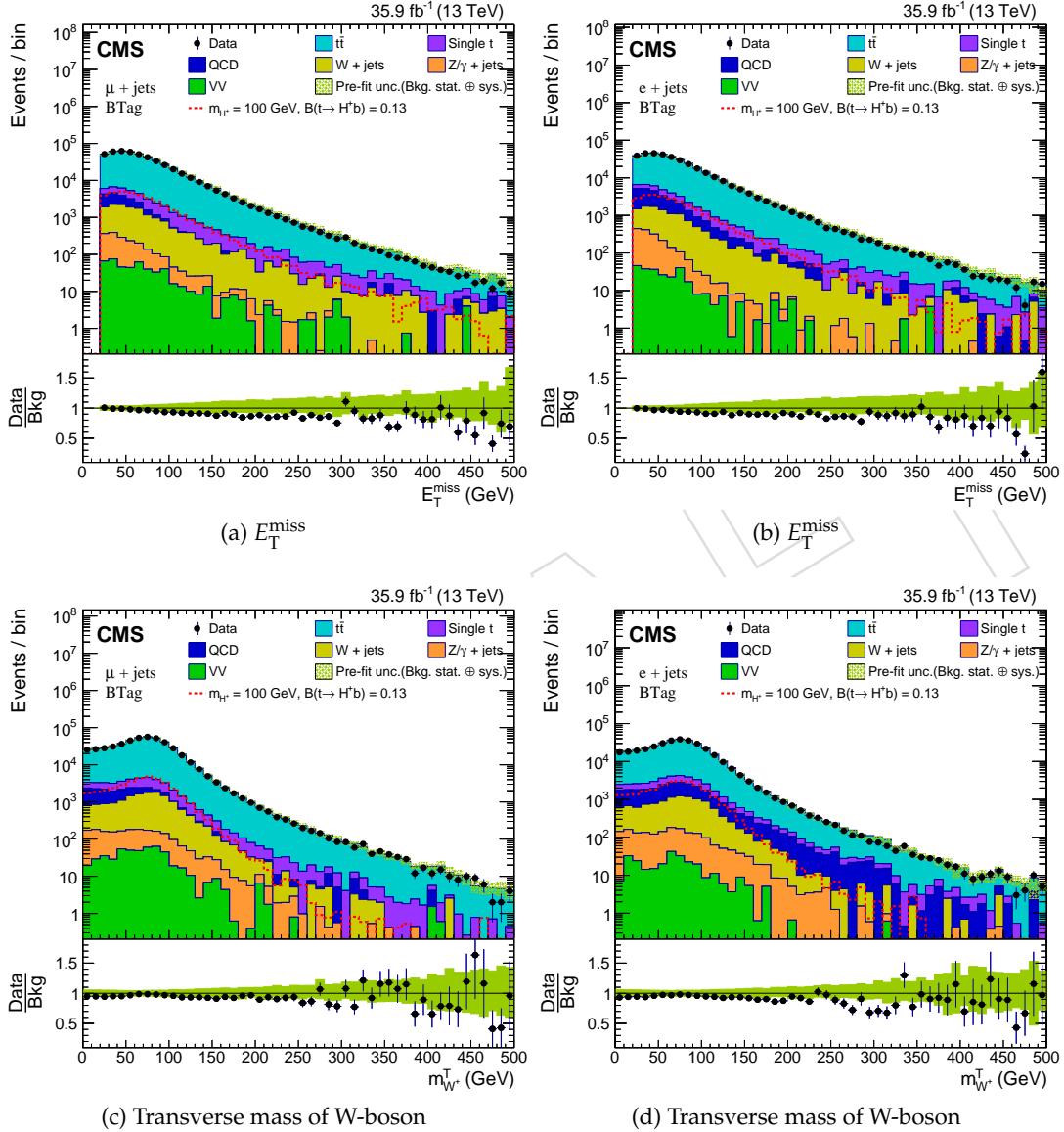


Figure 27: Distribution of reconstructed  $E_T^{\text{miss}}$  and  $m_{W^+}^T$  (transverse mass of W-boson, W decaying leptonically) after b-jet selection as described in Sec. 10, for muons + jets and  $e + \text{jets}$  channel.

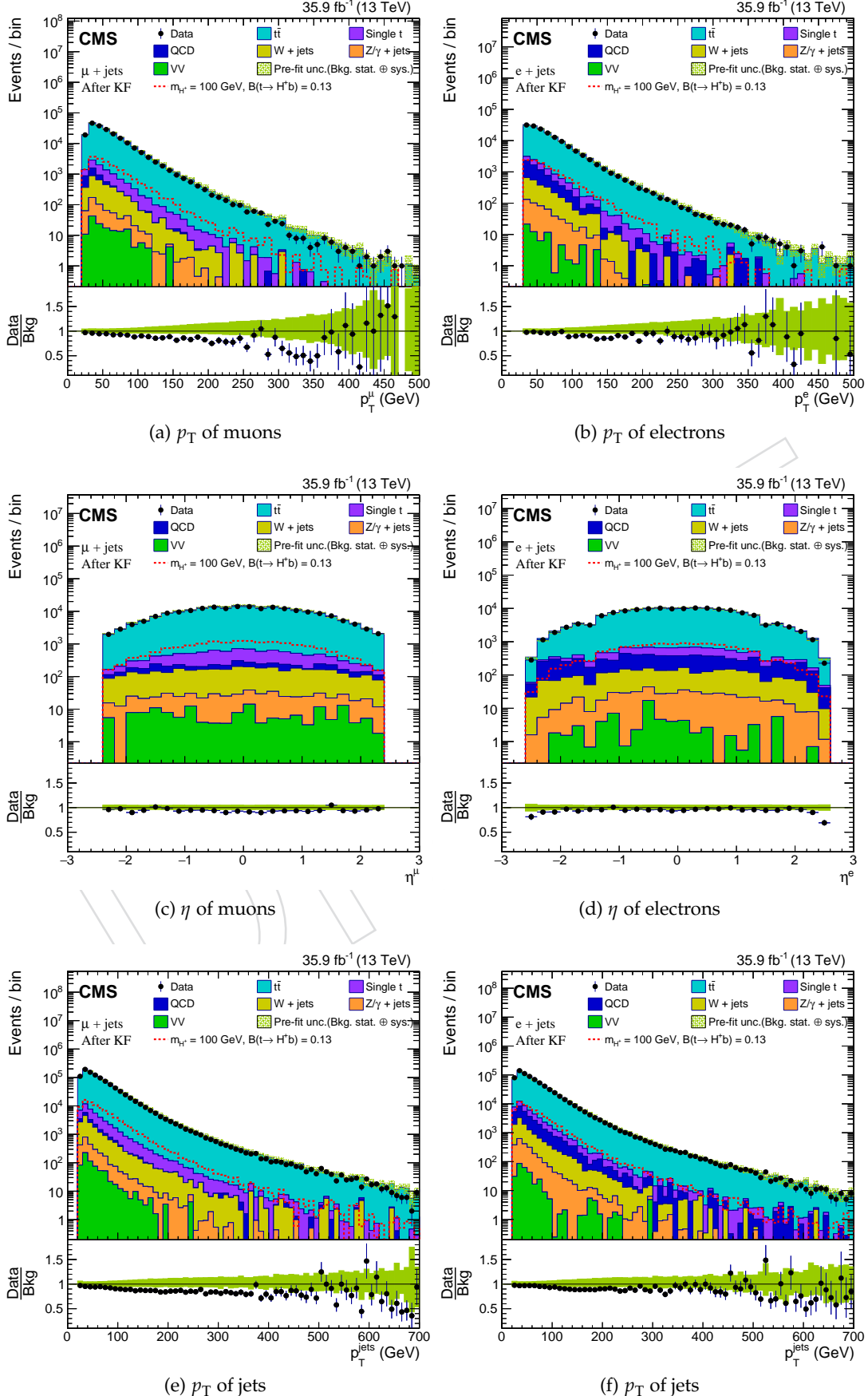


Figure 28: Distribution of  $p_T$ ,  $\eta$  of kinematic fitted lepton and  $p_T$  of jets after kinematic fit selection as described in Sec. 10, for muons + jets and e + jets channel.

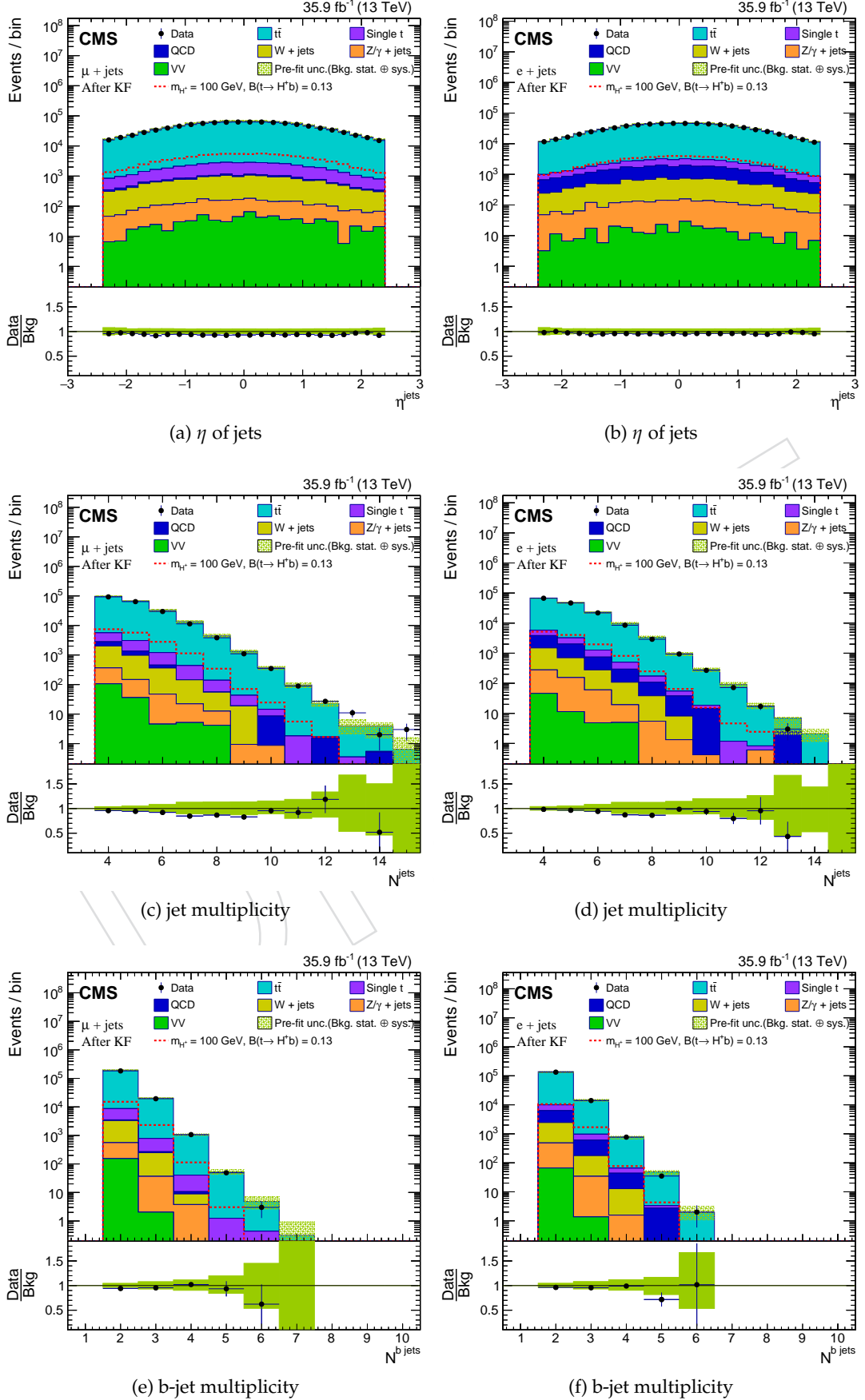


Figure 29: Distribution of kinematic fitted  $\eta$  of jets, jet-multiplicity, and b-jet multiplicity after kinematic fit selection as described in Sec. 10, for muons + jets and e + jets channel.

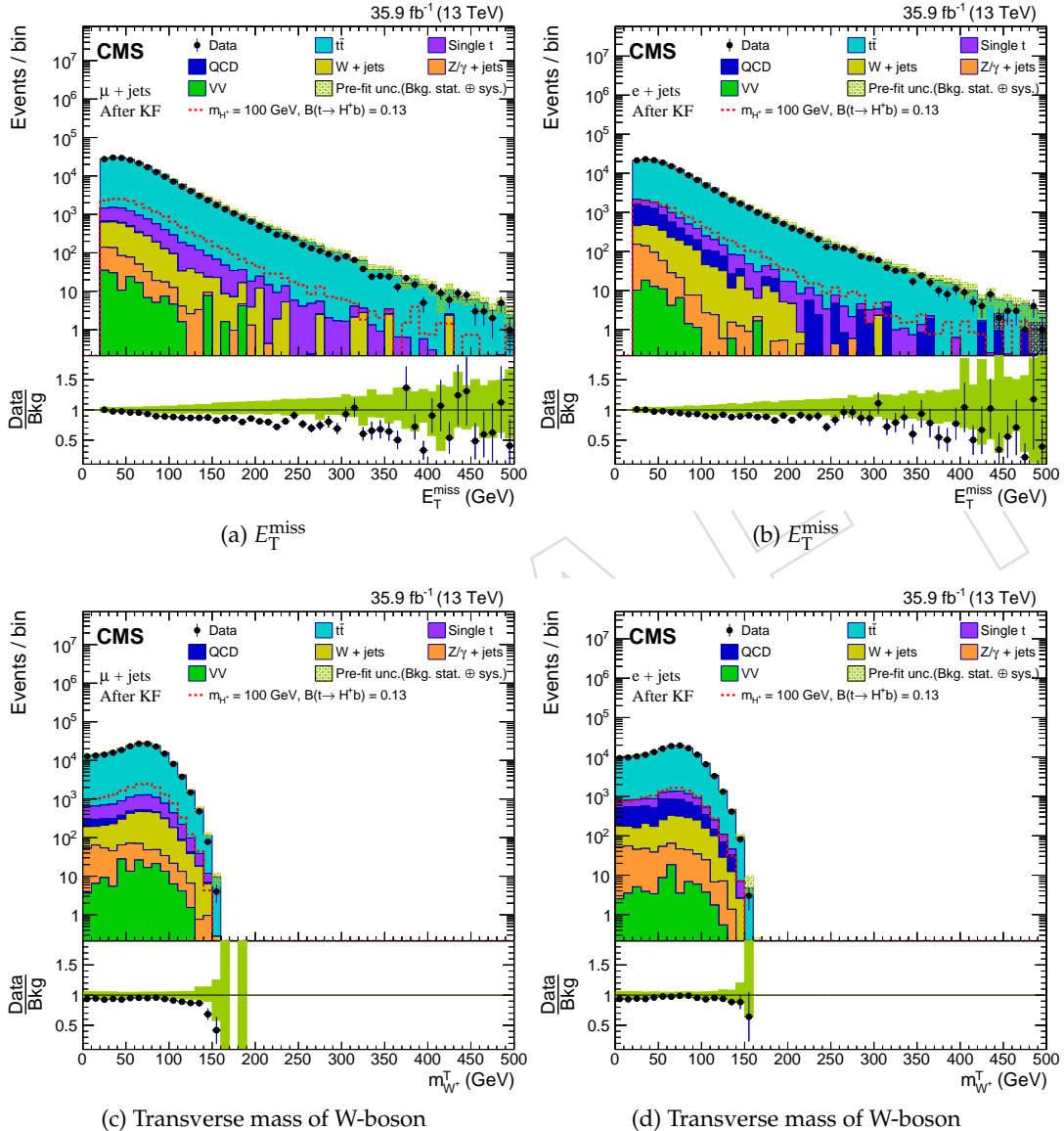


Figure 30: Distribution of kinematic fitted  $E_T^{\text{miss}}$  and  $m_W^T$  after kinematic fit selection as described in Sec. 10, for muons + jets and e + jets channel.

## 835 13 Mass Reconstruction

836 The charged Higgs ( $H^+$ ) decays to  $c\bar{s}(\bar{c}s)$ , thus the invariant mass ( $m_{jj}$ ) of  $c\bar{s}(\bar{c}s)$  pair will be  
 837 the mass of the  $H^+$ . Reconstruction and identification of jets coming from c-quark and s-quark  
 838 is very important to reconstruct the mass of charged Higgs ( $m_{H^+}$ ). We reconstruct ( $m_{H^+}$ ) with  
 839 and without kinematic fit as follows:

- 840 •  **$m_{H^+}$  reconstruction without kinematic fit:** The jets are reconstructed and selected  
 841 as described in Sec. 4.4. Events are required to have at least 4 jets. We use b-tagging  
 842 as described in Sec. 5 to tag 2-jets as b-tagged jet. The jets are sorted in descending  
 843 order of b- discriminator values and the first two jets are considered as b-jets. If an  
 844 event contains exactly 4 jets then the other 2 non-bjets are used to evaluate  $m_{jj}$ . How-  
 845 ever, if an event contains more than 4 jets, then the non-bjets are sorted in descend-  
 846 ing order of  $p_T$  and two highest  $p_T$  non-bjets are used to evaluate  $m_{jj}$ . The invariant  
 847 mass ( $m_{jj}$ ) distribution after b-jet selection as described in Sec. 10 is shown in Fig-  
 848 ure 12a, 12b for data and background for  $m_{H^+} = 100$  GeV and in Figure 31a, 31b for  
 849 all charged Higgs signal samples for  $\mu +$  jets and electron +jets channel respectively.
- 850 •  **$m_{H^+}$  reconstruction with kinematic fit:** The kinematic fit is performed on the recon-  
 851 structed jets of Sec. 4.4 as described in Sec. 6 in the semi-leptonic decay mode of  $t\bar{t}$   
 852 where W Boson from one of the top-quark decays leptonically and W Boson from the  
 853 other top-quark decays hadronically. The kinematic fitter also assigns jets as b-quark  
 854 jets that fulfill the b-tagging criteria discussed before and provide the best value for  
 855 the fit probability, these are shown in Figure 2 separately along with other two non  
 856 b-jets (coming from hadronic decay of one of the W Boson). We evaluate  $m_{jj}$  from  
 857 these two non b-jets. The  $m_{jj}$  distribution after kinematic fit selection as described  
 858 in Sec. 10 is shown in Figure 12c , 12d for data and background for  $m_{H^+} = 120$  GeV  
 859 and in Figure 31c, 31d for all charged Higgs signal samples for  $\mu +$  jets and e + jets  
 860 channel respectively. The  $m_{jj}$  distributions of Figure 12c, 12d, and 31c, 31d are used  
 861 to compute the exclusion limit on the  $BR(t \rightarrow H^+ b)$  in Sec. 18.

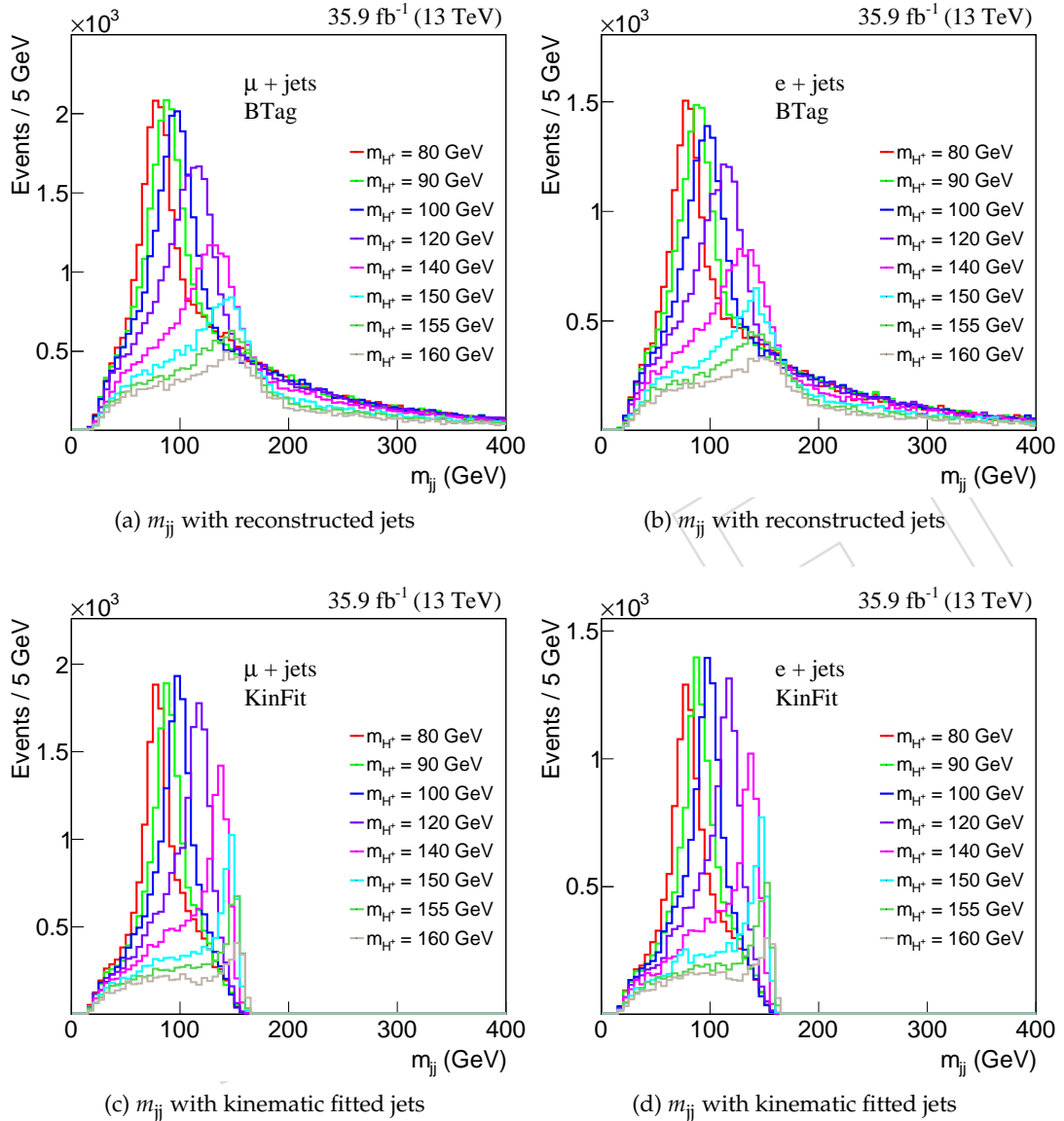


Figure 31:  $m_{jj}$  distributions of two non-b, highest Pt-jets from charged Higgs signal samples ( $m_{H^+} = 80, 90, 100, 120, 140, 150, 155, 160$  GeV) for  $\mu +$  jets and  $e +$  jets channel. The  $m_{jj}$  distributions of Figure 31a, 31b are evaluated using reconstructed jets after b-jet selection as described in Sec. 10. Whereas  $m_{jj}$  distributions of Figure 31c, 31d are evaluated using kinematic fitted jets after kinematic fit selection as described in Sec. 10.

## 862 14 Systematic Uncertainties

863 The event yields shown in Table 25 have two types of uncertainties: statistical and systemat-  
 864 ics. For  $N$  number of events, the absolute statistical uncertainty is  $\sqrt{N}$ . To calculate statistical  
 865 uncertainties with the scale factors, applied in Sec. 8, the histograms are filled with "Sumw2()"  
 866 method. The systematics uncertainties arise due to improper calibration of the detector, the un-  
 867 certainty in the efficiency of the reconstruction algorithm, uncertainty difference in theoretical  
 868 prediction etc. The systematics uncertainties considered in this analysis are divided into two  
 869 categories: experimental and theoretical uncertainties.

### 870 14.1 Experimental Uncertainties

- 871 • **Luminosity:** The uncertainty in the integrated luminosity is 2.5% for 2016 data tak-  
 872 ing [73].

- 873 • **Pileup reweighting:** The pileup weights as discussed in Sec. 8.2 are calculated us-  
 874 ing minimum bias cross-section 69.2 mb. The uncertainty in the minimum bias  
 875 cross-section affects the pileup distribution of data of Figure 15d. Hence the pileup  
 876 weights of Figure 15e is also affected. The minimum bias cross-section is varied up  
 877 and down by 4.7% and corresponding pileup weights are applied to the MC events.  
 878 The effect of pileup uncertainty on the  $m_{jj}$  shape is shown in Figure 64a, 64b and  
 879 Figure 68c, 68d from charged Higgs and  $t\bar{t} + \text{jets}$  sample, respectively.

- 880 • **Lepton trigger, tracking, identification and isolation:** The lepton scale factors as  
 881 discussed in Sec. 8.3 are applied to the MC samples. A conservative 3% uncertainty  
 882 is considered on combined lepton scale factors for both channels.

- 883 • **Jet energy,  $E_T^{\text{miss}}$  correction:** The  $p_T$  of jet in the MC are corrected using JES and  
 884 JER as discussed in Sec. 8.4. The jet correction is propagated to correct  $E_T^{\text{miss}}$ . The  
 885  $m_{jj}$  shape of Sec. 13 are also affected by the uncertainties in the JES, JER as shown  
 886 in Figures 64c, 64d, 64e, 64f for charged Higgs signal ( $m_{H^+} = 120$  GeV) and in Fig-  
 887 ures 66a, 66b, 66c, 66d for  $t\bar{t} + \text{jets}$  background in  $\mu + \text{jets}$  and  $e + \text{jets}$  channels.  
 888 The uncertainties in the event yield due to jet energy,  $E_T^{\text{miss}}$  correction are shown in  
 889 Tables 22, 24, and 26 for different event categories.

- 890 • **b/c-tagging uncertainty:** The b and c-jets are present within the same event. The b/c  
 891 tag scale factors (as described in Sec. 8.5 and Sec. 8.6) are correlated to each other as  
 892 shown in Fig 32. The correlated scale factors are varied up/down simultaneously.  
 893 From Figure 32, there are three nuisance parameters from various combination:

- 894 • CMS\_eff\_bcInc3 (correlating (a), (c), (d))
- 895 • CMS\_eff\_bcInc2 (correlating (e), (f))
- 896 • CMS\_eff\_bcInc1 (from (b))

897 After  $\geq 1$  c-jet selection, the effect of b/c-tagging systematics on the shape of  $m_{jj}$   
 898 distribution are shown in Figures 65a, 65c, 65e, and 65b, 65d, 65f for charged Higgs  
 899 signal ( $m_{H^+} = 120$  GeV) and in Figures 66e, 66g, 67a, and 66f, 66h, 67b for  $t\bar{t} + \text{jets}$   
 900 background in  $\mu + \text{jets}$  and  $e + \text{jets}$  channels. The uncertainties on the event yield  
 901 are shown in Tables 22, 24, and 26 for different event categories.

- 902 • **QCD data-driven uncertainty:** The relative isolation of muon(electron) are conser-  
 903 vatively shifted to 0.17 (0.11) and the corresponding change in the QCD yield is  
 904 determined. The percentage change in the yield is considered as systematic uncer-  
 905 tainty in the QCD estimation.

- 906 • **Bin-by-bin uncertainty:** In some of the bins of  $m_{jj}$  distributions, the statistics are

	b-tagged	c-tagged
c-quark	(a)	(b)
b-quark	(c)	(d)
l-quark	(e)	(f)

Figure 32: Correlation of b/c-tag scale factors. The region (a): c-quark tagged as b-jet, (b): c-quark tagged as c-jet, (c): b-quark tagged as b-jet, (d): b-quark tagged as c-jet, (e): light-quark tagged as b-jet, (f): light-quark tagged as c-jet.

907 small hence statistical uncertainty is large. In each bin of summed  $m_{jj}$  from all back-  
 908 grounds, one shape nuisance is considered using "autoMCStats" method (\* autoM-  
 909 CStats 0 1) of Higgs combine tool.

## 910 14.2 Theoretical Uncertainties

- 911 • **Normalization:** The MC events are normalised with the scale factor of Eq. 13. The  
 912 cross-section in Eq. 13 have uncertainties. The normalization uncertainties for MC  
 913 samples are shown in Tables 22, 24, and 26 for different event categories.
- **Top-quark  $p_T$  re-weighting:** The t quark  $p_T$  weights are determined from following  
 914 equation

$$w_{top} = \sqrt{SF(t) \times SF(\bar{t})}, \quad \text{where } SF \equiv \exp(0.09494 - 0.00084 \times p_T). \quad (24)$$

915 The values in the exponent are determined by fitting the inverse of the ratio plot  
 916 of Figure 3 of TOP-17-014 using the function  $\exp(a + bx)$ , where a and b are the  
 917 parameters of the fit and x is the  $p_T$  of parton level t quark. The corresponding  $\chi^2$   
 per number of degree of freedom of the fit is 0.000985.

918 The parton level  $p_T$  of t and  $\bar{t}$  quark is used to calculate SF. The PDG code "6" and  
 919 isLastCopy() is used to identify the t quark at parton level. The  $w_{top}$  is taken to be 1  
 920 for "down" and  $w_{top}^2$  for "up" systematic as recommended by TOP-PAG [74]. The re-  
 921 weighting is applied only on  $t\bar{t}$  + jets and charged Higgs samples shown in Table 2.  
 922 The effect of top-pt re-weighting uncertainties on the  $m_{jj}$  is shown in Figures 65g,  
 923 65h, for charged Higgs signal ( $m_{H^+} = 120$  GeV) and in Figures 68a, 68b for  $t\bar{t}$  + jets  
 924 background in  $\mu$  + jets and e + jets channels.

925 It is to be noted that the the analysis TOP-17-014 has dilepton in the final states  
 926 whereas in this analysis (HIG-18-021) we have one lepton. A series of checks [75]  
 927 were performed to make sure the SF are compatible with this analysis such as

- 928 • Kinematic selection of leptons and jets are very close between the two  
 929 analyses
- The dilepton selection in TOP-17-014 is orthogonal to lepton+jets selec-  
 930 tion of this analysis

- 932     • The range of  $p_T$  of t quark in the  $t\bar{t}$  MC in this analysis is in the range of  
 933       order of 500 GeV as beyond this range the extrapolation of weights are  
 934       not reliable  
 935     • The difference in the  $p_T$  spectrum of the t quark between nominal  $t\bar{t}$   
 936       (NLO PowHeg) and nominal signal (LO MadGraph) is 10% and between  
 937       reweighted  $t\bar{t}$  bkg (NLO PowHeg) and nominal signal (LO MadGraph) is  
 938       20%. Because of the small difference, the same SF is used for  $t\bar{t}$  and all  
 939       signal samples.
- 940     • **Top-quark mass:** The POWHEG  $t\bar{t} + \text{jets}$  sample shown in Table 2 was generated  
 941       with  $M_t = 172.5$  GeV. We used  $t\bar{t} + \text{jets}$  sample with  $M_t = 171.5$  GeV and  $M_t =$   
 942       173.5 GeV, as shown in Table 3, to observe the effect of top-quark mass on the  $m_{jj}$ .  
 943       The  $m_{jj}$  for different  $M_t$  are shown in Figures 67c, 67d for  $t\bar{t} + \text{jets}$  background in  
 944        $\mu + \text{jets}$  and  $e + \text{jets}$  channels.  
 945     • **Parton shower matching:** In the POWHEG + PYTHIA generated samples, the next-  
 946       to-leading order (NLO) matrix element parton shower matching is varied by  $h_{damp}$   
 947       parameter. The  $t\bar{t} + \text{jets}$  samples generated by varying  $h_{damp}$  "up" and "down", as  
 948       shown in Table 3 are used to see the effect of  $h_{damp}$  on the  $m_{jj}$  distribution as shown  
 949       in Figures 67g, 67h for  $t\bar{t} + \text{jets}$  background in  $\mu + \text{jets}$  and  $e + \text{jets}$  channels.  
 950     • **Renormalization and factorisation scale:** To see the effect of renormalization and  
 951       factorisation scale, the "up" and "down"  $t\bar{t} + \text{jets}$  samples as shown in Table 3. The  
 952       effect of these scales on the  $m_{jj}$  are shown in Figures 67e, 67f for  $t\bar{t} + \text{jets}$  background  
 953       in  $\mu + \text{jets}$  and  $e + \text{jets}$  channels.  
 954     The QCD is estimated from data. Hence none of the systematics (except the QCD data-driven  
 955       and normalization uncertainty) are considered on the QCD background. All the systematic and  
 956       statistical uncertainties are shown in Tables 22, 24, and 26 for different event categories.

Table 21: Event yield for inclusive category.

<b>Process</b>	$N_{events} \pm stat \pm sys$	$N_{events} \pm stat \pm sys$
	$\mu + jets$	$e + jets$
$m_{H^+} = 80$ GeV	$16719 \pm 114 \pm 778$	$11842 \pm 94 \pm 539$
$m_{H^+} = 90$ GeV	$16891 \pm 113 \pm 789$	$12197 \pm 95 \pm 594$
$m_{H^+} = 100$ GeV	$17548 \pm 115 \pm 857$	$12339 \pm 95 \pm 548$
$m_{H^+} = 120$ GeV	$16932 \pm 113 \pm 787$	$11959 \pm 94 \pm 547$
$m_{H^+} = 140$ GeV	$13404 \pm 101 \pm 680$	$9570 \pm 84 \pm 503$
$m_{H^+} = 150$ GeV	$9579 \pm 85 \pm 552$	$6948 \pm 71 \pm 421$
$m_{H^+} = 155$ GeV	$7562 \pm 77 \pm 458$	$5464 \pm 65 \pm 371$
$m_{H^+} = 160$ GeV	$5767 \pm 66 \pm 383$	$4225 \pm 56 \pm 289$
SM $t\bar{t}$ + jets	$205677 \pm 278 \pm 9885$	$143178 \pm 228 \pm 7200$
Single t	$5739 \pm 30 \pm 339$	$4030 \pm 25 \pm 244$
QCD multijet	$1104 \pm 117 \pm 0$	$4308 \pm 192 \pm 0$
W + jets	$2979 \pm 86 \pm 450$	$2115 \pm 72 \pm 173$
$Z/\gamma$ + jets	$441 \pm 17 \pm 45$	$453 \pm 15 \pm 47$
VV	$156 \pm 21 \pm 16$	$67 \pm 13 \pm 13$
All background	$216096 \pm 316 \pm 10593$	$154153 \pm 309 \pm 7604$
Data	$203178 \pm 451$	$148499 \pm 385$

## 15 Categorization of Events

To improve the exclusion limit on the  $\mathcal{B}(t \rightarrow H^+ b)$ , the  $m_{jj}$  from following event categories have been used for limit computation:

### 15.1 Inclusive Event Category without charm-jet Tagging

The  $m_{jj}$  distribution without further categorizing events based on charm tagging was used at 8 TeV [15] for limit computation due to the unavailability of dedicated charm taggers. For sake of comparison, at 13 TeV also the exclusion limit is computed using  $m_{jj}$  after kinematic fit selection, without the charm tagging. The event yields are shown in Table 21. Corresponding  $m_{jj}$  distributions are shown in Figures 12c, 12d, 31c, 31d. The corresponding systematics and statistical uncertainties from different sources are shown in Table 22. The exclusion limit for inclusive event category is computed in Sec. 18.1.

### 15.2 Inclusive Event Category with Loose charm-jet Tagging

The charm taggers as discussed in Sec. 7 are used to tag a jet as c-jet. One of the jets forming  $m_{jj}$  is required to pass the charm-tagging requirement. The event yields for loose charm working points after applying c-tag event weights are shown in Table 23. The  $m_{jj}$  distribution with inclusive loose charm tagging working points are shown in Figure 33. The corresponding systematics and statistical uncertainties from different sources are shown in Table 24. Exclusion limits using  $m_{jj}$  after applying loose charm tagging is computed in Sec. 18.2.

Table 22: Systematic and statistical uncertainties in %, from inclusive category for muon (electron) channel. The “—” indicates that the corresponding uncertainties are not considered for the given process.

Process	Luminosity	Pileup	Lepton	$\text{JES} + \text{JER} + E_{\text{T}}^{\text{miss}}$	b & c-jet tagging-1	b & c-jet tagging-2	b & c-jet tagging-3	Normalization	Statistical	top $p_{\text{T}}$
$m_{H^+} = 80 \text{ GeV}$	2.5 (2.5)	0.8 (0.9)	3.0 (3.0)	3.3 (3.1)	0.0 (0.0)	0.3 (0.3)	3.2 (3.2)	6.1 (6.1)	0.7 (0.8)	1.6 (1.9)
$m_{H^+} = 90 \text{ GeV}$	2.5 (2.5)	0.6 (0.8)	3.0 (3.0)	3.3 (3.5)	0.0 (0.0)	0.3 (0.3)	3.2 (3.2)	6.1 (6.1)	0.7 (0.8)	1.5 (2.1)
$m_{H^+} = 100 \text{ GeV}$	2.5 (2.5)	0.7 (0.8)	3.0 (3.0)	3.6 (2.9)	0.0 (0.0)	0.3 (0.3)	3.2 (3.2)	6.1 (6.1)	0.7 (0.8)	1.5 (1.9)
$m_{H^+} = 120 \text{ GeV}$	2.5 (2.5)	0.6 (1.1)	3.0 (3.0)	3.2 (3.0)	0.0 (0.0)	0.3 (0.3)	3.3 (3.3)	6.1 (6.1)	0.7 (0.8)	1.5 (1.9)
$m_{H^+} = 140 \text{ GeV}$	2.5 (2.5)	0.8 (1.0)	3.0 (3.0)	3.5 (3.8)	0.0 (0.0)	0.4 (0.4)	3.5 (3.5)	6.1 (6.1)	0.8 (0.9)	2.1 (2.4)
$m_{H^+} = 150 \text{ GeV}$	2.5 (2.5)	0.6 (0.9)	3.0 (3.0)	4.3 (4.6)	0.0 (0.0)	0.6 (0.6)	3.8 (3.7)	6.1 (6.1)	0.9 (1.0)	2.6 (3.3)
$m_{H^+} = 155 \text{ GeV}$	2.5 (2.5)	0.5 (0.6)	3.0 (3.0)	4.6 (5.5)	0.0 (0.0)	0.8 (0.7)	3.8 (3.9)	6.1 (6.1)	1.0 (1.2)	3.2 (3.5)
$m_{H^+} = 160 \text{ GeV}$	2.5 (2.5)	0.1 (0.8)	3.0 (3.0)	5.2 (5.5)	0.0 (0.0)	0.9 (1.0)	4.0 (3.9)	6.1 (6.1)	1.1 (1.3)	3.4 (3.7)
$t\bar{t} + \text{jets}$	2.5 (2.5)	0.7 (0.8)	3.0 (3.0)	3.3 (3.3)	0.0 (0.0)	0.3 (0.3)	3.1 (3.1)	6.1 (6.1)	0.1 (0.2)	1.5 (2.0)
Single t	2.5 (2.5)	0.3 (0.5)	3.0 (3.0)	4.7 (4.9)	0.0 (0.0)	0.7 (0.7)	3.5 (3.5)	5.0 (5.0)	0.5 (0.6)	—
W+jets	2.5 (2.5)	2.4 (0.6)	3.0 (3.0)	13.6 (5.9)	0.0 (0.0)	4.3 (3.8)	4.2 (4.2)	5.0 (5.0)	2.9 (3.4)	—
$Z/\gamma + \text{jets}$	2.5 (2.5)	1.9 (2.8)	3.0 (3.0)	8.6 (8.7)	0.0 (0.0)	3.8 (3.2)	3.5 (3.7)	4.5 (4.5)	3.9 (3.4)	—
VV	2.5 (2.5)	0.9 (4.9)	3.0 (3.0)	9.0 (17.9)	0.0 (0.0)	1.7 (1.3)	4.9 (3.3)	4.0 (4.0)	13.2 (18.9)	—
QCD multijet	—	—	—	—	—	—	—	10(10)	10.6 (4.5)	—

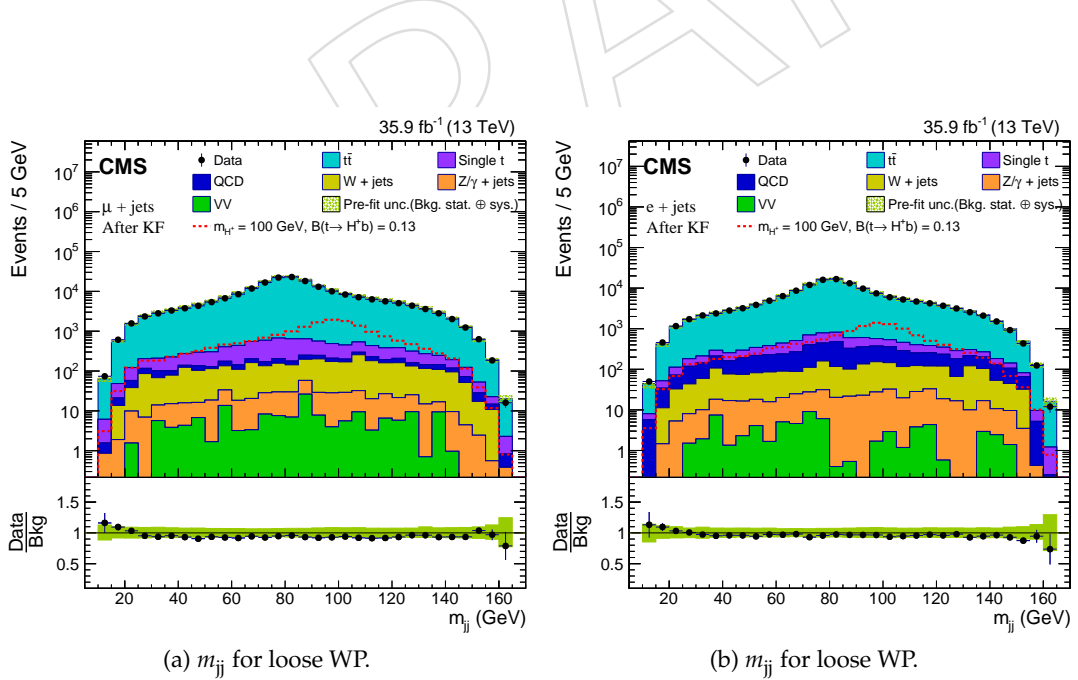


Figure 33: Distribution of  $m_{jj}$  for inclusive loose charm working point as described in Sec. 15.2 for  $\mu + \text{jets}$  and  $e + \text{jets}$  channel.

Table 23: Event yield for inclusive loose charm category.

<b>Process</b>	$N_{events} \pm stat \pm sys$	$N_{events} \pm stat \pm sys$
	$\mu + jets$	$e + jets$
$m_{H^+} = 80$ GeV	$16742 \pm 114 \pm 1191$	$11851 \pm 95 \pm 830$
$m_{H^+} = 90$ GeV	$16906 \pm 114 \pm 1202$	$12193 \pm 96 \pm 886$
$m_{H^+} = 100$ GeV	$17593 \pm 116 \pm 1285$	$12362 \pm 96 \pm 868$
$m_{H^+} = 120$ GeV	$16995 \pm 114 \pm 1247$	$11989 \pm 95 \pm 873$
$m_{H^+} = 140$ GeV	$13466 \pm 102 \pm 1062$	$9618 \pm 85 \pm 767$
$m_{H^+} = 150$ GeV	$9628 \pm 86 \pm 828$	$6980 \pm 72 \pm 618$
$m_{H^+} = 155$ GeV	$7609 \pm 78 \pm 697$	$5498 \pm 65 \pm 521$
$m_{H^+} = 160$ GeV	$5790 \pm 67 \pm 556$	$4245 \pm 57 \pm 416$
SM $t\bar{t}$ + jets	$204576 \pm 278 \pm 14666$	$142431 \pm 229 \pm 10408$
Single t	$5693 \pm 30 \pm 472$	$3995 \pm 25 \pm 338$
QCD multijet	$887 \pm 110 \pm 0$	$3993 \pm 185 \pm 0$
W + jets	$2932 \pm 86 \pm 522$	$2074 \pm 72 \pm 251$
Z/ $\gamma$ + jets	$423 \pm 16 \pm 55$	$439 \pm 15 \pm 57$
VV	$156 \pm 21 \pm 19$	$67 \pm 13 \pm 13$
All background	$214667 \pm 314 \pm 15619$	$153000 \pm 305 \pm 11022$
Data	$201331 \pm 449$	$147210 \pm 384$

Table 24: Systematic and statistical uncertainties in %, from inclusive loose charm-category for muon (electron) channel. The “—” indicates that the corresponding uncertainties are not considered for the given process.

Process	Luminosity	Pileup	Lepton	JES + JER + $E_T^{\text{miss}}$	b & c-jet tagging-1	b & c-jet tagging-2	b & c-jet tagging-3	Normalization	Statistical	top $p_T$
$m_{H^+} = 80$ GeV	2.5 (2.5)	0.8 (0.9)	3.0 (3.0)	3.3 (3.0)	1.4 (1.4)	4.0 (4.0)	4.6 (4.6)	6.1 (6.1)	0.7 (0.8)	1.6 (1.9)
$m_{H^+} = 90$ GeV	2.5 (2.5)	0.6 (0.8)	3.0 (3.0)	3.3 (3.6)	1.3 (1.3)	4.0 (4.0)	4.6 (4.6)	6.1 (6.1)	0.7 (0.8)	1.5 (2.1)
$m_{H^+} = 100$ GeV	2.5 (2.5)	0.7 (0.8)	3.0 (3.0)	3.5 (2.8)	1.3 (1.3)	4.0 (4.0)	4.8 (4.8)	6.1 (6.1)	0.7 (0.8)	1.5 (1.9)
$m_{H^+} = 120$ GeV	2.5 (2.5)	0.6 (1.1)	3.0 (3.0)	3.2 (3.0)	1.2 (1.3)	4.0 (4.0)	5.1 (5.0)	6.1 (6.1)	0.7 (0.8)	1.5 (1.9)
$m_{H^+} = 140$ GeV	2.5 (2.5)	0.8 (1.0)	3.0 (3.0)	3.5 (3.8)	1.2 (1.2)	4.1 (4.1)	5.6 (5.5)	6.1 (6.1)	0.8 (0.9)	2.1 (2.4)
$m_{H^+} = 150$ GeV	2.5 (2.5)	0.6 (0.9)	3.0 (3.0)	4.3 (4.7)	1.1 (1.2)	4.4 (4.4)	5.9 (5.9)	6.1 (6.1)	0.9 (1.0)	2.6 (3.3)
$m_{H^+} = 155$ GeV	2.5 (2.5)	0.5 (0.6)	3.0 (3.0)	4.7 (5.4)	1.1 (1.1)	4.7 (4.7)	6.2 (6.1)	6.1 (6.1)	1.0 (1.2)	3.2 (3.5)
$m_{H^+} = 160$ GeV	2.5 (2.5)	0.2 (0.8)	3.0 (3.0)	5.2 (5.5)	1.0 (1.1)	4.9 (5.0)	6.4 (6.3)	6.1 (6.1)	1.2 (1.3)	3.4 (3.6)
$t\bar{t}$ + jets	2.5 (2.5)	0.7 (0.9)	3.0 (3.0)	3.3 (3.3)	0.7 (0.7)	4.5 (4.5)	4.1 (4.1)	6.1 (6.1)	0.1 (0.2)	1.5 (2.0)
Single t	2.5 (2.5)	0.3 (0.5)	3.0 (3.0)	4.7 (4.8)	0.6 (0.6)	5.1 (5.2)	4.5 (4.6)	5.0 (5.0)	0.5 (0.6)	—
W+jets	2.5 (2.5)	2.3 (0.5)	3.0 (3.0)	14.2 (6.2)	0.4 (0.3)	9.1 (8.9)	5.3 (5.4)	5.0 (5.0)	2.9 (3.4)	—
Z/ $\gamma$ + jets	2.5 (2.5)	1.6 (2.6)	3.0 (3.0)	8.7 (8.7)	0.2 (0.2)	8.3 (7.7)	4.7 (5.3)	4.5 (4.5)	3.8 (3.5)	—
VV	2.5 (2.5)	0.9 (5.0)	3.0 (3.0)	8.9 (17.7)	0.5 (1.0)	5.7 (5.8)	5.9 (3.8)	4.0 (4.0)	13.1 (18.9)	—
QCD multijet	—	—	—	—	—	—	—	10(10)	12.4 (4.6)	—

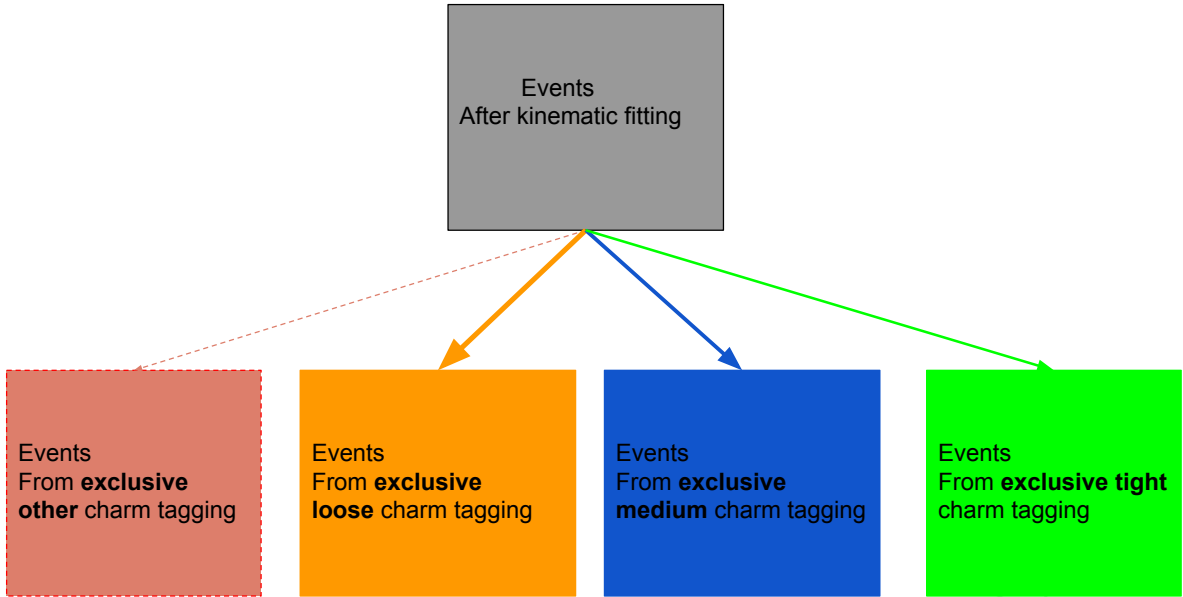


Figure 34: Exclusive event categories based on charm-tagging.

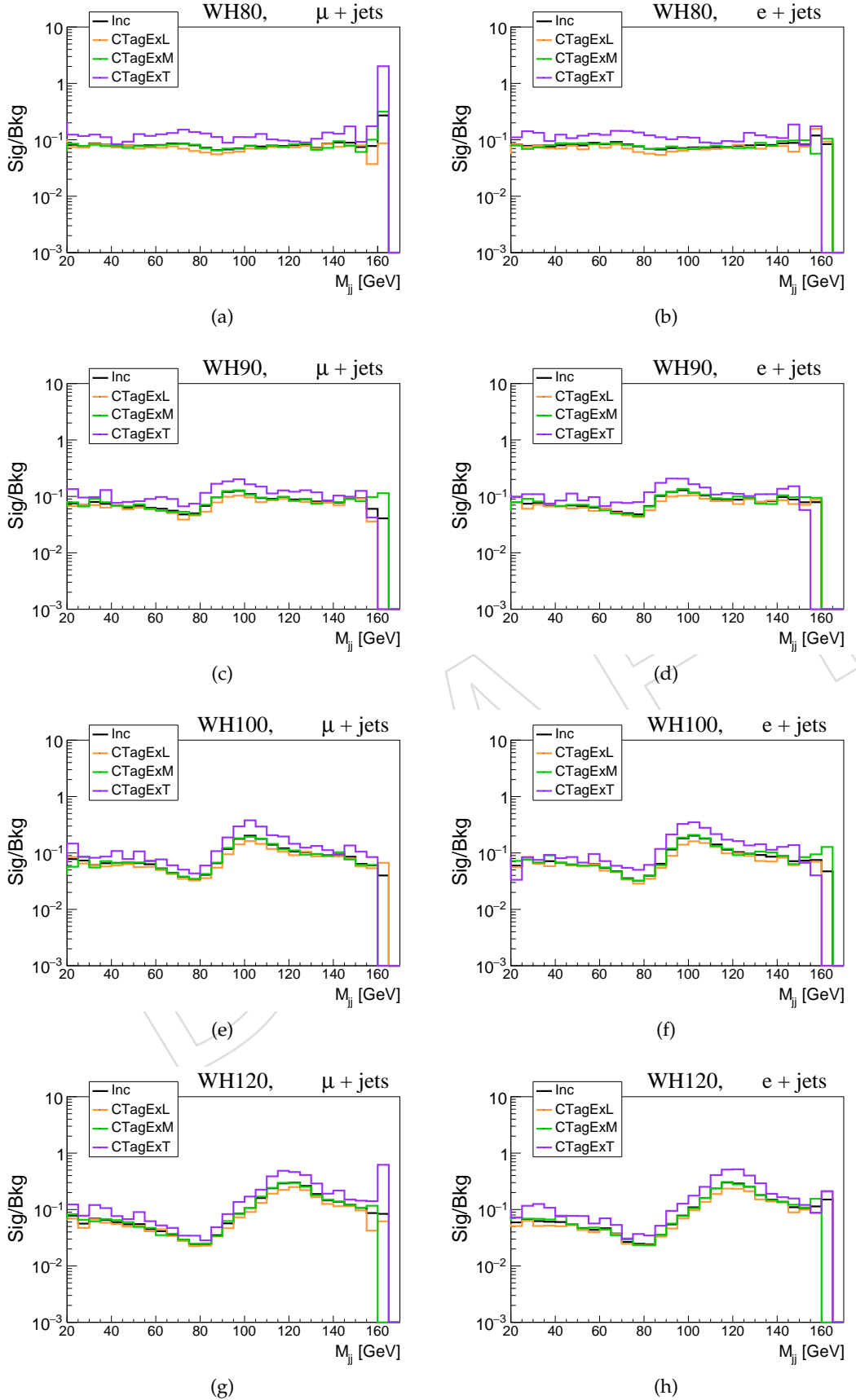
### 15.3 Exclusive Event Categories Based on charm-jet Tagging

The signal significance is different in different charm working points as can be seen from Figure 33. This property is exploited in improving the exclusion limits. Events are exclusively divided into the loose, medium, and tight categories as shown in Figure 34, based on whether one of the jets forming  $m_{jj}$  pass loose but not medium, medium but not tight, and tight working points of the charm-tagging requirements, respectively. The resulting  $m_{jj}$  are combined to compute the limit. The  $m_{jj}$  distribution from exclusive charm categories is shown in Figure 37. The corresponding event yields are shown in Table 25. The signal to background ratio (Sig/Bkg) is shown in Figures 35, 36 for different masses of charged Higgs for both channels. From these figures, one can see that the signal to background ratio is different in different categories. The corresponding systematics and statistical uncertainties from different sources are shown in Table 26. The data cards from these 3 categories are combined to compute limits as described in Sec. 18.3.

The charm-tag scale factors are officially not available for exclusive event categories. Therefore, conservatively, the inclusive scale factors are used for exclusive event categories. However, one extra systematic uncertainty is considered for exclusive categories. The mean of inclusive c-tag weights (Eq. 20) is calculated based on whether a jet is satisfying one of the charm WP and not satisfying other charm WP (e.g. the jet satisfies loose and medium but not tight WP, as shown in Table 27, 28).

- CMS\_eff\_ExL: The ratio (max/min) of mean of inclusive c-tag weights from four combinations ( $yLyMyT$ ,  $yLyMnT$ ,  $yLnMyT$ ,  $yLnMnT$ ) is considered as one extra NP (profiled as lnN) for exclusive loose charm category.
- CMS\_eff\_ExM: For exclusive medium charm category, the ratio (max/min) of event weights from two combinations ( $yMyT$ ,  $yMnT$ ) are considered as one extra NP (profiled as lnN).

The inclusive and exclusive event categories are same for tight charm working points, hence no extra NP is considered. The loose and medium c-tag event weight corresponding to Table 27,

Figure 35: Signal to background ratio for  $m_{H^+} = 80, 90, 100, 120$  GeV.

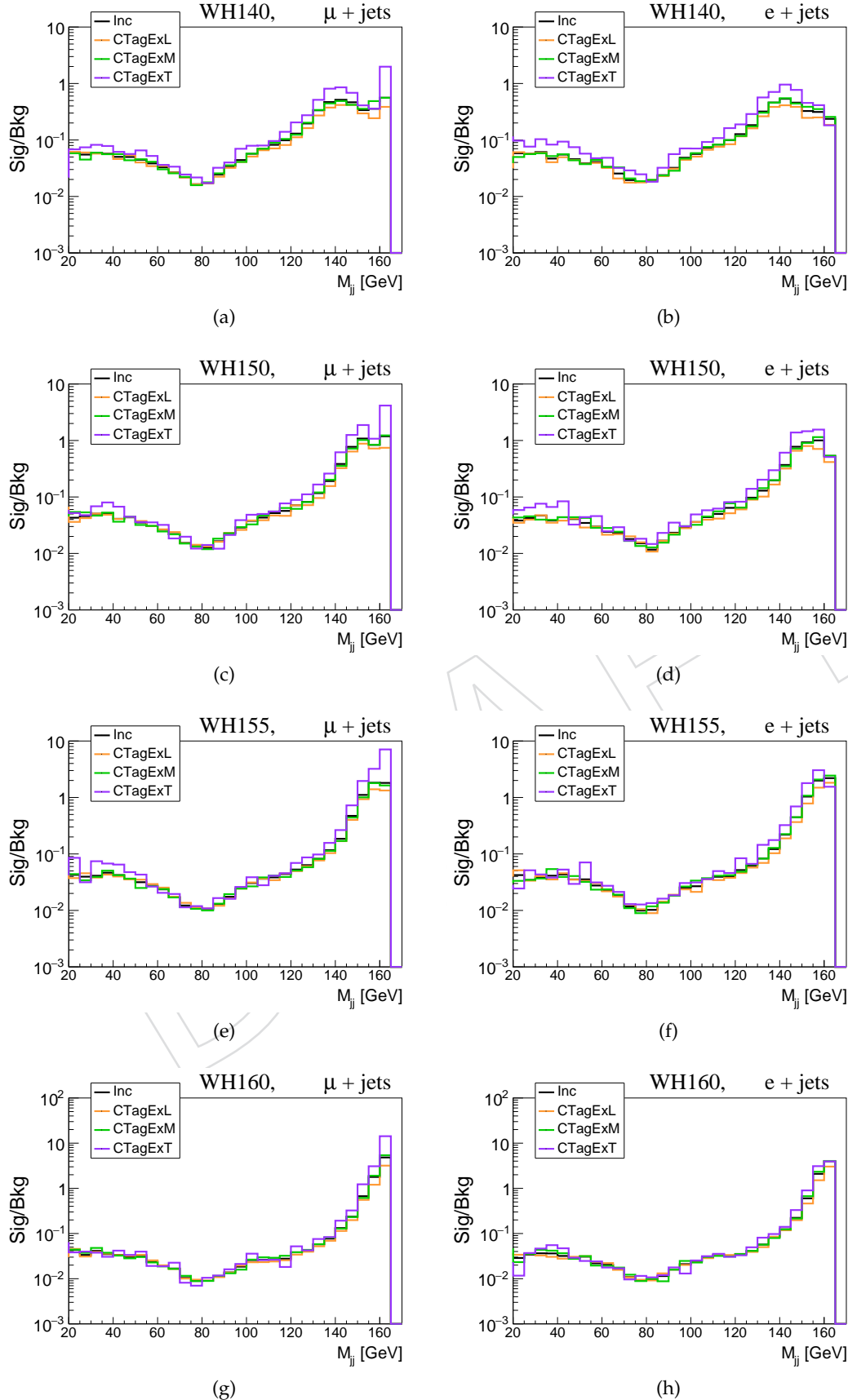


Figure 36: Signal to background ratio for  $m_{H^+} = 140, 150, 155, 160$  GeV.

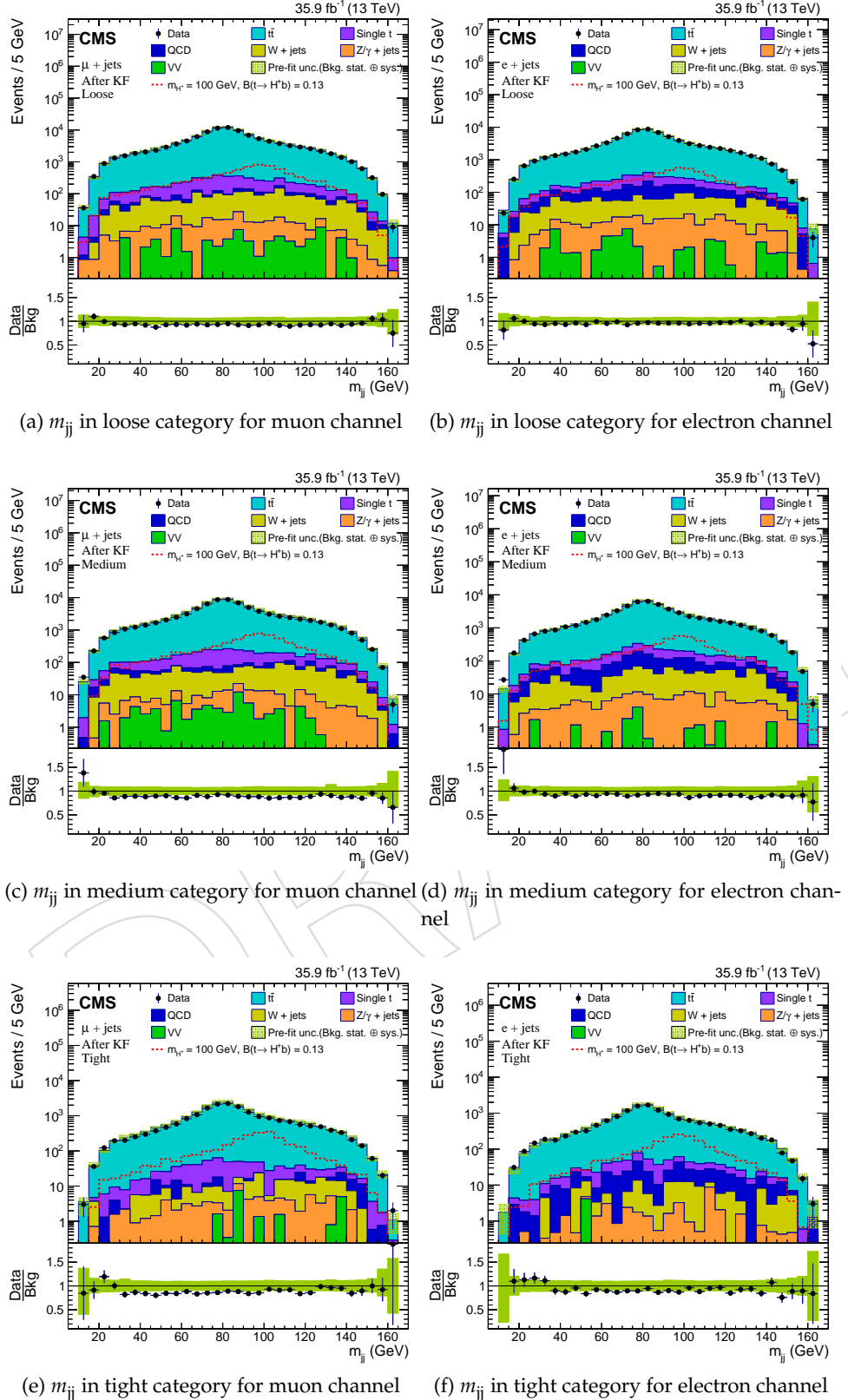


Figure 37: Distribution of  $m_{jj}$  from exclusive charm categories as described in Sec. 15.3 for  $\mu + \text{jets}$  and  $e + \text{jets}$  channel. The signal significance is different across different exclusive categories.

Table 25: Event yields with statistical and systematic uncertainties for signal ( $m_{H^+} = 80, 90, 100, 120, 140, 150, 155, 160$  GeV) and background processes in the  $\mu + \text{jets}$  and  $e + \text{jets}$  channel. Only statistical uncertainty in the QCD event is considered, as it is estimated from data.

Process	Exclusive loose category		Exclusive medium category		Exclusive tight category	
	$N_{\text{events}} \pm \text{stat} \pm \text{sys}$					
	$\mu + \text{jets}$	$e + \text{jets}$	$\mu + \text{jets}$	$e + \text{jets}$	$\mu + \text{jets}$	$e + \text{jets}$
$m_{H^+} = 80$ GeV	7691 $\pm$ 77 $\pm$ 541	5427 $\pm$ 64 $\pm$ 371	6564 $\pm$ 74 $\pm$ 484	4695 $\pm$ 61 $\pm$ 363	2668 $\pm$ 45 $\pm$ 263	1855 $\pm$ 37 $\pm$ 172
$m_{H^+} = 90$ GeV	7705 $\pm$ 77 $\pm$ 541	5616 $\pm$ 65 $\pm$ 397	6774 $\pm$ 74 $\pm$ 506	4856 $\pm$ 62 $\pm$ 377	2626 $\pm$ 44 $\pm$ 255	1865 $\pm$ 37 $\pm$ 184
$m_{H^+} = 100$ GeV	7949 $\pm$ 78 $\pm$ 588	5548 $\pm$ 64 $\pm$ 398	7065 $\pm$ 76 $\pm$ 538	4945 $\pm$ 62 $\pm$ 349	2765 $\pm$ 45 $\pm$ 264	1997 $\pm$ 38 $\pm$ 195
$m_{H^+} = 120$ GeV	7617 $\pm$ 76 $\pm$ 567	5360 $\pm$ 63 $\pm$ 390	6870 $\pm$ 75 $\pm$ 504	4780 $\pm$ 61 $\pm$ 355	2651 $\pm$ 44 $\pm$ 256	1962 $\pm$ 37 $\pm$ 188
$m_{H^+} = 140$ GeV	6155 $\pm$ 69 $\pm$ 498	4365 $\pm$ 57 $\pm$ 359	5420 $\pm$ 66 $\pm$ 414	3838 $\pm$ 55 $\pm$ 301	2010 $\pm$ 38 $\pm$ 201	1497 $\pm$ 33 $\pm$ 150
$m_{H^+} = 150$ GeV	4527 $\pm$ 59 $\pm$ 389	3227 $\pm$ 49 $\pm$ 278	3849 $\pm$ 56 $\pm$ 329	2795 $\pm$ 47 $\pm$ 242	1336 $\pm$ 31 $\pm$ 140	1027 $\pm$ 27 $\pm$ 117
$m_{H^+} = 155$ GeV	3700 $\pm$ 54 $\pm$ 337	2559 $\pm$ 45 $\pm$ 242	2976 $\pm$ 50 $\pm$ 260	2231 $\pm$ 43 $\pm$ 215	1024 $\pm$ 28 $\pm$ 116	766 $\pm$ 24 $\pm$ 83
$m_{H^+} = 160$ GeV	2777 $\pm$ 46 $\pm$ 267	2079 $\pm$ 39 $\pm$ 193	2371 $\pm$ 44 $\pm$ 228	1709 $\pm$ 37 $\pm$ 179	728 $\pm$ 23 $\pm$ 80	510 $\pm$ 19 $\pm$ 55
SM $t\bar{t} + \text{jets}$	107914 $\pm$ 201 $\pm$ 7633	75218 $\pm$ 166 $\pm$ 5400	81804 $\pm$ 184 $\pm$ 6571	56975 $\pm$ 152 $\pm$ 4638	21353 $\pm$ 90 $\pm$ 2112	14739 $\pm$ 73 $\pm$ 1486
Single t	3105 $\pm$ 22 $\pm$ 254	2180 $\pm$ 18 $\pm$ 187	2294 $\pm$ 20 $\pm$ 212	1609 $\pm$ 17 $\pm$ 146	504 $\pm$ 9 $\pm$ 54	353 $\pm$ 8 $\pm$ 38
QCD multijet	394 $\pm$ 78 $\pm$ 0	1539 $\pm$ 112 $\pm$ 0	399 $\pm$ 78 $\pm$ 0	1237 $\pm$ 116 $\pm$ 0	84 $\pm$ 40 $\pm$ 0	331 $\pm$ 57 $\pm$ 0
W + jets	1661 $\pm$ 65 $\pm$ 277	1228 $\pm$ 55 $\pm$ 151	1240 $\pm$ 59 $\pm$ 238	819 $\pm$ 47 $\pm$ 110	168 $\pm$ 20 $\pm$ 45	123 $\pm$ 18 $\pm$ 17
Z/ $\gamma$ + jets	222 $\pm$ 13 $\pm$ 31	266 $\pm$ 11 $\pm$ 33	160 $\pm$ 9 $\pm$ 24	158 $\pm$ 9 $\pm$ 25	67 $\pm$ 6 $\pm$ 11	36 $\pm$ 5 $\pm$ 6
VV	73 $\pm$ 14 $\pm$ 15	50 $\pm$ 11 $\pm$ 8	71 $\pm$ 14 $\pm$ 13	15 $\pm$ 5 $\pm$ 8	18 $\pm$ 7 $\pm$ 7	4 $\pm$ 4 $\pm$ 1
All background	113370 $\pm$ 227 $\pm$ 8155	80480 $\pm$ 209 $\pm$ 5757	85968 $\pm$ 210 $\pm$ 7000	60811 $\pm$ 198 $\pm$ 4899	22195 $\pm$ 101 $\pm$ 2204	15586 $\pm$ 95 $\pm$ 1542
Data	105474 $\pm$ 325	77244 $\pm$ 278	76807 $\pm$ 277	56051 $\pm$ 237	19437 $\pm$ 139	14179 $\pm$ 119

<sup>1002</sup> 28 are shown in Figure 38 for both channels, for SM  $t\bar{t} + \text{jets}$  sample. Similar event weights are  
<sup>1003</sup> found for signal MC samples.

Table 26: Systematic and statistical uncertainties in %, from exclusive charm categories for muon (electron) channel. The “—” indicates that the corresponding uncertainties are not considered for the given process.

Category	Process	Luminosity	Pileup	Lepton	JES + JER + $E_T^{\text{miss}}$	b & c-jet tagging <sup>1</sup>	b & c-jet tagging <sup>2</sup>	b & c-jet tagging <sup>3</sup>	Normalization	Statistical	$\text{top } p_T$
$m_{H^+}$ =80 GeV	2.5 (2.5)	0.8 (1.0)	3.0 (3.0)	3.7 (3.1)	1.1 (1.0)	4.2 (4.2)	4.0 (4.2)	6.1 (6.1)	1.0 (1.2)	1.5 (1.9)	
$m_{H^+}$ =90 GeV	2.5 (2.5)	0.5 (0.7)	3.0 (3.0)	3.7 (3.7)	0.9 (0.9)	4.2 (4.2)	4.1 (4.2)	6.1 (6.1)	1.0 (1.1)	1.4 (2.0)	
$m_{H^+}$ =100 GeV	2.5 (2.5)	0.6 (1.1)	3.0 (3.0)	4.2 (3.5)	0.9 (0.9)	4.2 (4.3)	4.3 (4.3)	6.1 (6.1)	1.0 (1.2)	1.4 (1.8)	
$m_{H^+}$ =120 GeV	2.5 (2.5)	0.6 (1.3)	3.0 (3.0)	4.0 (3.5)	0.8 (1.0)	4.2 (4.2)	4.6 (4.6)	6.1 (6.1)	1.0 (1.2)	1.4 (1.9)	
$m_{H^+}$ =140 GeV	2.5 (2.5)	0.9 (1.3)	3.0 (3.0)	4.3 (4.6)	0.8 (0.7)	4.3 (4.3)	5.2 (5.1)	6.1 (6.1)	1.1 (1.3)	2.1 (2.4)	
$m_{H^+}$ =150 GeV	2.5 (2.5)	0.7 (0.9)	3.0 (3.0)	4.6 (4.6)	0.5 (0.8)	4.6 (4.4)	5.5 (5.6)	6.1 (6.1)	1.3 (1.5)	2.6 (3.2)	
$m_{H^+}$ =155 GeV	2.5 (2.5)	0.9 (0.8)	3.0 (3.0)	4.8 (5.6)	0.7 (0.6)	5.0 (4.9)	5.8 (5.8)	6.1 (6.1)	1.5 (1.7)	3.1 (3.5)	
$m_{H^+}$ =160 GeV	2.5 (2.5)	0.5 (1.0)	3.0 (3.0)	5.7 (5.1)	0.7 (0.5)	5.0 (5.1)	5.9 (5.7)	6.1 (6.1)	1.7 (1.9)	3.2 (3.3)	
t̄t	2.5 (2.5)	0.9 (1.1)	3.0 (3.0)	3.6 (3.6)	0.4 (0.4)	4.5 (4.5)	3.7 (3.7)	6.1 (6.1)	0.2 (0.2)	1.5 (1.9)	
Single t	2.5 (2.5)	0.6 (0.8)	3.0 (3.0)	4.9 (5.4)	0.4 (0.4)	5.0 (5.1)	4.2 (4.2)	5.0 (5.0)	0.7 (0.8)	—	
W + jets	2.5 (2.5)	2.3 (0.4)	3.0 (3.0)	12.9 (6.9)	0.1 (0.2)	9.1 (8.9)	5.0 (4.9)	5.0 (5.0)	3.9 (4.5)	—	
Z/γ + jets	2.5 (2.5)	1.8 (2.4)	3.0 (3.0)	10.6 (8.4)	0.0 (0.1)	8.2 (7.7)	4.2 (4.7)	4.5 (4.5)	5.7 (4.2)	—	
VV	2.5 (2.5)	1.5 (7.9)	3.0 (3.0)	18.6 (12.9)	0.4 (0.7)	4.8 (5.8)	5.3 (3.9)	4.0 (4.0)	19.0 (22.0)	—	
QCD multijet	—	—	—	—	—	—	—	10(10)	19.9 (7.3)	—	
$m_{H^+}$ =80 GeV	2.5 (2.5)	0.6 (0.6)	3.0 (3.0)	2.8 (3.7)	2.7 (2.8)	5.1 (5.0)	3.6 (3.5)	6.1 (6.1)	1.1 (1.3)	1.6 (2.0)	
$m_{H^+}$ =90 GeV	2.5 (2.5)	0.7 (0.6)	3.0 (3.0)	3.1 (3.8)	2.7 (2.7)	5.0 (5.0)	3.6 (3.6)	6.1 (6.1)	1.1 (1.3)	1.6 (2.2)	
$m_{H^+}$ =100 GeV	2.5 (2.5)	0.4 (0.3)	3.0 (3.0)	3.5 (2.0)	2.7 (2.7)	5.0 (5.0)	3.7 (3.7)	6.1 (6.1)	1.1 (1.3)	1.6 (1.9)	
$m_{H^+}$ =120 GeV	2.5 (2.5)	0.3 (0.7)	3.0 (3.0)	2.8 (3.0)	2.7 (2.7)	4.9 (4.9)	3.9 (3.8)	6.1 (6.1)	1.1 (1.3)	1.6 (2.0)	
$m_{H^+}$ =140 GeV	2.5 (2.5)	0.4 (0.5)	3.0 (3.0)	2.9 (3.5)	2.7 (2.6)	5.0 (5.0)	4.2 (4.1)	6.1 (6.1)	1.2 (1.4)	2.2 (2.5)	
$m_{H^+}$ =150 GeV	2.5 (2.5)	0.1 (0.6)	3.0 (3.0)	4.3 (4.3)	2.5 (2.6)	5.4 (5.5)	4.4 (4.4)	6.1 (6.1)	1.5 (1.7)	2.6 (3.4)	
$m_{H^+}$ =155 GeV	2.5 (2.5)	0.1 (0.4)	3.0 (3.0)	4.4 (5.8)	2.3 (2.4)	5.5 (5.6)	4.6 (4.6)	6.1 (6.1)	1.7 (1.9)	3.2 (3.5)	
$m_{H^+}$ =160 GeV	2.5 (2.5)	0.3 (0.4)	3.0 (3.0)	5.3 (6.8)	2.2 (2.2)	6.0 (6.0)	4.9 (4.8)	6.1 (6.1)	1.9 (2.2)	3.4 (3.7)	
t̄t	2.5 (2.5)	0.3 (0.4)	3.0 (3.0)	3.0 (3.0)	1.5 (1.5)	6.2 (6.2)	3.4 (3.4)	6.1 (6.1)	0.2 (0.3)	1.5 (2.0)	
Single t	2.5 (2.5)	0.3 (0.1)	3.0 (3.0)	4.4 (4.1)	1.2 (1.2)	7.0 (7.0)	3.8 (3.9)	5.0 (5.0)	0.9 (1.0)	—	
W + jets	2.5 (2.5)	2.9 (1.6)	3.0 (3.0)	14.4 (6.8)	0.7 (0.7)	11.5 (10.4)	4.5 (4.8)	5.0 (5.0)	4.8 (5.7)	—	
Z/γ + jets	2.5 (2.5)	0.7 (3.4)	3.0 (3.0)	9.0 (10.7)	0.5 (0.4)	11.0 (10.7)	4.1 (4.1)	4.5 (4.5)	5.9 (5.9)	—	
VV	2.5 (2.5)	0.6 (4.4)	3.0 (3.0)	15.5 (49.2)	1.5 (1.9)	8.6 (8.6)	5.3 (3.2)	4.0 (4.0)	20.4 (36.1)	—	
QCD multijet	—	—	—	—	—	—	—	10(10)	19.5 (9.4)	—	
$m_{H^+}$ =80 GeV	2.5 (2.5)	1.3 (1.3)	3.0 (3.0)	3.2 (1.5)	5.7 (5.6)	4.9 (4.8)	5.3 (5.3)	6.1 (6.1)	1.7 (2.0)	1.7 (1.8)	
$m_{H^+}$ =90 GeV	2.5 (2.5)	0.8 (1.5)	3.0 (3.0)	3.0 (3.2)	5.7 (5.6)	5.0 (5.1)	5.3 (5.2)	6.1 (6.1)	1.7 (2.0)	1.4 (2.1)	
$m_{H^+}$ =100 GeV	2.5 (2.5)	1.2 (1.3)	3.0 (3.0)	2.2 (3.0)	5.6 (5.7)	4.9 (5.0)	5.4 (5.3)	6.1 (6.1)	1.6 (1.9)	1.4 (1.8)	
$m_{H^+}$ =120 GeV	2.5 (2.5)	1.0 (1.3)	3.0 (3.0)	2.6 (2.2)	5.7 (5.7)	4.9 (4.9)	5.4 (5.3)	6.1 (6.1)	1.7 (1.9)	1.4 (1.8)	
$m_{H^+}$ =140 GeV	2.5 (2.5)	1.3 (1.3)	3.0 (3.0)	3.1 (3.1)	6.0 (5.9)	4.9 (5.0)	5.4 (5.4)	6.1 (6.1)	1.9 (2.2)	1.9 (2.3)	
$m_{H^+}$ =150 GeV	2.5 (2.5)	1.4 (1.5)	3.0 (3.0)	3.6 (5.6)	6.1 (6.0)	5.0 (5.1)	5.7 (5.8)	6.1 (6.1)	2.3 (2.6)	2.8 (3.2)	
$m_{H^+}$ =155 GeV	2.5 (2.5)	0.5 (0.6)	3.0 (3.0)	5.5 (4.6)	5.7 (6.0)	5.5 (5.2)	5.9 (5.6)	6.1 (6.1)	2.7 (3.1)	3.2 (3.6)	
$m_{H^+}$ =160 GeV	2.5 (2.5)	0.1 (1.4)	3.0 (3.0)	4.4 (4.2)	5.9 (5.7)	5.7 (5.6)	5.8 (5.9)	6.1 (6.1)	3.2 (3.7)	4.2 (4.5)	
t̄t	2.5 (2.5)	0.9 (1.0)	3.0 (3.0)	2.7 (3.1)	4.7 (4.8)	6.3 (6.3)	5.1 (5.1)	6.1 (6.1)	0.4 (0.5)	1.4 (1.8)	
Single t	2.5 (2.5)	0.4 (0.5)	3.0 (3.0)	4.3 (4.5)	4.2 (4.4)	6.9 (6.8)	5.4 (5.5)	5.0 (5.0)	1.8 (2.1)	—	
W + jets	2.5 (2.5)	1.1 (2.8)	3.0 (3.0)	23.3 (3.4)	4.4 (2.7)	9.8 (11.3)	6.8 (5.9)	5.0 (5.0)	12.2 (14.4)	—	
Z/γ + jets	2.5 (2.5)	3.7 (2.7)	3.0 (3.0)	7.5 (10.3)	0.9 (2.4)	12.4 (9.2)	4.6 (6.8)	4.5 (4.5)	9.1 (15.2)	—	
VV	2.5 (2.5)	2.3 (8.9)	3.0 (3.0)	36.1 (0.3)	5.7 (7.4)	5.4 (6.9)	7.3 (2.3)	4.0 (4.0)	38.5 (100.0)	—	
QCD multijet	—	—	—	—	—	—	—	10(10)	47.3 (17.2)	—	

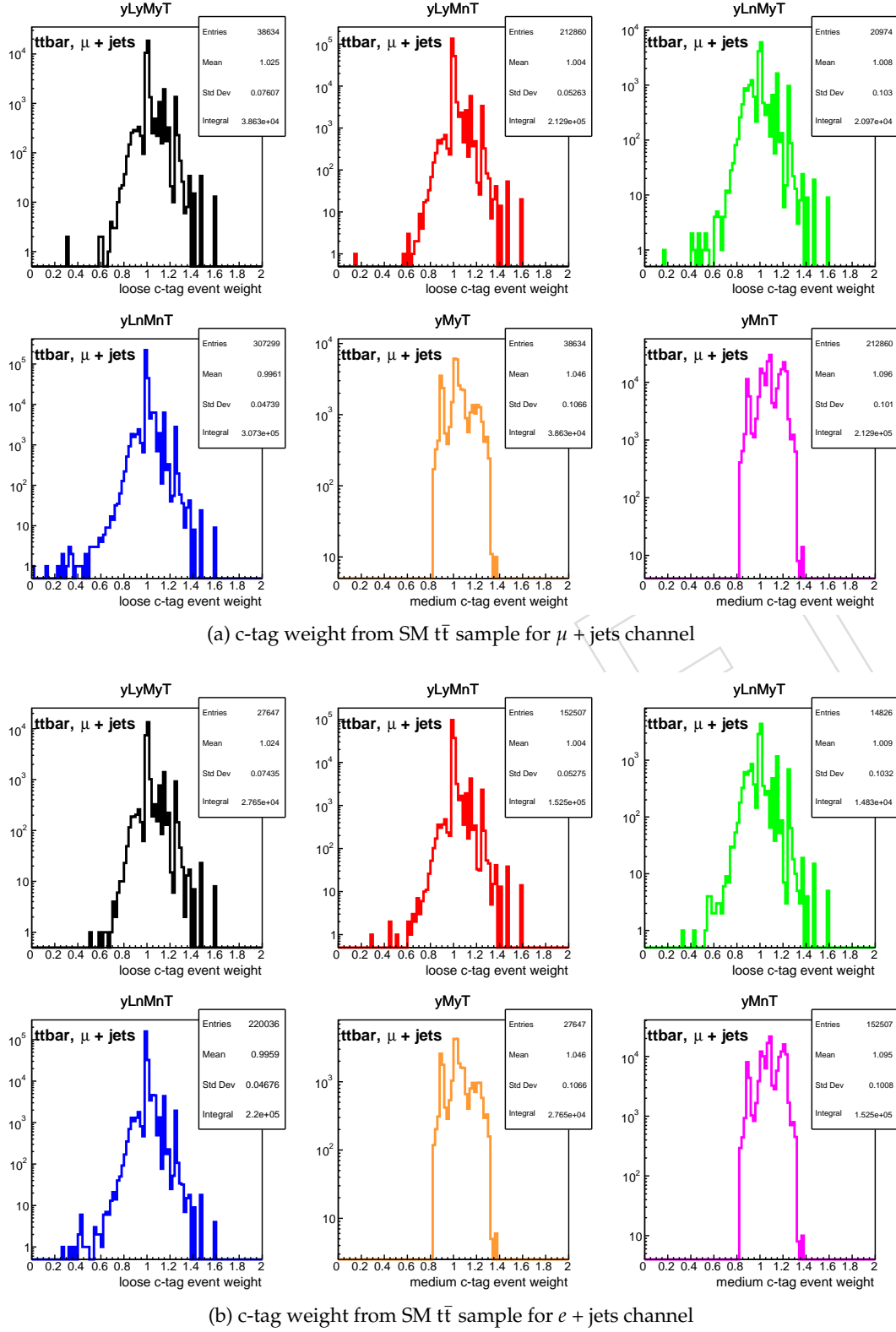


Figure 38: The c-tag event weight for different cases from SM  $t\bar{t}$  sample. For exclusive loose charm category, the value of  $CMS_{eff\_ExL} = 1.025/0.99$  ( $1.024/0.99$ ) for  $\mu + \text{jets}$  ( $e + \text{jets}$ ) channel. For exclusive medium charm category, the value of  $CMS_{eff\_ExM} = 1.096/1.046$  ( $1.096/1.046$ ) for  $\mu + \text{jets}$  ( $e + \text{jets}$ ) channel.

<b>Loose WP</b>	<b>Medium WP</b>	<b>Tight WP</b>	<b>Acronym</b>
Y	Y	Y	yLyMyT
Y	Y	N	yLyMnT
Y	N	Y	yLnMyT
Y	N	N	yLnMnT

Table 27: Inclusive loose c-tag types. The acronym yLyMnT refers to the case where a jet satisfies loose and medium, but not tight WP.

<b>Medium WP</b>	<b>Tight WP</b>	<b>Acronym</b>
Y	Y	yMyT
Y	N	yMnT

Table 28: Inclusive medium c-tag types.

## 16 Post-fit Analysis from Charm Categories

### 16.1 Profile of Nuisance Parameter: shape vs lnN

The statistical and systematic uncertainties are treated as nuisance parameters (NP) for limit computation. The statistical uncertainty is propagated through the `autoMCStats` tool. Which adds histograms of each individual background process and assigns one nuisance in each bin of the total background. For each systematic uncertainty, one NP is assigned. There are different types of probability distribution function (PDF) associated with each NP that goes in the likelihood for limit computation. If for the given NP, the PDF is log-normal (Gaussian) distribution then the corresponding NP is said to be profiled as lnN (shape). Since the final observable is  $m_{jj}$ , a NP is profiled as shape (lnN) based on whether its value is different (same) for all the bins of  $m_{jj}$ . From Figures 39–44, it can be seen that the ratio of up and down template with the base is compatible with a flat line for jet energy scale, jet energy resolution, b/c tagging, and t quark  $p_T$  systematics. Therefore, these NPs are profiled as lnN. The trend for t quark mass (`topMass_tt`), renormalization and factorization scale (`scaleRF_tt`), and parton showering matching (`hDamp_tt`) is mixed. Hence these are also, conservatively, profiled as lnN. A description of the acronyms used to denote the NPs is shown in Table 29.

Table 29: Description of nuisance parameters corresponding to the systematic and statistical uncertainties.

NP name	Profile	NP description
<b>Systematics:</b>		
lumi_13TeV	lnN	uncertainty in the luminosity measurement at 13 TeV
CMS_eff_l	lnN	lepton ( $e, \mu$ ) selection uncertainty
CMS_eff_bcInc1	lnN	uncertainty from inclusive b/c tagging-1
CMS_eff_bcInc2	lnN	uncertainty from inclusive b/c tagging-2
CMS_eff_bcInc3	lnN	uncertainty from inclusive b/c tagging-3
CMS_pileup	lnN	uncertainty from pileup reweighting
CMS_scale_j	lnN	uncertainty from jet energy scale (JES)
CMS_res_j	lnN	uncertainty from jet energy resolution (JER)
CMS_norm_tt	lnN	uncertainty on the $t\bar{t} + \text{jets}$ cross section
CMS_norm_stop	lnN	uncertainty on the single t cross section
CMS_norm_wjet	lnN	uncertainty on the $W + \text{jets}$ cross section
CMS_norm_zjet	lnN	uncertainty on the $Z/\gamma + \text{jets}$ cross section
CMS_norm_qcd	lnN	uncertainty from the data-driven QCD multijet
CMS_norm_vv	lnN	uncertainty on the $VV$ cross section
CMS_topPtReweight	lnN	uncertainty from t quark $p_T$ reweighting
scaleRF_tt	lnN	uncertainty from renormalisation (R) and factorization (F) scale
hDamp_tt	lnN	uncertainty from parton-shower matching
topMass_tt	lnN	uncertainty from t mass $\pm 1$ GeV
<b>Statistical:</b>		
prop_binch*bin*	shape	bin-by-bin autoMCStats
		statistical uncertainties from

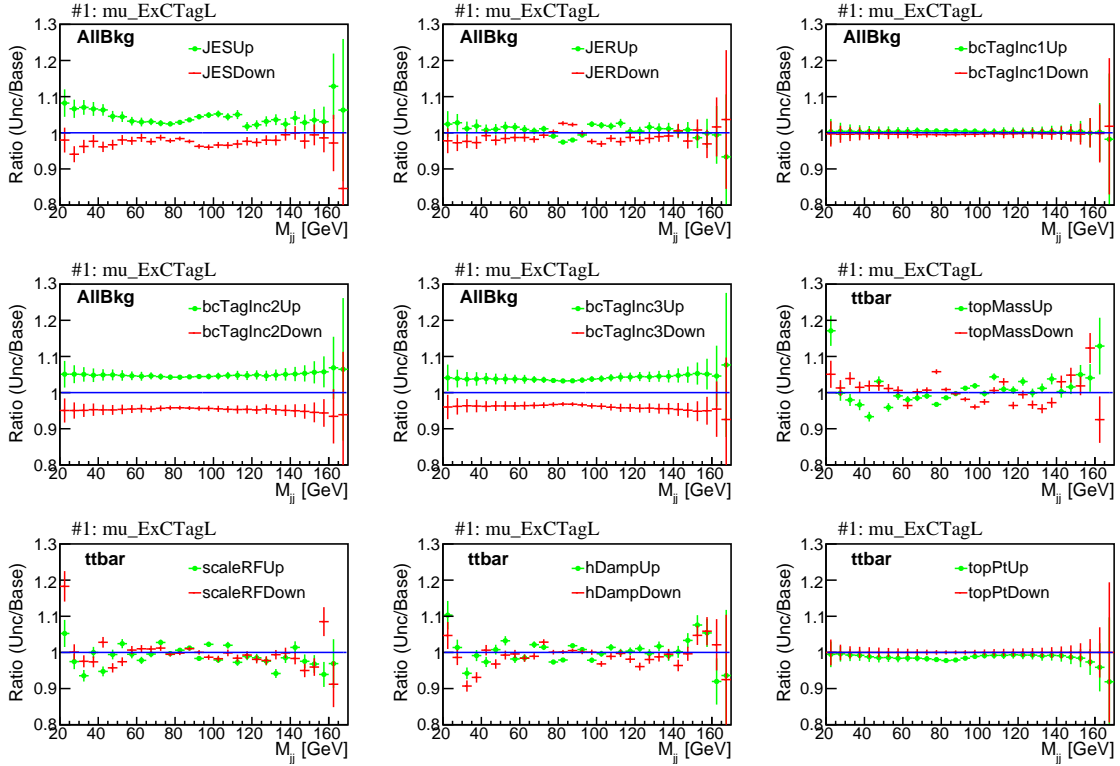


Figure 39: Ratio of up and down with base template for exclusive loose charm category for  $\mu + \text{jets}$  channel.

## 16.2 Distributions of Pulls

A maximum likelihood fit is performed on the data. After the fit, the background yield as well as uncertainties are changed so that the backgrounds fit well with the data. The extent of change in the individual uncertainty is shown in Figures 45-48 for lepton channel for charged Higgs mass 100 GeV. In these figures, the error bars on the left-hand side represents the ratio of post (after the background-only) and pre-fit (prior to the fit to data) uncertainty. If the length of the error bar is small (say 0.80) then the post-fit uncertainty is reduced (by 20%). On the right hand side of the plot, the correlation between the BR and uncertainty is shown. From these figures, one can see that the NPs from autoMCStats have almost no correlation with BR. The background-only fit is obtained by setting the signal strength to zero. The signal+ background fit is obtained by using floating signal strength. The distributions of pulls are produced using the Command (37).

## 16.3 Post-fit Yields and Distributions

The event yields, after a background-only fit to the data, of all the background process for both channels from all charm-tagging categories are shown in Table 31. The corresponding  $m_{jj}$  distributions are shown in Figure 49. From these plots, one can see that the uncertainty band is reduced. Which indicates that the fit has reduced the uncertainties. Since the SM  $t\bar{t} + \text{jets}$  is the dominant background, the pre-fit and post-fit distribution of this process is shown in Figure 50 to gauge the change after the fit. From this figure, one can also see that the post-fit yields are getting reduced as one goes from loose to the tight charm-category.

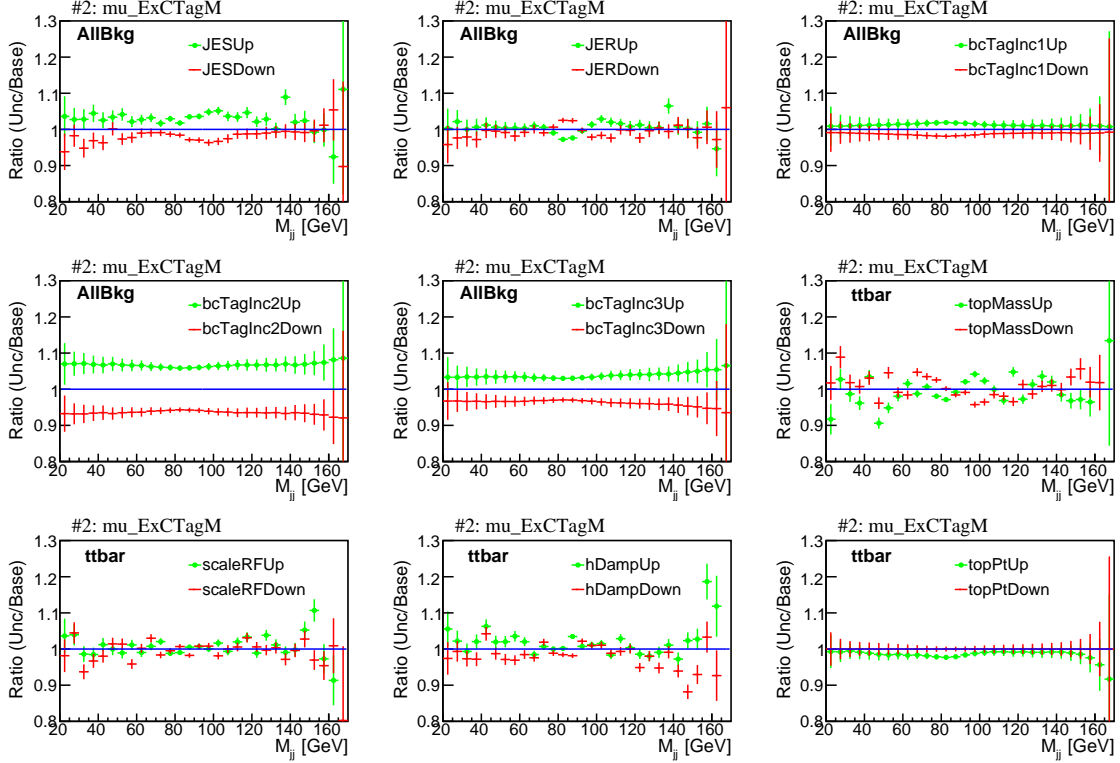


Figure 40: Ratio of up and down with base template for exclusive medium charm category for  $\mu + \text{jets}$  channel.

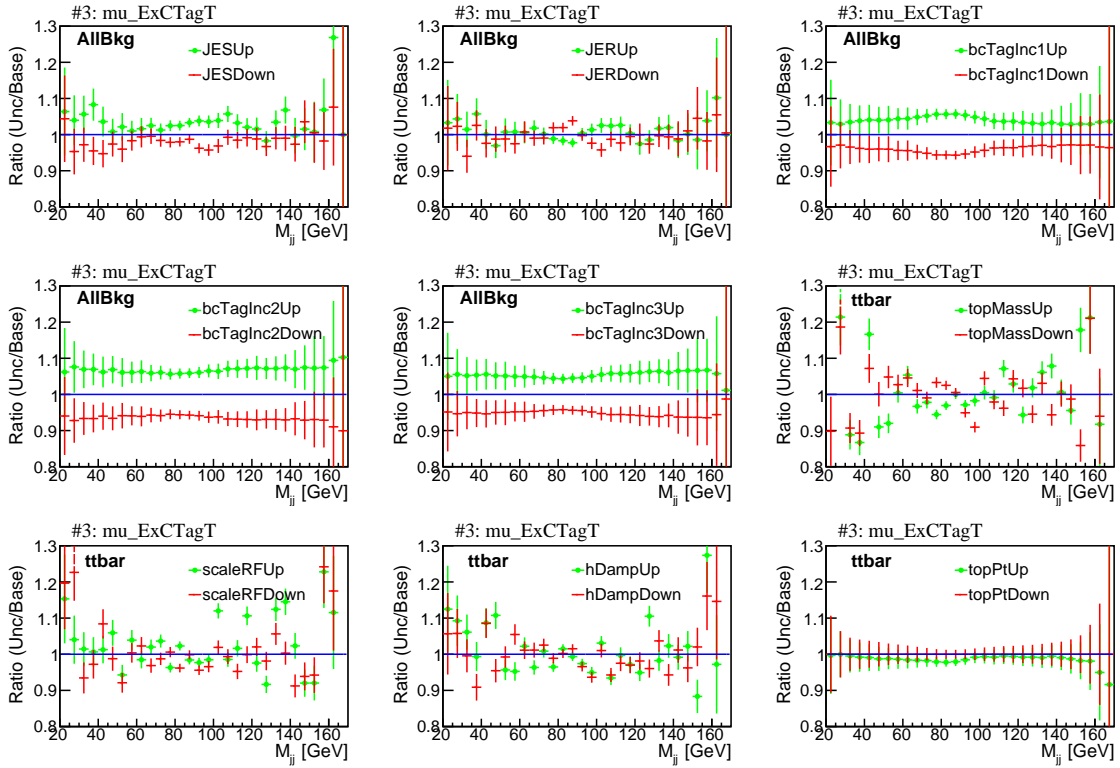


Figure 41: Ratio of up and down with base template from exclusive tight charm category for  $\mu + \text{jets}$  channel.

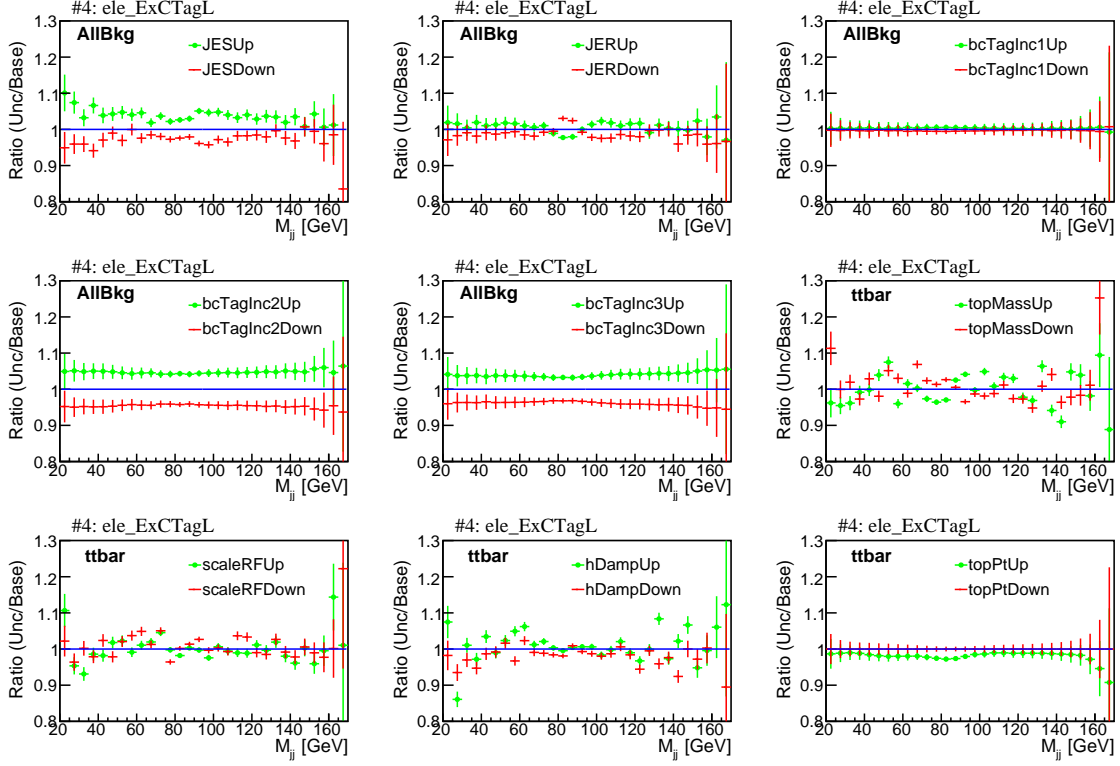


Figure 42: Ratio of up and down with base template from exclusive loose charm category for  $e + \text{jets}$  channel.

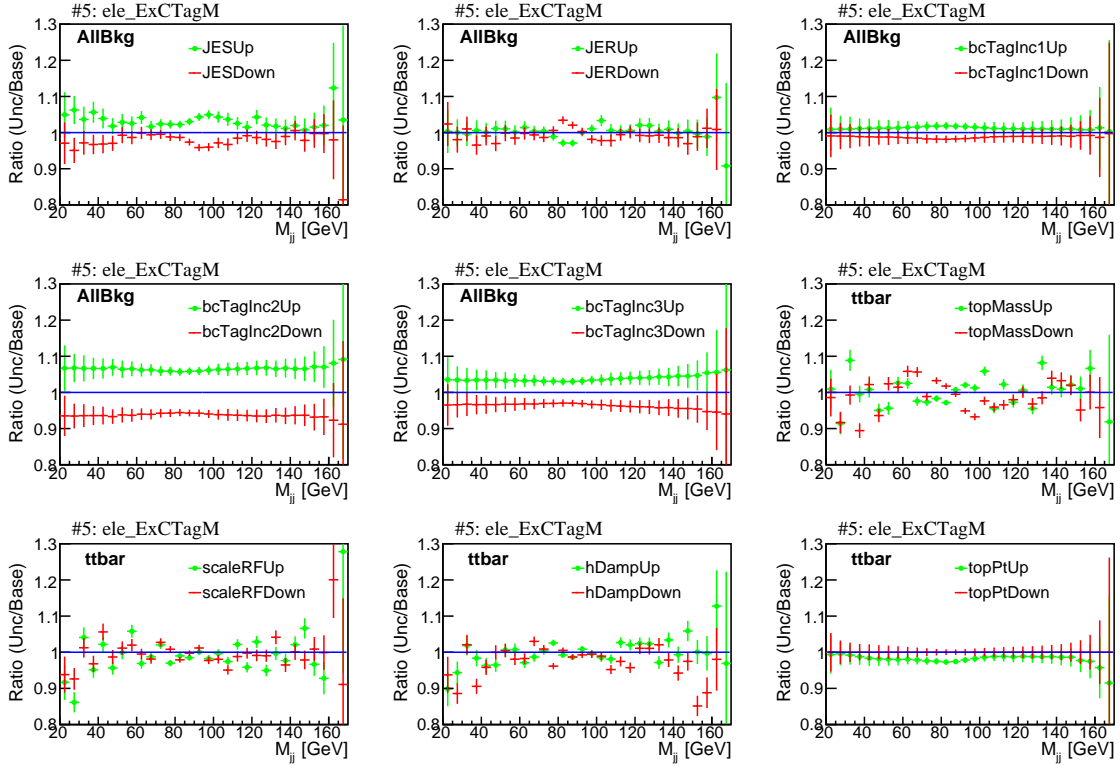


Figure 43: Ratio of up and down with base template from exclusive medium charm category for  $e + \text{jets}$  channel.

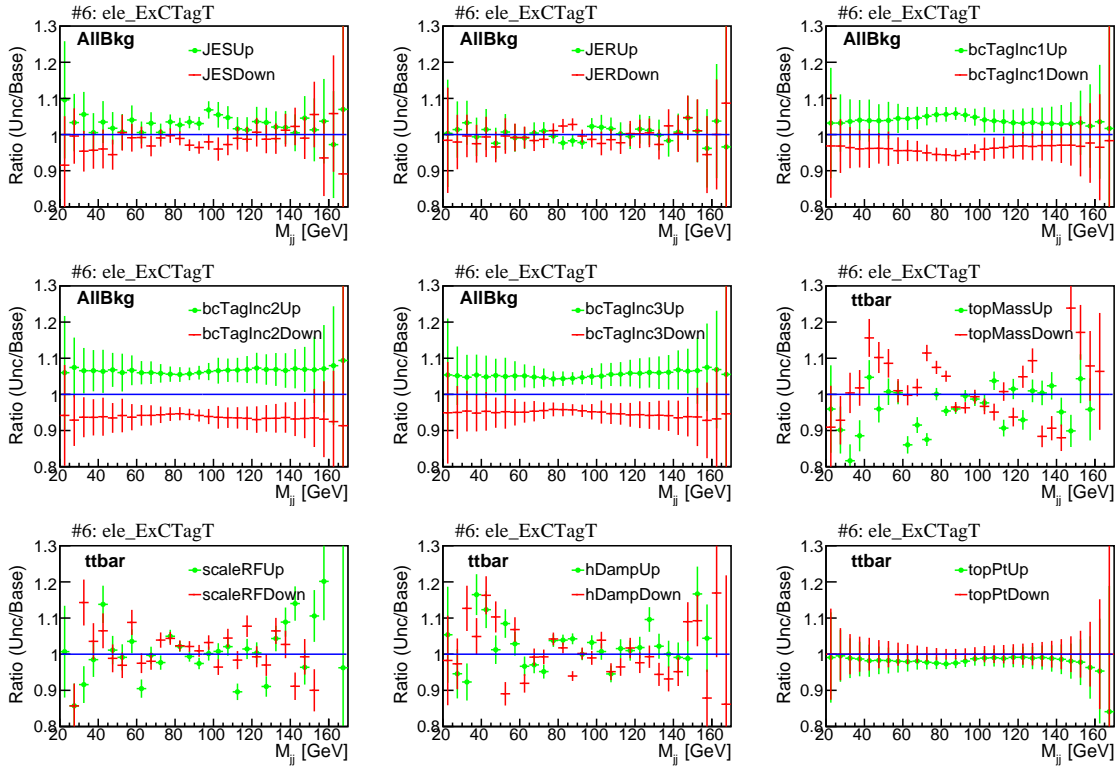


Figure 44: Ratio of up and down with base template from exclusive tight charm category for  $e + \text{jets}$  channel.

Acronym	channel	Event category
binch1	$\mu + \text{jets}$	exclusive loose
binch2	$\mu + \text{jets}$	exclusive medium
binch3	$\mu + \text{jets}$	exclusive tight
binch4	$e + \text{jets}$	exclusive loose
binch5	$e + \text{jets}$	exclusive medium
binch6	$e + \text{jets}$	exclusive tight

Table 30: Acronym used in the autoMCStat tool for naming nuisance parameters.

## Nuisance Parameters

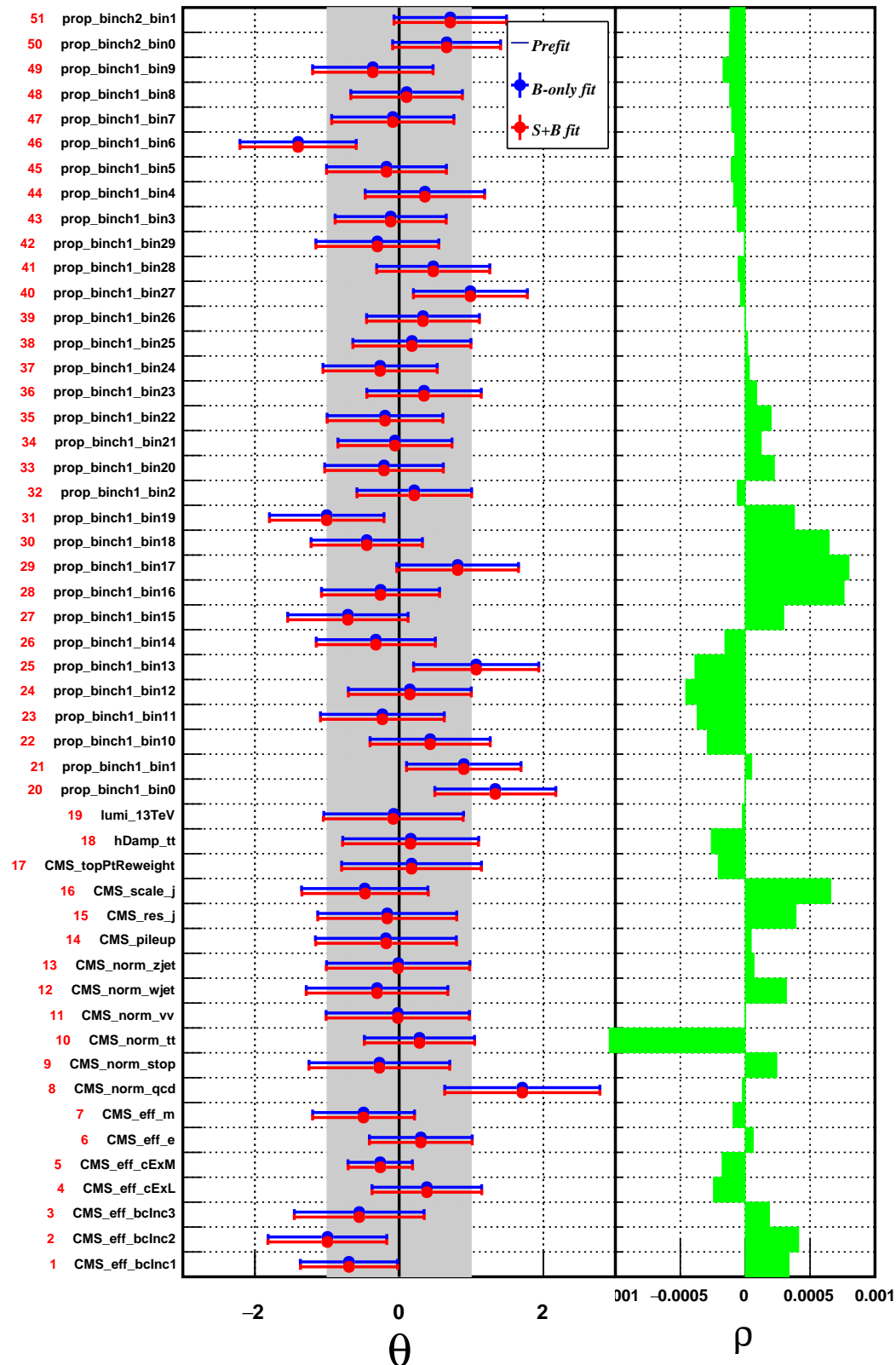


Figure 45: Output of the *FitDiagnostics* using  $m_{jj}$  from exclusive event categories based on charm-tagging for  $m_{H^+} = 100$  GeV from 1 + jets channel. The pre-fit value  $\theta_0 = 0$  and the uncertainty on the pre-fit value  $\Delta\theta = 1$ . The  $\rho$  is the correlation between NPs and  $BR$ . Contd ...

### Nuisance Parameters

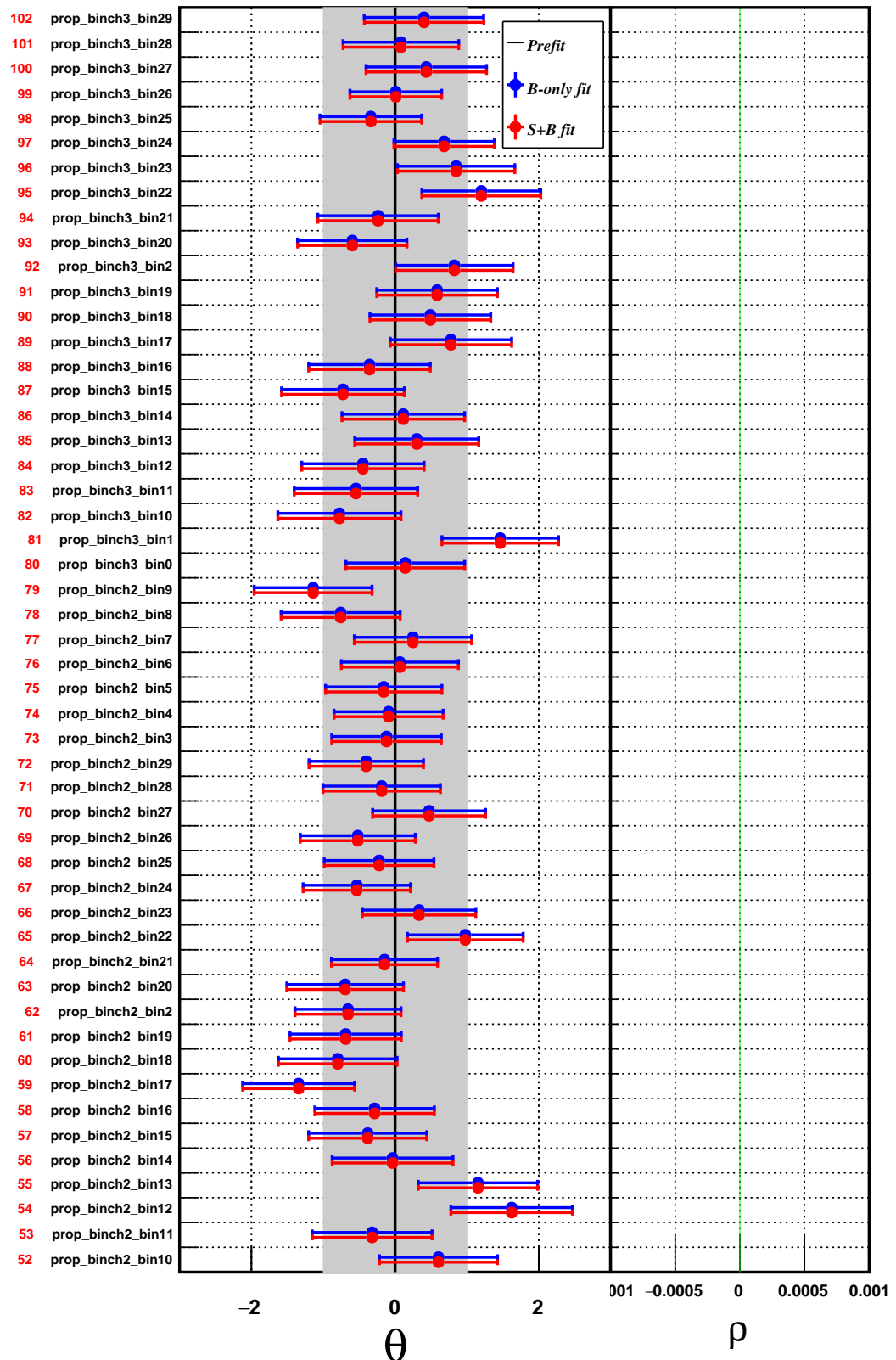


Figure 46: Output of the *FitDiagnostics* using  $m_{jj}$  from exclusive event categories based on charm-tagging for  $m_{H^+} = 100$  GeV from 1 + jets channel. The pre-fit value  $\theta_0 = 0$  and the uncertainty on the pre-fit value  $\Delta\theta = 1$ . The  $\rho$  is the correlation between NPs and *BR*. Contd ...

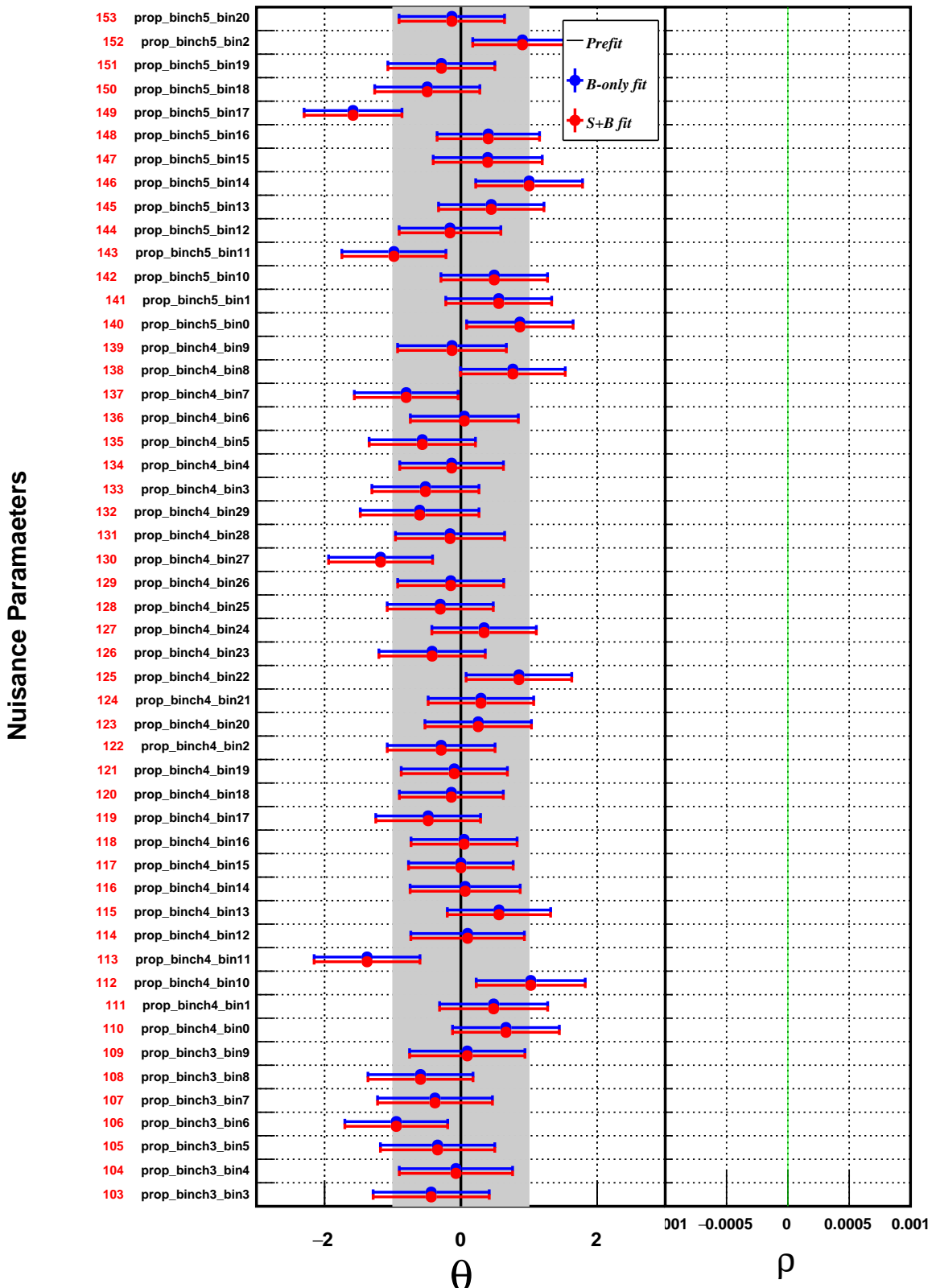


Figure 47: Output of the *FitDiagnostics* using  $m_{jj}$  from exclusive event categories based on charm-tagging for  $m_{H^+} = 100$  GeV from 1 + jets channel. The pre-fit value  $\theta_0 = 0$  and the uncertainty on the pre-fit value  $\Delta\theta = 1$ . The  $\rho$  is the correlation between NPs and  $BR$ . Contd ...

### Nuisance Parameters

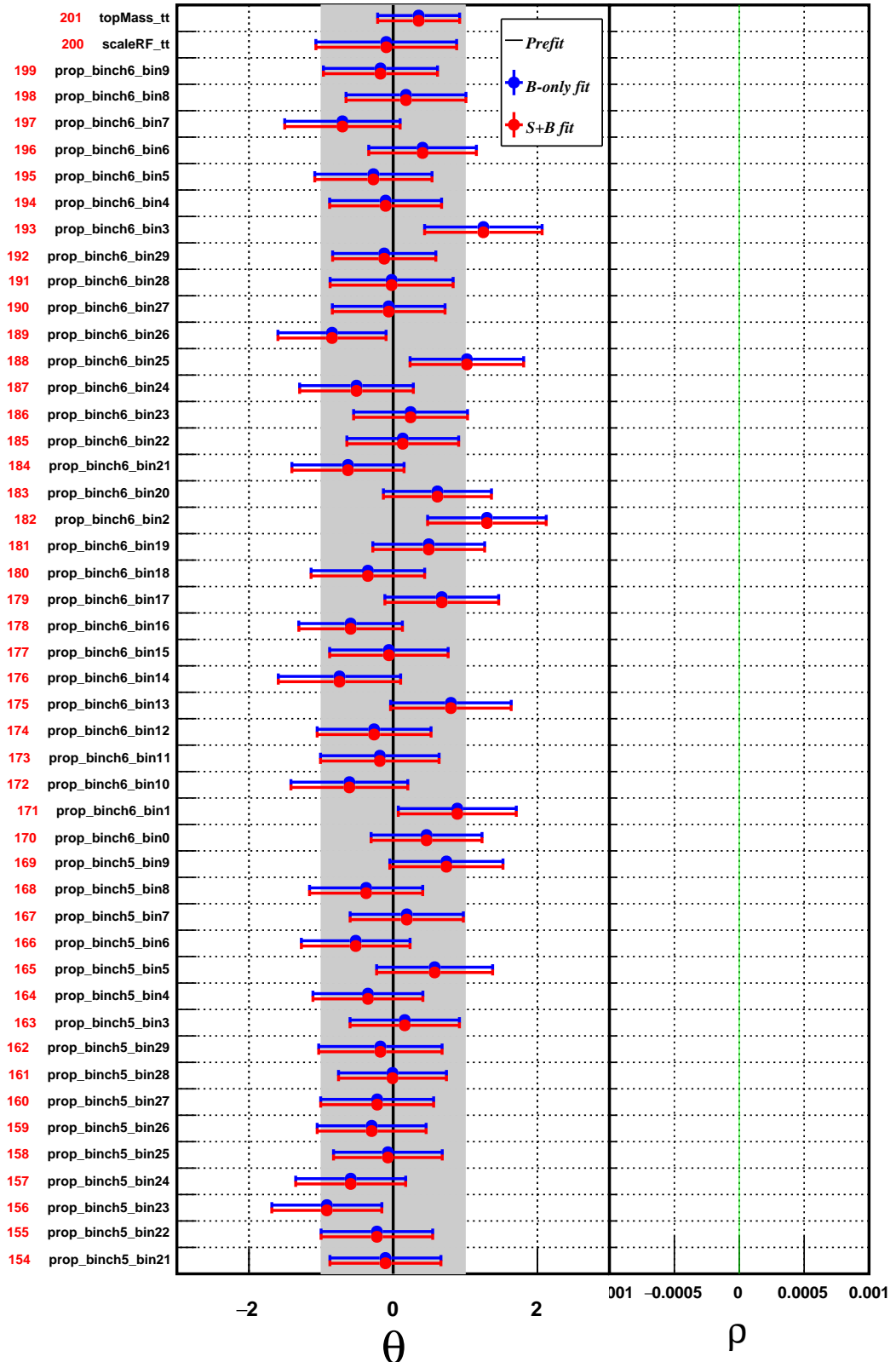


Figure 48: Output of the *FitDiagnostics* using  $m_{jj}$  from exclusive event categories based on charm-tagging for  $m_{H^+} = 100$  GeV from 1 + jets channel. The pre-fit value  $\theta_0 = 0$  and the uncertainty on the pre-fit value  $\Delta\theta = 1$ . The  $\rho$  is the correlation between NPs and  $BR$ .

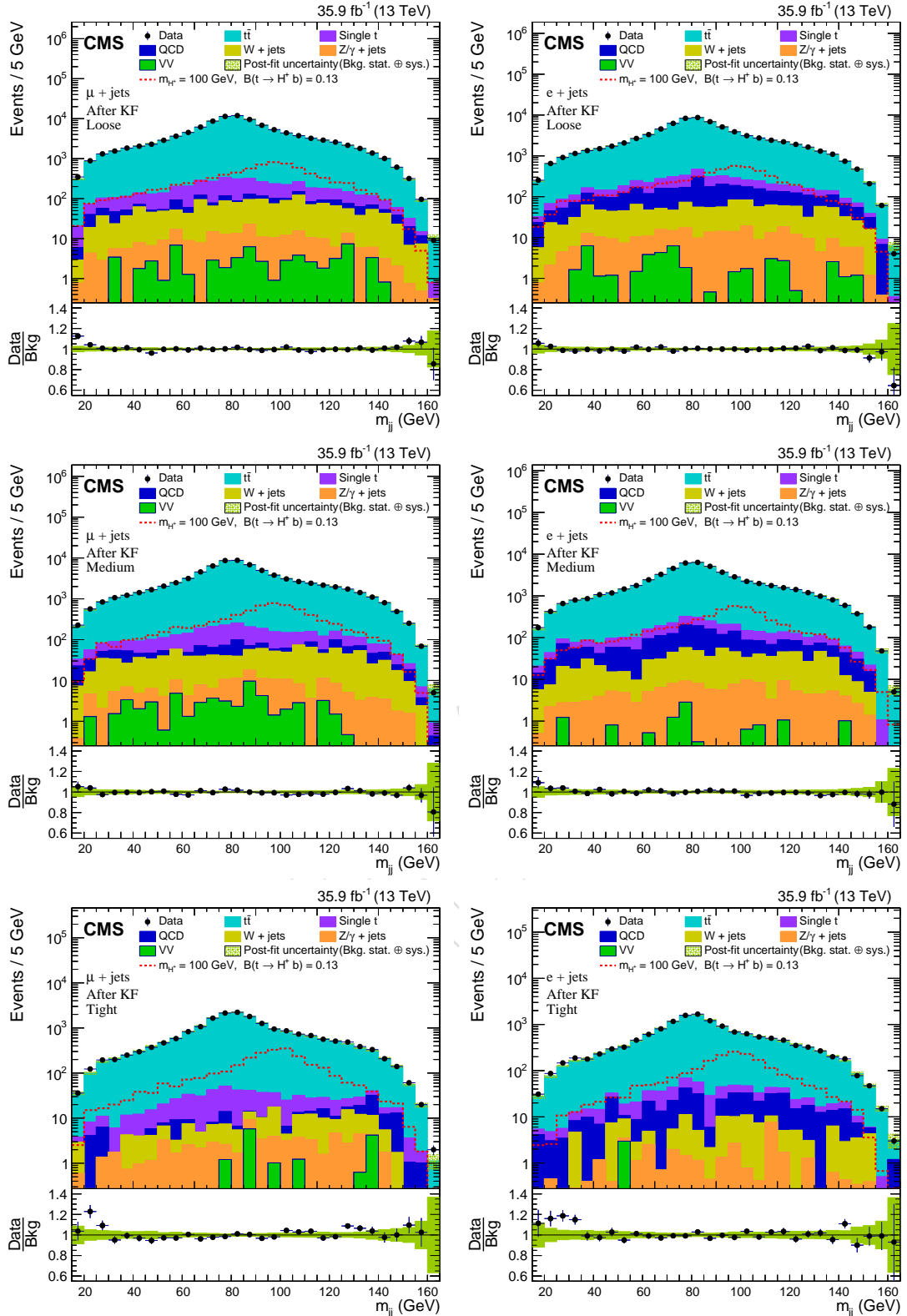


Figure 49: Post-fit distributions of  $m_{jj}$  from the exclusive charm categories for the  $\mu + \text{jets}$  (left column) and  $e + \text{jets}$  (right column) channel. The upper row shows the exclusive loose category, the middle row shows the exclusive medium category, and the lower row shows the exclusive tight category. The uncertainty band includes statistical as well as systematic uncertainties. The expected signal is shown prior to the fit to data.

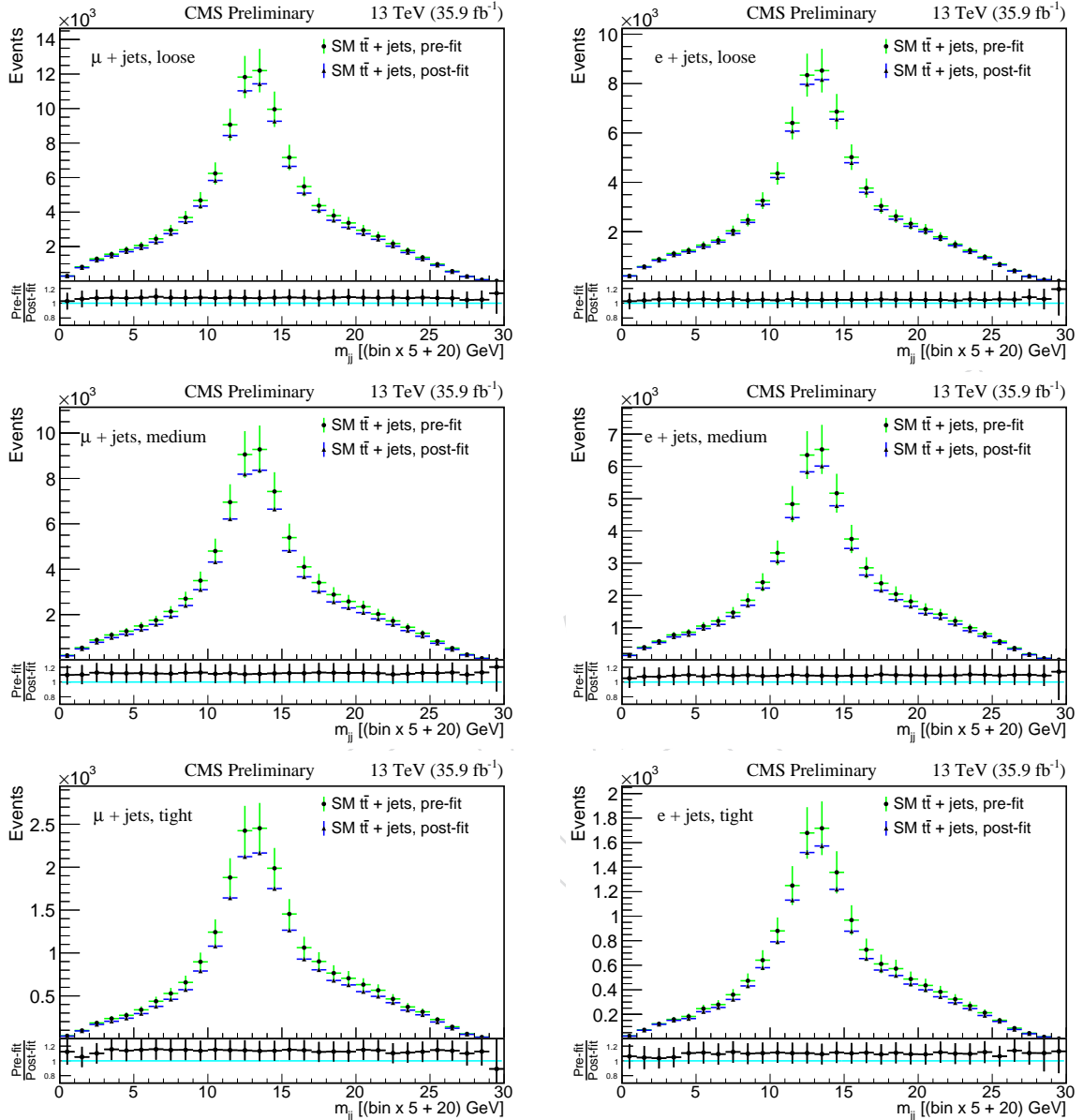


Figure 50: Pre-fit and post-fit distributions of  $m_{jj}$  from SM  $t\bar{t} + \text{jets}$  background for the exclusive charm categories for the  $\mu + \text{jets}$  (left column) and  $e + \text{jets}$  (right column) channel. The upper row shows the exclusive loose category, the middle row shows the exclusive medium category, and the lower row shows the exclusive tight category. The uncertainty includes statistical as well as systematic uncertainties.

Table 31: Expected event yields for background processes, after a background-only fit to the data, in each of the channels and event category. The number of events, along with the uncertainty (including statistical and systematic effects), is shown.

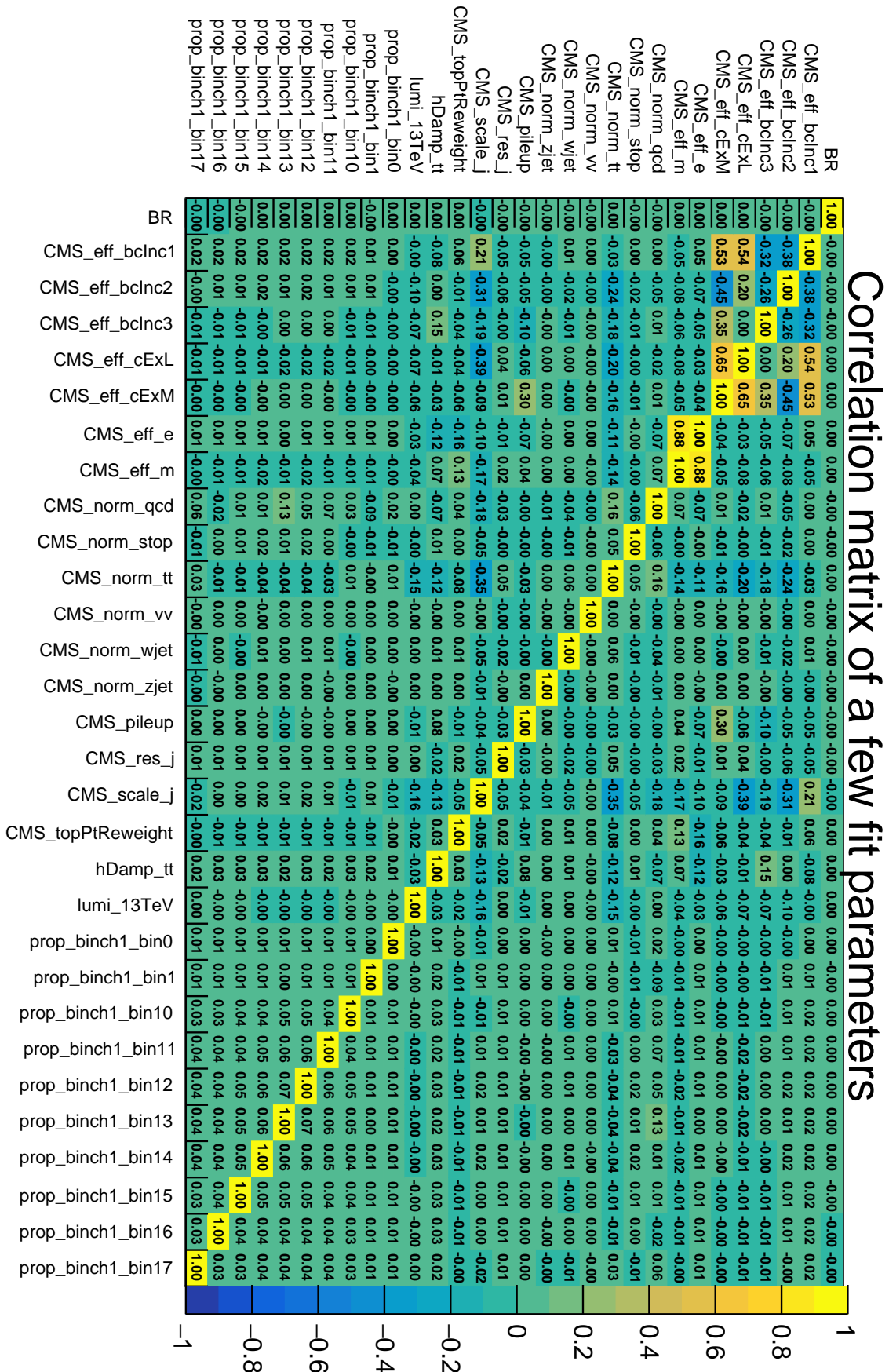
Process	Loose		Medium		Tight	
	$\mu + \text{jets}$	$e + \text{jets}$	$\mu + \text{jets}$	$e + \text{jets}$	$\mu + \text{jets}$	$e + \text{jets}$
SM $t\bar{t} + \text{jets}$	$100537 \pm 410$	$71803 \pm 473$	$73211 \pm 320$	$52340 \pm 288$	$18762 \pm 134$	$13376 \pm 127$
Single t	$2747 \pm 215$	$1968 \pm 162$	$1939 \pm 155$	$1397 \pm 114$	$421 \pm 35$	$302 \pm 26$
QCD multijet	$517 \pm 130$	$2123 \pm 468$	$498 \pm 98$	$1456 \pm 213$	$88 \pm 28$	$346 \pm 39$
W + jets	$1359 \pm 139$	$1061 \pm 90$	$948 \pm 110$	$681 \pm 58$	$127 \pm 23$	$102 \pm 9$
Z/ $\gamma$ + jets	$189 \pm 18$	$240 \pm 25$	$132 \pm 13$	$132 \pm 14$	$56 \pm 7$	$31 \pm 4$
VV	$61 \pm 9$	$43 \pm 6$	$56 \pm 8$	$11 \pm 4$	$15 \pm 5$	$3 \pm 1$
All background	$105410 \pm 501$	$77238 \pm 692$	$76784 \pm 386$	$56017 \pm 381$	$19469 \pm 144$	$14160 \pm 136$
Data	105474	77244	76807	56051	19437	14179

## 16.4 Corelation Among the Nuisance Parameters

The reduction in the post-fit uncertainty can not be explained by looking at the post-fit values of nuisance parameters shown in Figures 45-48. If the NPs are very tightly constrained then the post-fit uncertainty is expected to be heavily reduced. However, that is not the case. Reductions in the post-fit uncertainty are not only caused by constraints on the nuisance parameters, but also by anti-correlations between the parameters. The size of the reduction can be quite different for the different background processes because these processes are not always affected by the same nuisance parameters, and even when the same nuisance parameter applies to different processes, the effect on the yield is not always the same.

The correlation among the leading nuisance parameters is shown in Figure 51. From this figure, it can be seen that there is a large anti-correlation among the NPs. We also have positive correlations. Therefore, the final uncertainty which is computed by taking into account all the correlations is reduced after the post-fit. Note that, the pre-fit uncertainties are either positively-correlated or not correlated at all among themselves.

Figure 51: Correlation among the leading NPs for  $1 + \text{jets}$  channel,  $m_{H^+} = 100$  GeV. All the systematics and a few statistical NPs are shown. The systematic NPs have positive as well as negative correlation with other NPs. However, the statical NPs are mostly positively correlated.



## 1054 17 Goodness of Fit

The goodness of the fit (GOF) indicates how well the model PDF (probability distribution function) agrees with the data. There are various algorithms to compute the GOF such as **saturated** (Baker-Cousins) [76], KS (Kolmogorov-Smirnov) [77], [78], and AD (Anderson-Darling) [79]. The saturated algorithm is used in this analysis for GOF. The test statistics as a measure of GOF is given as [76]

$$q_{GoF,saturated} = -2 \ln \left( \frac{L_{nominal}(n|\mu s(\theta) + b(\theta))}{L_{saturated}(n|n)} \right) \quad (25)$$

The likelihood functions of Eq. 25 are given by

$$L_{nominal}(n|\mu s(\theta) + b(\theta)) = \prod_{j=1}^N \frac{(\mu s_j(\theta) + b_j(\theta))^{n_j}}{n_j!} \exp(-(\mu s_j(\theta) + b_j(\theta))) \quad (26)$$

and,

$$L_{saturated}(n|n) = \prod_{j=1}^N \frac{(n_j)^{n_j}}{n_j!} \exp(-n_j) \quad (27)$$

1055 Where,  $n_j$  is the expectation value in  $j^{th}$  bin of data, N is the total number of bins. The  $s_j(\theta)$   
 1056 and  $b_j(\theta)$  are mean number of events in  $j^{th}$  bin of signal and background process and depend  
 1057 on the nuisance parameters ( $\theta$ ). The  $\mu$  is the signal strength which is zero for background only  
 1058 hypothesis and non-zero for signal+background hypothesis. In  $j^{th}$  bin,  $s_j(\theta)$  and  $b_j(\theta)$  are given  
 1059 by [80]

$$s_j(\theta) = s_{tot} \int_{j^{th}bin} f_s(x; \theta_s) dx, \quad (28)$$

$$b_j(\theta) = b_{tot} \int_{j^{th}bin} f_b(x; \theta_b) dx. \quad (29)$$

1060 The  $f_s(x; \theta_s)$  and  $f_b(x; \theta_b)$  are PDFs for signal and background events. The  $s_{tot}$  and  $b_{tot}$  are mean  
 1061 of total number of events from signal and background process.

Using Eq. 26, and Eq. 27,

$$q_{GoF,saturated} = 2 \sum_j \left( \mu s_j(\theta) + b_j(\theta) - n_j + n_j \ln \left( \frac{n_j}{\mu s_j(\theta) + b_j(\theta)} \right) \right) \quad (30)$$

1062 The goodness of fit ( $q_{GoF,saturated}$ ) is shown in Figure 52 for lepton channel from exclusive charm  
 1063 categories for all signal mass points using observed data and toys MC. Lower the value of GOF,  
 1064 the better is the agreement between data and model PDF. For different channels and various  
 1065 event categories, the GOF is linearly added over different bins, which can be seen from different  
 1066 columns of Tables 32, 33, and 34. The GOF is performed using the Command (38).

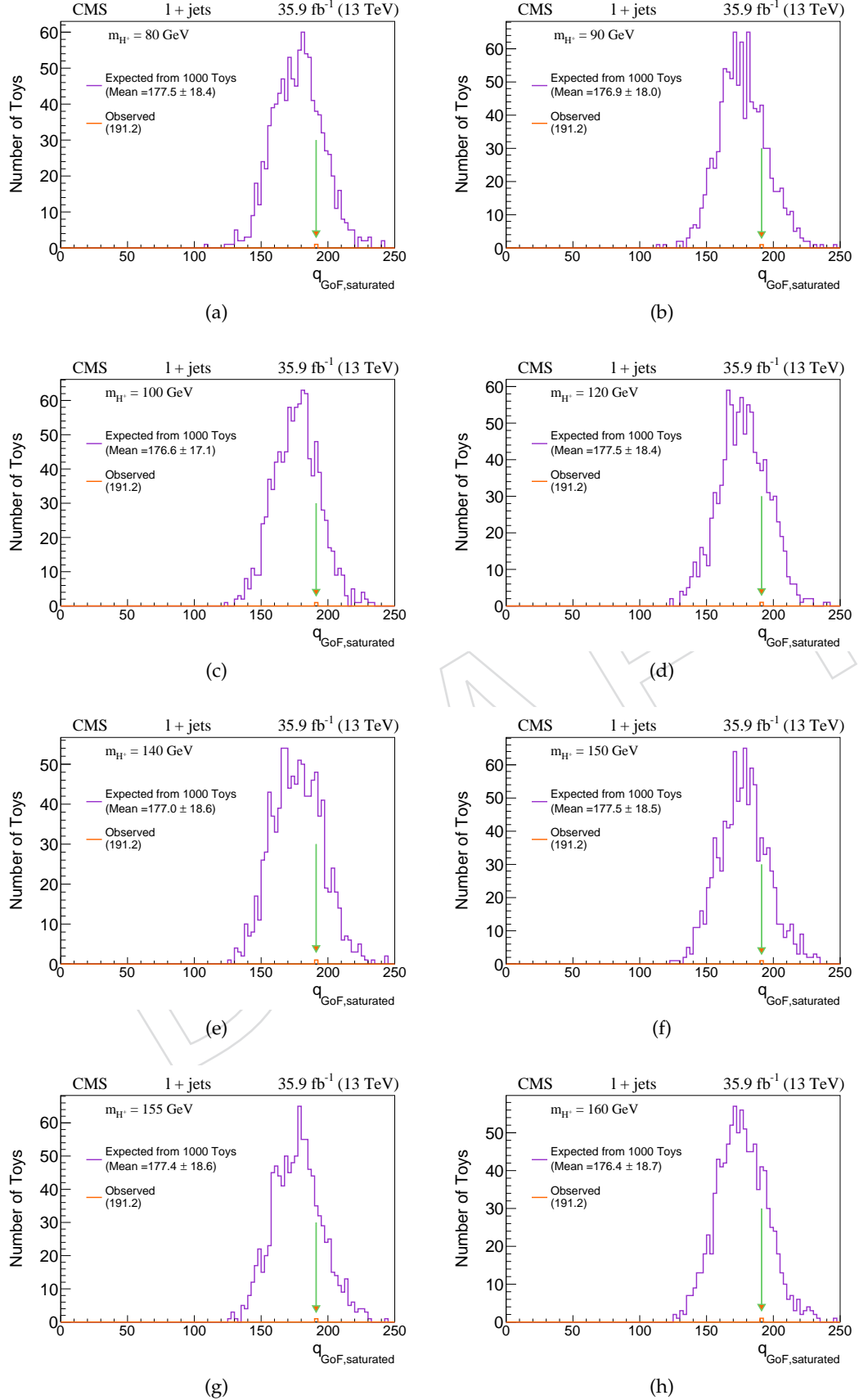


Figure 52: Goodness of fit for lepton channel from exclusive charm categories.

Table 32: Goodness of fit for  $\mu + \text{jets}$  channel, from different event categories.

$m_{H^\pm}$ (GeV)	$m_{jj}(Inc)$		$m_{jj}(Inc\ CTagL)$		$m_{jj}(Ex\ CTag)$	
	from toys	from data	from toys	from data	from toys	from data
80	$29.4 \pm 7.5$	54.4	$29.7 \pm 7.8$	56.3	$89.8 \pm 13.6$	111.6
90	$29.8 \pm 7.6$	54.4	$30.0 \pm 8.0$	56.3	$89.0 \pm 13.3$	111.5
100	$29.4 \pm 8.3$	54.4	$29.4 \pm 7.8$	56.3	$89.7 \pm 13.1$	111.5
120	$30.1 \pm 8.2$	54.4	$29.4 \pm 7.7$	56.3	$89.1 \pm 13.1$	111.5
140	$29.9 \pm 7.7$	53.2	$29.4 \pm 7.9$	56.2	$90.0 \pm 13.2$	111.3
150	$29.7 \pm 7.8$	52.6	$30.0 \pm 7.8$	55.4	$89.2 \pm 13.6$	110.5
155	$29.5 \pm 8.2$	52.2	$29.6 \pm 8.3$	54.9	$89.9 \pm 13.3$	109.9
160	$29.4 \pm 7.6$	53.7	$29.3 \pm 8.0$	55.9	$89.6 \pm 12.9$	111.0

Table 33: Goodness of fit for  $e + \text{jets}$  channel, from different event categories.

$m_{H^\pm}$ (GeV)	$m_{jj}(Inc)$		$m_{jj}(Inc\ CTagL)$		$m_{jj}(Ex\ CTag)$	
	from toys	from data	from toys	from data	from toys	from data
80	$29.5 \pm 7.4$	34.1	$29.6 \pm 7.9$	34.7	$89.5 \pm 12.8$	81.8
90	$29.2 \pm 7.7$	33.1	$29.2 \pm 7.8$	34.7	$88.7 \pm 13.2$	81.8
100	$29.8 \pm 7.6$	34.1	$29.8 \pm 7.4$	34.7	$89.0 \pm 13.7$	81.8
120	$29.4 \pm 7.5$	33.8	$29.2 \pm 7.5$	34.7	$89.3 \pm 12.9$	81.8
140	$29.7 \pm 7.9$	34.1	$29.3 \pm 7.5$	34.7	$89.8 \pm 13.2$	81.8
150	$29.6 \pm 9.1$	34.1	$29.0 \pm 7.5$	34.7	$88.7 \pm 13.3$	81.8
155	$29.0 \pm 7.3$	34.1	$29.4 \pm 7.6$	34.7	$89.4 \pm 12.9$	81.8
160	$29.4 \pm 7.4$	34.1	$29.4 \pm 7.8$	34.7	$89.8 \pm 13.5$	81.8

Table 34: Goodness of fit for  $l + \text{jets}$  channel, from different event categories.

$m_{H^\pm}$ (GeV)	$m_{jj}(Inc)$		$m_{jj}(Inc\ CTagL)$		$m_{jj}(Ex\ CTag)$	
	from toys	from data	from toys	from data	from toys	from data
80	$59.0 \pm 10.8$	87.0	$59.0 \pm 11.1$	89.6	$173.6 \pm 15.1$	191.2
90	$59.5 \pm 11.1$	87.0	$58.5 \pm 10.5$	89.6	$173.0 \pm 14.6$	191.2
100	$59.7 \pm 10.5$	87.0	$58.7 \pm 10.4$	89.6	$173.8 \pm 14.5$	191.2
120	$58.3 \pm 10.3$	87.0	$59.5 \pm 10.6$	89.6	$173.4 \pm 15.3$	191.2
140	$59.5 \pm 10.9$	87.0	$59.5 \pm 10.7$	89.6	$173.0 \pm 15.3$	191.2
150	$58.6 \pm 10.2$	87.0	$59.4 \pm 10.7$	89.6	$173.5 \pm 15.0$	191.2
155	$59.4 \pm 10.5$	87.0	$59.0 \pm 10.9$	89.6	$173.2 \pm 14.9$	191.2
160	$59.9 \pm 10.8$	87.0	$59.8 \pm 10.9$	89.6	$172.6 \pm 15.4$	191.2

## 1067 18 Exclusion Limits

1068 The event yields from different event categories with systematics and statistical uncertainties  
 1069 are shown in Table 21, 23, and 25 for  $\mu + \text{jets}$  and  $e + \text{jets}$  channel. From these tables, it can  
 1070 be seen that the total background event matches well with the data within the uncertainties.  
 1071 In view of this, an expected exclusion limit with 95% CL has been put on the  $\mathcal{B}(t \rightarrow H^+ b)$ ,  
 1072 assuming  $\mathcal{B}(H^+ \rightarrow c\bar{s}) = 100\%$ .

1073 The absence of a charged Higgs boson signal in the data is characterized by setting exclusion  
 1074 limits on the branching fraction  $\mathcal{B}(t \rightarrow H^+ b)$ . An asymptotic 95% CL limit on  $\mathcal{B}(t \rightarrow H^+ b)$  is  
 1075 calculated using the  $\text{CL}_s$  method [81, 82] with likelihood ratios [80]:

$$\tilde{q}_x = -2 \ln \frac{\mathcal{L}(\text{data}|x, \hat{\Theta}_x)}{\mathcal{L}(\text{data}|\hat{x}, \hat{\Theta})}. \quad (31)$$

1076 where the likelihood is defined as

$$\mathcal{L}(\text{data}|x, \Theta) = \prod_{j=1}^3 \prod_{i=1}^N \frac{N_{ij}(x, \Theta)^{n_{ij}}}{n_{ij}!} e^{-N_{ij}(x, \Theta)} \prod_k p(\tilde{\Theta}_k | \Theta_k). \quad (32)$$

1077 In this equation,  $x = \mathcal{B}(t \rightarrow H^+ b)$  is the parameter of interest, the first product over  $j$  designates the three charm tagging categories, and  $i$  runs over the bins of the  $m_{jj}$  distributions shown in Fig. 37. For a given mass bin  $i$  and charm tagging category  $j$ ,  $n_{ij}$  is the observed number of events in that bin and charm tagging category, and  $N_{ij}(\Theta)$  is the expected number of events. The last term is the product over the individual nuisance parameters  $k$  of the probability density function  $p(\tilde{\Theta}_k | \Theta_k)$ , where  $\Theta_k$  is the value of the nuisance parameter. The estimators  $\hat{x}$  and  $\hat{\Theta}$  correspond to the global maximum of the likelihood defined in Eq. 32. The expected number of events  $N_{ij}(\Theta)$  is given by, in the presence of signal:

$$N_{ij}(x, \Theta) = 2x(1-x)N_{ij}^{t\bar{t} \rightarrow H^+ W^-}(\Theta) + (1-x)^2 N_{ij}^{t\bar{t} \rightarrow W^\pm W^\mp}(\Theta) + N_{ij}^{\text{other}}(\Theta), \quad (33)$$

1085 and in the absence:

$$N_{ij}(\Theta) = N_{ij}^{t\bar{t} \rightarrow W^\pm W^\mp}(\Theta) + N_{ij}^{\text{other}}(\Theta), \quad (34)$$

1086 where  $N_{ij}^{t\bar{t} \rightarrow H^+ W^-}(\Theta)$  and  $N_{ij}^{t\bar{t} \rightarrow W^\pm W^\mp}(\Theta)$  are the number of events from the simulated signal process and the SM  $t\bar{t}$  process, respectively. Both are normalized to the expected  $t\bar{t}$  cross sections, as described in Section 3. The factor of 2 in Eq. 33 is derived from the assumption that the event yield and  $\mathcal{B}(\bar{t} \rightarrow H^- \bar{b})$  for  $H^-$  are the same as those of  $H^+$ .

### 1090 18.1 Limits from inclusive event category without c tagging

1091 To extract possible signal, the  $m_{jj}$  distribution as shown in Figures 12c, 12d, 31c, and 31d are  
 1092 used in the binned maximum-likelihood fit. The upper limit on the  $\mathcal{B}(t \rightarrow H^+ b)$  as a function  
 1093 of  $m_{H^+}$  is shown in Figures 53a, 53b, and 53c for the  $\mu + \text{jets}$  and  $e + \text{jets}$  and  $l + \text{jets}$  channel,  
 1094 respectively. Corresponding values of the expected (observed) limits, for the charged Higgs  
 1095 mass from 80 to 160 GeV, are in the range 0.37–4.38% (0.44–5.29%), 0.43–5.04% (0.27–3.94%),  
 1096 and 0.30–3.45% (0.28–2.89) respectively. The expected (observed) limits using  $m_{jj}$  from inclusive  
 1097 event category the 8 TeV analysis, for the mass of charged Higgs boson in the range 90 to 160  
 1098 GeV, was in range 1.4–3.6% (1.2–6.5%) for  $l + \text{jets}$  channel [15].

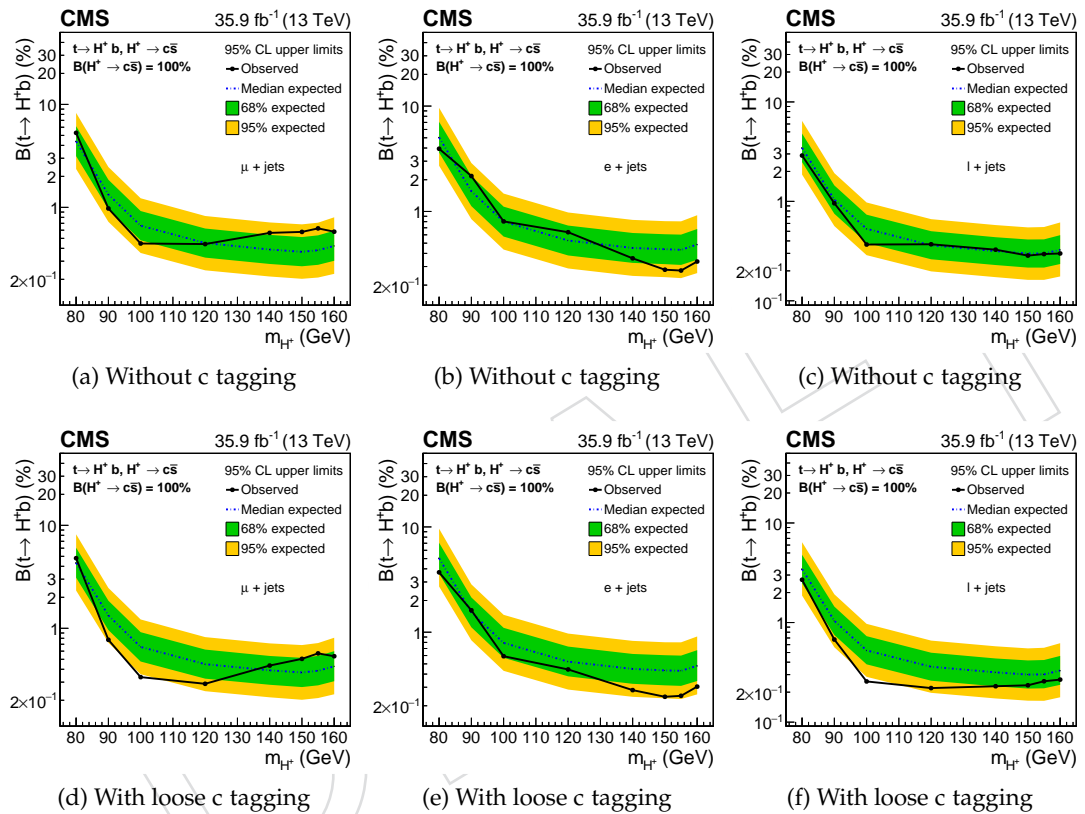


Figure 53: The upper limit in % on  $\mathcal{B}(t \rightarrow H^+ b)$  as a function of  $m_{H^+}$  using  $m_{jj}$  after kinematic fit selection without c tagging, and with loose c tagging, as discussed in Section 15.1 and 15.2, for  $\mu + \text{jets}$ ,  $e + \text{jets}$ , and  $l + \text{jets}$  channel.

Table 35: 95% CL exclusion limit in % for  $\mu + \text{jets}$  channel from different event categories.

$m_{H^+}$ (GeV)	$m_{jj}(\text{Inc})$		$m_{jj}(\text{Inc CTagL})$		$m_{jj}(\text{Ex CTag})$	
	Expected (%)	Observed (%)	Expected (%)	Observed (%)	Expected (%)	Observed (%)
80	$4.38^{+1.76}_{-1.23}$	5.29	$4.32^{+1.74}_{-1.21}$	4.79	$2.95^{+1.21}_{-0.85}$	2.44
90	$1.33^{+0.52}_{-0.37}$	0.97	$1.33^{+0.52}_{-0.37}$	0.77	$1.28^{+0.51}_{-0.36}$	0.72
100	$0.66^{+0.26}_{-0.18}$	0.45	$0.66^{+0.26}_{-0.18}$	0.34	$0.64^{+0.25}_{-0.18}$	0.34
120	$0.45^{+0.17}_{-0.13}$	0.44	$0.45^{+0.17}_{-0.12}$	0.29	$0.44^{+0.17}_{-0.12}$	0.32
140	$0.39^{+0.15}_{-0.11}$	0.56	$0.39^{+0.15}_{-0.11}$	0.43	$0.39^{+0.15}_{-0.11}$	0.47
150	$0.37^{+0.14}_{-0.10}$	0.58	$0.37^{+0.14}_{-0.10}$	0.50	$0.37^{+0.15}_{-0.10}$	0.52
155	$0.38^{+0.15}_{-0.11}$	0.62	$0.39^{+0.15}_{-0.11}$	0.57	$0.38^{+0.15}_{-0.11}$	0.57
160	$0.42^{+0.17}_{-0.12}$	0.58	$0.43^{+0.17}_{-0.12}$	0.54	$0.42^{+0.17}_{-0.12}$	0.53

## 1099 18.2 Limits from inclusive event category with loose c tagging

1100 The  $m_{jj}$  distribution from the events with inclusive loose c tagging as discussed in Section 15.2  
 1101 are used to compute upper limits as shown in Figures 53d, 53e, and 53f. From these figures,  
 1102 it can be seen that the limits are marginally better compared to that of Figures 53a, 53b, and  
 1103 53c. For different charged Higgs masses, the expected (observed) limits for loose c tagging are  
 1104 in the range 0.37–4.32% (0.29–4.79%), 0.43–5.04% (0.24–3.70%), and 0.30–3.44 (0.22–2.69%) for  
 1105  $\mu + \text{jets}$ ,  $e + \text{jets}$ , and  $l + \text{jets}$  channel, respectively.

## 1106 18.3 Limits from exclusive event categories based on c tagging

1107 The signal significance is different in different charm categories as described in Section 15.3.  
 1108 The  $m_{jj}$  distributions from loose, medium, and tight exclusive charm tagging categories are  
 1109 combined to compute the expected limits as shown in Figure 54. From this figure, it can be  
 1110 seen that the upper limits from exclusive categories are better compared to that obtained from  
 1111 inclusive working points. For different charged Higgs masses, the expected (observed) limits  
 1112 from combined categories are in the range 0.37–2.95% (0.32–2.44%), 0.42–3.63% (0.26–2.77%),  
 1113 and 0.29–2.39% (0.25–1.68) for  $\mu + \text{jets}$ ,  $e + \text{jets}$ , and  $l + \text{jets}$  channel, respectively.

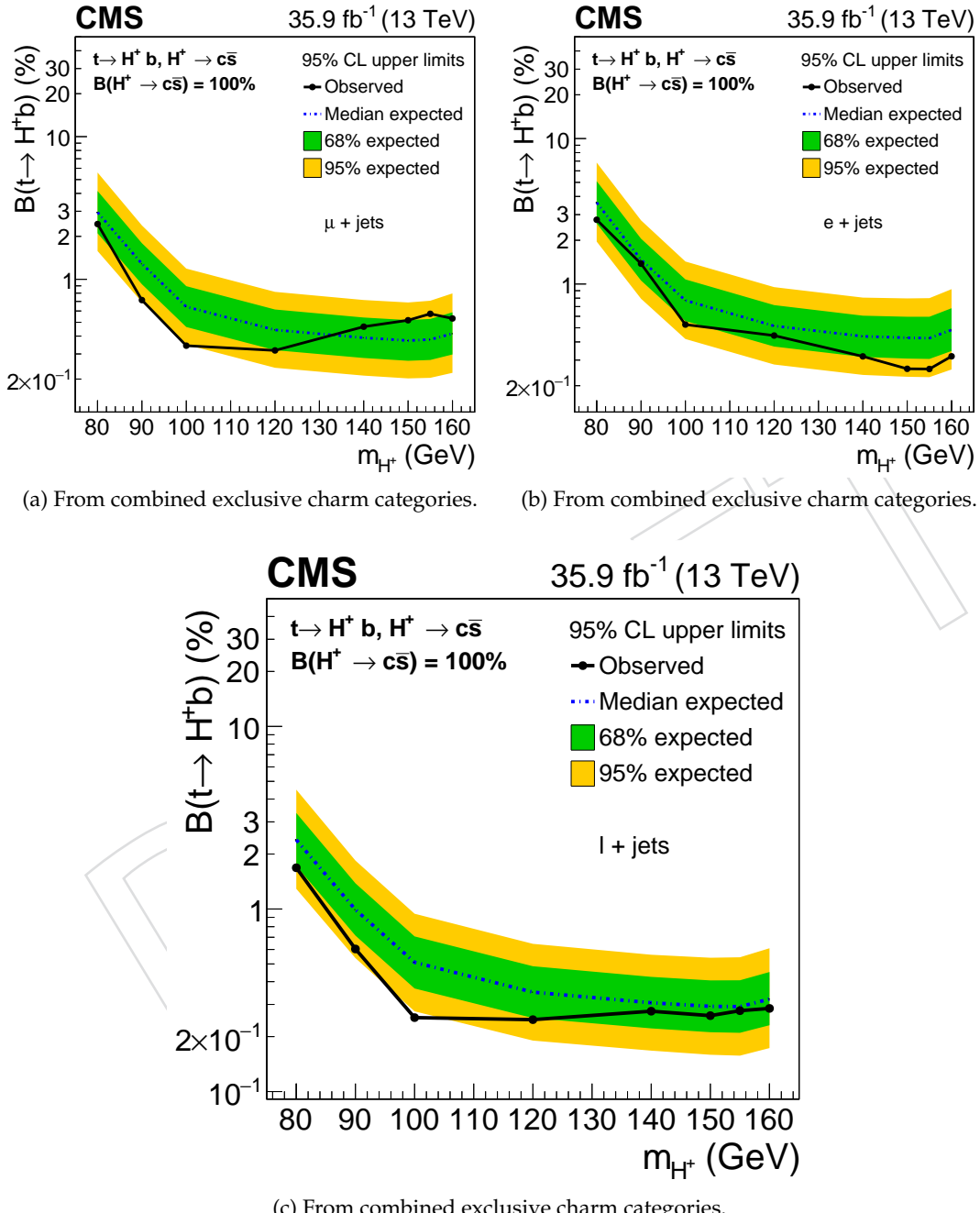


Figure 54: The upper limit in % on  $\mathcal{B}(t \rightarrow H^+ b)$  as a function of  $m_{H^+}$  by combining  $m_{jj}$  distributions from different exclusive charm categories as discussed in Section 15.3 for  $\mu + \text{jets}$ ,  $e + \text{jets}$ , and  $l + \text{jets}$  channel.

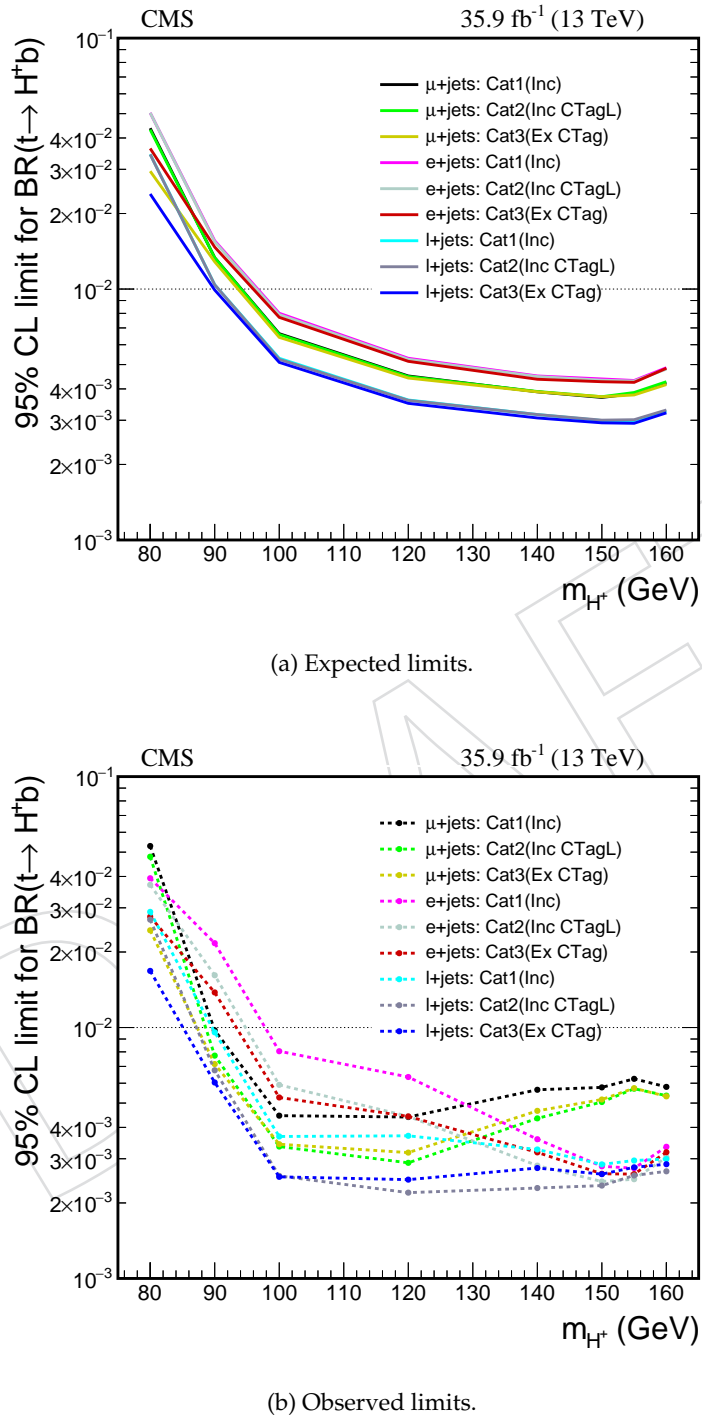


Figure 55: The upper limit in % on  $\mathcal{B}(t \rightarrow H^+ b)$  as a function of  $m_{H^+}$  using  $m_{jj}$  from all event categories for  $\mu + \text{jets}$ ,  $e + \text{jets}$ , and  $l + \text{jets}$  channel.

Table 36: 95% CL exclusion limit in % for e + jets channel from different event categories.

$m_{H^+}$ (GeV)	$m_{jj}(Inc)$		$m_{jj}(Inc\ CTagL)$		$m_{jj}(Ex\ CTag)$	
	Expected (%)	Observed (%)	Expected (%)	Observed (%)	Expected (%)	Observed (%)
80	$5.04^{+2.05}_{-1.42}$	3.94	$5.04^{+2.03}_{-1.43}$	3.70	$3.63^{+1.46}_{-1.02}$	2.77
90	$1.56^{+0.61}_{-0.43}$	2.17	$1.54^{+0.60}_{-0.43}$	1.62	$1.47^{+0.58}_{-0.41}$	1.38
100	$0.80^{+0.31}_{-0.22}$	0.80	$0.79^{+0.31}_{-0.22}$	0.59	$0.77^{+0.30}_{-0.21}$	0.53
120	$0.53^{+0.20}_{-0.15}$	0.64	$0.52^{+0.21}_{-0.14}$	0.44	$0.52^{+0.20}_{-0.14}$	0.44
140	$0.45^{+0.17}_{-0.13}$	0.36	$0.45^{+0.17}_{-0.12}$	0.28	$0.44^{+0.17}_{-0.12}$	0.32
150	$0.44^{+0.17}_{-0.12}$	0.28	$0.43^{+0.17}_{-0.12}$	0.24	$0.43^{+0.17}_{-0.12}$	0.26
155	$0.43^{+0.17}_{-0.12}$	0.27	$0.43^{+0.17}_{-0.12}$	0.25	$0.42^{+0.17}_{-0.12}$	0.26
160	$0.49^{+0.20}_{-0.14}$	0.33	$0.48^{+0.20}_{-0.14}$	0.30	$0.48^{+0.20}_{-0.14}$	0.32

Table 37: 95% CL exclusion limit in % for 1 + jets channel from different event categories.

$m_{H^+}$ (GeV)	$m_{jj}(Inc)$		$m_{jj}(Inc\ CTagL)$		$m_{jj}(Ex\ CTag)$	
	Expected (%)	Observed (%)	Expected (%)	Observed (%)	Expected (%)	Observed (%)
80	$3.45^{+1.36}_{-0.97}$	2.89	$3.44^{+1.36}_{-0.96}$	2.69	$2.39^{+0.96}_{-0.67}$	1.68
90	$1.04^{+0.41}_{-0.29}$	0.96	$1.04^{+0.41}_{-0.29}$	0.68	$0.99^{+0.39}_{-0.28}$	0.60
100	$0.53^{+0.20}_{-0.15}$	0.37	$0.52^{+0.21}_{-0.14}$	0.26	$0.51^{+0.20}_{-0.14}$	0.25
120	$0.36^{+0.14}_{-0.10}$	0.37	$0.36^{+0.14}_{-0.10}$	0.22	$0.35^{+0.14}_{-0.10}$	0.25
140	$0.32^{+0.12}_{-0.09}$	0.33	$0.32^{+0.12}_{-0.09}$	0.23	$0.31^{+0.12}_{-0.08}$	0.28
150	$0.30^{+0.11}_{-0.08}$	0.28	$0.30^{+0.12}_{-0.08}$	0.23	$0.29^{+0.11}_{-0.08}$	0.26
155	$0.30^{+0.12}_{-0.08}$	0.30	$0.30^{+0.12}_{-0.08}$	0.26	$0.29^{+0.12}_{-0.08}$	0.28
160	$0.33^{+0.13}_{-0.09}$	0.30	$0.33^{+0.13}_{-0.09}$	0.27	$0.32^{+0.13}_{-0.09}$	0.29

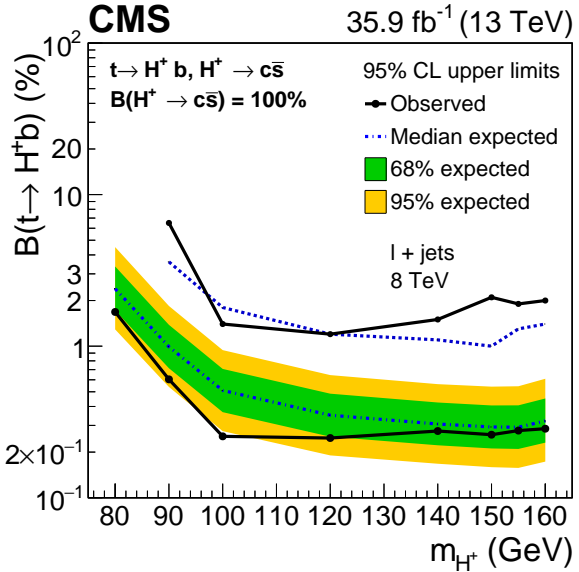


Figure 56: The upper limit on  $\mathcal{B}(t \rightarrow H^+ b)$  as a function of  $m_{H^+}$  for 1+jets channel. The limits from 13 TeV analysis (lower curves) are obtained by combining exclusive charm categories. The limits from 8 TeV analysis (upper curves) were obtained from inclusive events without applying charm tagging. The 80 GeV signal mass point was not considered at 8 TeV analysis.

## 1114 19 Conclusion

1115 In order to explain some failures of the standard model, the 2HDM postulated existence of an  
 1116 additional Higgs doublet. It leads to two charged and three neutral physical scalar particles.  
 1117 A charged Higgs boson decays to various channels depending on the parameter space corre-  
 1118 sponding to its mass and  $\tan \beta$ . A search for the charged Higgs in the  $H^+ \rightarrow c\bar{s}$  channel has been  
 1119 performed in this analysis with the data collected by the CMS experiment at the center-of-mass  
 1120 energy of 13 TeV with an integrated luminosity of  $35.9 \text{ fb}^{-1}$ . The observed data and standard  
 1121 model predictions are in agreement within the statistical and systematic uncertainties. That is,  
 1122 no signal has been observed in the data for the mass of charged Higgs in the range 80 to 160  
 1123 GeV. In the absence of an excess, a 95% CL upper limit has been put on  $\mathcal{B}(t \rightarrow H^+ b)$ , assuming  
 1124  $\mathcal{B}(H^+ \rightarrow c\bar{s}) = 100\%$ . The kinematic fitting and a new technique which uses c tagging has been  
 1125 intensively exploited to improve the limits. The final limits from combined charm categories  
 1126 are shown in Tables 38 and 39. The observed limits are in the range 0.32–2.44%, 0.26–2.77%, and  
 1127 0.26–1.68% for  $\mu + \text{jets}$ ,  $e + \text{jets}$ , and 1+jets channel, respectively. The observed limits at 13 TeV  
 1128 are better by an average factor of 7.6 as compared to the earlier CMS results at 8 TeV [15]. The  
 1129 improvement in the limit is partly due to higher luminosity and partly due the new technique  
 1130 used in this analysis.

Table 38: Expected and observed 95% CL exclusion limits in % on  $\mathcal{B}(t \rightarrow H^+ b)$  in the muon + jets (electron + jets) channel, after the individual charm tagging categories have been combined.

$m_{H^+}$ (GeV)	Expected				Observed
	$-2\sigma$	$-1\sigma$	median	$+1\sigma$	
80	1.58 (1.96)	2.10 (2.61)	2.95 (3.63)	4.16 (5.10)	5.61 (6.84)
90	0.69 (0.79)	0.92 (1.06)	1.28 (1.47)	1.79 (2.05)	2.39 (2.74)
100	0.35 (0.42)	0.46 (0.56)	0.64 (0.77)	0.90 (1.08)	1.19 (1.43)
120	0.24 (0.28)	0.32 (0.37)	0.44 (0.52)	0.61 (0.72)	0.82 (0.95)
140	0.21 (0.24)	0.28 (0.32)	0.39 (0.44)	0.54 (0.61)	0.72 (0.81)
150	0.20 (0.23)	0.27 (0.31)	0.37 (0.43)	0.52 (0.60)	0.69 (0.80)
155	0.20 (0.23)	0.27 (0.31)	0.38 (0.42)	0.53 (0.60)	0.71 (0.80)
160	0.22 (0.26)	0.30 (0.35)	0.42 (0.48)	0.59 (0.68)	0.80 (0.92)
					0.53 (0.32)

Table 39: Expected and observed 95% CL exclusion limits in % on  $\mathcal{B}(t \rightarrow H^+ b)$ , after the individual charm tagging categories and the muon and electron channels have been combined.

$m_{H^+}$ (GeV)	Expected				Observed
	$-2\sigma$	$-1\sigma$	median	$+1\sigma$	
80	1.29	1.72	2.39	3.36	4.50
90	0.54	0.72	0.99	1.38	1.84
100	0.28	0.37	0.51	0.71	0.94
120	0.19	0.25	0.35	0.49	0.64
140	0.17	0.22	0.31	0.42	0.56
150	0.16	0.21	0.29	0.41	0.54
155	0.16	0.21	0.29	0.41	0.54
160	0.17	0.23	0.32	0.45	0.61
					0.29

## References

- [1] CMS Collaboration, “Observation of a new boson at a mass of 125 GeV with the CMS experiment at the LHC”, *Phys.Lett.* **B716** (2012) 30–61,  
doi:10.1016/j.physletb.2012.08.021, arXiv:1207.7235.
- [2] ATLAS Collaboration, “Observation of a new particle in the search for the Standard Model Higgs boson with the ATLAS detector at the LHC”, *Phys.Lett.* **B716** (2012) 1–29,  
doi:10.1016/j.physletb.2012.08.020, arXiv:1207.7214.
- [3] H. Murayama, “Supersymmetry”, in *22nd INS International Symposium on Physics with High-energy Colliders Tokyo, Japan, March 8-10, 1994*, pp. 0357–380. 1994.  
arXiv:hep-ph/9410285.
- [4] Y. Golfand and E. Likhtman, “Extension of the Algebra of Poincare Group Generators and Violation of p Invariance”, *JETP Lett.* **13** (1971) 323–326.
- [5] J. Wess and B. Zumino, “Supergauge Transformations in Four-Dimensions”, *Nucl.Phys.* **B70** (1974) 39–50, doi:10.1016/0550-3213(74)90355-1.

- [6] G. C. Branco et al., "Theory and phenomenology of two-Higgs-doublet models", *Phys. Rept.* **516** (2012) 1–102, doi:10.1016/j.physrep.2012.02.002, arXiv:1106.0034.
- [7] M. Aoki, S. Kanemura, K. Tsumura, and K. Yagyu, "Models of yukawa interaction in the two higgs doublet model, and their collider phenomenology", *Phys. Rev. D* **80** (Jul, 2009) 015017, doi:10.1103/PhysRevD.80.015017.
- [8] L3 Collaboration, "Search for charged Higgs bosons at LEP", *Phys. Lett.* **B575** (2003) 208–220, doi:10.1016/j.physletb.2003.09.057, arXiv:hep-ex/0309056.
- [9] ALEPH Collaboration, "Search for charged Higgs bosons in  $e^+e^-$  collisions at energies up to  $\sqrt{s} = 209\text{-GeV}$ ", *Phys. Lett.* **B543** (2002) 1–13, doi:10.1016/S0370-2693(02)02380-8, arXiv:hep-ex/0207054.
- [10] DELPHI Collaboration, "Search for charged Higgs bosons at LEP in general two Higgs doublet models", *Eur. Phys. J.* **C34** (2004) 399–418, doi:10.1140/epjc/s2004-01732-6, arXiv:hep-ex/0404012.
- [11] OPAL Collaboration, "Search for Charged Higgs Bosons in  $e^+e^-$  Collisions at  $\sqrt{s} = 189 - 209\text{ GeV}$ ", *Eur. Phys. J.* **C72** (2012) 2076, doi:10.1140/epjc/s10052-012-2076-0, arXiv:0812.0267.
- [12] CDF Collaboration, "Search for charged Higgs bosons in decays of top quarks in p anti-p collisions at  $s^{**}(1/2) = 1.96\text{ TeV}$ ", *Phys.Rev.Lett.* **103** (2009) 101803, doi:10.1103/PhysRevLett.103.101803, arXiv:0907.1269.
- [13] D0 Collaboration, "Search for charged Higgs bosons in top quark decays", *Phys.Lett.* **B682** (2009) 278–286, doi:10.1016/j.physletb.2009.11.016, arXiv:0908.1811.
- [14] ATLAS Collaboration, "Search for a light charged Higgs boson in the decay channel  $H^+ \rightarrow c\bar{s}$  in  $t\bar{t}$  events using pp collisions at  $\sqrt{s} = 7\text{ TeV}$  with the ATLAS detector", *Eur.Phys.J.* **C73** (2013) 2465, doi:10.1140/epjc/s10052-013-2465-z, arXiv:1302.3694.
- [15] CMS Collaboration, "Search for a light charged Higgs boson decaying to  $c\bar{s}$  in pp collisions at  $\sqrt{s} = 8\text{ TeV}$ ", *JHEP* **12** (2015) 178, doi:10.1007/JHEP12(2015)178, arXiv:1510.04252.
- [16] "A search of charged Higgs in the decay products of pair-produced top quarks.". [https://www-cdf.fnal.gov/physics/new/top/2005/1jets/charged\\_higgs/higgs/V2/HiggsAnalysis\\_publicV2.html](https://www-cdf.fnal.gov/physics/new/top/2005/1jets/charged_higgs/higgs/V2/HiggsAnalysis_publicV2.html).
- [17] C. E. Gerber and C. Vellidis, "Review of Physics Results from the Tevatron: Top Quark Physics", *Submitted to: Int. J. Mod. Phys. A* (2014) arXiv:1409.5038.
- [18] L. Fiorini, "Top-Quark Physics Results From LHC", in *Helmholtz Alliance Linear Collider Forum: Proceedings of the Workshops Hamburg, Munich, Hamburg 2010-2012, Germany*, pp. 38–45, DESY, Hamburg, 2013. arXiv:1201.5844.
- [19] J. Alwall et al., "MadGraph 5 : Going Beyond", *JHEP* **06** (2011) 128, doi:10.1007/JHEP06(2011)128, arXiv:1106.0522.

- [20] J. Alwall et al., "The automated computation of tree-level and next-to-leading order differential cross sections, and their matching to parton shower simulations", *JHEP* **07** (2014) 079, doi:10.1007/JHEP07(2014)079, arXiv:1405.0301.
- [21] S. Frixione, P. Nason, and C. Oleari, "Matching NLO QCD computations with Parton Shower simulations: the POWHEG method", *JHEP* **11** (2007) 070, doi:10.1088/1126-6708/2007/11/070, arXiv:0709.2092.
- [22] P. Nason, "A New method for combining NLO QCD with shower Monte Carlo algorithms", *JHEP* **11** (2004) 040, doi:10.1088/1126-6708/2004/11/040, arXiv:hep-ph/0409146.
- [23] S. Alioli, P. Nason, C. Oleari, and E. Re, "A general framework for implementing NLO calculations in shower Monte Carlo programs: the POWHEG BOX", *JHEP* **06** (2010) 043, doi:10.1007/JHEP06(2010)043, arXiv:1002.2581.
- [24] T. Sjostrand, S. Mrenna, and P. Z. Skands, "PYTHIA 6.4 Physics and Manual", *JHEP* **05** (2006) 026, doi:10.1088/1126-6708/2006/05/026, arXiv:hep-ph/0603175.
- [25] T. Sjostrand, S. Mrenna, and P. Z. Skands, "A Brief Introduction to PYTHIA 8.1", *Comput. Phys. Commun.* **178** (2008) 852–867, doi:10.1016/j.cpc.2008.01.036, arXiv:0710.3820.
- [26] CMS Collaboration, "Investigations of the impact of the parton shower tuning in Pythia 8 in the modelling of  $t\bar{t}$  at  $\sqrt{s} = 8$  and 13 TeV", Technical Report CMS-PAS-TOP-16-021, CERN, Geneva, 2016.
- [27] GEANT4 Collaboration, "GEANT4: A Simulation toolkit", *Nucl. Instrum. Meth.* **A506** (2003) 250–303, doi:10.1016/S0168-9002(03)01368-8.
- [28] NNPDF Collaboration, "Parton distributions for the LHC Run II", *JHEP* **04** (2015) 040, doi:10.1007/JHEP04(2015)040, arXiv:1410.8849.
- [29] M. Beneke, P. Falgari, S. Klein, and C. Schwinn, "Hadronic top-quark pair production with NNLL threshold resummation", *Nucl. Phys.* **B855** (2012) 695–741, doi:10.1016/j.nuclphysb.2011.10.021, arXiv:1109.1536.
- [30] M. Aliev et al., "HATHOR: HAdronic Top and Heavy quarks crOss section calculatoR", *Comput. Phys. Commun.* **182** (2011) 1034–1046, doi:10.1016/j.cpc.2010.12.040, arXiv:1007.1327.
- [31] P. Kant et al., "HatHor for single top-quark production: Updated predictions and uncertainty estimates for single top-quark production in hadronic collisions", *Comput. Phys. Commun.* **191** (2015) 74–89, doi:10.1016/j.cpc.2015.02.001, arXiv:1406.4403.
- [32] J. Alwall et al., "Comparative study of various algorithms for the merging of parton showers and matrix elements in hadronic collisions", *Eur. Phys. J.* **C53** (2008) 473–500, doi:10.1140/epjc/s10052-007-0490-5, arXiv:0706.2569.
- [33] Particle Data Group Collaboration, "Review of Particle Physics (RPP)", *Phys. Rev.* **D86** (2012) 010001, doi:10.1103/PhysRevD.86.010001.

- [34] CMS Collaboration Collaboration, "Particle-Flow Event Reconstruction in CMS and Performance for Jets, Taus, and MET", Technical Report CMS-PAS-PFT-09-001, CERN, Geneva, Apr, 2009.
- [35] CMS Collaboration Collaboration, "Commissioning of the Particle-flow Event Reconstruction with the first LHC collisions recorded in the CMS detector", Technical Report CMS-PAS-PFT-10-001, CERN, 2010.
- [36] CMS Collaboration, "Description and performance of track and primary-vertex reconstruction with the CMS tracker", *JINST* **9** (2014), no. 10, P10009, doi:10.1088/1748-0221/9/10/P10009, arXiv:1405.6569.
- [37] CMS Collaboration, "Offline primary vertex reconstruction with deterministic annealing clustering", *CMS Internal Note IN-11-014* (2011).
- [38] K. Rose, "Deterministic annealing for clustering, compression, classification, regression, and related optimization problems", *Proceedings of the IEEE* **86** (Nov, 1998) 2210–2239, doi:10.1109/5.726788.
- [39] R. Fruhwirth, W. Waltenberger, and P. Vanlaer, "Adaptive Vertex Fitting", Technical Report CMS-NOTE-2007-008, CERN, Geneva, Mar, 2007.
- [40] CMS Collaboration, "Measurement of jet activity in ttbar events using lepton + jets final states in proton-proton collisions at 13 tev", *CMS Analysis Note CMS AN-17-003* (2017).
- [41] CMS Collaboration, "Measurement of the top quark decay width in the dilepton channel at  $\sqrt{s} = 13$  tev with cms", *CMS Analysis Note CMS AN-17-116* (2017).
- [42] M. Cacciari and G. P. Salam, "Dispelling the  $N^3$  myth for the  $k_t$  jet-finder", *Phys. Lett. B* **641** (2006) 57–61, doi:10.1016/j.physletb.2006.08.037, arXiv:hep-ph/0512210.
- [43] M. Cacciari, G. P. Salam, and G. Soyez, "FastJet User Manual", *Eur. Phys. J. C* **72** (2012) 1896, doi:10.1140/epjc/s10052-012-1896-2, arXiv:1111.6097.
- [44] M. Cacciari and G. P. Salam, "Pileup subtraction using jet areas", *Phys. Lett. B* **659** (2008) 119–126, doi:10.1016/j.physletb.2007.09.077, arXiv:0707.1378.
- [45] R. Fruhwirth, "Application of kalman filtering to track and vertex fitting", *Nuclear Instruments and Methods in Physics Research Section A: Accelerators, Spectrometers, Detectors and Associated Equipment* **262** (1987), no. 2, 444 – 450, doi:https://doi.org/10.1016/0168-9002(87)90887-4.
- [46] CMS Collaboration, "Performance of CMS muon reconstruction in  $pp$  collision events at  $\sqrt{s} = 7$  TeV", *JINST* **7** (2012) P10002, doi:10.1088/1748-0221/7/10/P10002, arXiv:1206.4071.
- [47] CMS Collaboration, "CMS RPC tracker muon reconstruction", *JINST* **9** (2014), no. 10, C10027, doi:10.1088/1748-0221/9/10/C10027.
- [48] "Muon efficiencies and scale factors". <https://twiki.cern.ch/twiki/bin/viewauth/CMS/MuonWorkInProgressAndPagResults>.
- [49] A. Bodek et al., "Extracting Muon Momentum Scale Corrections for Hadron Collider Experiments", *Eur. Phys. J. C* **72** (2012) 2194, doi:10.1140/epjc/s10052-012-2194-8, arXiv:1208.3710.

- [50] CMS Collaboration, “Performance of the CMS muon detector and muon reconstruction with proton-proton collisions at  $\sqrt{s} = 13$  TeV”, *JINST* **13** (2018), no. 06, P06015, doi:10.1088/1748-0221/13/06/P06015, arXiv:1804.04528.
- [51] CMS Collaboration, “Performance of Electron Reconstruction and Selection with the CMS Detector in Proton-Proton Collisions at  $\text{sqrt}s = 8$  TeV”, *JINST* **10** (2015), no. 06, P06005, doi:10.1088/1748-0221/10/06/P06005, arXiv:1502.02701.
- [52] “Electron efficiencies and scale factors”. [https://twiki.cern.ch/twiki/bin/view/CMS/EgammaIDRecipesRun2#Efficiencies\\_and\\_scale\\_factors](https://twiki.cern.ch/twiki/bin/view/CMS/EgammaIDRecipesRun2#Efficiencies_and_scale_factors).
- [53] A. M. Polyakov, “Quark Confinement and Topology of Gauge Groups”, *Nucl. Phys.* **B120** (1977) 429–458, doi:10.1016/0550-3213(77)90086-4.
- [54] M. Cacciari, G. P. Salam, and G. Soyez, “The anti- $k_t$  jet clustering algorithm”, *JHEP* **04** (2008) 063, doi:10.1088/1126-6708/2008/04/063, arXiv:0802.1189.
- [55] “Jet Identification for the 13 TeV data Run2016”. <https://twiki.cern.ch/twiki/bin/viewauth/CMS/JetID13TeVRun2016>.
- [56] CMS Collaboration Collaboration, “Pileup Removal Algorithms”, Technical Report CMS-PAS-JME-14-001, CERN, Geneva, 2014.
- [57] CMS Collaboration, “Identification of b-quark jets with the CMS experiment”, *JINST* **8** (2013) P04013, doi:10.1088/1748-0221/8/04/P04013, arXiv:1211.4462.
- [58] CMS Collaboration Collaboration, “Identification of b quark jets at the CMS Experiment in the LHC Run 2”, Technical Report CMS-PAS-BTV-15-001, CERN, Geneva, 2016.
- [59] C. Ferro, “B-tagging in CMS”, *EPJ Web Conf.* **28** (2012) 12055, doi:10.1051/epjconf/20122812055, arXiv:1201.5292.
- [60] W. Waltenberger, “Adaptive Vertex Reconstruction”, Technical Report CMS-NOTE-2008-033, CERN, Geneva, Jul, 2008.
- [61] CMS Collaboration, “Measurement of  $B\bar{B}$  Angular Correlations based on Secondary Vertex Reconstruction at  $\sqrt{s} = 7$  TeV”, *JHEP* **03** (2011) 136, doi:10.1007/JHEP03(2011)136, arXiv:1102.3194.
- [62] CMS Collaboration, “Identification of heavy-flavour jets with the CMS detector in pp collisions at 13 TeV”, *JINST* **13** (2018), no. 05, P05011, doi:10.1088/1748-0221/13/05/P05011, arXiv:1712.07158.
- [63] J. D’Hondt et al., “Fitting of Event Topologies with External Kinematic Constraints in CMS”, Technical Report CMS-NOTE-2006-023, CERN, Geneva, Jan, 2006.
- [64] “Application of kinematic fitting to top quark mass reconstruction in the  $\mu + \text{jets}$  channel at  $\text{sqrt}s = 7$  TeV with the CMS detector”. [https://lib.ugent.be/fulltxt/RUG01/001/892/467/RUG01-001892467\\_2012\\_0001\\_AC.pdf](https://lib.ugent.be/fulltxt/RUG01/001/892/467/RUG01-001892467_2012_0001_AC.pdf).
- [65] CMS Collaboration Collaboration, “Identification of c-quark jets at the CMS experiment”, Technical Report CMS-PAS-BTV-16-001, CERN, Geneva, 2016.
- [66] CMS Collaboration, “Jet energy scale and resolution in the CMS experiment in pp collisions at 8 TeV”, *JINST* **12** (2017), no. 02, P02014, doi:10.1088/1748-0221/12/02/P02014, arXiv:1607.03663.

- 1304 [67] "Methods to apply b-tagging efficiency scale factors".  
 1305 <https://twiki.cern.ch/twiki/bin/viewauth/CMS/BTagSFMETHODS>.
- 1306 [68] "Usage of b/c Tag Objects for 13 TeV Data in 2016 and 80X MC". <https://twiki.cern.ch/twiki/bin/viewauth/CMS/BtagRecommendation80XReReco>.
- 1308 [69] "BTagCalibration Documentation".  
 1309 <https://twiki.cern.ch/twiki/bin/view/CMS/BTagCalibration>.
- 1310 [70] "MET Filter Recommendations for Run II". [https://twiki.cern.ch/twiki/bin/viewauth/CMS/MissingETOptionalFiltersRun2#2016\\_data](https://twiki.cern.ch/twiki/bin/viewauth/CMS/MissingETOptionalFiltersRun2#2016_data).
- 1312 [71] CMS Collaboration,  
 1313 "<https://twiki.cern.ch/twiki/bin/view/CMS/MuonReferenceEffsRun2>", *CMS Twiki*.
- 1314 [72] "Electron Triggers Efficiencies with 2016 data".  
 1315 [https://indico.cern.ch/event/570560/contributions/2389651/attachments/1380332/2098249/EGMTriggers\\_Approval\\_v2.pdf](https://indico.cern.ch/event/570560/contributions/2389651/attachments/1380332/2098249/EGMTriggers_Approval_v2.pdf).
- 1317 [73] CMS Collaboration Collaboration, "CMS Luminosity Measurements for the 2016 Data  
 1318 Taking Period", Technical Report CMS-PAS-LUM-17-001, CERN, Geneva, 2017.
- 1319 [74] "pt(top-quark) based reweighting of ttbar MC".  
 1320 <https://twiki.cern.ch/twiki/bin/viewauth/CMS/TopPtReweighting>.
- 1321 [75] CMS Collaboration,  
 1322 "[https://twiki.cern.ch/twiki/pub/CMS/HIG18021Review/HIG\\_18\\_021\\_TopoPtSystematicsPart2.pdf](https://twiki.cern.ch/twiki/pub/CMS/HIG18021Review/HIG_18_021_TopoPtSystematicsPart2.pdf)",  
 1323 *CMS Twiki* (2019).
- 1324 [76] S. Baker and R. D. Cousins, "Clarification of the Use of Chi Square and Likelihood  
 1325 Functions in Fits to Histograms", *Nucl. Instrum. Meth.* **221** (1984) 437–442,  
 1326 doi:10.1016/0167-5087(84)90016-4.
- 1327 [77] A. Kolmogorov, "Sulla determinazione empirica di una legge di distribuzione", *G. Ist.  
 1328 Ital. Attuari.* **4** (1933) 83–91.
- 1329 [78] N. Smirnov, "Table for estimating the goodness of fit of empirical distributions", *Ann.  
 1330 Math. Statist.* **19** (06, 1948) 279–281, doi:10.1214/aoms/1177730256.
- 1331 [79] T. W. Anderson and D. A. Darling, "Asymptotic theory of certain goodness of fit criteria  
 1332 based on stochastic processes", *Ann. Math. Statist.* **23** (06, 1952) 193–212,  
 1333 doi:10.1214/aoms/1177729437.
- 1334 [80] G. Cowan, K. Cranmer, E. Gross, and O. Vitells, "Asymptotic formulae for  
 1335 likelihood-based tests of new physics", *Eur.Phys.J.* **C71** (2011) 1554, doi:10.1140/  
 1336 epjc/s10052-011-1554-0, 10.1140/epjc/s10052-013-2501-z,  
 1337 arXiv:1007.1727.
- 1338 [81] T. Junk, "Confidence level computation for combining searches with small statistics",  
 1339 *Nucl. Instrum. Meth. A* **434** (1999) 435, doi:10.1016/S0168-9002(99)00498-2,  
 1340 arXiv:hep-ex/9902006.
- 1341 [82] A. L. Read, "Presentation of search results: The CL<sub>s</sub> technique", *J. Phys. G* **28** (2002) 2693,  
 1342 doi:10.1088/0954-3899/28/10/313.
- 1343 [83] "SM Higgs production cross sections at sqrt(s) = 13 TeV". <https://twiki.cern.ch/twiki/bin/view/LHCPhysics/CERNYellowReportPageAt13TeV>.

## 1345 A Background Contribution from SM Higgs Production Process

1346 The production and decay process of SM Higgs Boson can also have 1-lepton, 4-jets, and MET  
 1347 in the final states. We consider major production process of SM Higgs such as

- 1348 • SM Higgs production from gluon-gluon fusion via quark loop,  $\sigma(ggF) = 48.58 \text{ pb}$
- 1349 • Associate production of SM Higgs with W/Z Bosons,  $\sigma(W^+H) = 0.84 \text{ pb}$ ,  $\sigma(W^-H)$   
    $= 0.53 \text{ pb}$ ,  $\sigma(ZH) = 0.88 \text{ pb}$ ,  $\sigma(ggZH) = 0.12 \text{ pb}$
- 1351 • SM Higgs production from vector Boson fusion,  $\sigma(VBF) = 3.78 \text{ pb}$
- 1352 • Associate production of SM Higgs with top/bottom quarks,  $\sigma(ttH) = 0.51 \text{ pb}$ ,  
    $\sigma(bbH) = 0.49 \text{ pb}$

1354 And following decay process

- 1355 •  $H \rightarrow b\bar{b}$ ,  $BR(H \rightarrow b\bar{b}) = 0.58$
- 1356 •  $H \rightarrow \tau^+\tau^-$ ,  $BR(H \rightarrow \tau^+\tau^-) = 0.06$
- 1357 •  $H \rightarrow c\bar{c}$ ,  $BR(H \rightarrow c\bar{c}) = 0.03$
- 1358 •  $H \rightarrow gg$ ,  $BR(H \rightarrow gg) = 0.08$
- 1359 •  $H \rightarrow W^+W^-$ ,  $BR(H \rightarrow W^+W^-) = 0.21$
- 1360 •  $H \rightarrow ZZ$ ,  $BR(H \rightarrow ZZ) = 0.03$

1361 The cross-sections and branching ratios are taken from [83]. The datasets  
 1362 of SM production process are shown in Table 40. Where, **XXX** =  
 1363 13TeV\_powheg\_pythia8/RunII Summer16 MiniAODv2-PUMoriond17\_  
 1364 80X\_mcRun2\_asymptotic\_2016\_TrancheIV\_v6-v1/MINIAODSIM,  
 1365 PPP = pythia8/RunII Summer16 MiniAODv2-PUMoriond17\_  
 1366 80X\_mcRun2\_asymptotic\_2016\_TrancheIV\_v6-v1/MINIAODSIM,  
 1367 HHH = "RunII Summer16 MiniAODv2-PUMoriond17\_HIG083\_  
 1368 80X\_mcRun2\_asymptotic\_2016\_TrancheIV\_v6",  
 1369 JJJ = JHUGenV709\_pythia8/HHH, M = MINIAODSIM. The cuflow tables for  $\mu +$  jets and  
 1370 e + jets channel are shown in Tables 41 and 42 respectively. Since the number of events after  
 1371 kinematic fit selection is very small compared to SM  $t\bar{t} +$  jets background therefore we do not  
 1372 consider SM Higgs background process in the limit computation.

## 1373 B MadGraph vs POWHEG Sample

1374 The  $t\bar{t} +$  jets process is the most dominant background for this analysis. Two types of  $t\bar{t} +$  jets  
 1375 MC samples, one generated with MadGraph-MLM and other with POWHEG are officially  
 1376 available. However, choice of  $t\bar{t} +$  jets sample from these two depends on the number of jets  
 1377 present in the final states. For high jet multiplicity, the MadGraph-MLM sample is not properly  
 1378 modeled. In this analysis, we require each event to have at least 4 jets so the POWHEG  $t\bar{t} +$  jets  
 1379 sample is preferred over that from MadGraph-MLM.

1380 For the sake of comparison,  $t\bar{t} +$  jets sample from both generator is analysed. The number of  
 1381 events after various selection cuts are shown in Figure 57 for  $\mu +$  jets and e + jets channels. For  
 1382 both channels, the number of events is exactly the same up to the relative isolation selection.  
 1383 After requiring the events to have  $N_{jets} \geq 4$ , the  $t\bar{t} +$  jets sample from both generator give  
 1384 different event yields. The data, MC agreement after the kinematic fit selection is better with  
 1385 POWHEG  $t\bar{t} +$  jets sample as compared to that from MadGraph-MLM. In view of this the  
 1386 POWHEG  $t\bar{t} +$  jets sample is used in this analysis.

Table 40: Background process from SM Higgs production. Where  $BR(W \rightarrow l\nu) = 0.32$ ,  $BR(W \rightarrow q\bar{q}') = 0.68$ ,  $BR(Z \rightarrow \nu\bar{\nu}) = 0.20$ ,  $BR(Z \rightarrow l^+l^-) = 0.10$ , and  $BR(Z \rightarrow q\bar{q}) = 0.70$ .

MC Samples from Higgs production	$\sigma$ (pb)	Events
/GluGluHToBB_M125_XXX	48.58 * 0.58	4856192
/GluGluHToTauTau_M125_XXX	48.58 * 0.06	1471061
/GluGluHToCC_M125_XXX	48.58 *0.03	9782840
/GluGluHToGG_M-125_XXX	48.58 *0.08	998200
/GluGluHToWWTo2L2Nu_M125_XXX	48.58 *0.2137 * (0.324 * 0.324)	499473
/GluGluHToWWToLNuQQ_M125_13TeV_powheg_JHUGenV628_PPP	48.58 *0.2137 * (2*0.324*0.676)	198585
/GluGluHToZZTo2L2Q_M125_13TeV_powheg2_JJJ-v2/M	48.58 *0.0262 *(2*0.1097* 0.6991)	1000000
/GluGluHToZZTo4L_M125_13TeV_powheg2_JHUGenV709_PPP	48.58 *0.0262 *(0.1097 * 0.1097)	992224
/WplusH_HToBB_WToLNu_M125_XXX	0.84 *0.5824*0.324	999800
/WplusH_HToBB_WToQQ_M125_XXX	0.84 *0.5824*0.676	499093
/WplusHToTauTau_M125_XXX	0.84 *0.06	428036
/WplusH_HToCC_WToLNu_M125_XXX	0.84 *0.0289*0.324	1482024
/WplusH_HToCC_WToQQ_M125_XXX	0.84 *0.0289*0.676	459565
/WplusH_HToGG_WToAll_M125_XXX	0.84 *0.08	300000
/WminusH_HToBB_WToQQ_M125_XXX	0.53 *0.5824*0.676	499994
/WminusHToTauTau_M125_XXX	0.53 *0.06	445200
/WminusH_HToCC_WToLNu_M125_XXX	0.53 *0.0289*0.324	1477656
/WminusH_HToCC_WToQQ_M125_XXX	0.53 *0.0289*0.676	457517
/WminusH_HToGG_WToAll_M125_XXX	0.53 *0.08	300000
/WminusH_HToZZTo2L2X_M125_13TeV_powheg2-minlo-HWJ_JJJ-v1/M	0.53 *0.03	978136
/ZH_HToBB_ZToNuNu_M125_13TeV_powheg_pythia8/run_ext1-v1/M	0.88 *0.5824*0.20	2924580
/ZH_HToBB_ZToLL_M125_XXX	0.88 *0.5824*0.101	1979860
/ZH_HToBB_ZToQQ_M125_XXX	0.88 *0.5824*0.6991	499200
/ZHToTauTau_M125_XXX	0.88 *0.06	571597
/ZH_HToCC_ZToNuNu_M125_XXX	0.88 *0.0289*0.20	1183744
/ZH_HToCC_ZToLL_M125_XXX	0.88 *0.0289*0.101	4885552
/ZH_HToCC_ZToQQ_M125_XXX	0.88 *0.0289*0.6991	499384
/ZH_HToGG_ZToAll_M125_XXX	0.88 *0.08	299739
/ZH_HToZZ_2LFilter_M125_13TeV_powheg2-minlo-HZJ_JJJ-v2/M	0.88 *0.0262*0.10	942259
/ggZH_HToBB_ZToNuNu_M125_XXX	0.12 *0.5824*0.20	250000
/ggZH_HToBB_ZToLL_M125_XXX	0.12 *0.5824*0.101	250000
/ggZH_HToBB_ZToQQ_M125_XXX	0.12 *0.5824*0.6991	499130
/ggZH_HToCC_ZToNuNu_M125_XXX	0.12 *0.0289*0.20	2457116
/ggZH_HToCC_ZToLL_M125_XXX	0.12 *0.0289*0.101	2921029
/ggZH_HToCC_ZToQQ_M125_XXX	0.12 *0.0289*0.6991	478600
/GluGluZH_HToWW_M125_XXX	0.12 *0.21	148525
/ttHToCC_M125_TuneCUETP8M2_XXX	0.51 *0.03	4784344
/ttHToGG_M125_13TeV_powheg_pythia8_v2/run-v1/M	0.51 *0.08	768410
/bbHToBB_M-125_4FS_yb2_13TeV_amcatnlo/run-v1/M	0.49 *0.58	749600
/bbHToGG_M-125_4FS_yb2_13TeV_amcatnlo/run-v1/M	0.49 *0.08	746400
/bbHToWWTo2L2Nu_M-125_4FS_yb2_13TeV_amcatnlo/run-v1/M	0.49 *0.2137 *(0.324 * 0.324)	749998
/bbH_HToZZTo4L_M125_13TeV_JHUGenV702_PPP	0.49 *0.0262*0.1097*0.1097	1000000
/VBFHToBB_M-125_XXX	3.78 *0.58	1000000
/VBFHToTauTau_M125_XXX	3.78 *0.06	1499400
/VBFHToCC_M-125_XXX	3.78 *0.03	4980094
/VBFHToGG_M-125_XXX	3.78 *0.08	1000000
/VBFHToWWTo2L2Nu_M125_XXX	3.78 *0.2137 *(0.324 * 0.324)	486510
/VBFHToWWToLNuQQ_M125_13TeV_powheg_JHUGenV628_PPP	3.78 *0.2137 *(2 * 0.324 * 0.676)	198937

Table 41: Number of events after various cuts from SM Higgs production process for  $\mu + \text{jets}$  channel.

Process	$HLT\_IsoMu24$	$N_{\mu\text{on}} = 1$	$N_{\text{jets}} \geq 4$	$E_T \geq 20\text{GeV}$	$\geq 2 \text{ b-jets}$	KinFit Sel.	$\geq 1 \text{ c-jet}$
GluGluHToBB	872	244	7.39	5.24	0.45	0.238	0.238
GluGluHToTauTau	8.68e+03	5.44e+03	180	167	2.72	0.886	0.886
GluGluHToCC	12.5	4.08	0.192	0.166	0	0	0
GluGluHToGG	763	360	7.73	5.43	0.124	0.124	0.124
GluGluHToWWTo2L2Nu	9.51e+03	4.41e+03	81.2	76.5	1.1	0.244	0.244
GluGluHToWWToLNuQQ	2e+04	1.43e+04	608	517	5.15	2.41	2.41
GluGluHToZZTo2L2Q	1.19e+03	297	18.8	13.9	0.604	0.321	0.321
GluGluHToZZTo4L	176	22.9	0.737	0.589	0.00873	0.000847	0.000847
WplusH_HToBB_WToLNu	1.18e+03	871	82.5	75.8	24.8	7.21	7.08
WplusH_HToBB_WToQQ	10.4	2.78	0.597	0.447	0.0725	0	0
WplusHToTauTau	282	152	17.9	16.6	0.273	0.104	0.104
WplusH_HToCC_WToLNu	59.1	44.6	4.57	4.2	0.129	0.0351	0.0346
WplusH_HToCC_WToQQ	0.225	0.058	0.0153	0.0102	0	0	0
WplusH_HToGG_WToAll	179	123	10.3	9.41	0.0469	0.000641	0.000641
WminusH_HToBB_WToQQ	6.27	1.54	0.29	0.257	0.0312	0.0153	0.0153
WminusHToTauTau	178	96.2	11.8	10.9	0.125	0.0476	0.0476
WminusH_HToCC_WToLNu	34.5	26.2	2.92	2.66	0.0978	0.0291	0.0289
WminusH_HToCC_WToQQ	0.132	0.0447	0.0154	0.0137	0.000994	0	0
WminusH_HToGG_WToAll	109	75.6	6.98	6.31	0.0382	0.00547	0.00547
WminusH_HToZZTo2L2X	122	32.6	5.15	4.12	0.164	0.0756	0.074
ZH_HToBB_ZToNuNu	3.09	0.778	0.0328	0.0315	0.00271	0	0
ZH_HToBB_ZToLL	548	136	16.8	13.8	4.33	1.58	1.52
ZH_HToBB_ZToQQ	13.5	3.63	0.706	0.653	0.167	0.0566	0.0566
ZHToTauTau	232	115	17.2	15.7	1.16	0.449	0.445
ZH_HToCC_ZToNuNu	0.053	0.0162	0.000343	0.000343	0	0	0
ZH_HToCC_ZToLL	31.4	7.96	1.07	0.876	0.0338	0.0113	0.0111
ZH_HToCC_ZToQQ	0.333	0.0846	0.0204	0.0188	0.00392	0.00131	0.00131
ZH_HToGG_ZToAll	89.5	23.9	2.99	2.51	0.081	0.0272	0.0272
ZH_HToZZ_2L	17.3	4.24	0.698	0.56	0.0509	0.0231	0.0222
ggZH_HToBB_ZToNuNu	0.533	0.115	0.0106	0.0106	0	0	0
ggZH_HToBB_ZToLL	87.8	16	5.25	4.56	1.59	0.338	0.334
ggZH_HToBB_ZToQQ	2.26	0.571	0.266	0.21	0.0594	0.0257	0.0252
ggZH_HToCC_ZToNuNu	0.0155	0.00406	0.000565	0.000534	0	0	0
ggZH_HToCC_ZToLL	0	0	0	0	0	0	0
ggZH_HToCC_ZToQQ	0.0466	0.0119	0.00376	0.00343	0.00113	9.75e-05	9.75e-05
GluGluZH_HToWW	193	59.4	12.6	11.7	0.192	0.0281	0.0281
ttHToCC	71.5	42.2	38.1	35.6	14	5.68	5.62
ttHToGG	209	118	104	97	29.2	11.5	10.8
bbHToBB	9.85	2.98	0.484	0.422	0.173	0.0748	0.0748
bbHToGG	7.95	3.8	0.563	0.423	0.0421	0.00928	0.00928
bbHToWWTo2L2Nu	98.9	45.6	4.23	3.9	0.626	0.186	0.183
bbH_HToZZTo4L	0	0	0	0	0	0	0
VBFHToBB	75	20.4	1.28	1.02	0.0809	0.0809	0.0809
VBFHToTauTau	849	551	24.9	23.1	0.352	0.0719	0.0719
VBFHToCC	1.47	0.429	0.0306	0.0279	0.00139	0.000541	0.000541
VBFHToGG	61.5	26.3	1.04	0.74	0.0113	0	0
VBFHToWWTo2L2Nu	828	359	9.41	8.84	0.161	0.0477	0.0477
VBFHToWWToLNuQQ	1.75e+03	1.25e+03	95.2	80.3	1.08	0.428	0.428
Total Higgs Bkg.	4.86e+04	2.93e+04	1.38e+03	1.22e+03	89.3	32.4	31.4

Table 42: Number of events after various cuts from SM Higgs production process for e + jets channel.

Process	<i>HLT_Ele27</i>	$N_{ele} = 1$	$N_{jets} \geq 4$	$\cancel{E}_T \geq 20\text{GeV}$	$\geq 2\text{-bjets}$	KinFit Sel.	$\geq 1\text{ c-jet}$
GluGluHToBB	273	74.4	4.51	4.13	0.852	0.235	0.235
GluGluHToTauTau	5.78e+03	3.49e+03	143	134	1.87	0.731	0.731
GluGluHToCC	7.85	1.99	0.196	0.153	0	0	0
GluGluHToGG	8.67e+03	2.6e+03	89.2	64.6	0.558	0	0
GluGluHToWWTo2L2Nu	6.15e+03	2.9e+03	60.8	57.6	0.916	0.305	0.305
GluGluHToWWToLNuQQ	1.26e+04	9.15e+03	421	354	8.62	3.56	3.56
GluGluHToZZTo2L2Q	864	254	17.3	12.7	0.502	0.187	0.187
GluGluHToZZTo4L	132	21.2	0.857	0.659	0.00983	0.00229	0.00229
WplusH_HToBB_WToLNu	904	719	68.6	63.1	20.2	5.86	5.79
WplusH_HToBB_WToQQ	4.47	0.977	0.247	0.175	0.0261	0.000723	0.000723
WplusHToTauTau	214	117	13.8	12.8	0.176	0.0599	0.0599
WplusH_HToCC_WToLNu	45	36.3	3.82	3.5	0.115	0.0286	0.0281
WplusH_HToCC_WToQQ	0.181	0.0359	0.0154	0.0131	0	0	0
WplusH_HToGG_WToAll	292	139	15.3	13	0.141	0.0366	0.0366
WminusH_HToBB_WToQQ	2.95	0.774	0.114	0.0842	0	0	0
WminusHToTauTau	133	73.4	8.89	8.12	0.0959	0.0472	0.0472
WminusH_HToCC_WToLNu	26.7	21.7	2.47	2.25	0.0803	0.0223	0.0221
WminusH_HToCC_WToQQ	0.1	0.018	0.0053	0.00384	0	0	0
WminusH_HToGG_WToAll	179	86	9.85	8.1	0.0701	0.0056	0.0056
WminusH_HToZZTo2L2X	92.4	29.4	4.88	3.9	0.116	0.0537	0.0523
ZH_HToBB_ZToNuNu	0.997	0.273	0.0224	0.0211	0.00136	0	0
ZH_HToBB_ZToLL	466	155	24.2	18.9	5.88	2.08	2.02
ZH_HToBB_ZToQQ	5.54	1.32	0.474	0.423	0.0652	0.00653	0.00653
ZHToTauTau	177	88.9	13.2	12.1	0.771	0.298	0.284
ZH_HToCC_ZToNuNu	0.0326	0.0089	0.00134	0.00134	0	0	0
ZH_HToCC_ZToLL	26.7	8.91	1.5	1.15	0.0427	0.0139	0.0136
ZH_HToCC_ZToQQ	0.253	0.058	0.0236	0.0213	0.00423	0.00136	0.00136
ZH_HToGG_ZToAll	239	72.3	11	8.37	0.4	0.102	0.102
ZH_HToZZ_2L	13.7	4.3	0.789	0.617	0.0489	0.0204	0.0196
ggZH_HToBB_ZToNuNu	0.162	0.0371	0.00396	0.00396	0.00332	0	0
ggZH_HToBB_ZToLL	79.6	22.1	8.33	6.85	2.22	0.437	0.429
ggZH_HToBB_ZToQQ	0.979	0.279	0.155	0.129	0.0477	0.011	0.011
ggZH_HToCC_ZToNuNu	0.00962	0.00195	0.000602	0.000587	7.71e-05	1.69e-05	1.69e-05
ggZH_HToCC_ZToLL	0	0	0	0	0	0	0
ggZH_HToCC_ZToQQ	0.0331	0.00724	0.00469	0.00408	0.000675	1.46e-05	1.46e-05
GluGluZH_HToWW	158	54.4	13.4	11.7	0.231	0.0317	0.0317
ttHToCC	54.5	37.7	33.5	31.3	11.8	4.62	4.58
ttHToGG	235	123	108	98.9	28.5	10.7	10
bbHToBB	3.7	0.962	0.22	0.192	0.0818	0.0251	0.0251
bbHToGG	84.4	25.9	4.14	3.04	0.35	0.0839	0.082
bbHToWWTo2L2Nu	63.6	30.4	3.03	2.77	0.428	0.122	0.122
bbH_HToZZTo4L	0	0	0	0	0	0	0
VBFHToBB	34.7	8.2	0.965	0.597	0.177	0	0
VBFHToTauTau	622	401	18.8	17.6	0.302	0.0693	0.0693
VBFHToCC	1.43	0.313	0.049	0.0429	0.00152	0.000784	0.000784
VBFHToGG	746	243	12.6	9.04	0.132	0.0107	0.0107
VBFHToWWTo2L2Nu	585	262	6.9	6.45	0.101	0.0195	0.0195
VBFHToWWToLNuQQ	1.16e+03	900	73.7	63.7	0.786	0.192	0.192
Total Higgs Bkg.	4.11e+04	2.22e+04	1.2e+03	1.04e+03	86.8	30	29.1

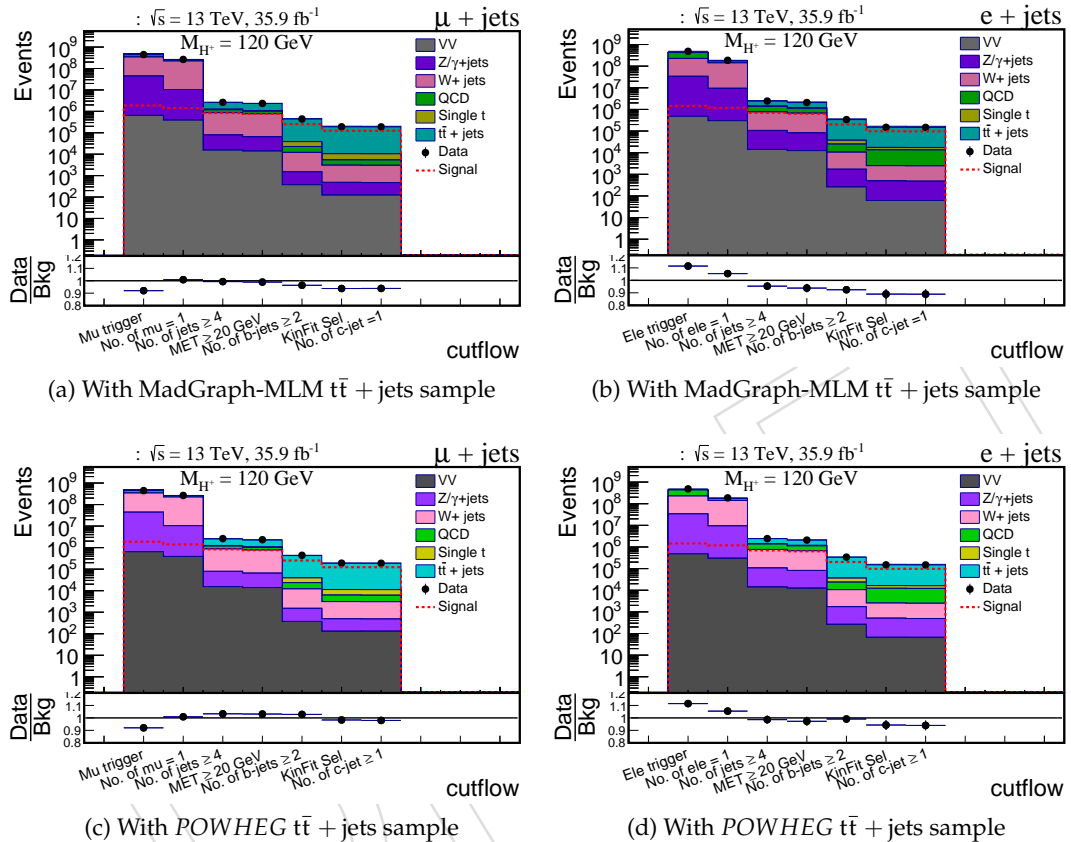


Figure 57: Number of events for MC and data samples after various selection cuts for muon + jets and e + jets channel. Number of events differ only after  $N_{jets} \geq 4$  cut as can be seen from Figure 57a, 57c for  $\mu$  + jets channel and from Figure 57b, 57d for electron + jets channel. From Figure 57c, 57d, it can be seen that the data, MC has better agreement with POWHEG  $t\bar{t}$  + jets sample. Except for  $t\bar{t}$  + jets, all the other MC samples are same in Figure 57a, 57c for  $\mu$  + jets channel and in Figure 57b, 57d for e + jets channel. The muon(electron) enriched MC QCD samples as shown in Table 2 are used for muon(electron) + jets channels.

Mass (GeV)	Inclusive category a (b) [c]	b-jet $p_T$ categories a (b) [c]	Exclusive c-tag categories
			a (b) [c]
90	2.27 (2.78) [2.77]	1.52 (2.70) [2.57]	1.61 (1.94) [1.98]
100	0.93 (1.13) [1.13]	0.75 (1.25) [1.20]	0.81 (0.97) [0.99]
120	0.56 (0.68) [0.68]	0.48 (0.83) [0.79]	0.53 (0.64) [0.65]
140	0.49 (0.57) [0.57]	0.40 (0.64) [0.63]	0.45 (0.54) [0.55]
150	0.47 (0.54) [0.54]	0.39 (0.56) [0.63]	0.43 (0.52) [0.53]
155	0.45 (0.52) [0.53]	0.43 (0.62) [0.67]	0.42 (0.49) [0.52]
160	0.50 (0.58) [0.61]	0.51 (0.67) [0.77]	0.50 (0.56) [0.62]

Table 43: Limits from b-jet  $p_T$  categories for e + jets channel using different methods. Where the bin-by-bin uncertainties were considered by different methods, a: manually on signal and three backgrounds (ttbar, stop, wjet), (b): manually on signal and All backgrounds (ttbar, stop, wjet, qcd, dyjet, vv), [c]: by autoMCStats on signal and All backgrounds (ttbar, stop, wjet, qcd, dyjet, vv)

## C Event Categorization in Bins of b-jet pT

To improve the exclusion limit on the  $\mathcal{B}(t \rightarrow H^+ b)$ , even without invoking the charm tagging, there is another variable that can be used to discriminate signal from backgrounds thus improve the exclusion limit. The signal mass range is from 80 to 160 GeV in this analysis. The b-jet produced, in association with W Boson or charged Higgs Boson in one of the top decay will have different  $p_T$  distribution for a different mass of charged Higgs. We denote the  $p_T$  of bjet (where associated  $W^+$  decays hadronically) as  $p_{T_{bjet}}^{Had}$ . The  $m_{jj}$  distribution is obtained in different  $p_{T_{bjet}}^{Had}$  bins. To have uniform statistics in each bin of  $p_{T_{bjet}}^{Had}$ , following bin-ranges are considered: 25 – 42, 42 – 57, 57 – 74, 74 – 99, 99 – 500 GeV. In each of these bins there are around 20% of total events of  $p_{T_{bjet}}^{Had}$  from  $t\bar{t} + \text{jets}$  process for  $\mu + \text{jets}$  channel. Following the 8 TeV analysis, in the previous version of the AN (AN2018\_061\_v4), one nuisance parameter was considered in each bin of  $m_{jj}$  distribution from SM ttbar + jets, Single top, W + jets channels. Since QCD, DY + jets and VV backgrounds are small, hence we did not consider bin-by-bin uncertainty in these backgrounds. In that case, the events from b-jet  $p_T$  categorization were improving the limits. However, when we used autoMCStats (which considers bin-by-bin uncertainty from the sum of all backgrounds) the b-jet  $p_T$  categorization does not improve the limits. The limits for electron channel (similar results hold for muon channel also) where bin-by-bin uncertainty is considered using different methods are shown in Table 43.

## D Data, MC Comparison in Low MET Region

The  $E_T^{\text{miss}}$  cut applied in the signal region is  $E_T^{\text{miss}} > 20$  GeV. Therefore the region  $E_T^{\text{miss}} < 20$  GeV can be taken as a control region. In the control region, the data, and MC comparison after kinematic fit selection are shown in Figures 58, 59, 60, 61, 62, 63. In these plots, the MC QCD events have been used which are concentrated in few bins only. Overall, there is a good agreement between data and MC in the control region.

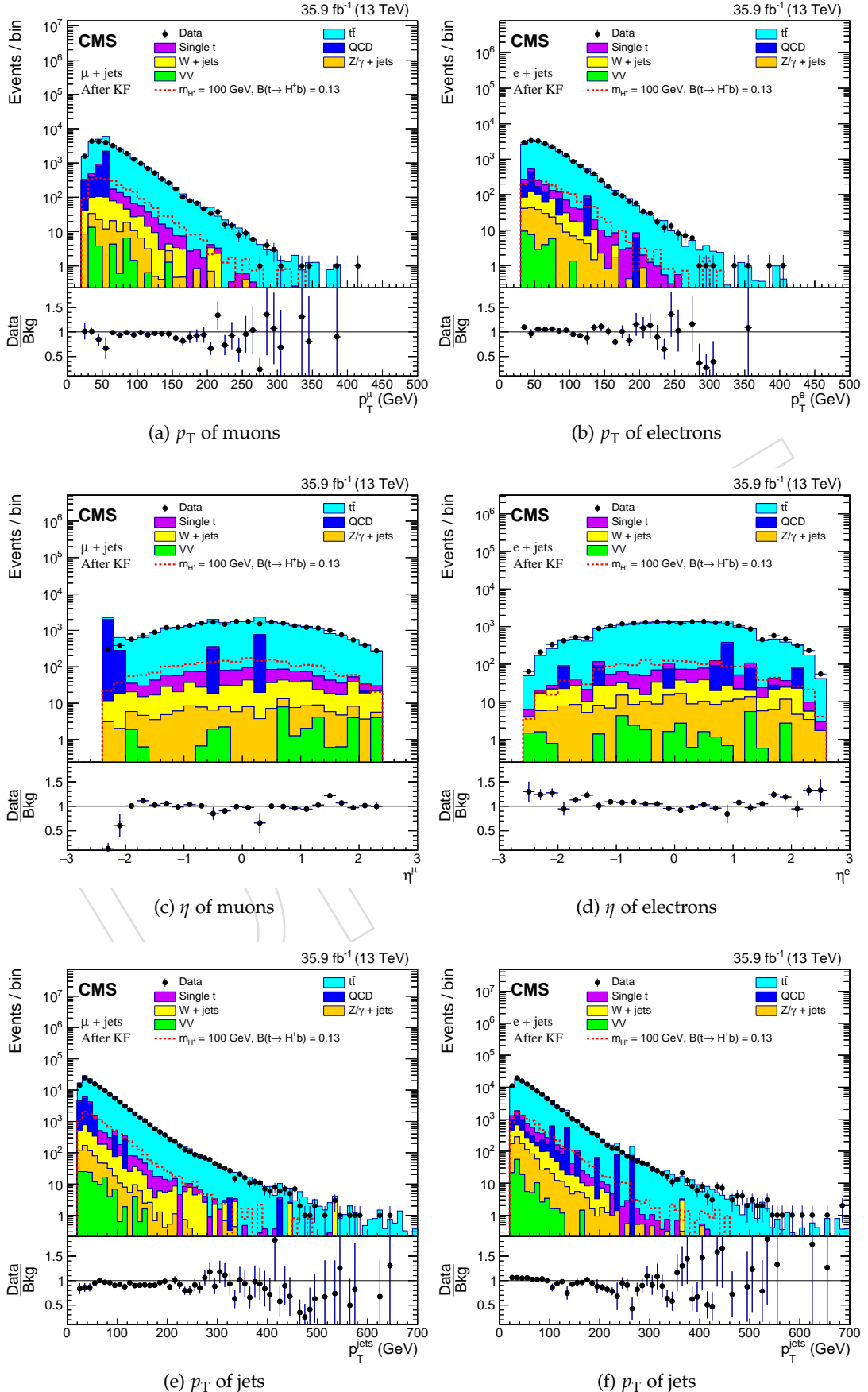


Figure 58: Control plots in  $E_T^{\text{miss}} < 20$  GeV region, after kinematic fit selection as described in Sec. 10, for muons + jets and e + jets channel.

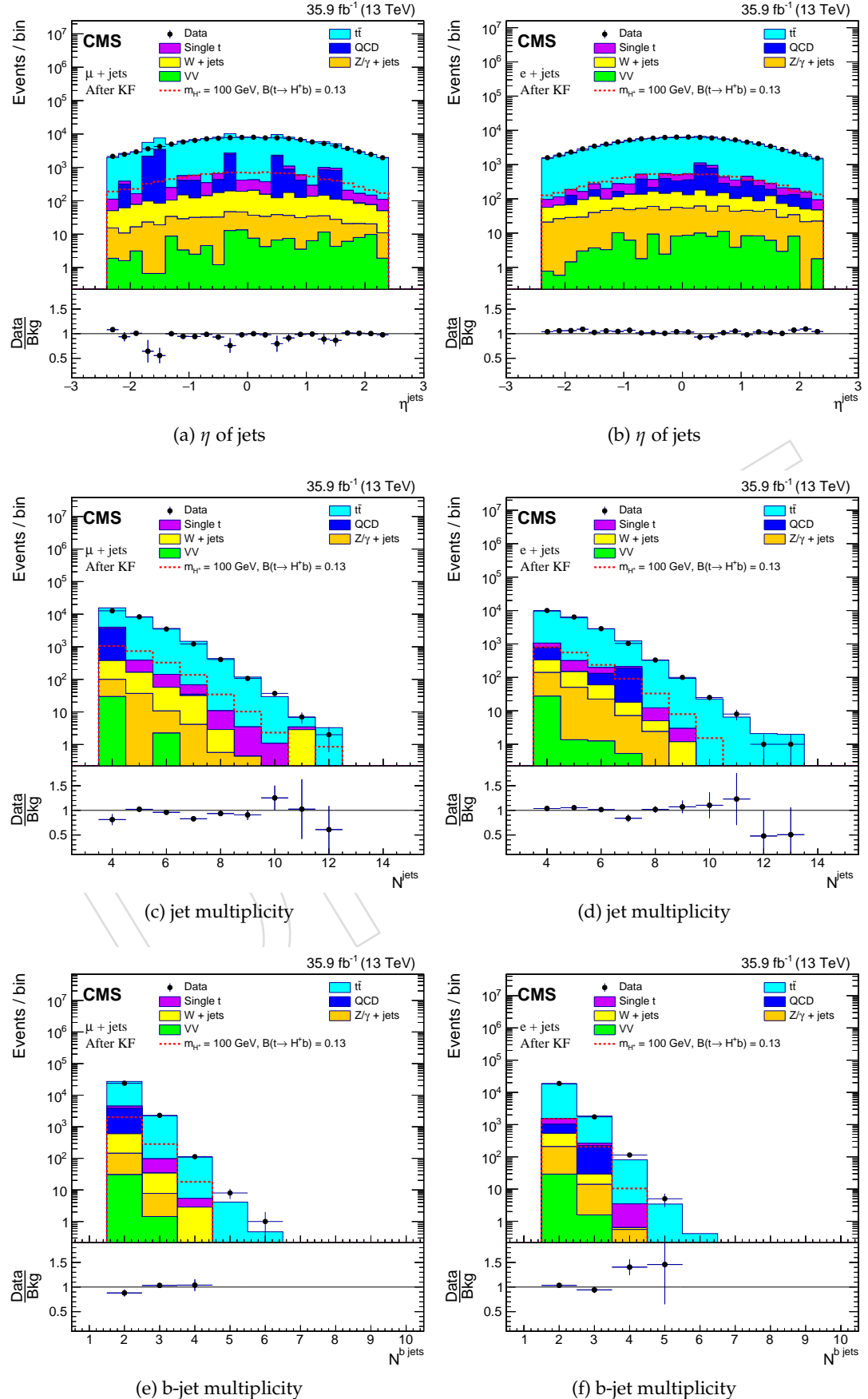


Figure 59: Control plots in  $E_T^{\text{miss}} < 20 \text{ GeV}$  region, after kinematic fit selection as described in Sec. 10, for muons + jets and  $e + \text{jets}$  channel.

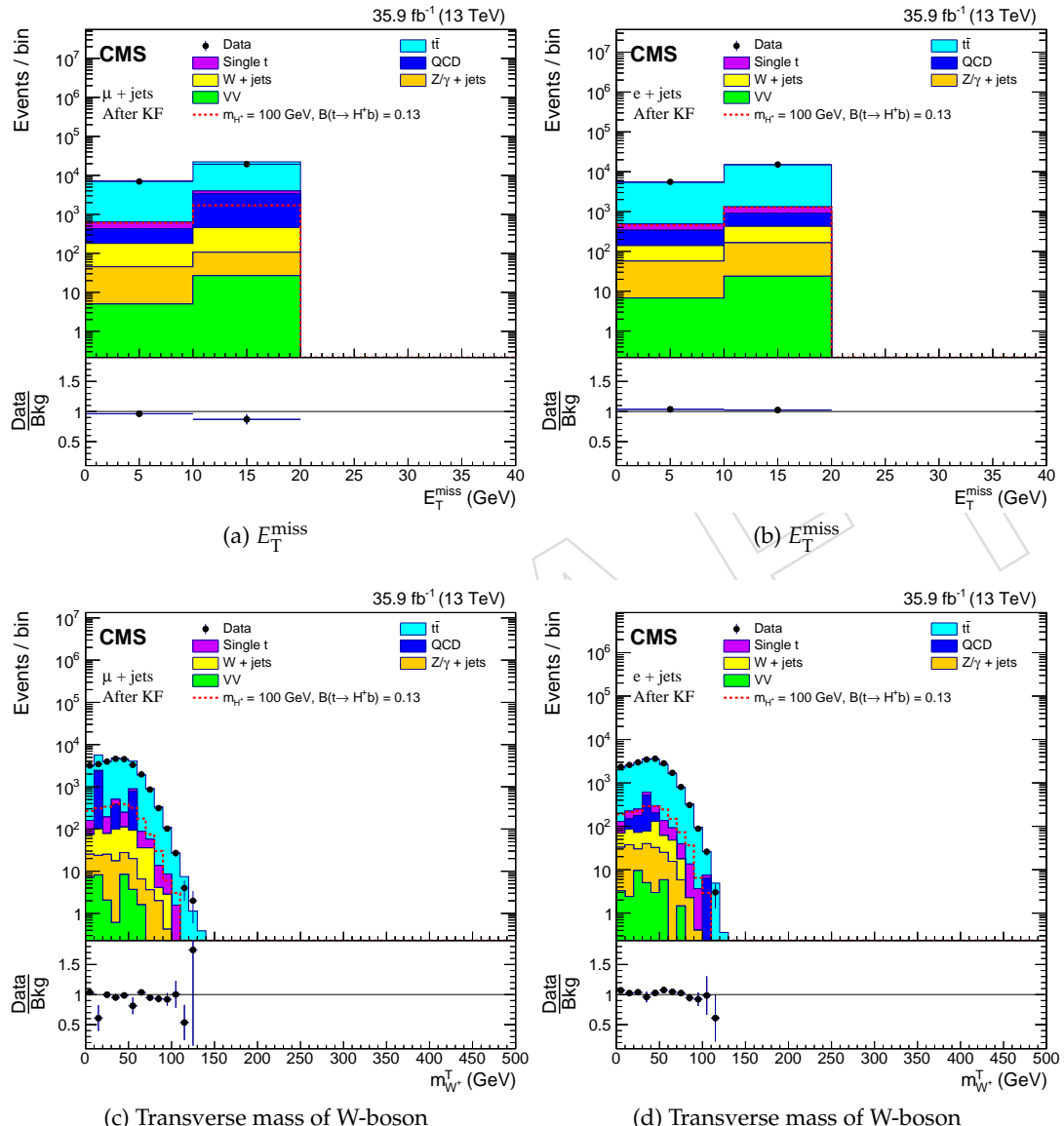


Figure 60: Control plots in  $E_T^{\text{miss}} < 20$  GeV region, after kinematic fit selection as described in Sec. 10, for muons + jets and e + jets channel.

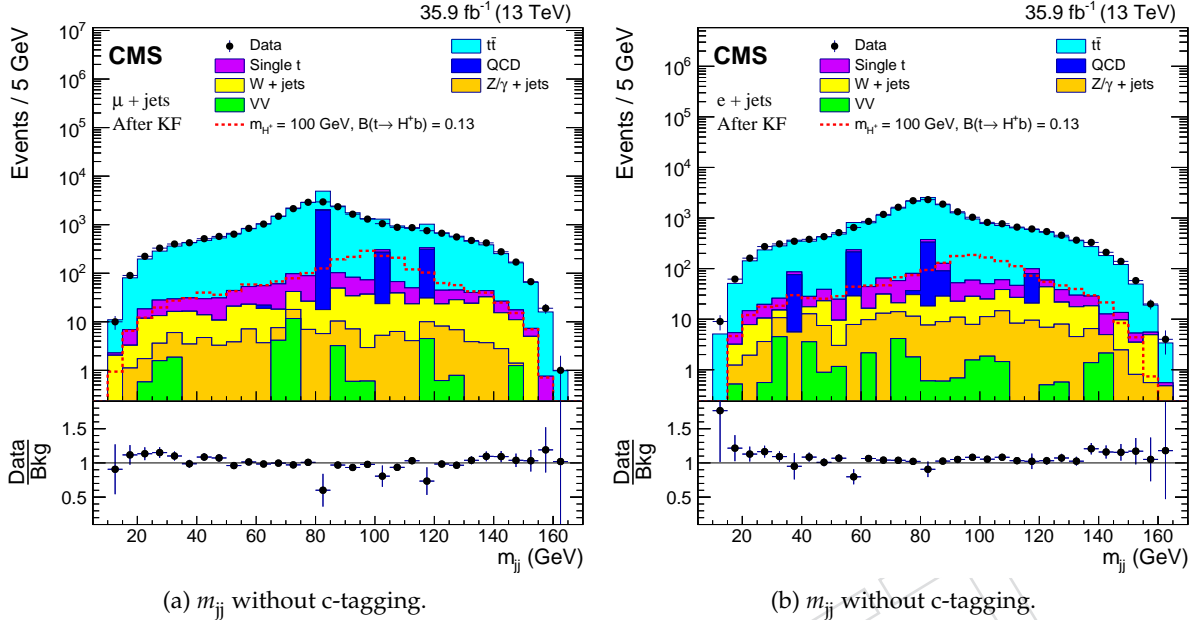


Figure 61: Control plots in  $E_T^{\text{miss}} < 20$  GeV region: distribution of  $m_{jj}$  from inclusive event category without charm-tagging for  $\mu + \text{jets}$  and  $e + \text{jets}$  channel.

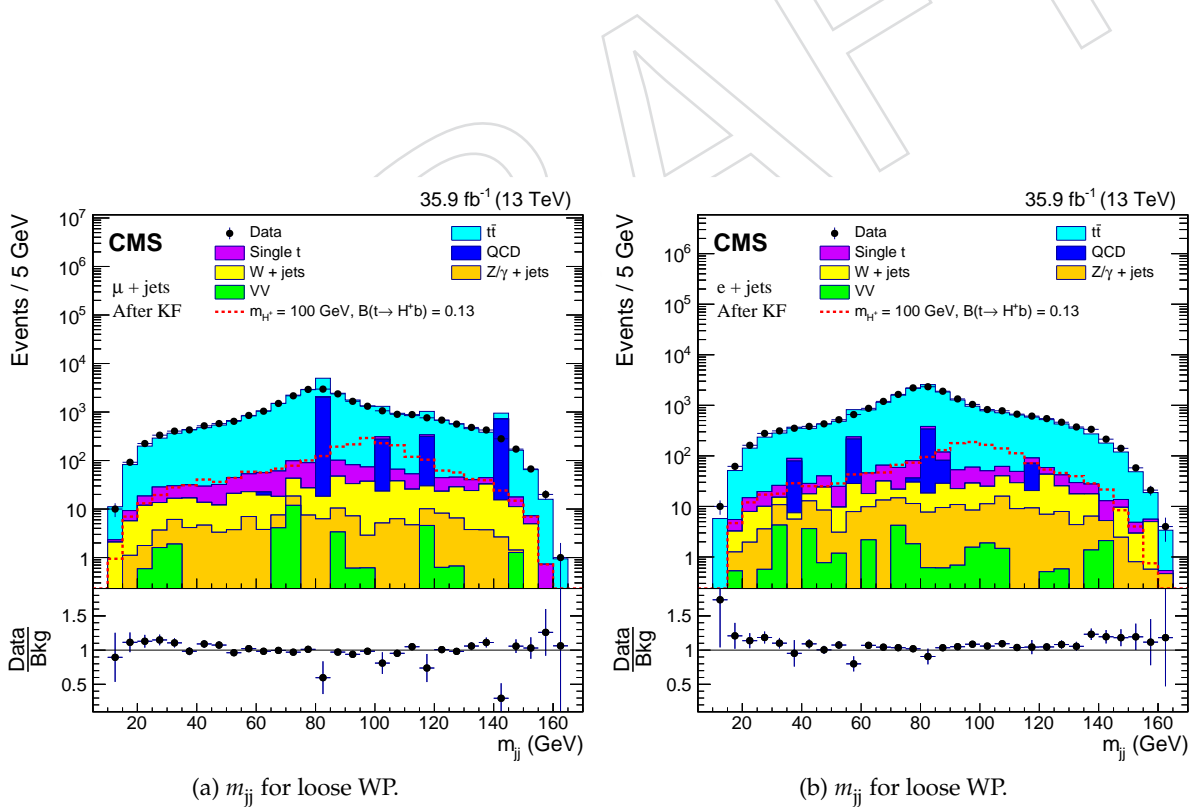


Figure 62: Control plots in  $E_T^{\text{miss}} < 20$  GeV region: distribution of  $m_{jj}$  for loose inclusive charm working point for  $\mu + \text{jets}$  and  $e + \text{jets}$  channel.

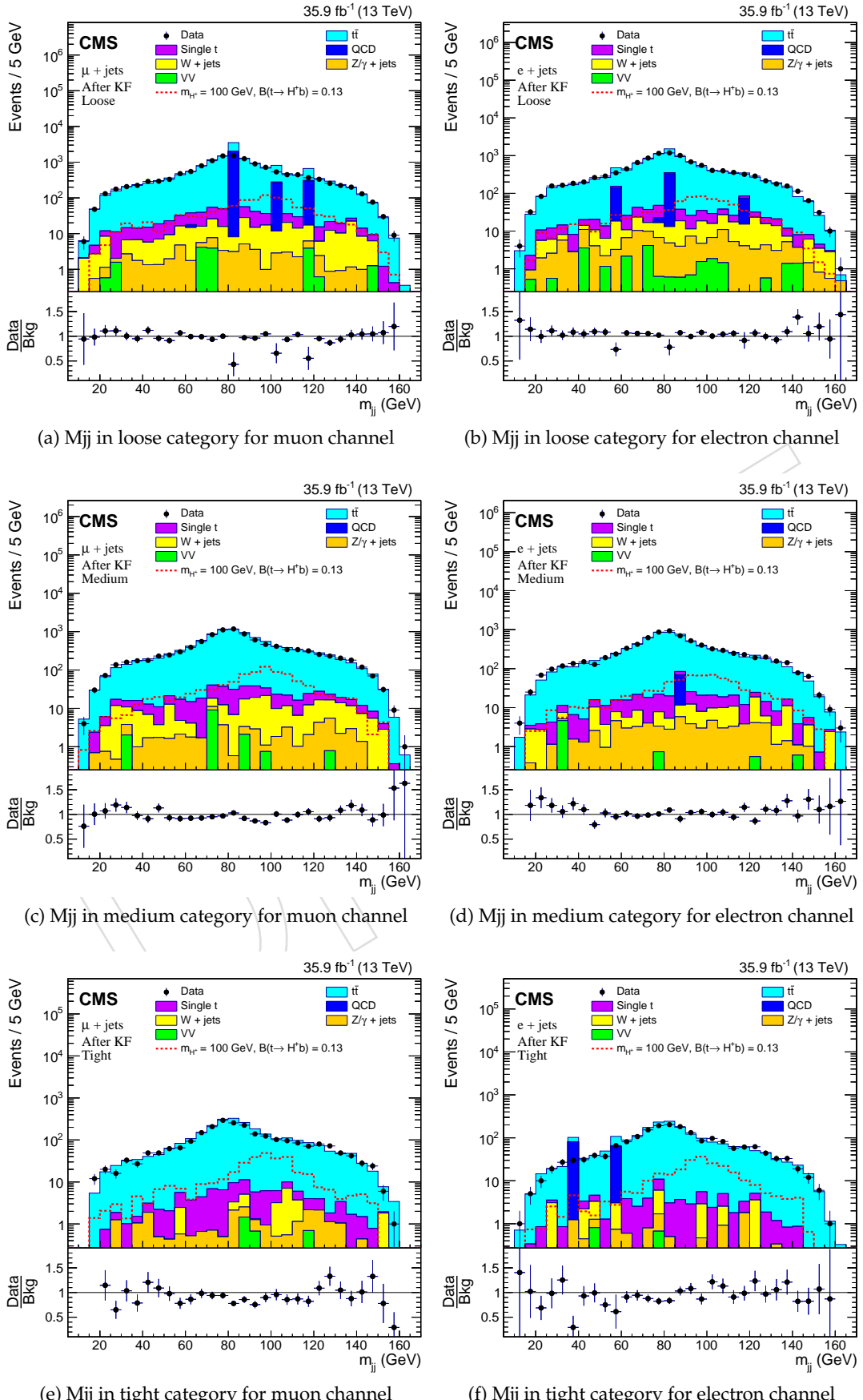


Figure 63: Control plots in  $E_T^{\text{miss}} < 20 \text{ GeV}$  region: distribution of  $m_{jj}$  from exclusive charm categories as described in Sec. 15.3 for  $\mu + \text{jets}$  and  $e + \text{jets}$  channel. The signal significance is different across different exclusive categories.

## 1412 E Effect of Systematics on dijet Distributions

1413 All the systematic uncertainties described above may affect the  $m_{jj}$  distribution differently. For  
 1414 example, some of the uncertainties may have a different effect in each bin and the others may  
 1415 have the same effect in every bin. Therefore, it is very important to compare the base  $m_{jj}$  dis-  
 1416 tributions with those obtained considering systematic uncertainties. The scale factors for the  
 1417 given systematic are varied up/down and the corresponding  $m_{jj}$  distributions are obtained.  
 1418 We have studied the effect of following systematics: JES, JER, t quark  $p_T$  reweighting ( $topPt$ ),  
 1419 b and c tagging ( $bcTag1$ ,  $bcTag2$ , and  $bcTag3$ ), t quark mass ( $topMass_tt$ ), factorisa-  
 1420 tion and renormalization scale ( $scaleRF_tt$ ), and parton shower matching ( $hDamp_tt$ ). The  
 1421  $m_{jj}$  distributions for these systematics are shown in Figures 64, 65 for charged Higgs signal  
 1422 ( $m_{H^+} = 120$  GeV) and in Figures 66, 67 for  $t\bar{t}$  + jets process. From these figures one can see that  
 1423 some of the systematics (JES, b and c tagging) have a significant effect, others have a marginal  
 1424 effect.

## 1425 F Impact of Uncertainties: Multi-dimensional Fit

1426 All the systematics and statistical uncertainties (nuisance parameters) are included in the like-  
 1427 lihood function along with the parameter of interest (POI). The POI is the  $\mathcal{B}(t \rightarrow H^+b)$  of this  
 1428 analysis. For the sake of convenience, we will denote  $\mathcal{B}(t \rightarrow H^+b)$  as BR in this section. The  
 1429 impact of nuisance parameters (NP) on the BR indicates which NP plays dominant role in the  
 1430 limit computation. To see the impact, each NP is individually varied by  $\pm 1\sigma$  of its pre-fit value  
 1431 and the corresponding change in the BR is computed. The distribution of post-fit pulls and  
 1432 impacts of nuisance parameters is shown in Figures 69, 70, 71, and 72, using  $m_{jj}$  from exclusive  
 1433 event categories based on c tagging for  $m_{H^+} = 100$  GeV from 1 + jets channel. In these figures,  
 1434  $\theta_0$  is the pre-fit value,  $\hat{\theta}$  is the post-fit value, and  $\Delta\theta = 1$  is the difference in the uncertainties  
 1435 from pre and post-fit values. The  $\widehat{BR}$  is the best-fit value of BR. The  $\Delta\widehat{BR}$  is the change in the  
 1436 value of  $\widehat{BR}$  when the pull of a nuisance parameter is varied  $\pm 1\sigma$  of its pre-fit value.

1437 Larger the value of  $\Delta\widehat{BR}$ , larger is the correlation between BR and the corresponding nuisance  
 1438 parameter. Also, if the change in BR is positive (negative) when an NP is varied  $+1\sigma$  ( $-1\sigma$ ) of  
 1439 its pre-fit value then they are positively correlated. However, if the change in BR is opposite  
 1440 to the variation in NP then they are said to be anti-correlated. One of the most important  
 1441 feature of the plots shown in Figures 69, 70, 71, and 72 is the ordering (or indexing) of the NPs.  
 1442 The nuisance parameter having highest impact on the BR is placed at the top (index is 1) of  
 1443 the plot. Those placed at bottom have relatively small impact on BR thereby don't affect the  
 1444 limit. One another important feature in these plots is the  $\pm 1\sigma$  values of the NPs. If an NP has  
 1445 smaller  $\pm 1\sigma$  value then it is said to be constrained. In such case the constraint on that NP has  
 1446 to be relieved by scrutinizing its pre-fit values. A large constraint on the NPs leads to larger  
 1447 mismatch between the expected and observed limits.

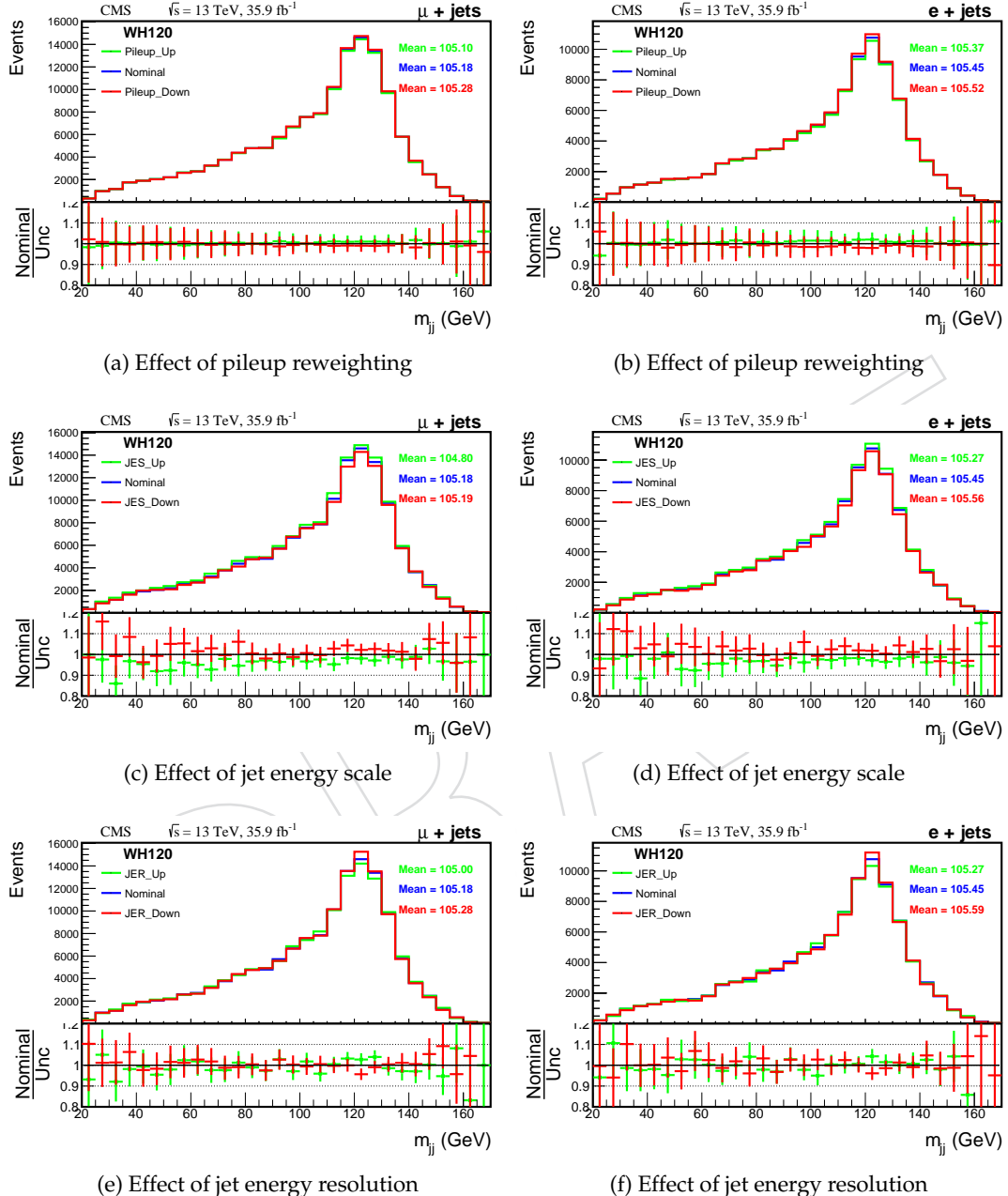


Figure 64: Effect of pileup, jet energy scale, and jet energy resolution systematics on the  $m_{jj}$  distribution for the charged Higgs signal ( $m_{H^+} = 120$  GeV) for the  $\mu + \text{jets}$  and  $e + \text{jets}$  channels, after  $\geq 1$  c jet selection.

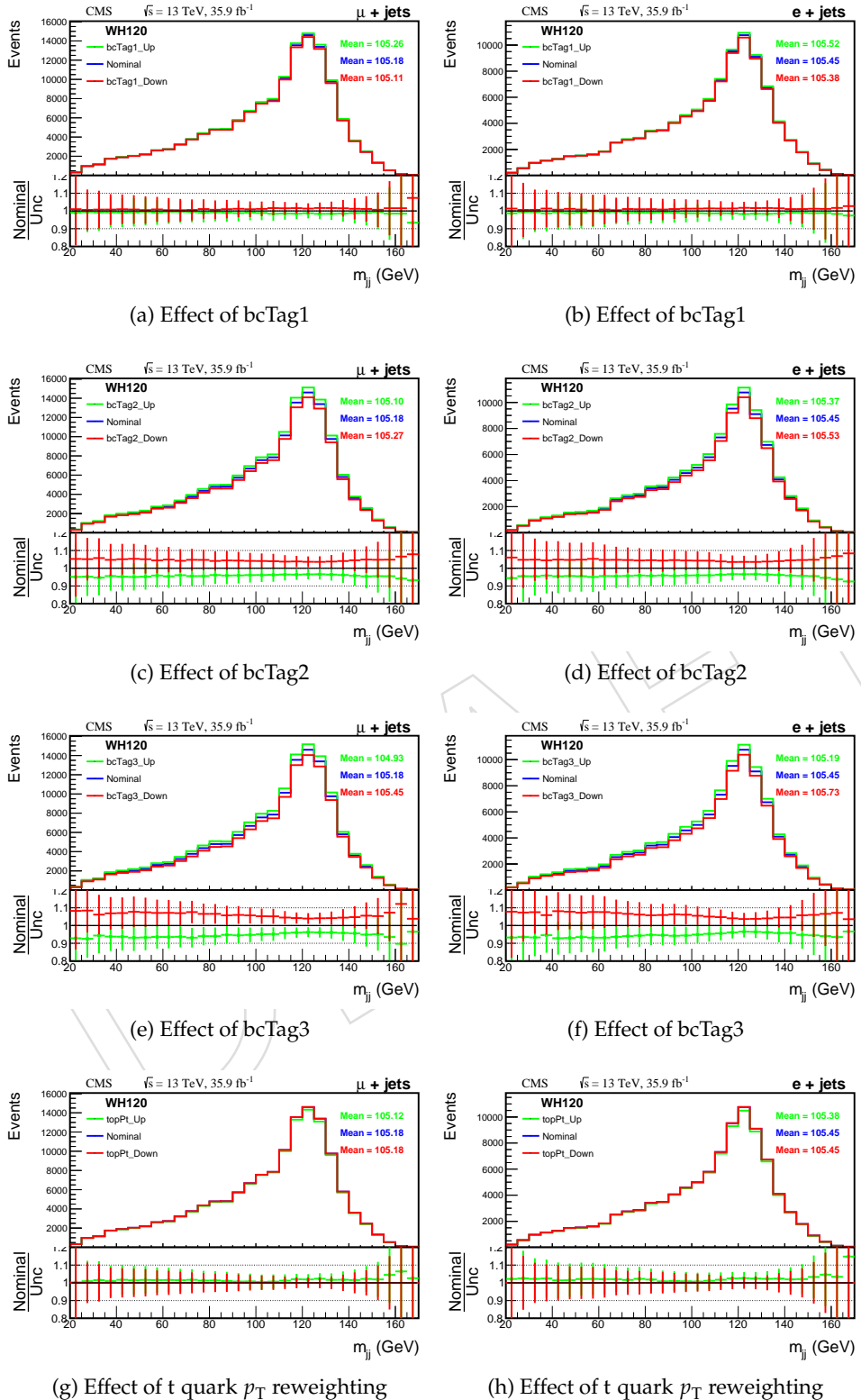


Figure 65: Effect of b/c tagging and t quark  $p_T$  systematics on the  $m_{jj}$  distribution from charged Higgs signal ( $m_{H^+} = 120$  GeV) for  $\mu + \text{jets}$  and  $e + \text{jets}$  channel, after  $\geq 1$  c jet selection.

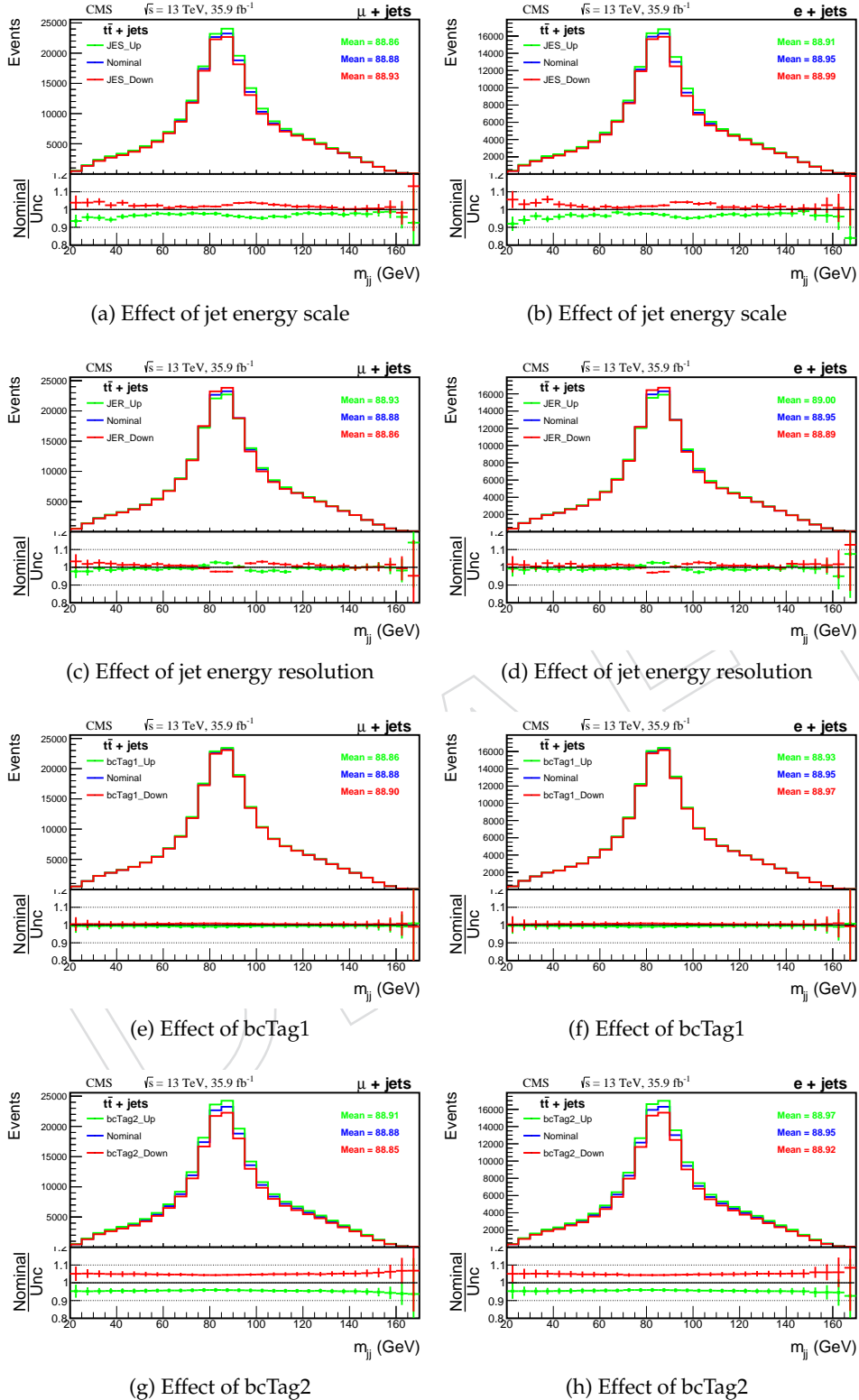


Figure 66: Effect of jet energy scale, jet energy resolution, and b / c tagging systematics on the  $m_{jj}$  distribution from  $t\bar{t} + \text{jets}$  background for  $\mu + \text{jets}$  and  $e + \text{jets}$  channel, after  $\geq 1$  c jet selection.

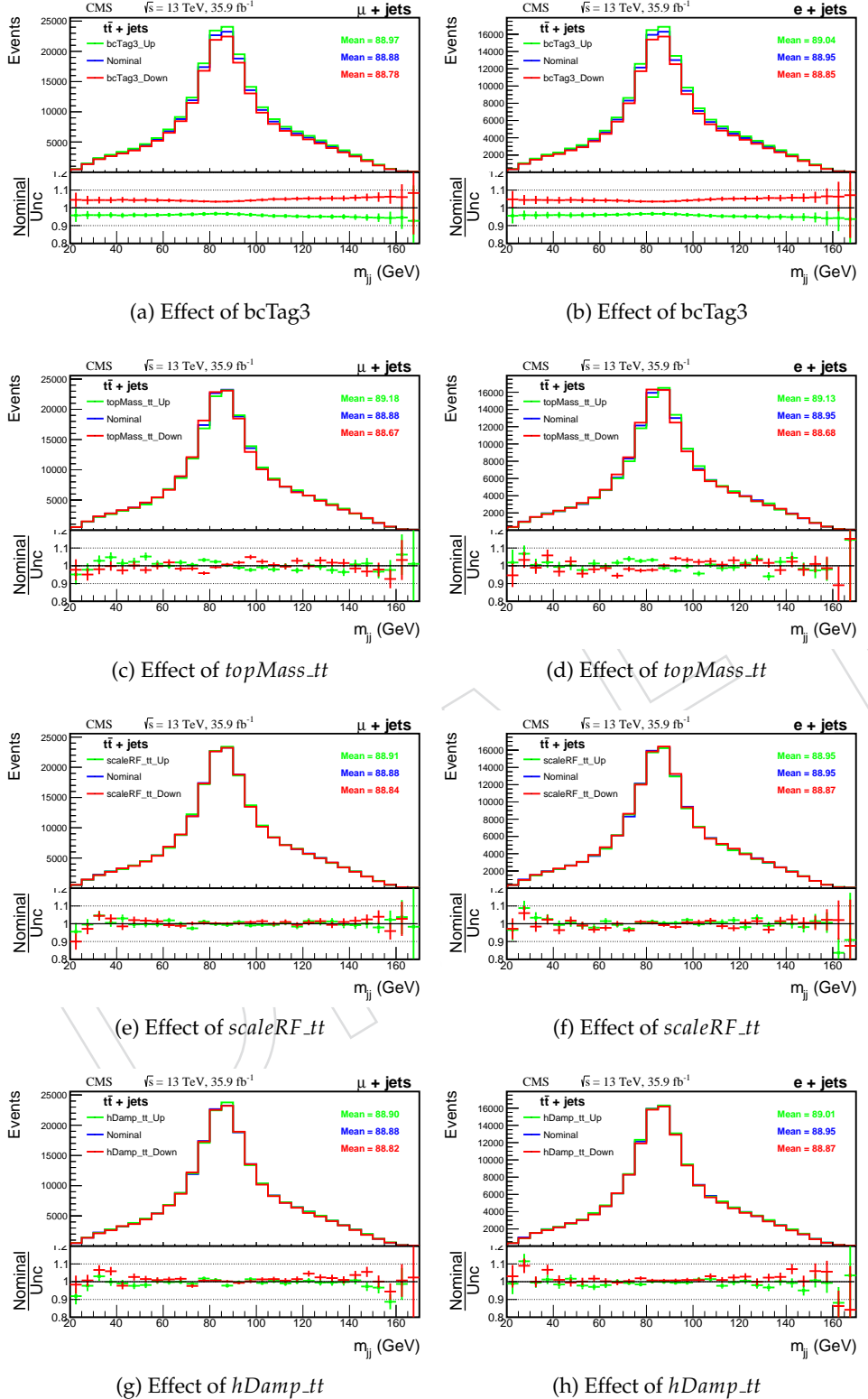


Figure 67: Effect of c tagging, t quark mass, renormalization and factorisation scale, and parton shower matching systematics on the  $m_{jj}$  distribution from  $t\bar{t} + \text{jets}$  background for  $\mu + \text{jets}$  and  $e + \text{jets}$  channel, after  $\geq 1$  c jet selection.

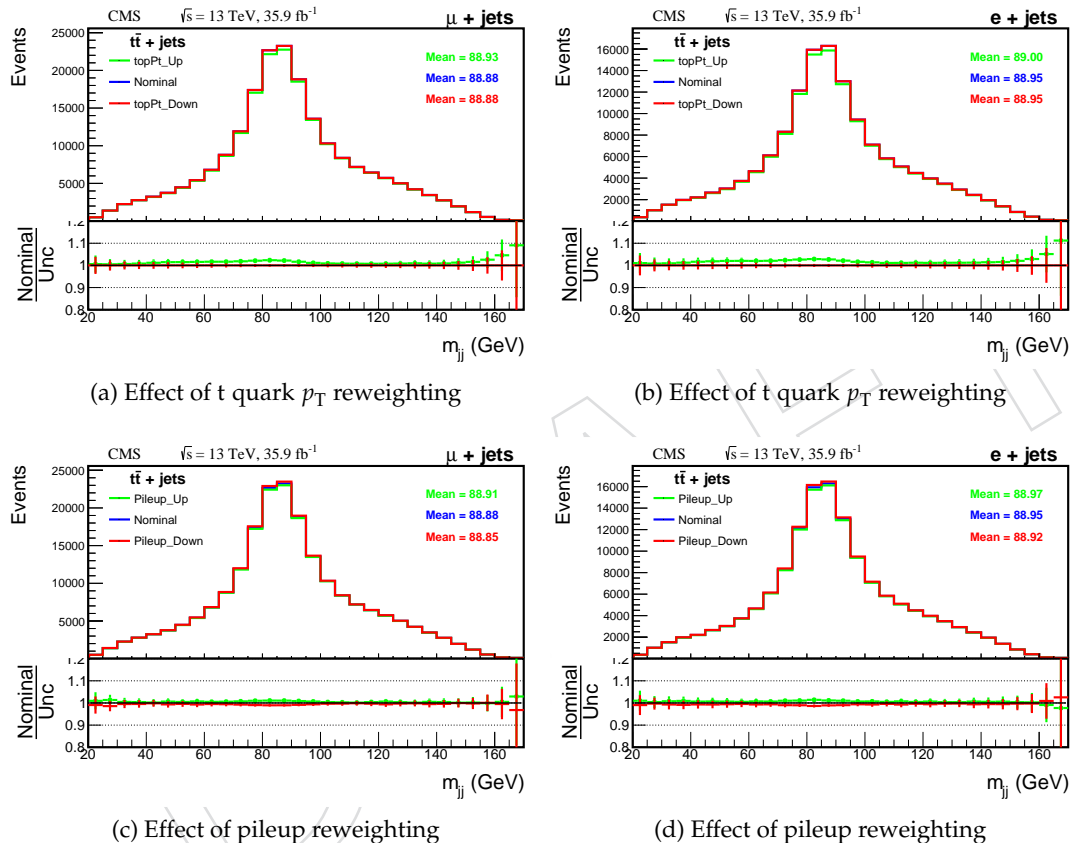


Figure 68: Effect of t quark  $p_T$  and pileup reweighting systematics on the  $m_{jj}$  distribution from  $t\bar{t} + \text{jets}$  background for  $\mu + \text{jets}$  and  $e + \text{jets}$  channel, after  $\geq 1$  c jet selection.

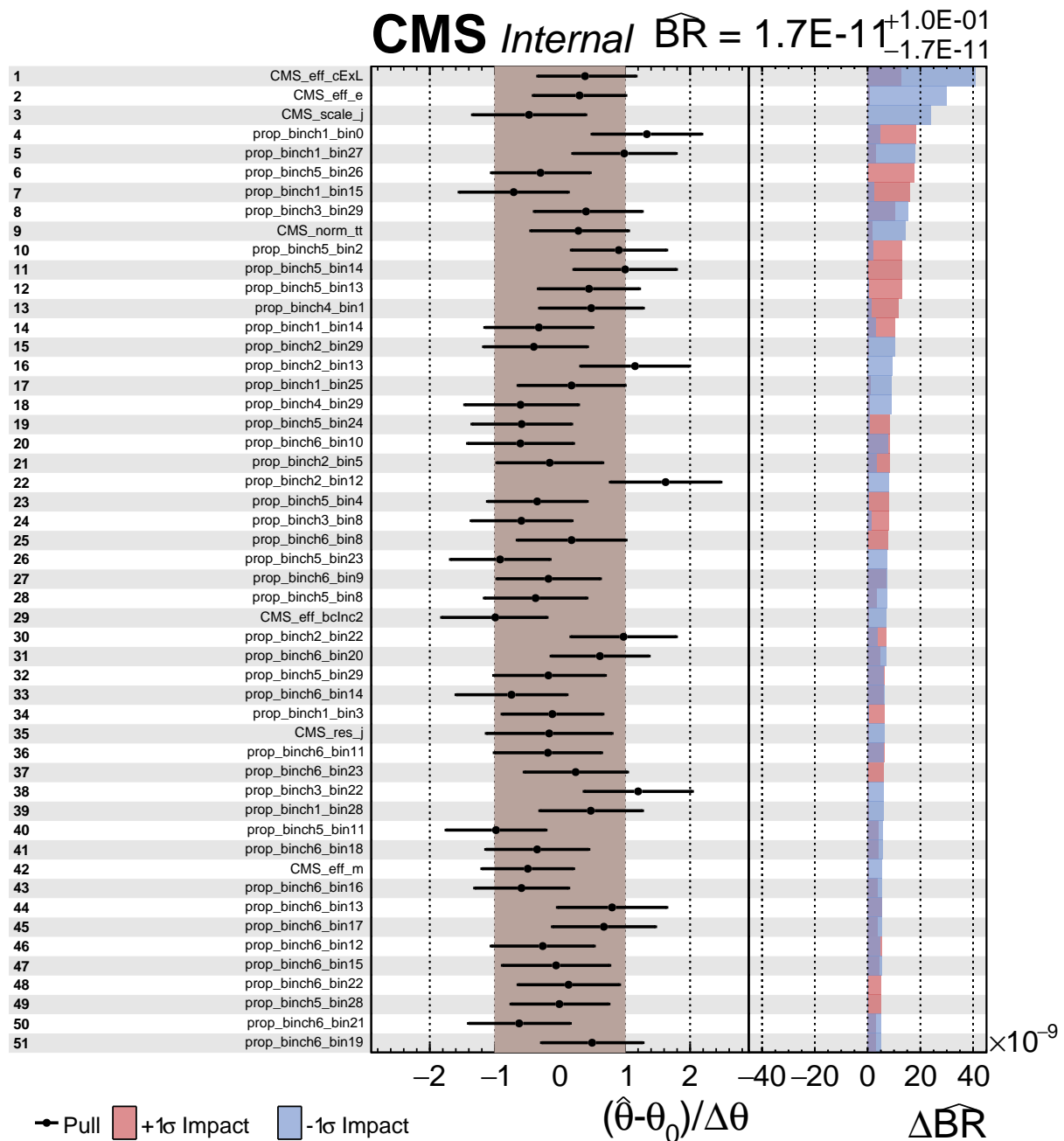


Figure 69: Distribution of post-fit pulls and impacts of nuisance parameters from exclusive event categories based on charm-tagging for  $m_{H^+} = 100$  GeV from 1 + jets channel. Contd ...

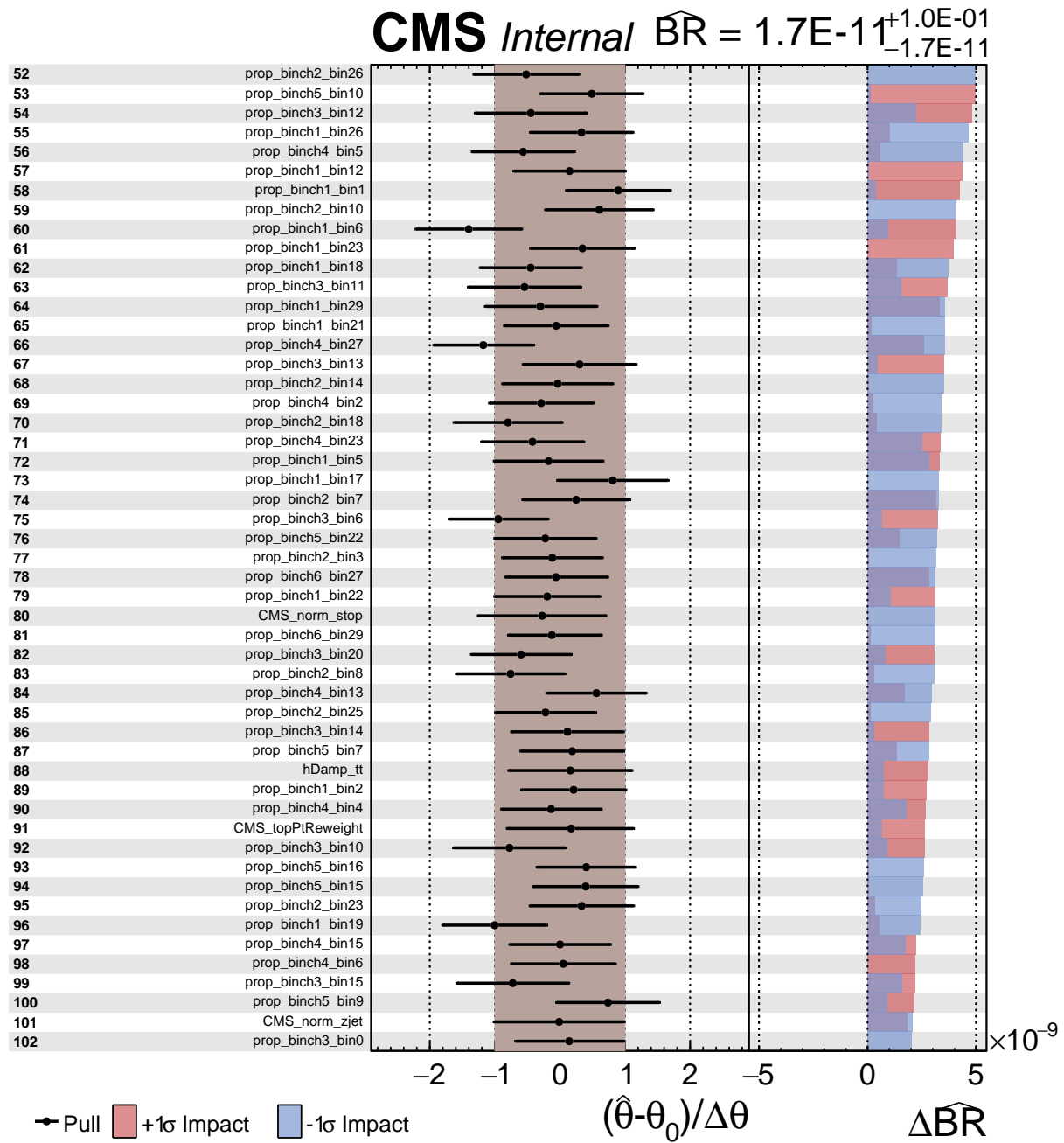


Figure 70: Distribution of post-fit pulls and impacts of nuisance parameters from exclusive event categories based on charm-tagging for  $m_{H^+} = 100$  GeV from 1 + jets channel. Contd ...

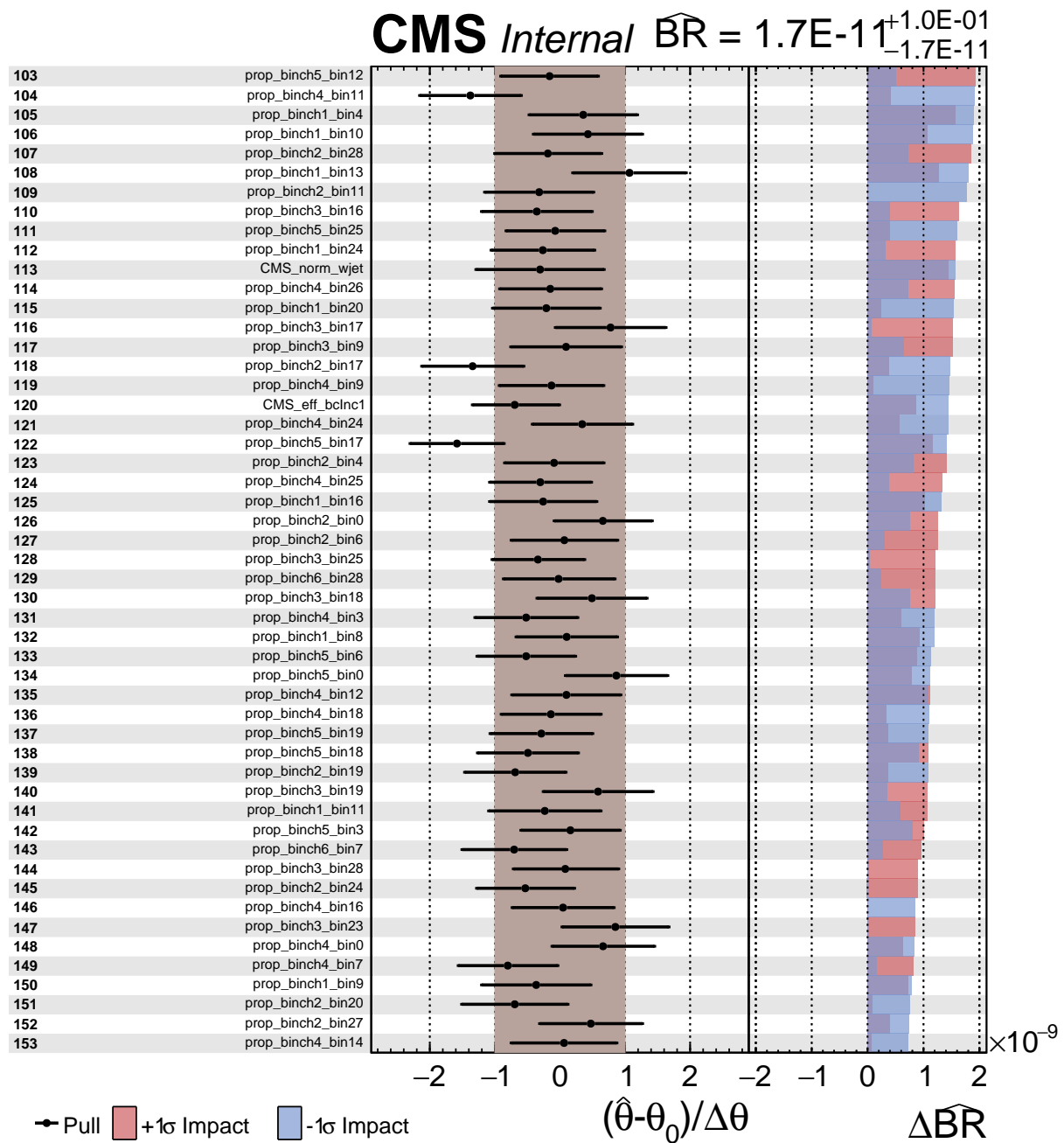


Figure 71: Distribution of post-fit pulls and impacts of nuisance parameters from exclusive event categories based on charm-tagging for  $m_{H^+} = 100$  GeV from 1 + jets channel. Contd ...

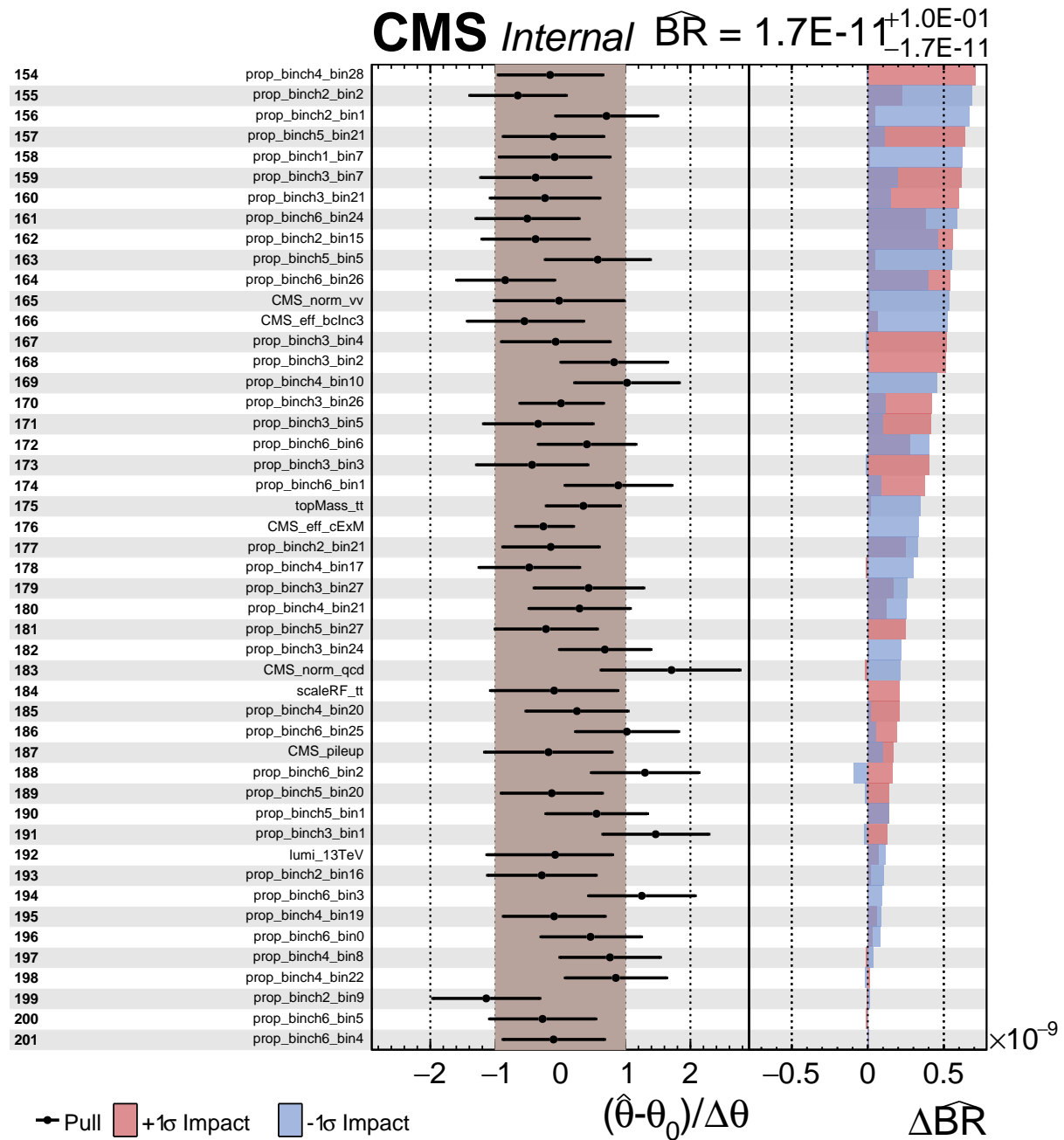


Figure 72: Distribution of post-fit pulls and impacts of nuisance parameters from exclusive event categories based on charm-tagging for  $m_{H^+} = 100$  GeV from 1 + jets channel.

## 1448 G Useful Commands

### 1449 Luminosity

The luminosity is calculated using the following command

```
brilcalc lumi -b "STABLE BEAMS" --normtag DATACERT.json  
-u /fb -i processedLumis.json
```

(35)

### 1450 Pileup

The pileup distribution in the data is calculated using the following command

```
pileupCalc.py -i JSONfile --inputLumiJSON pileup_latest.txt --calcMode true  
--minBiasXsec 69200 --maxPileupBin 101 --numPileupBins 101 puHist.root
```

(36)

1451 where `JSONfile` is the golden JSON file which contains good lumi section.

### 1452 Fit Diagnostics

The following commands are used for maximum likelihood fit inside the *combine* tool

```
combine t2wDataCard.root -m 100 -M FitDiagnostics --expectSignal 1  
--redefineSignalPOIs BR --setParameterRanges BR=0,0.10 --plots  
--saveShapes --saveWithUncertainties --saveNormalizations  
--cminDefaultMinimizerStrategy 0
```

(37a)

```
python diffNuisances.py -a fitDiagnostics.root --poi=BR -g fitDiag.pdf
```

(37b)

1453

### 1454 Goodness of Fit

The following commands are used to compute the GOF

```
combine t2wDataCard.root -M GoodnessOfFit --algo saturated
```

(38a)

```
combine t2wDataCard.root -M GoodnessOfFit --algo saturated -t 1000 -s -1
```

(38b)

1455

### 1456 Impact of Parameters

Following commands are used to compute the impact of NPs

```
combineTool.py -M Impacts -d t2wDataCard.root -m 100 --doInitialFit  
--robustFit 1 --redefineSignalPOIs BR --setParameterRanges BR=0,0.1  
--cminDefaultMinimizerStrategy 0
```

(39a)

```
combineTool.py -M Impacts -d t2wDataCard.root -m 100 --doFit  
--robustFit 1 --redefineSignalPOIs BR --setParameterRanges BR=0,0.1  
--cminDefaultMinimizerStrategy 0 --parallel 50
```

(39b)

```
combineTool.py -M Impacts -d t2wDataCard.root -m 100 -o nuisImpactJSON
```

(39c)

```
plotImpacts.py --cms-label "Internal" -i nuisImpactJSON -o nuisImpactPDF
```

(39d)

1457

**1458 Limit**

Following commands are used to compute the limit

```
text2workspace.py DATACARD.txt -o t2wDATACARD.root  
-P HiggsAnalysis.CombinedLimit.ChargedHiggs:brChargedHiggs
```

(40a)

```
combine --rAbsAcc 0.000001 t2wDATACARD.root -M AsymptoticLimits
```

(40b)

1459 where `DATACARD.txt` is the input data card file which contains the name of the histogram for  
1460 each process, and information about the statistical and systematics uncertainties.

**1461 Scan Parameters**

The  $2\Delta NLL$  as a function of NPs is computed using the following command

```
combine -M MultiDimFit -d t2wDataCard.root -m 100 --redefineSignalPOIs BR  
--setParameterRanges BR=0.0,0.10 -P nameNP --trackParameters BR  
--algo=grid points 20 -n nameNP
```

(41)

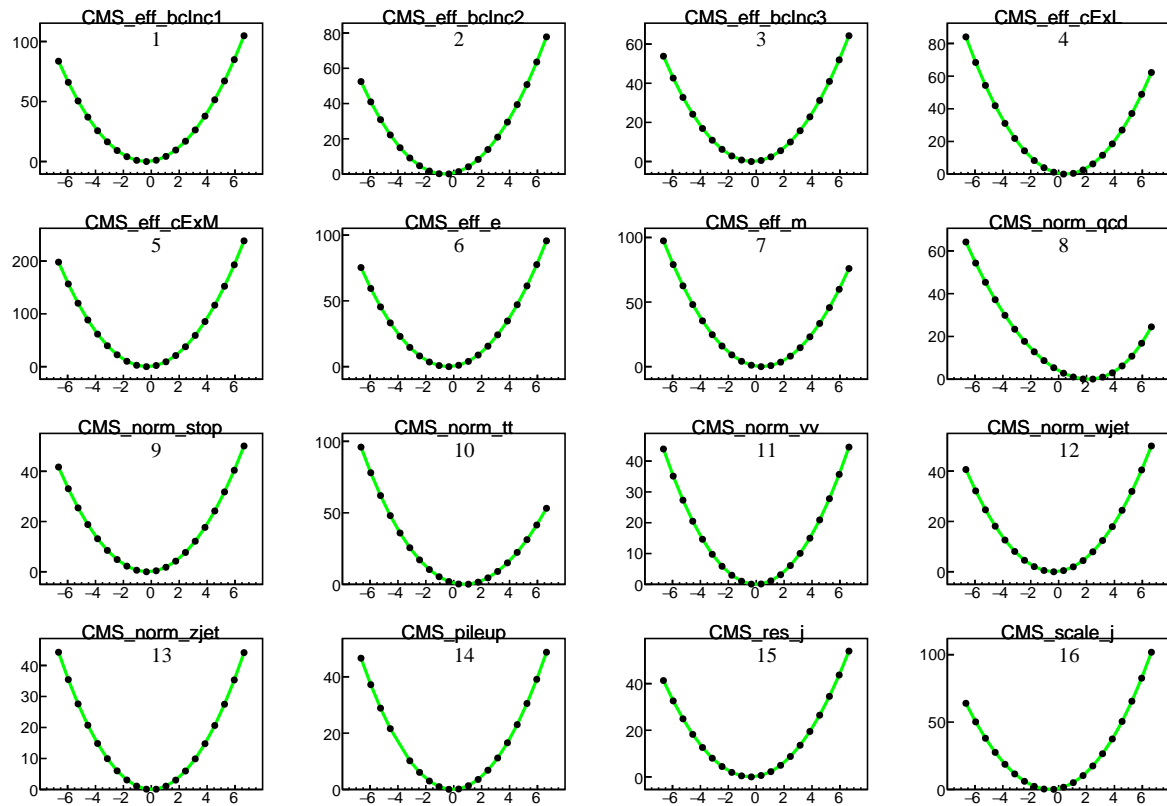
1462

DRAFT

**H 2 DeltaNLL vs NPs: Multi-dimensional Fit**

The  $2\Delta NLL$  (two times of difference in the negative of log likelihood) as a function of NPs is computed using the Command (41). The plots showing the variation of  $2\Delta NLL$  for different values of NPs are shown in Figure 73–85. From these figures, one can see that  $2\Delta NLL$  is symmetric for most of the parameters. However, the  $2\Delta NLL$  is a bit constrained for those NPs which are profiled as "shape" in the data cards such as `hDamp_tt`, `scaleRF_tt`. Also, the  $2\Delta NLL$  is asymmetric for few NPs which correspond to far higher and far lower bins of  $m_{jj}$  distribution (where the number of events is very small) such as `prop_binch1_bin29`, `prop_binch1_bin28`, `prop_binch1_bin3` etc. Please note that the bin29 correspond to  $30 \times 5 + 20 = 170$  GeV of  $m_{jj}$ , because the binning in autoMCStats starts from 0 and the bin width is 5 GeV and there is a  $20 \geq m_{jj} \geq 170$  GeV cut.

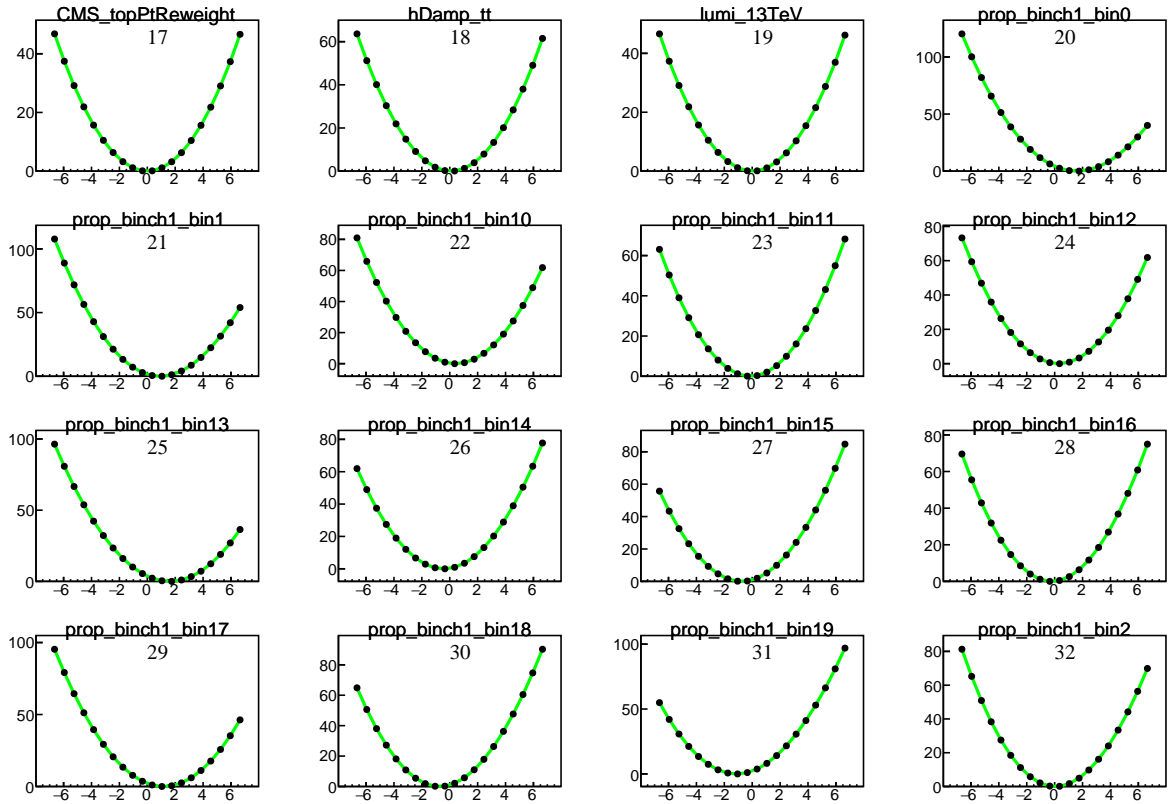
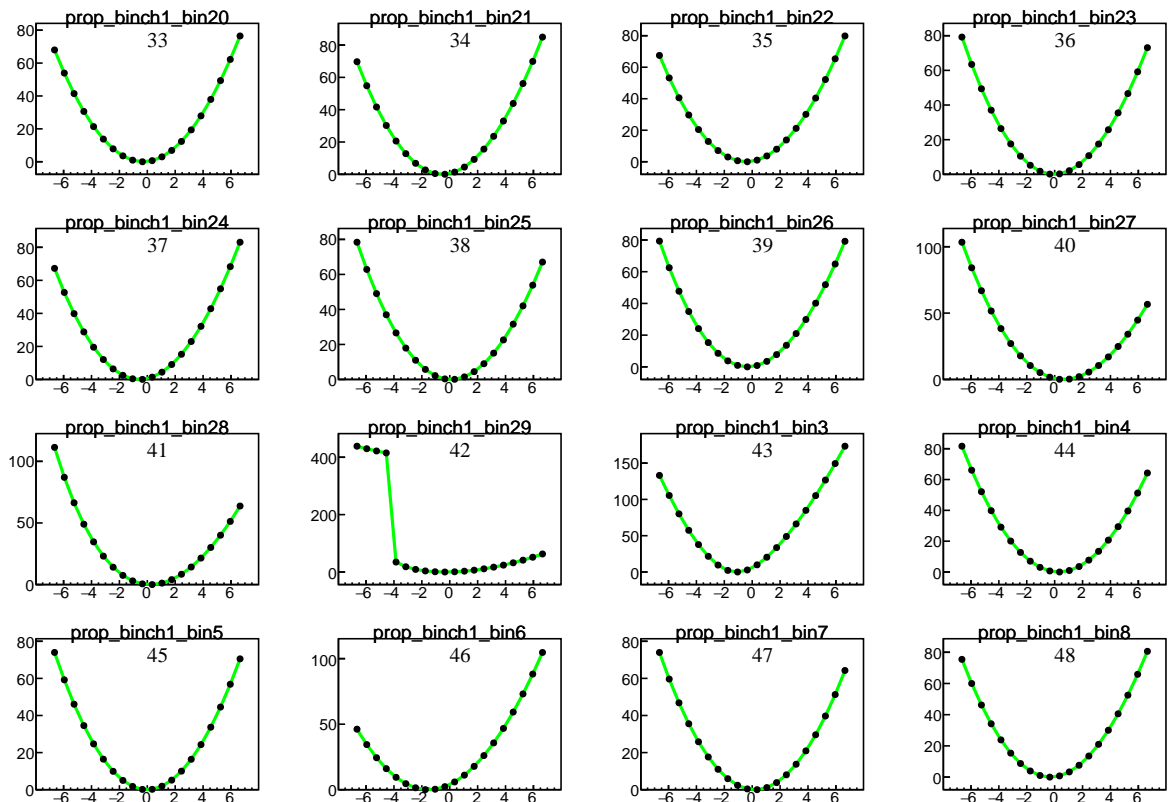
DRAFT

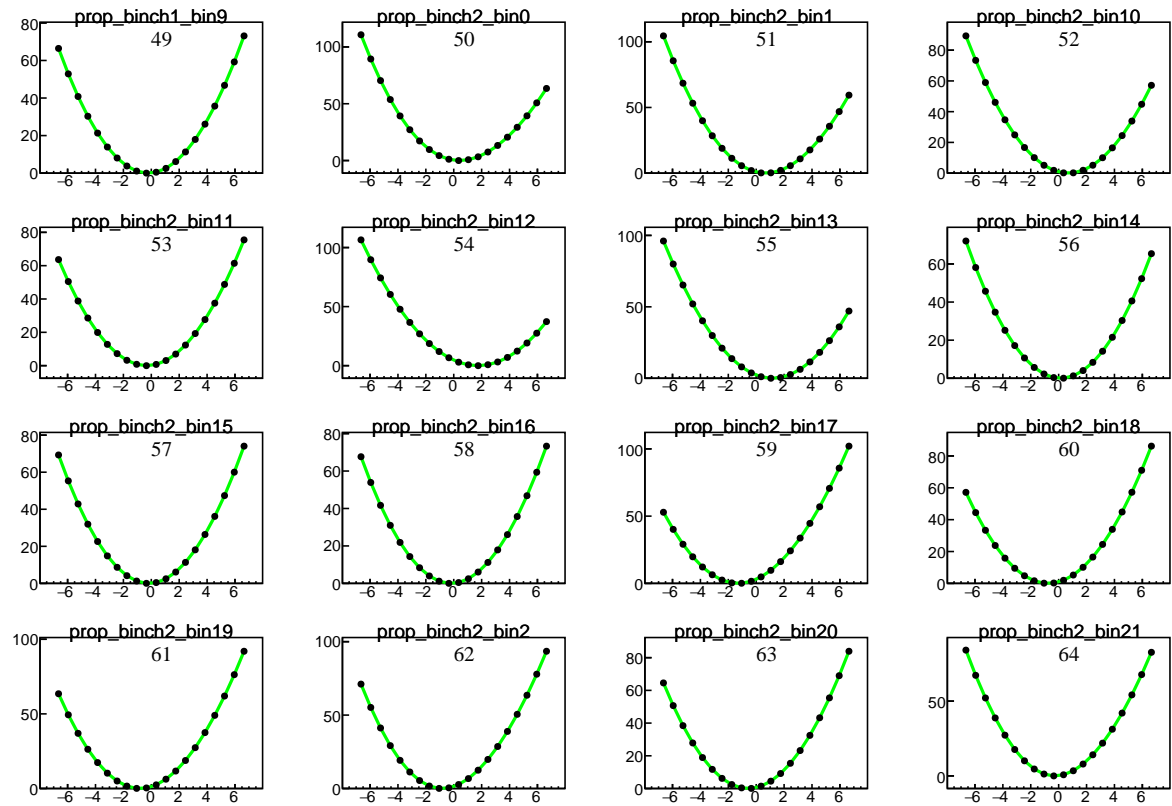
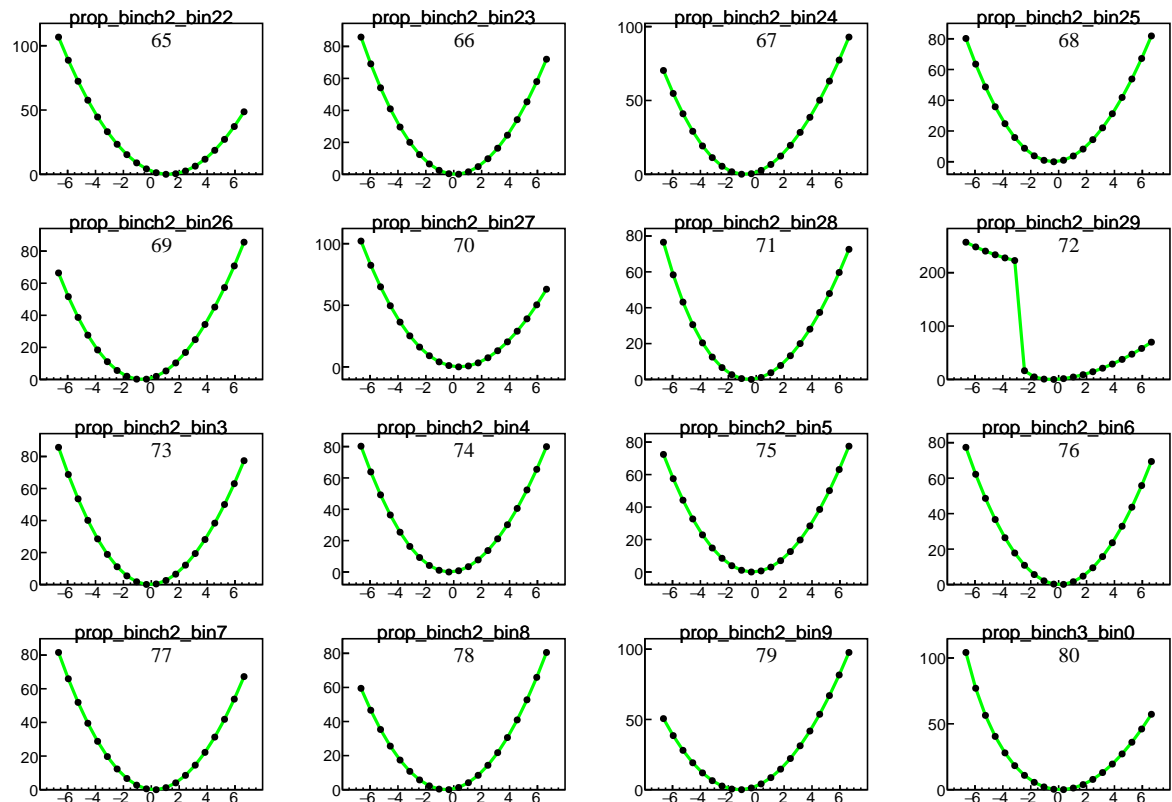
Figure 73:  $2\Delta NLL$  vs nuisance parameters. Contd ...

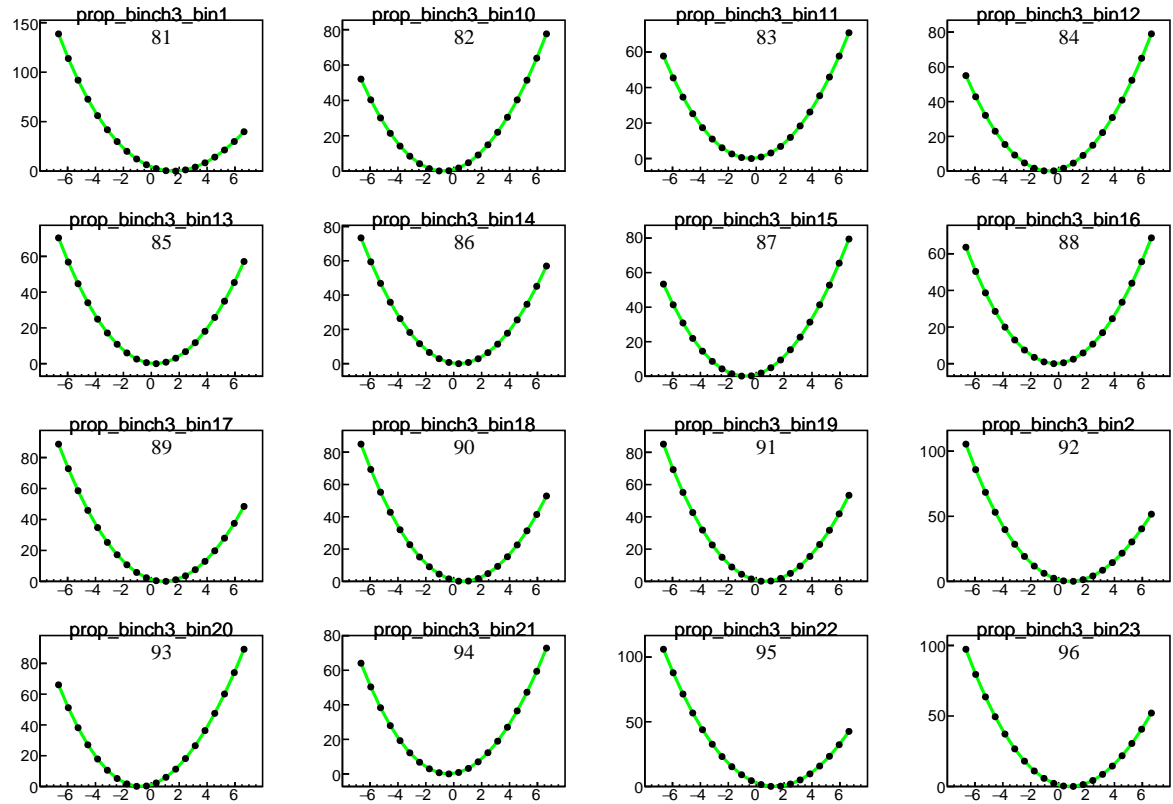
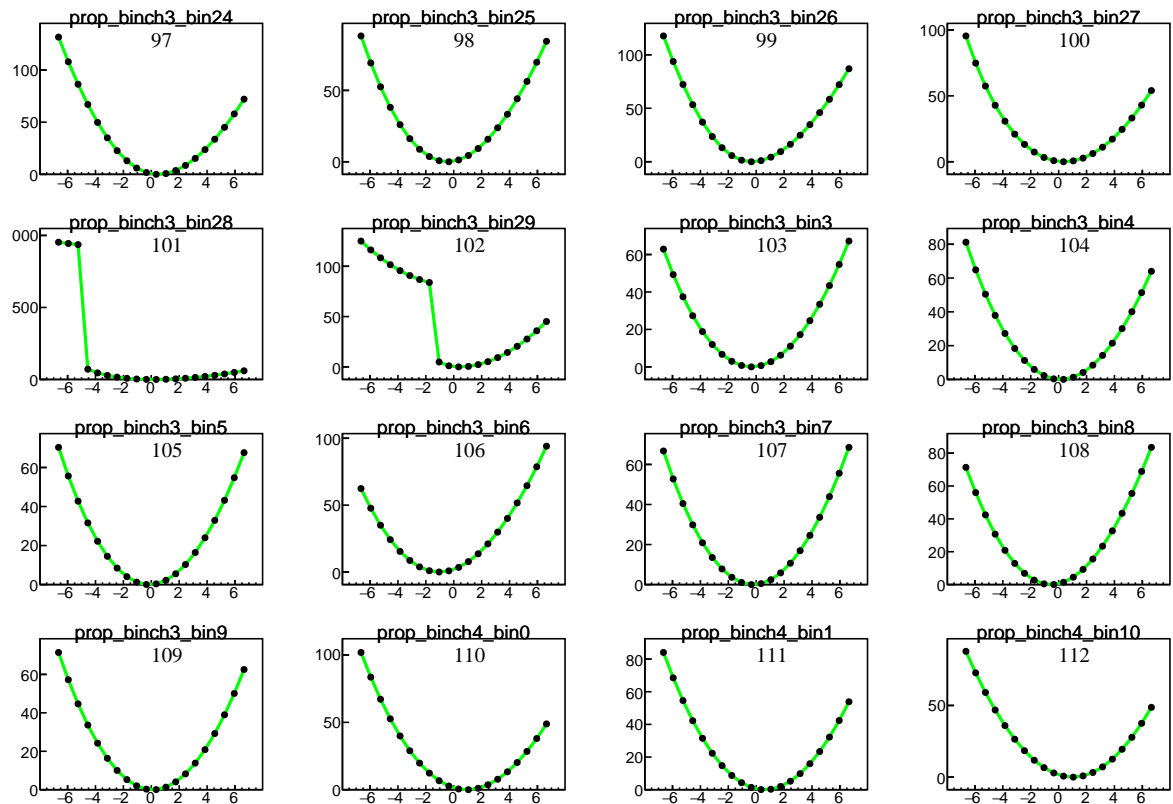
## **I Revision history of the Analysis Note**

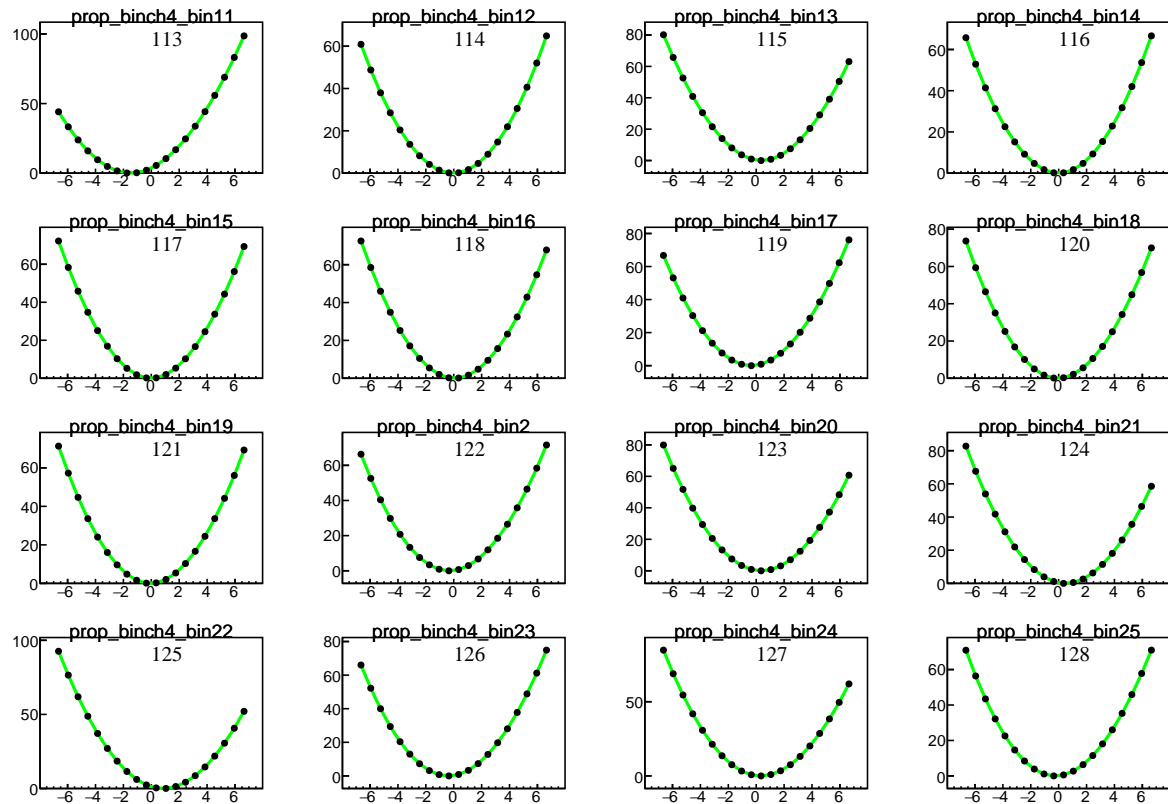
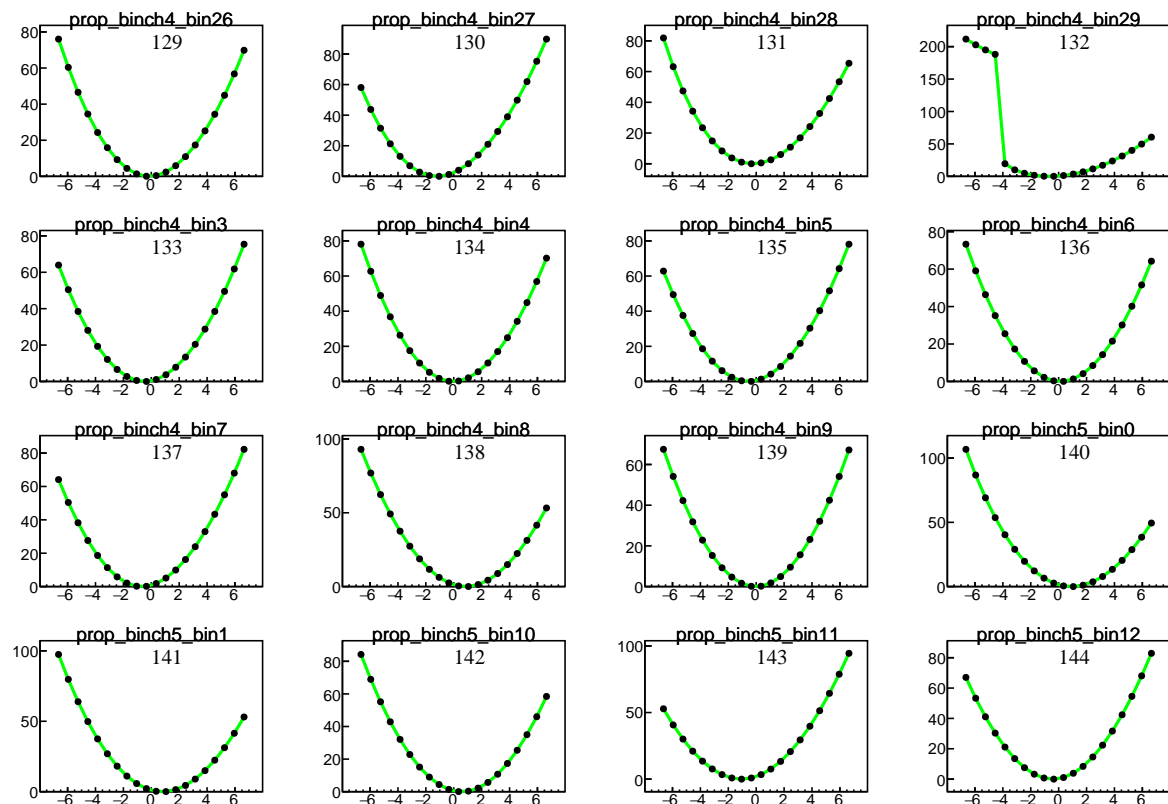
1474     **I Revision history of the Analysis Note**

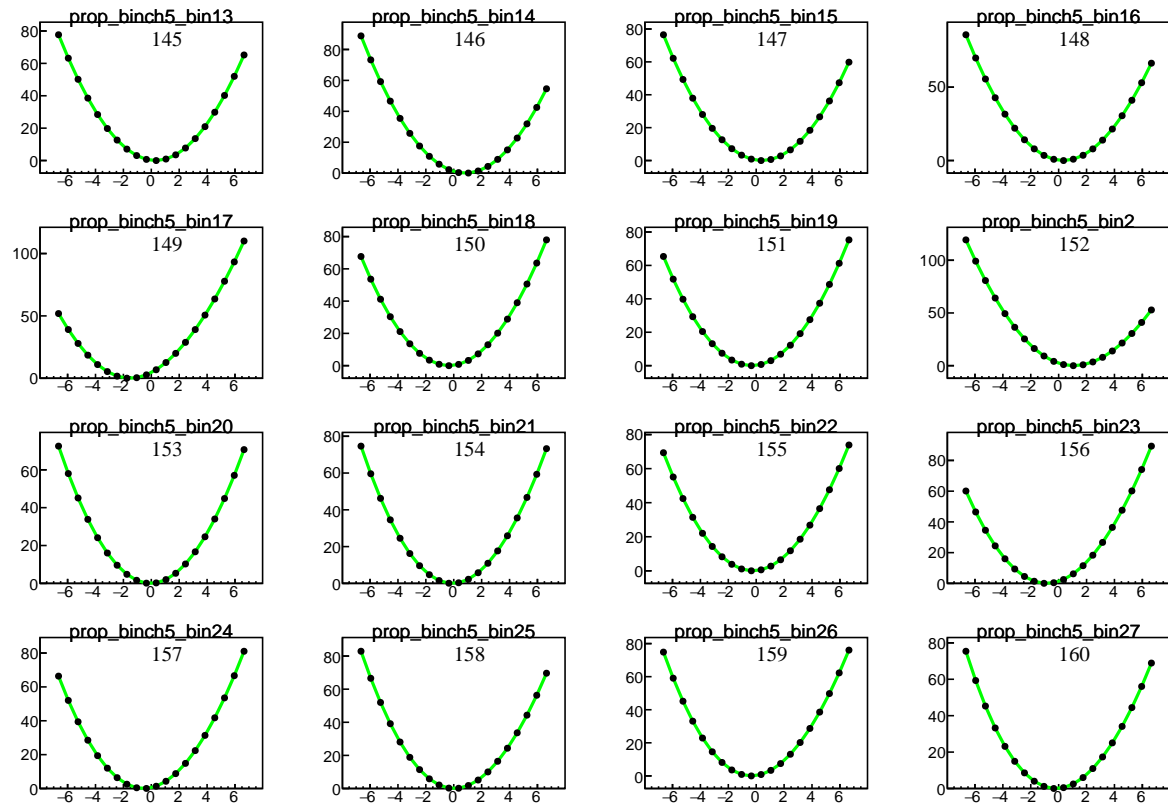
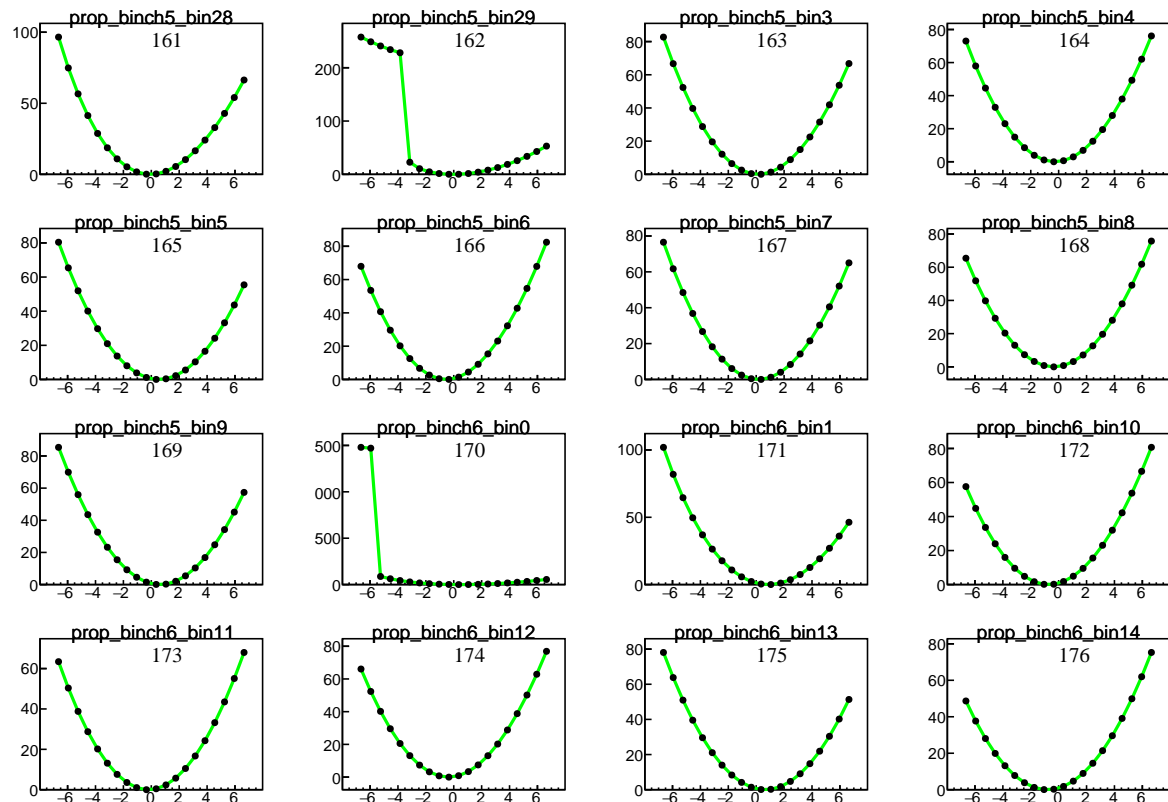
1475     The analysis was started in early 2016 and published in late 2020. A detailed timeline of the  
 1476     analysis is shown in the above figure. For every new version of the analysis note (AN), there  
 1477     were a few major changes w.r.t the previous version. In total there were 12 versions of the  
 1478     AN. A detailed comparison of all major changes in the all versions of the AN are listed in the  
 1479     following tables.

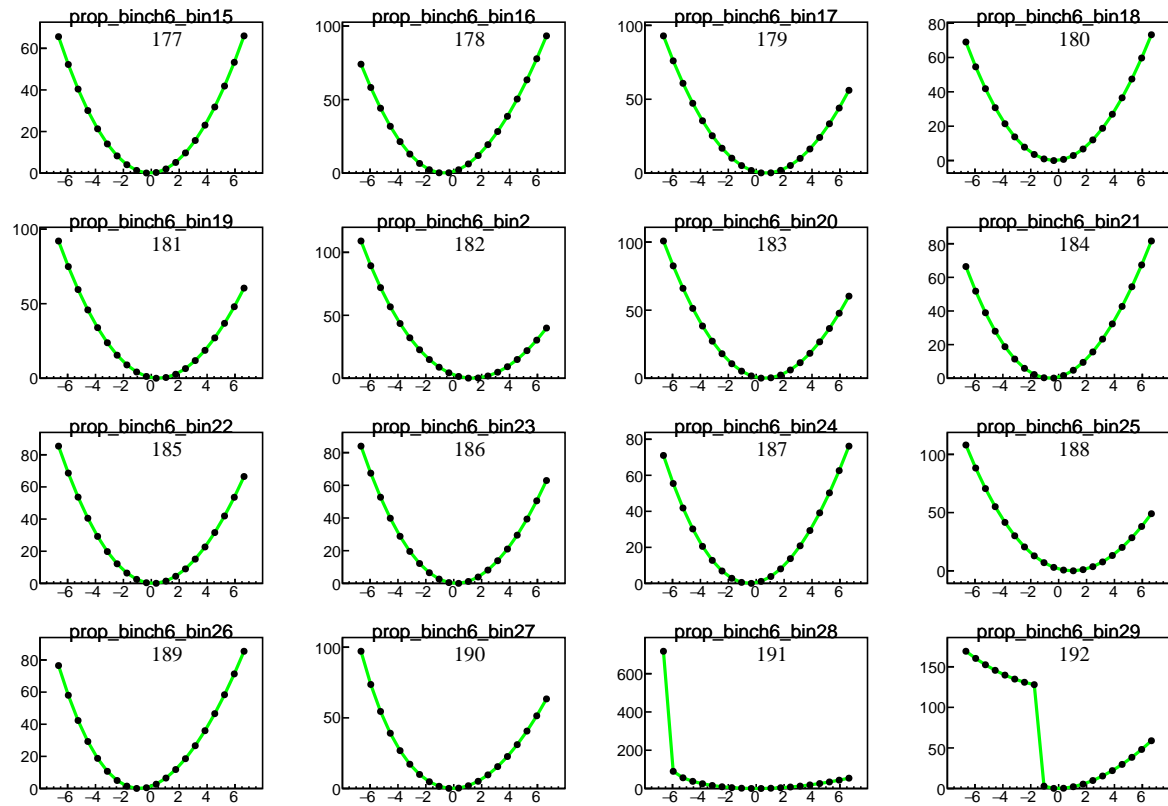
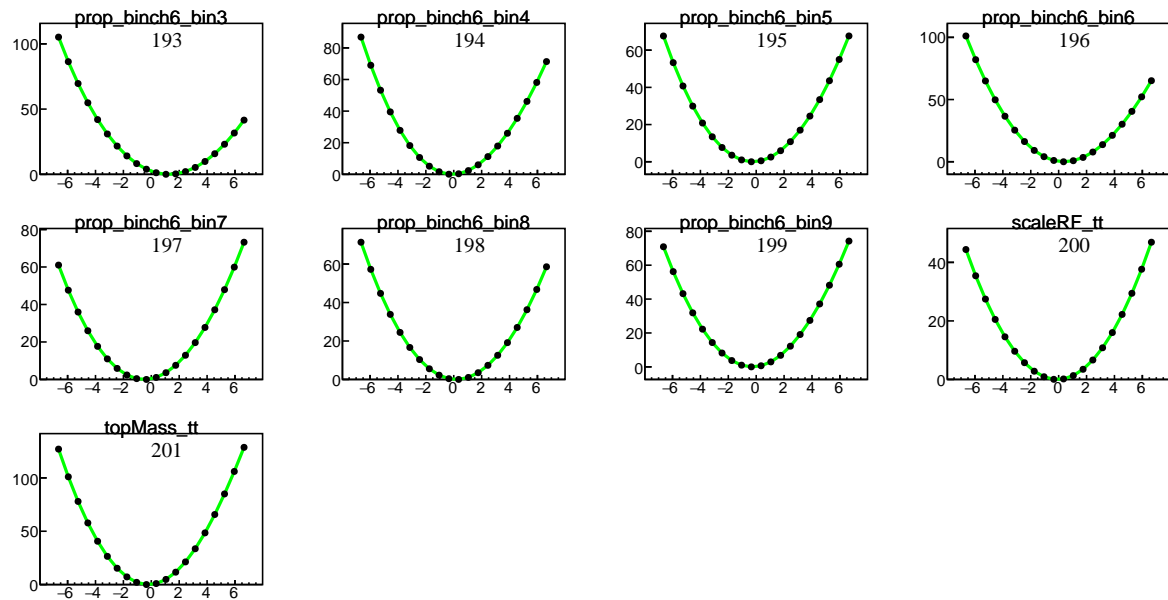
Figure 74:  $2\Delta NLL$  vs nuisance parameters. Contd ...Figure 75:  $2\Delta NLL$  vs nuisance parameters. Contd ...

Figure 76:  $2\Delta NLL$  vs nuisance parameters. Contd ...Figure 77:  $2\Delta NLL$  vs nuisance parameters. Contd ...

Figure 78:  $2\Delta NLL$  vs nuisance parameters. Contd ...Figure 79:  $2\Delta NLL$  vs nuisance parameters. Contd ...

Figure 80:  $2\Delta NLL$  vs nuisance parameters. Contd ...Figure 81:  $2\Delta NLL$  vs nuisance parameters. Contd ...

Figure 82:  $2\Delta NLL$  vs nuisance parameters. Contd ...Figure 83:  $2\Delta NLL$  vs nuisance parameters. Contd ...

Figure 84:  $2\Delta NLL$  vs nuisance parameters. Contd ...Figure 85:  $2\Delta NLL$  vs nuisance parameters.

Authors and principal reviewers of the analysis note

<b>Authors</b>	Shashi Dugad, Gouranga Kole, Gagan Mohanty, Arun Nayak, and Ravindra Kumar Verma
<b>Higgs-EXO conveners</b>	Abdollah Mohammadi and Anne-Marie
<b>Higgs-combine conveners</b>	David Sperka, Andrea Marini, and Giacomo Ortona
<b>Higgs conveners</b>	Giovanni Petrucciani, Roberto Salerno, and Maria Cepeda
<b>Analysis review committee</b>	Meenakshi Narain (chair), Varun Sharma (interim chair), Paul Lujhan (language editor for paper), Sourabh Dube, and Anna Kropivnitskaya
<b>Introduction section</b>	Pankaj Jain (IIT Kanpur)

Comparison of major changes in the AN from v11 and v12.

<b>AN2018_061_v11 (23/09/2019)</b>	<b>AN2018_061_v12 (29/12/2020)</b>
The lepton data-to-simulation scale factors were 1 for $p_T$ greater than the maximum $p_T$ -range of 2D histograms	For $p_T > p_T^{max}$ , scale factors are taken for $p_T^{max}$ . Although they are close to 1
Used different seed for random number generation for Rochester correction for all systematics	Used same seed for all systematics
Used <code>rc.kScaleFromGenMC()</code> function with incorrect arguments for Rochester correction	Used <code>rc.kScaleAndSmearMC()</code> function with correct arguments
Description about the addition of exclusive and inclusive W/Z + jets samples was based on luminosity	Described them based on hepNUP variable
$SF = \exp(0.0615 - 0.0005p_T)$ for t-quark $p_T$ systematics with parton level t-quark. Relative difference between the event yields without and applying SF <sup>2</sup> was considered as the systematics uncertainty	$SF = \exp(0.076 - 0.00076p_T)$ with particle level t-quark. Difference between nominal and SF applied. Rewrote t-quark $p_T$ reweighting section in more detail
QCD multijet sample QCD_Pt-15to20_EMEnriched for electron channel	Removed it
Global tag 80X_mcRun2_asymptotic_2016_TrancheIV_v6	80X_mcRun2_asymptotic_2016_TrancheIV_v10
-	Described the likelihood functions used for setting the upper limit
Only one table for showing the changes w.r.t. the current and previous versions of the analysis note	Kept all previous tables
-	Added timeline of the analysis
<b>Total 134 pages</b>	<b>Total 140 pages</b>

Comparison of major changes in the AN from v10 and v11.

<b>AN2018_061_v10 (09/09/2019)</b>	<b>AN2018_061_v11 (23/09/2019)</b>
-	Added correlation matrix of most significant fit parameters
-	Reproduced impact plots by using additional argument "- - cminDefaultMinimizerStrategy 0" in the command line
-	Used "newpage" latex command before a few sections
-	Rewrote and reshuffled a few sections for a better clarity
Fit diagnostics in appendix	It is in the main part
Impact plot in main part	It is in the appendix
Useful commands in main part	Put all commands in the appendix and referred them appropriately
<b>Total 127 pages</b>	<b>Total 134 pages</b>

Comparison of major changes in the AN from v9 and v10.

<b>AN2018_061_v9 (04/07/2019)</b>	<b>AN2018_061_v10 (09/09/2019)</b>
Pre-fit yields and distributions	Pre and post-fit yields and distributions
-	Added $\mathcal{B}(t \rightarrow H^+ b) = 0.065$ in plots
-	Added a plot showing final limits from 8 TeV and 13 TeV analysis
<b>Total 124 pages</b>	<b>Total 127 pages</b>

Comparison of major changes in the AN from v8 and v9.

<b>AN2018_061_v8 (26/06/2019)</b>	<b>AN2018_061_v9 (04/07/2019)</b>
Conservative styles for figures, plots, and tables	Followed CMS guidelines for each of them
Blinded analysis	Un-blinded analysis
<b>Total 120 pages</b>	<b>Total 124 pages</b>

Comparison of major changes in the AN from v7 and v8.

<b>AN2018_061_v7 (17/04/2019)</b>	<b>AN2018_061_v8 (26/06/2019)</b>
$M_{H^\pm}, M_{jj}$	$m_{H^+}, m_{jj}$
Considered systematic uncertainty in the QCD estimation as change in the transfer scale factor	Considered it as a change in the yield
-	Added uncertainty table for exclusive charm categories
<b>Total 118 pages</b>	<b>Total 120 pages</b>

Comparison of major changes in the AN from v6 and v7.

<b>AN2018_061_v6 (01/02/2019)</b>	<b>AN2018_061_v7 (17/04/2019)</b>
Muon: <code>HLT_IsoMu24*</code>	<code>HLT_IsoMu24* OR HLT_IsoTkMu*</code>
Muon: $\eta < 2.1$	$\eta < 2.4$
Electron: $d0 < 0.05, dz < 0.20$	$d0 < 0.05, dz < 0.10$ (in barrel), and $d0 < 0.10, dz < 0.20$ (in endcap)
Electron: relative isolation $< 0.08$	Relative isolation $< 0.0821$ for barrel and $< 0.0695$ for endcap
-	For jets: charged hadron multiplicity $> 0$ , number of constituent $> 1$ , charged hadron electromagnetic energy fraction $< 0.99$
$p_T^{\text{miss}}$ filters not applied	All filters have been applied
-	Scaled signal events by the maximum observed upper limit at 8 TeV in the plots.
-	Added table for event yields from exclusive charm categories.
A brief description of the kinematic fitting	Described it in detail
-	Added reconstruction, identification, and trigger efficiency plots for electron and muon
-	Added tables for b/c tagging efficiency
-	Updated all the tables and plots for a better visibility
Unblinded analysis	Blinded analysis
<b>Total 110 pages</b>	<b>Total 118 pages</b>

Comparison of major changes in the AN from v5 and v6.

<b>AN2018_061_v5 (11/01/2019)</b>	<b>AN2018_061_v6 (01/02/2019)</b>
Blinded analysis i.e. the observed data was shown only in the control regions and the exclusion limits were computed using MC simulation	Un-blinded analysis i.e. the observed data was also used in the signal region and limit computation
-	Added goodness-of-fit test
The systematic uncertainties corresponding to the renormalization and factorisation scale and damping parameters were profiled as "shape"	These are profiled as "lnN" as the ratio of these with nominal histograms is consistent with a flat line
<b>Total 109 pages</b>	<b>Total 110 pages</b>

Comparison of major changes in the AN from v4 and v5.

AN2018_061_v4 (14/05/2018)	AN2018_061_v5 (11/01/2019)
$p_{T\mu} > 25 \text{ GeV}$	$p_{T\mu} > 26 \text{ GeV}$
Applied b/c tag data-to-simulation scale factors using the promote-demote method	Applied these scale factors using event-by-event reweighting
-	Added TProfile plots between $p_T^{\text{miss}}$ and $I_{\text{rel}}$ for simulated QCD multijet sample. Removed few columns (after applying various scale factors) from cutflow tables. Considered one extra nuisance parameter as a systematic uncertainty for exclusive charm categories. Applied a proper correlation between b/c-tagged scale factors. Added signal to background ratio plot from exclusive charm categories for all masses of the charged Higgs. Added a section on the profiling of nuisance parameters in the likelihood. For comparison, added plots showing the ratio between base and up or down histograms for the different systematic uncertainties
Considered one nuisance parameter in each bin of only $t\bar{t}$ , single t, W+jets, and charged Higgs signal samples, manually, for bin-by-bin uncertainties	Assigned one nuisance parameter in each bin in the sum of all background and signal processes using autoMCStats tool which is based on Barlow-Beeston-lite approach. <span style="color:red">After using autoMCStats, event categorisation in bins of <math>p_T</math> of b jets does not improve the expected limit.</span> Hence, moved b jet $p_T$ binning section in the appendix
Systematic uncertainty in the luminosity measurement = 2.7% and lepton selection = 3.1%	It is 2.5% and 3.0%, respectively
Various systematic uncertainties such as those from b/c tagging, jet energy corrections (jet energy scale and resolution), pileup reweighting, t-quark $p_T$ reweighting, and measurement in the t-quark mass were profiled as "shape" in the data card for limit computation	Now these profiled as "lnN"
NPs from statistical uncertainty in the total number of events from each simulated sample were included in the data card	These NPs are removed from the data card, as they are internally included from autoMCStats tool
The NPs were named following the conventions of 8 TeV analysis.	They are renamed using recommended conventions at 13 TeV
-	Added plots for fit diagnostics, the variation of likelihood as function of individual NP, and showing the impacts of NPs on the parameter of interest
-	Updated all tables with latest results, proper fonts etc
The stacked and ratio plots were in a different pads	They are in the same pad
-	Added plots showing the observed data and simulated events from a control region ( $p_T^{\text{miss}} <$ ) 20 GeV
-	Added a section on the background contribution from all SM Higgs production processes. Included limits for the charged Higgs mass of 80 GeV
Total 81 pages	Total 109 pages

Comparison of major changes in the AN from v3 and v4.

<b>AN2018_061_v3 (04/05/2018)</b>	<b>AN2018_061_v4 (14/05/2018)</b>
-	Added columns in table 17 and 18 for the systematic uncertainties corresponding to the mis-identified b and c jet tagging
<b>Total 81 pages</b>	<b>Total 81 pages</b>

Comparison of major changes in the AN from v2 and v3.

<b>AN2018_061_v2 (06/04/2018)</b>	<b>AN2018_061_v3 (04/05/2018)</b>
Integrated luminosity = $35.50 \text{ fb}^{-1}$	$35.9 \text{ fb}^{-1}$
Muon isolated data-to-simulation scale factors were applied to all muons (isolated and non-isolated)	Only applied to isolated muons
Kinematic cuts (Table-4) + medium muon ID for second muon to be vetoed	Only Kinematic cuts (Table-4) for the second muon to be vetoed with no requirement on tracker related or $\chi^2$ cuts
Electron relative isolation cut was, by mistake, not applied inside the code on the second electron to be vetoed (although it is shown in Table-5)	Now applied
While evaluating data-to-simulation normalization, the cross-section for the charged Higgs sample was taken to be $0.32 \times \sigma_{t\bar{t}}$	Now, it is taken to be $0.2132 \times \sigma_{t\bar{t}}$
A fixed 3.3% pileup uncertainty was considered for all simulated samples	The minimum bias cross section is varied by 4.7% up and down and the corresponding pileup weights are applied. The pileup uncertainty is determined from the change w.r.t to base value
The b and c-tagged data-to-simulated scale factors were applied for the $t\bar{t}$ , charged Higgs signal, and single top production processes. For the rest simulated samples such as as W+jets, Z+jets, VV processes, the corresponding mis-tagged scale factors were applied	Now the b and c-tagged scale factors are applied for all simulated samples
<b>Total 79 pages</b>	<b>Total 81 pages</b>

Comparison of major changes in the AN from v1 and v2.

<b>AN2018_061_v1 (12/03/2018)</b>	<b>AN2018_061_v2 (06/04/2018)</b>
Being the first version of the AN, the documentation was too preliminary	Following the suggestions from authors, updated whole AN to be reviewed by the Higgs-EXO conveners
<b>Total 57 pages</b>	<b>Total 79 pages</b>